THE MINISTRY OF SCIENCE AND HIGHER EDUCATION OF THE RUSSIAN FEDERATION

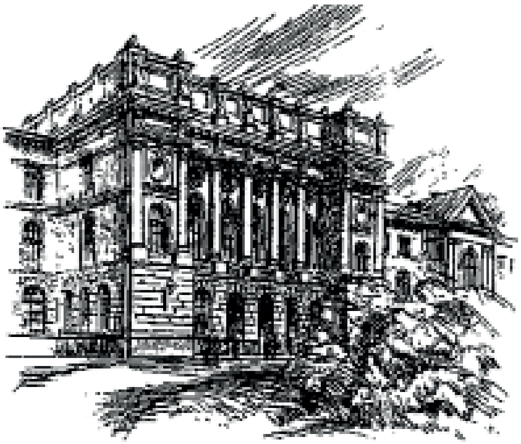

ST. PETERSBURG STATE POLYTECHNICAL UNIVERSITY JOURNAL

Physics and Mathematics

VOLUME 17, No.1.1,
2024

Peter the Great St. Petersburg
Polytechnic University
2024

ST. PETERSBURG STATE POLYTECHNICAL UNIVERSITY JOURNAL. PHYSICS AND MATHEMATICS

JOURNAL EDITORIAL COUNCIL

A.I. Borovkov – vice-rector for perspective projects;
V.A. Glukhikh – full member of RAS;
D.A. Indeitsev – corresponding member of RAS;
VA.I. Rudskoy – full member of RAS;
R.A. Suris – full member of RAS;
A.E. Zhukov – corresponding member of RAS.

JOURNAL EDITORIAL BOARD

V.K. Ivanov – Dr. Sci. (phys.-math.), prof., SPbPU, St. Petersburg, Russia, – editor-in-chief;
A.E. Fotiadi – Dr. Sci. (phys.-math.), prof., SPbPU, St. Petersburg, Russia, – deputy editor-in-chief;
V.M. Kapralova – Candidate of Phys.-Math. Sci., associate prof., SPbPU, St. Petersburg, Russia, – executive secretary;
V.I. Antonov – Dr. Sci. (phys.-math.), prof., SPbPU, St. Petersburg, Russia;
I.B. Bezprozvanny – Dr. Sci. (biology), prof., The University of Texas Southwestern Medical Center, Dallas, TX, USA;
A.V. Blinov – Dr. Sci. (phys.-math.), prof., SPbPU, St. Petersburg, Russia;
A.S. Cherepanov – Dr. Sci. (phys.-math.), prof., SPbPU, St. Petersburg, Russia;
D.V. Donetski – Dr. Sci. (phys.-math.), prof., State University of New York at Stony Brook, NY, USA;
V.V. Dubov – Dr. Sci. (phys.-math.), prof., SPbPU, St. Petersburg, Russia;
D.A. Firsov – Dr. Sci. (phys.-math.), prof., SPbPU, St. Petersburg, Russia;
P.A. Karasev – Dr. Sci. (phys.-math.), prof., SPbPU, St. Petersburg, Russia;
A.S. Kheifets – Ph.D., prof., Australian National University, Canberra, Australia;
O.S. Loboda – Candidate of Phys.-Math. Sci., associate prof., SPbPU, St. Petersburg, Russia;
J.B. Malherbe – Dr. Sci. (physics), prof., University of Pretoria, Republic of South Africa;
V.M. Ostryakov – Dr. Sci. (phys.-math.), prof., SPbPU, St. Petersburg, Russia;
V.E. Privalov – Dr. Sci. (phys.-math.), prof., SPbPU, St. Petersburg, Russia;
E.M. Smirnov – Dr. Sci. (phys.-math.), prof., SPbPU, St. Petersburg, Russia;
A.V. Solov'yov – Dr. Sci. (phys.-math.), prof., MBN Research Center, Frankfurt am Main, Germany;
A.K. Tagantsev – Dr. Sci. (phys.-math.), prof., Swiss Federal Institute of Technology, Lausanne, Switzerland;
I.N. Toptygin – Dr. Sci. (phys.-math.), prof., SPbPU, St. Petersburg, Russia;

The journal is included in the List of leading peer-reviewed scientific journals and other editions to publish major findings of theses for the research degrees of Doctor of Sciences and Candidate of Sciences.

The publications are presented in the VINITI RAS Abstract Journal and Ulrich's Periodical Directory International Database.

The journal is published since 2008 as part of the periodical edition 'Nauchno-tekhnicheskie vedomosti SPb-GPU'.

The journal is registered with the Federal Service for Supervision in the Sphere of Telecom, Information Technologies and Mass Communications (ROSKOMNADZOR). Certificate ПИ № ФС77-52144 issued December 11, 2012.

The journal is distributed through the CIS countries catalogue, the «Press of Russia» joint catalogue and the «Press by subscription» Internet catalogue. The subscription index is 71823.

The journal is in the **Web of Science** (Emerging Sources Citation Index), **Scopus,** the **Russian Science Citation Index** (RSCI) and the **Directory of Open Access Journals** (DOAJ) databases.

© Scientific Electronic Library (http://www.elibrary.ru).

No part of this publication may be reproduced without clear reference to the source.

The views of the authors may not represent the views of the Editorial Board.

Address: 195251 Politekhnicheskaya St. 29, St. Petersburg, Russia.

Phone: (812) 294-22-85.
http://ntv.spbstu.ru/physics

PREFACE

RYCPS 2023
XXV RUSSIAN YOUTH CONFERENCE
ON PHYSICS OF SEMICONDUCTORS AND NANOSTRUCTURES,
OPTO- AND NANOELECTRONICS
25
Nov 27 - Dec 1, 2023
St.Petersburg, Russia
http://www.semicond.ru/conf2023

25th Russian Youth Conference on Physics of Semiconductors and Nanostructures, Opto- and Nanoelectronics (RYCPS-2023)/ 25 Всероссийская молодежная конференция по физике полупроводников и наноструктур, полупроводниковой опто- и наноэлектронике

The 25th Russian Youth Conference on Physics of Semiconductors and Nanostructures, Opto- and Nanoelectronics (RYCPS-2023) was held in Saint Petersburg at Alferov University on November 27 – December 1, 2023. It was organized by Peter the Great St. Petersburg Polytechnic University, Alferov University, St. Petersburg State University, Ioffe Institute and Russian-Armenian University (Yerevan).

The program of the Conference included semiconductor technology, heterostructures with quantum wells and quantum dots, bulk properties of semiconductors, opto- and nanoelectronic devices and new materials. The Conference was held in face-to-face format and provided an opportunity for valuable discussions between the conference participants and experienced scientists.

The Conference included two invited talks given by leading scientists from Ioffe Institute, devoted to actual problems and major advances in physics and technology. The keynote speakers were *Nikolai Rozanov* (presentation "Extremely short electromagnetic pulses") and *Vladimir Shabaev* (presentation "Vacuum decay in a supercritical Coulomb field"). Young scientists, students, graduate and postgraduate students presented their results on plenary and poster sessions. The total number of accepted abstracts published in Russian (the official conference language) was 107. Here we publish 28 selected papers in English.

Following the traditions of the conference, the participants were involved in the competition for the best reports. Certificates and cash prizes were awarded to a number of participants for the presentations selected by the Program Committee. *Zakhar Yakovlev* (Information Technologies, Mechanics and Optics University, St. Petersburg) was awarded for the best conference presentation among students with a report " Fine structure of the energy spectrum of Fermi polarons in transition metal dichalcogenides". *Alexey Kuznetsov* (Moscow Institute of Physics and Technology) was awarded for the best conference presentation among postgraduate students with a report "Self-catalytic epitaxial gallium phosphide nanowires – waveguides for integrated nanophotonics". *Arina Yanzer*, a student at Lobachevsky State University of Nizhny Novgorod, received the Evgeni Gross Prize for the best presentation on semiconductor optics with a report "Thresholdless Auger recombination in quantum wells based on HgCdTe heterostructures in the range of 3 – 5 μm". The Evgeni Gross Prize for the best presentation on semiconductor optics among post graduate students was awarded to *Mikhail Ragoza* (Ioffe Institute) for report "Electrical resistance due to scattering of optically oriented electrons in n-GaAs". Works with potential applications were recommended for participation in the following competition for support from the Russian Foundation for Assistance to Small Innovative Enterprises in Science and Technology.

The conference was supported by the Ministry of Science and Higher Education of the Russian Federation (state assignment 075-03-2023-004), St. Petersburg Electrotechnical University and Tydex LLC, St. Petersburg.

The official conference website is http://www.semicond.ru/conf2023

Editors
R.A. Suris
D.A. Firsov
V.A. Shalygin
H.A. Sarkisyan

Contents

Bulk properties of semiconductors

Zhilyakov V. L., Yugova I. A. *Spin-dependent photon echo for an ensemble of three-level systems.......* 6

Melentev G. A., Karaulov D. A., Kostromin N. A., Vinnichenko M. Ya., Firsov D. A., Shalygin V. A. *Optical properties of GaN epitaxial layers in mid- and far-infrared ranges..* 12

Zdoroveyshchev D. A., Vikhrova O. V., Danilov Yu. A., Dudin Yu. A., Zdoroveyshchev A. V., Parafin A. E., Drozdov M. N. *Features of isovalent doping of gallium arsenide with bismuth ions......* 20

Pshenichnyi V. A., Dubinina T. V., Drozdov K. A. *Destruction of the conducting state by ac electric field in naphthalocyanine complexes..* 25

Berdnikov V. S., Kuznetsova M. S., Kavokin K. V., Dzhioev R. I. *Dynamics of electron-nuclear spin system in GaAs:Mn epitaxial layers..* 31

Structure growth, surface, and interfaces

Kozodaev D. A., Novikov I. A., Moshnikov V. A. *Investigation of nanosized structures using internal friction effect...* 37

Osinnykh I. V., Malin T. V., Milakhin D. S, Zhuravlev K. S. *Effect of growth temperature on photoluminescence properties of* NH_3*-MBE grown GaN-on-Si layers..* 43

Gogina O. A., Petrov Yu. V., Vyvenko O. F., Kovalchuk S., Bolotin K. *Electron irradiation as a method for controlling luminescence of hexagonal boron nitride...* 49

Heterostructures, superlattices, quantum wells

Domoratsky E. V., Zakharchenko M. V., Glinskii G. F. *Effects of resonant tunneling in GaAs/AlAs heterostructure...* 55

Chumanov I. V., Firsov D. D., Kolyada D. V., Komkov O. S., Skvortsov I. V, Mashanov V. I., Timofeev V. A. *Study of the band structure of GeSiSn/Ge/Si heterostructures by FTIR photoreflectance spectroscopy...* 62

Adamov R. B., Melentev G. A., Podoskin A. A., Slipchenko S. O., Sedova I. V., Sorokin S. V., Makhov I. S., Firsov D. A., Shalygin V. A., *Luminescence in nanostructures with compensated quantum wells under optical and electrical pumping...* 68

Ruzhevich M. S., Mynbaev K. D., Bazhenov N. L., Romanov V. V., Moiseev K. D. *Electroluminescence of narrow-gap InAs/*$InAs_{1-y}Sb_y$*/InAsSbP heterostructures with* $y = 0.07–0.12$*...........................* 77

Khakhulin S. A., Firsov D. D., Komkov O. S., Timofeev V. A., Skvortsov I. V., Mashanov V. I., Utkin D. E. *Polarized reflectance spectroscopy of aluminum nanoantennas on the surface of emitting GeSiSn/Si heterostructures...* 83

Sarypov D. I., Pokhabov D. A., Pogosov A. G., Egorov D. A., Zhdanov E. Yu., Bakarov A. K. *Gurzhi effect in point contacts in GaAs..* 89

Quantum wires, quantum dots, and other low-dimensional systems

Mashinsky K. V., Popov V. V., Fateev D. V. *Excitation of plasmon modes localized at the edge of a graphene rectangle by teraherz wave*........ 95

Zhivopistsev A. A., Romshin A. M., Gritsienko A. V., Lega P. V., Bagramov R. K., Filonenko V. P., Vitukhnovsky A. G., Vlasov I. I. *Single photon emission of “silicon-vacancy” centers in nanodiamonds placed in cylindrical pits on a gold film*........ 100

Ustimenko R.V., Karaulov D. A., Vinnichenko M. Ya., Makhov I. S., Firsov D. A., Sarkisyan H. A., Sargsian T. A., Hayrapetyan D. B., *Photoinduced light absorption in Ge/Si quantum dots*........ 105

Kozko I. A., Karaseva E. P., Sosnovitskaia Z. F., Istomina M. S., Fedorov V. V., Shmakov S. V., Kondratev V. M., Bolshakov A. D. *Photosensitive nanostructures based on gallium phosphide nanowires and carbon dots*........ 113

Karaseva E. P., Kozko I. A., Rider M. A., Kovova M. S., Zakharov V. V., Fedina S. V., Kondratev V. M., Bolshakov A. D. *Temperature evolution of GaP nanowires photoelectronic properties*........ 119

Sharov V. A., Alekseev P. A., Fedorov V. V., Mukhin I. S. *Individual GaP nanowire conductivity studied with atomic force microscopy and numerical modeling*........ 125

Eghbali A., Vyshnevyy A. A., *Quality factor enhancement of spherical resonators by radial anisotropy* 131

Optoelectronic and nanoelectronic devices

Nikolaeva A. V., Kondratev V. M., Kadinskaya S. A., Markina D. E., Lendyashova V. V., Dvoretckaia L. N., Monastyrenko A. O., Kochetkov F. M., Bolshakov A. D. *Potentially flexible sensor based on the ZnO-PDMS matrix for measuring mechanical load*........ 137

Kharin N. Yu., Panevin V. Yu., Vinnichenko M. Ya., Norvatov I. A., Fedorov V. V., Firsov D. A., *Terahertz and infrared photoluminescence in a structure based on n-GaAs with a waveguide for the near-infrared range*........ 143

Hamoud G. A, Kamaev G.N, Vergnat M., Volodin V.A., *Photocurrent in MIS structures based on germanosilicate films*........ 149

Soldatenkov F. Yu., Ivanov A.E., Malevskiy D. A., Levin S. V., *High-temperature high-voltage p–i–n diodes based on low doped heteroepitaxial layers AlGaAs and AlGaAsSb*........ 155

Mikhaylov O. P., Baranov A. I., Gudovskik A. S., Terukov E. I. *Deep-level transient spectroscopy of solar cells based on HJT architecture under influence of electron irradiation*........ 160

Kalinovskii V. S., Maleev N. A., Vasilyev A. P., Kontrosh E. V., Tolkachev I. A., Prudchenko K. K., Ustinov V. M., *Thermally stable connecting GaAs/AlGaAs tunnel diodes for laser radiation multi-junction photoconverters*........ 165

Novel materials

Matyunina K. S., Nikolskaya A. A., Kriukov R. N., Yunin P. A., Korolev D. S., *Formation and light-emitting properties of ion-synthesized Ga_2O_3 nanoinclusions in the Al_2O_3/Si matrix*........ 171

Conference Organizers and Sponsors........ 178

Bulk properties of semiconductors

Conference paper
UDC 537.6
DOI: https://doi.org/10.18721/JPM.171.101

Spin-dependent photon echo for an ensemble of three-level systems

V.L. Zhilyakov [1] ✉, I.A. Yugova [1]

[1] St. Petersburg State University, St. Petersburg, Russia

✉ st087753@student.spbu.ru

Abstract. We consider the action of a polarized rectangular laser pulse on a three-level system as a model of the interaction of electromagnetic radiation with matter. We managed to get the analytical solution for non-resonant excitation by light of a system with degenerate excited energy states without taking relaxation into account. The found analytical expressions were applied then to model the signal of a two-pulse photon echo from an ensemble of three-level systems.

Keywords: coherent dynamics, computer modeling

Funding: The authors acknowledge the Saint-Petersburg State University (Grant No. 94030557) and the Russian Science Foundation (Grant No. 19-72-20039) for the financial support of the theoretical analysis performed in this work.

Citation: Zhilyakov V.L., Yugova I.A., Spin-dependent photon echo for an ensemble of three-level systems, St. Petersburg State Polytechnical University Journal. Physics and Mathematics. 17 (1.1) (2024) 6–11. DOI: https://doi.org/10.18721/JPM.171.101

This is an open access article under the CC BY-NC 4.0 license (https://creativecommons.org/licenses/by-nc/4.0/)

Материалы конференции
УДК 537.6
DOI: https://doi.org/10.18721/JPM. 171.101

Спин-зависимое фотонное эхо для ансамбля трехуровневых систем

В.Л. Жиляков [1] ✉, И.А. Югова [1]

[1] Санкт-Петербургский государственный университет, Санкт-Петербург, Россия

✉ st087753@student.spbu.ru

Аннотация. В данной работе рассмотрена модель взаимодействия электромагнитного излучения с веществом на примере действия поляризованного прямоугольного лазерного импульса на трехуровневую систему. Получено решение для нерезонансного возбуждения светом системы с вырожденными возбужденными энергетическими состояниями без учета релаксации. Найденные аналитические выражения были применены при моделировании сигнала двухимпульсного фотонного эха от ансамбля трехуровневых систем.

Ключевые слова: когерентная динамика, компьютерное моделирование

Финансирование: Авторы благодарят Санкт-Петербургский Государственный Университет, грант № 94030557, и Российский Научный Фонд, грант № 19-72-20039, за финансовую поддержку исследований.

Ссылка при цитировании: Жиляков В.Л., Югова И.А. Спин-зависимое фотонное эхо для ансамбля трехуровневых систем // Научно-технические ведомости СПбГПУ. Физико-математические науки. 2024. Т. 17. № 1.1. С. 6–11. DOI: https://doi.org/10.18721/JPM.171.101

Статья открытого доступа, распространяемая по лицензии CC BY-NC 4.0 (https://creativecommons.org/licenses/by-nc/4.0/)

© Zhilyakov V.L., Yugova I.A., 2024. Published by Peter the Great St. Petersburg Polytechnic University.

Introduction

The study of the interaction of electromagnetic radiation with matter is one of the fundamental aspects of physics. The investigations of processes occurring in a medium under the influence of radiation allows one to obtain unique information about the physical properties of the matter, its composition, and structure. This plays an important role in our understanding of the nature [1]. Currently, knowledge about the interaction of radiation with matter is actively used for the development of the technology. This is confirmed by advances in electronics, the creation of new ways of working with optical information, and the development of new types of lasers. Thus, a fundamentally important task is the creation of theoretical models. Despite the apparent complexity of a comprehensive description of the processes that occur in matter under the action of a radiation, there are models that explain important phenomena by simplifying them from a physical point of view. For example, the influence of the radiation on multielectron atoms in some cases can be reduced to the consideration of electron transitions between certain levels since the influence of other levels is much less significant or even negligible. Such models, in particular, make it possible to describe the effects of four-wave mixing and photon echo, which have promise as a physical implementation of quantum memory underlying quantum communication [2,3]. In recent studies of trions in charged InGaAs quantum dots it was shown that using control pulses it is possible to separate the photon echo signal into two circular components [4]. In the trion system transitions with different circular polarizations are not coupled and can be excited independently by control pulses because in the absence of a magnetic field the system represents in fact two two-level systems. For a three-level exciton system, transitions with different spins are connected through a common ground state. Therefore, it is interesting to compare the behavior of the excitonic system under the action of control pulses by analogy with what was obtained for trions. In our work a model of interaction between electromagnetic radiation and matter was studied. We examined the effect of a polarized rectangular laser pulse on a three-level system. For the case when a system with degenerate excited states is excited by non-resonant light analytical solutions were obtained. We analyzed the dependence of the probability of the system being in a certain state on the frequency detuning and the pulse area. Then we applied the resulting analytical expressions to model the two-pulse photon echo signal from an ensemble of three-level systems. We investigated the sequential action of two short polarized laser pulses on three-level systems and the free dynamics of the system. As a result, time profiles of the photon echo signal were obtained for various excitation protocols with pulses of different polarization and power.

Theoretical model

An important example of radiation that well describes the real effect on matter is a rectangular laser pulse. It is considered further and the expression for the pulse has the following form:

$$E_{\pm}(t) = E_0^{\pm}(t) \cdot e^{-i\omega t}, \tag{1}$$

here $E_0^{\pm}(t) = \begin{cases} E_0^{\pm}, 0 < t < t_p \\ 0, t > t_p \end{cases}$ and ω are the amplitude and the frequency of the electromagnetic wave, t_p is the pulse duration.

We consider a three-level system as a medium, i.e., a model of matter that has three energy states. The description of the behavior of such a medium is given by the Schrödinger equation. The use of perturbation theory allows us to take into account the influence of electromagnetic radiation on the system.

In this case, the Hamiltonian in the Schrödinger equation consists of the Hamiltonian H_0 of the unperturbed system and of the term which is responsible for the interaction with electromagnetic radiation V.

$$\widehat{H}_0 = \begin{pmatrix} 0 & 0 & 0 \\ 0 & \hbar\omega_0 & 0 \\ 0 & 0 & \hbar\omega_0 \end{pmatrix}, \tag{2}$$

© Жиляков В.Л., Югова И.А., 2024. Издатель: Санкт-Петербургский политехнический университет Петра Великого.

where ω_0 is the frequency of the transition between the ground and the excited states.

$$\hat{V} = \begin{pmatrix} 0 & (d_+E_+)^* & (d\_E\_)^* \\ d_+E_+ & 0 & 0 \\ d\_E\_ & 0 & 0 \end{pmatrix}, \tag{3}$$

here $d_+ = \left\langle 1 \middle| \hat{d} \middle| 0 \right\rangle$, $d_- = \left\langle 2 \middle| \hat{d} \middle| 0 \right\rangle$ are matrix elements of the dipole moment operator. We can assume, for example, that transitions to different excited states can be allowed for different polarizations of an electromagnetic wave.

The Schrödinger equation can be written as follows:

$$i\hbar \begin{pmatrix} \dot{\alpha}_0 \\ \dot{\alpha}_1 \\ \dot{\alpha}_2 \end{pmatrix} = \begin{pmatrix} 0 & (d_+E_+)^* & (d\_E\_)^* \\ d_+E_+ & \hbar\omega_0 & 0 \\ d\_E\_ & 0 & \hbar\omega_0 \end{pmatrix} \begin{pmatrix} \alpha_0 \\ \alpha_1 \\ \alpha_2 \end{pmatrix}, \tag{4}$$

where $\psi = \begin{pmatrix} \alpha_0 \\ \alpha_1 \\ \alpha_2 \end{pmatrix}$ is the wave function expanded over the basis of eigenstates.

Thus, the Schrödinger equation for a three-level system interacting with a rectangular laser pulse is a system of the three ordinary differential equations. Taking into account the initial conditions (the value of the wave functions at the initial time), analytical solutions were obtained:

$$\alpha_0(t) = e^{-i\frac{\Delta}{2}t} \cdot \left[\alpha_0^0 \left(\cos\left(\frac{\Omega}{2}t\right) + i\frac{\Delta}{\Omega}\sin\left(\frac{\Omega}{2}t\right) \right) - 2i\frac{f_+^*\alpha_1^0 + f_-^*\alpha_2^0}{\Omega}\sin\left(\frac{\Omega}{2}t\right) \right], \tag{5}$$

here $\Delta = \omega_0 - \omega$ is the detuning from the laser carrier frequency, $\Omega = \sqrt{\Delta^2 + 4|f_+|^2 + 4|f_-|^2}$ is the generalized Rabi frequency, $f_\pm = \dfrac{d_\pm E_0^\pm}{\hbar}$ is the pulse area.

$$\begin{aligned} \alpha_1(t) = {} & \left[\alpha_1^0 - \frac{M_+\alpha_1^0 + f_-^* f_+ \alpha_2^0}{M_+ + M_-} \right] \cdot e^{-i\omega_0 t} - 2i\frac{f_+\alpha_0^0}{\Omega}\sin\left(\frac{\Omega}{2}t\right) \cdot e^{i(\frac{\Delta}{2} - \omega_0)t} + \\ & + \left[\frac{M_+\alpha_1^0 + f_-^* f_+ \alpha_2^0}{M_+ + M_-} \left(\cos\left(\frac{\Omega}{2}t\right) - i\frac{\Delta}{\Omega}\sin\left(\frac{\Omega}{2}t\right) \right) \right] \cdot e^{i(\frac{\Delta}{2} - \omega_0)t}, \end{aligned} \tag{6}$$

$$\begin{aligned} \alpha_2(t) = {} & \left[\alpha_2^0 - \frac{M_-\alpha_2^0 + f_+^* f_- \alpha_1^0}{M_+ + M_-} \right] \cdot e^{-i\omega_0 t} - 2i\frac{f_-\alpha_0^0}{\Omega}\sin(\tfrac{\Omega}{2}t) \cdot e^{i(\frac{\Delta}{2} - \omega_0)t} + \\ & + \left[\frac{M_-\alpha_2^0 + f_+^* f_- \alpha_1^0}{M_+ + M_-} \left(\cos\left(\frac{\Omega}{2}t\right) - i\frac{\Delta}{\Omega}\sin\left(\frac{\Omega}{2}t\right) \right) \right] \cdot e^{i(\frac{\Delta}{2} - \omega_0)t}, \end{aligned} \tag{7}$$

where $M_\pm = |f_\pm|^2$.

Fig. 1 shows the dependencies of the probabilities of the system being in the ground and excited states on the detuning and on the magnitude of the pulse area when interacting with light occurs for one excited state only ($f_- = 0$), that is, in fact, a two-level system. It is assumed that the system was initially in the ground state. As can be seen from the figure, the populations of the levels oscillate. The magnitude of the detuning has a great influence, so with the same pulse power but with different detuning the transitions are different. The analysis shows that if the initial condition is that the system is in an excited state, then the graphs, as expected, are inverted relative to each other. Fig. 2 shows the dependences of the probabilities of the system being in both excited states on the detuning and the magnitude of the pulse area ($f_+ = f_-$). It is assumed that initially the system was in one of the excited states. Calculations show that the probability of the system being in the ground state looks similar to the probability for a two-level system. Moreover, it is clear from Fig. 2 that the probabilities of being in excited states form a complex checkerboard structure, since now they are distributed. The oscillations in the probabilities of finding the system between these states can be observed.

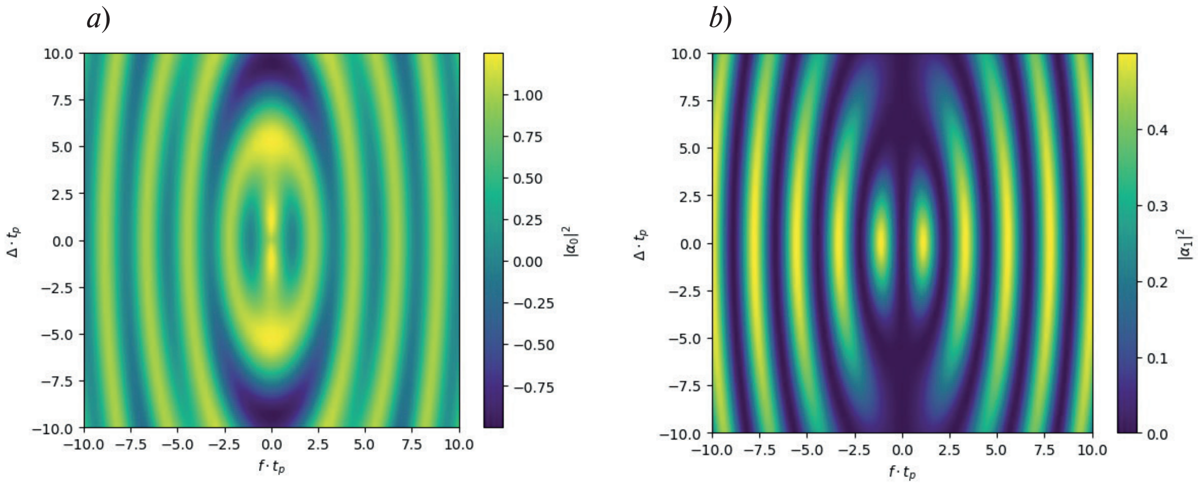

Fig.1. Dependences of the probabilities of the system being in the ground state (*a*) and in the excited state (*b*) on the pulse area and the detuning of the light frequency from the resonance of the system. Only one excited state interacts with light

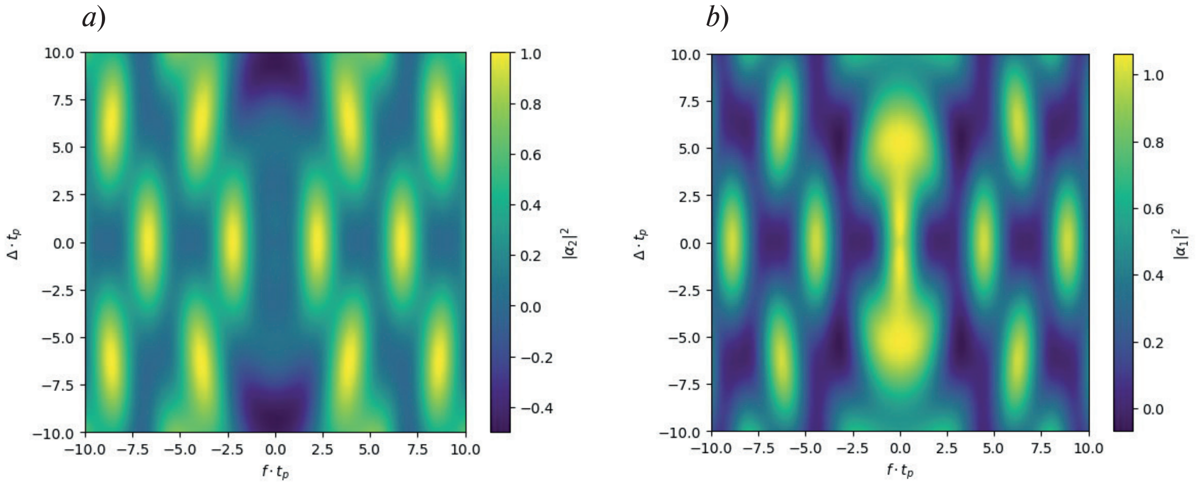

Fig. 2. Dependences of the probabilities of the system being in excited states 1 (*a*) and 2 (*b*) as a function of the pulse area and the detuning. Initially, the system was in an excited state 1

The density matrix formalism was used to model the photon echo signal. The evolution of the three-level system was determined by the Lindbland equation:

$$i\hbar \frac{\partial \rho}{\partial t} = \left[\widehat{H}, \rho \right] + i\hbar\Gamma, \tag{8}$$

here ρ is the density matrix, $\Gamma = \begin{pmatrix} (\rho_{11} + \rho_{22})/T_1 & -\rho_{01}/T_2 & -\rho_{02}/T_2 \\ -\rho_{10}/T_2 & -\rho_{11}/T_1 & -\rho_{12}/T_1 \\ -\rho_{20}/T_2 & -\rho_{21}/T_1 & -\rho_{22}/T_1 \end{pmatrix}.$

As in the previous part the Hamiltonian consisted of the Hamiltonian of the unperturbed system H_0 and the perturbation V for both impulses. The sequential action of two short laser pulses separated in time by a value of τ was considered taking into account the free precession between them. It was assumed that the time of the pulses action on the system is much shorter than the relaxation time which is in good agreement with experimental conditions in most cases. With such assumptions the problem can be divided into two parts: the consideration the interaction with light without taking into account relaxation during the pulses action; and the consideration the dynamics of the system. Using previously obtained expressions for the action of the pulse, we found the elements of the density matrix responsible for the contribution to the formation of the echo signal:

$$\tilde{\rho}_{01} \sim e^{-i\omega_0(t-2\tau)} e^{-t/T_2} \cdot \left|\alpha_0^0\right|^2 \cdot iL_1 \cdot L_2^2 \cdot M_1^* \left(f_{+1}^* f_{+2}^2 + f_{-1}^* f_{+2} f_{-2}\right), \qquad (9)$$

$$\tilde{\rho}_{02} \sim e^{-i\omega_0(t-2\tau)} e^{-t/T_2} \cdot \left|\alpha_0^0\right|^2 \cdot iL_1 \cdot L_2^2 \cdot M_1^* \left(f_{-1}^* f_{-2}^2 + f_{+1}^* f_{+2} f_{-2}\right), \qquad (10)$$

where $L_{1,2} = \dfrac{\sin(\Omega_{1,2} \cdot t_p)}{\Omega_{1,2} \cdot t_p}$, $\Omega_{1,2} = \sqrt{\nu_{1,2}^2 + \left|f_{-1,2}^2\right| + \left|f_{+1,2}^2\right|}$, $M_1 = \cos\left(\Omega_1 \cdot t_p\right) - i\dfrac{\nu}{\Omega_1}\sin\left(\Omega_1 \cdot t_p\right)$, $\nu = \dfrac{\Delta}{2}$.

The final expression for the polarization in the direction of four-wave mixing is:

$$P_\nu = \left\langle \hat{d} \right\rangle = Tr\left(\hat{d}\rho\right) \propto \mathrm{Re}\left(d_+ \tilde{\rho}_{01} + d_- \tilde{\rho}_{02}\right). \qquad (11)$$

We consider the case when the spectral width of the pulse is comparable to the distribution width of the systems under study:

$$P = \int_{-\infty}^{\infty} P_\nu \cdot e^{-\frac{\nu^2}{2\sigma^2}} d\nu, \qquad (12)$$

here σ is the variance of the normal distribution of three-level systems.

Numerical integration was used to obtain time profiles of the photon echo signal. The result is shown in Fig. 3.

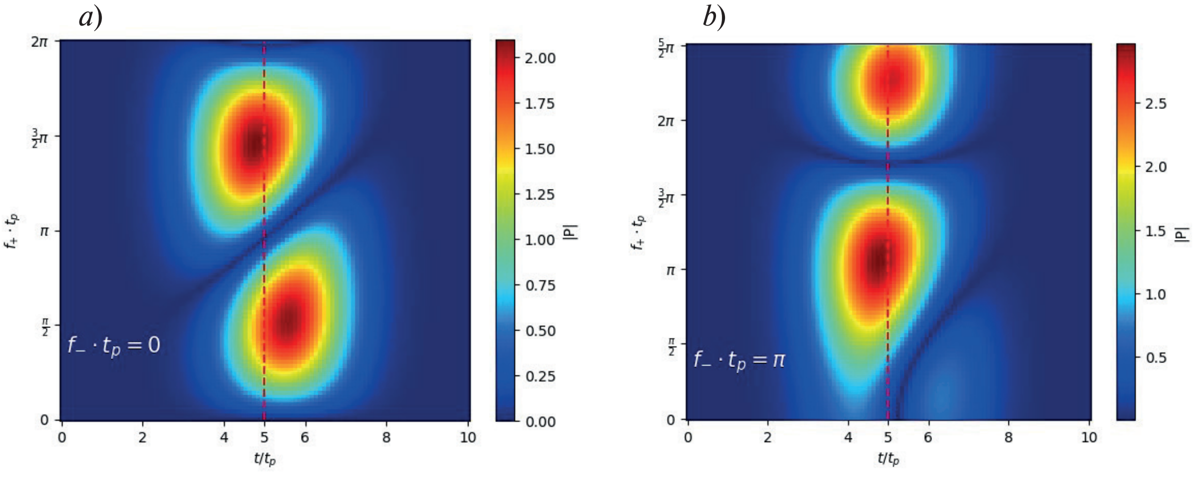

Fig. 3. Time profiles of the photon echo signal at $f_- = 0$ (*a*) and at $f_- = \pi$ (*b*)

It can be seen from the figure that the maximum of the photon echo signal is shifted in time relative to the time of occurrence of the echo signal at resonant excitation of the systems (marked by dashed line). The time of the echo signal occurrence can be controlled by changing the pulse areas. The analysis shows that, due to the common ground state, the excited states of the three-level exciton system is not separated by polarization in the photon echo protocol in contrast to the trion system, which in the absence of a magnetic field represents two two-level systems [4]. In the case when the transition to one of the excited states is prohibited, the results obtained coincide with the result for an ensemble of two-level systems [5].

Conclusion

In this work the action of a polarized rectangular laser pulse on a three-level system was studied. A solution was obtained for non-resonant excitation by light of a system with degenerate excited energy states without taking relaxation into account. The dependence of the probability of the system being in a certain state on the frequency detuning and on the pulse area was analyzed. The obtained analytical expressions were used to simulate the signal of a two-pulses photon echo from an ensemble of three-level systems. Time profiles of the echo signal were obtained for excitation protocols with pulses of different polarization and different powers. It turned out that if the detuning is taken into account the photon echo signal is shifted in time.

REFERENCES

1. **Allen N., Eberly J. H.,** Optical Resonance and Two-Level Atoms, Wiley, New York, 1975.
2. **Damon V., Bonarota M., Louchet-Chauvet A.,** Revival of silenced echo and quantum memory for light, New J. Phys. 13 (9) (2011) 093031.
3. **Minnegaliev M.M., Gerasimov K.I., Sabirov T.N., Urmancheev R.V., Moiseev S.A.,** Implementation of an Optical Quantum Memory Protocol in the $^{167}Er^{3+}$:Y_2SiO_5 Crystal, JETP Letters. 115 (12) (2022) 720–727.
4. **Grisard S., Trifonov A.V., Rose H., Reichhardt R., Reichelt M., Schneider C., Kamp M., Höfling S., Bayer M., Meier T., Akimov I.A.,** Temporal Sorting of Optical Multiwave-Mixing Processes in Semiconductor Quantum Dots, ACS Photonics. 10 (9) (2023) 3161–3170.
5. **Poltavtsev S.V., Salewski M., Kapitonov Yu.V., Yugova I.A., Akimov I.A., Schneider C., Kamp M., Hofling S., Yakovlev D.R., Kavokin A.V., Bayer M.,** Photon echo transients from an inhomogeneous ensemble of semiconductor quantum dots, Physical Review B. 93 (12) (2016) 121304.

THE AUTHORS

ZHILYAKOV Vladimir L.
st087753@student.spbu.ru

YUGOVA Irina A.
i.yugova@spbu.ru
ORCID: 0000-0003-0020-3679

Received 14.12.2023. Approved after reviewing 15.01.2024. Accepted 01.02.2024.

Conference paper
UDC 535.3
DOI: https://doi.org/10.18721/JPM.171.102

Optical properties of GaN epitaxial layers in mid- and far-infrared ranges

G.A. Melentev [1] ✉, D.A. Karaulov [1], N.A. Kostromin [1],
M.Ya. Vinnichenko [1], D.A. Firsov [1], V.A. Shalygin [1]

[1] Peter the Great St. Petersburg Polytechnic University, St. Petersburg, Russia
✉ gamelen@spbstu.ru

Abstract. In this work, the transmission of microstructures based on gallium nitride with different doping levels in the mid- and far-infrared spectral ranges at $T = 300$ K was experimentally studied. The transmission of the studied structures in these spectral ranges was modeled using the transfer matrix method. It is shown that the contribution of the lattice, according to the single-phonon resonance model, and the contribution of free electrons, according to the Drude model, to the dielectric constant allows one to satisfactorily describe the optical properties of the studied microstructures up to a quantum energy of 300 meV. The absorption coefficient for CO_2 laser radiation (photon energy 117 meV) has been calculated. It has been shown that in gallium nitride absorption on free electrons at a given photon energy can be observed experimentally at an electron concentration exceeding $6 \cdot 10^{16}$ cm^{-3}. The optimal thickness of GaN layers for experimental observation of the absorption modulation of CO_2 laser radiation in electric field for different doping levels was determined.

Keywords: gallium nitride, free electrons, light transmission, absorption, mid-infrared spectral range, terahertz spectral range

Funding: The work was carried out with financial support from the Russian Science Foundation (grant No. 23-12-00036, https://rscf.ru/project/23-12-00036/).

Citation: Melentev G.A., Karaulov D.A., Kostromin N.A., Vinnichenko M.Ya., Firsov D.A., Shalygin V.A., Optical properties of GaN epitaxial layers in mid- and far-infrared ranges, St. Petersburg State Polytechnical University Journal. Physics and Mathematics. 17 (1.1) (2024) 12–19. DOI: https://doi.org/10.18721/JPM.171.102

This is an open access article under the CC BY-NC 4.0 license (https://creativecommons.org/licenses/by-nc/4.0/)

Материалы конференции
УДК 535.3
DOI: https://doi.org/10.18721/JPM.171.102

Оптические свойства эпитаксиальных слоев GaN в среднем и дальнем инфракрасных диапазонах

Г.А. Мелентьев [1] ✉, Д.А. Караулов [1], Н.А. Костромин [1],
М.Я. Винниченко [1], Д.А. Фирсов [1], В.А. Шалыгин [1]

[1] Санкт-Петербургский политехнический университет Петра Великого, Санкт-Петербург, Россия
✉ gamelen@spbstu.ru

Аннотация. В работе экспериментально исследовано пропускание микроструктур на основе нитрида галлия с разным уровнем легирования в среднем и дальнем инфракрасном диапазонах при $T = 300$ K. Проведено моделирование пропускания исследуемых структур в данных спектральных диапазонах с помощью метода матриц переноса. Показано, что вклад решетки, согласно модели однофононного резонанса, и вклад свободных

© Melentev G. A., Karaulov D. A., Kostromin N. A., Vinnichenko M. Ya., Firsov D. A., Shalygin V. A., 2024. Published by Peter the Great St. Petersburg Polytechnic University.

электронов, согласно модели Друде, в диэлектрическую проницаемость позволяет удовлетворительно описывать оптические свойства исследованных микроструктур вплоть до энергии кванта 300 мэВ. Рассчитан коэффициент поглощения для излучения CO_2-лазера (энергия кванта 117 мэВ). Показано, что в нитриде галлия поглощение на свободных электронах при данной энергии кванта экспериментально можно наблюдать при концентрации электронов, превышающей $6 \cdot 10^{16}$ см$^{-3}$. Определена оптимальная толщина пленок GaN для экспериментального наблюдения модуляции поглощения излучения CO_2-лазера в электрическом поле для разных уровней легирования.

Ключевые слова: нитрид галлия, свободные электроны, пропускание, поглощение, средний инфракрасный диапазон, терагерцовый диапазон

Финансирование: Исследование выполнено за счет гранта Российского научного фонда № 23-12-00036, https://rscf.ru/project/23-12-00036/.

Ссылка при цитировании: Мелентьев Г.А., Караулов Д.А., Костромин Н.А., Винниченко М.Я., Фирсов Д.А., Шалыгин В.А. Оптические свойства эпитаксиальных слоев GaN в среднем и дальнем инфракрасных диапазонах // Научно-технические ведомости СПбГПУ. Физико-математические науки. 2024. Т. 17. № 1.1. С. 12–19. DOI: https://doi.org/10.18721/ JPM.171.102

Статья открытого доступа, распространяемая по лицензии CC BY-NC 4.0 (https:// creativecommons.org/licenses/by-nc/4.0/)

Introduction

Modern opto- and nanoelectronics devices use various III-V group semiconductors. Gallium nitride stands out as a promising material for developing optical devices in the visible and infrared spectral ranges due to its unique combination of physical properties. The operation of many optoelectronic devices is accompanied by heating of charge carriers in an electric field; their functioning is also significantly affected by the absorption of radiation on nonequilibrium charge carriers. To analyze the absorption of radiation in an electric field, information about absorption under equilibrium conditions is required. The goal of this work is experimental and theoretical study of the equilibrium absorption of radiation by free electrons in epitaxial layers of gallium nitride.

Materials and Methods

In this work, we studied films of hexagonal *n*-type gallium nitride grown by metalorganic vapor phase epitaxy on a sapphire substrate with a buffer layer of specially undoped GaN. The thickness of the epitaxial films was 4.3 μm, the thickness of the buffer layer was 2 μm, and the thickness of the sapphire substrate was 440 μm. Films with different doping levels were studied. Based on the study of the Hall effect and electrical conductivity at room temperature, the following values of concentration (mobility) of free electrons were obtained: $3.1 \cdot 10^{17}$ cm^{-3} (246 cm^2/V·s), $1.4 \cdot 10^{18}$ cm^{-3} (231 cm^2/V·s) and $3.4 \cdot 10^{18}$ cm^{-3} (205 cm^2/V·s) for samples No. 1, 2 and 3, respectively. The optical transmission spectra of the microstructures were studied at room temperature in the mid- and far-infrared spectral ranges. The experiments were carried out using a Bruker Vertex 80v vacuum Fourier spectrometer operating in fast scanning mode. The radiation source was a globar. For studies in the mid-infrared (MIR) spectral range, a DLaTGS pyroelectric photodetector and a KBr beam splitter were used, and for studies in the far-infrared (terahertz) spectral range, a DLaTGS FIR pyroelectric photodetector and a Mylar beam splitter were used. The sample was placed in a Fourier transform spectrometer, which was evacuated to a pressure of 5 hPa; radiation from the globar, incident normal to the surface, passed through the sample and was measured by a photodetector.

Results and Discussion

Our samples are multilayer structures: GaN film / GaN buffer layer / sapphire substrate. It is convenient to model the transmission and reflection of radiation by such structures using the transfer matrix method [1, 2]. In this method, the reflection coefficients *R* and transmission

© Мелентьев Г.А., Караулов Д.А., Костромин Н.А., Винниченко М.Я., Фирсов Д.А., Шалыгин В.А., 2024. Издатель: Санкт-Петербургский политехнический университет Петра Великого.

coefficients T are calculated using a matrix M of size 2×2. To obtain the matrix M, matrices describing the passage of an electromagnetic wave through each j-th layer P_j, as well as describing the passage of an electromagnetic wave through the boundary between the j-th and (j+1) layer $D_{j/(j+1)}$. In the case of normal incidence of light, the matrix P_j is calculated as follows:

$$P_j = \begin{pmatrix} \exp(i\phi_j) & 0 \\ 0 & \exp(-i\phi_j) \end{pmatrix}, \tag{1}$$

where $\varphi_j = \frac{\omega}{c}\tilde{n}_j d_j$ is the phase change of the electric field of the wave when passing through layer j, ω is the angular frequency of the electromagnetic wave, c is the speed of light, $\tilde{n}_j = n_j + ik_j$ is the complex refractive index of layer j, n_j, k_j and d_j are the real refractive index, the extinction coefficient and the thickness for the layer j, respectively. In the case of normal incidence of light, the matrix $D_{j/(j+1)}$ is calculated as follows:

$$D_{j+1/j} = \frac{1}{2\tilde{n}_{j+1}} \begin{pmatrix} \tilde{n}_{j+1} + \tilde{n}_j & \tilde{n}_{j+1} - \tilde{n}_j \\ \tilde{n}_{j+1} - \tilde{n}_j & \tilde{n}_{j+1} + \tilde{n}_j \end{pmatrix}. \tag{2}$$

The transfer matrix M for our structure is written as follows:

$$M = D_{4/3}P_3D_{3/2}P_2D_{2/1}P_1D_{1/0}, \tag{3}$$

where index 0 corresponds to vacuum, index 1 to the doped GaN epitaxial layer, index 2 to the GaN buffer layer, index 3 to the sapphire substrate, and index 4 to vacuum. Knowing the elements of the matrix M, we can calculate the coefficients of reflection:

$$R = \left| \frac{M_{21}}{M_{22}} \right|^2, \tag{4}$$

and transmission:

$$T = \left| M_{11} - \frac{M_{21}M_{12}}{M_{22}} \right|^2. \tag{5}$$

The spectra of reflection and transmission coefficients calculated using (4) and (5) contain oscillations with a small period caused by interference in the “thick” substrate. However, we did not observe them experimentally due to insufficient resolution. Therefore, according to [2], it is possible to exclude these oscillations by considering the substrate as an “incoherent layer.” Then for the substrate, the matrix P is transformed to the following form:

$$P_3(\theta) = \begin{pmatrix} \exp\left(i\left[\phi_3 + \frac{\theta}{2}\right]\right) & 0 \\ 0 & \exp\left(-i\left[\phi_3 + \frac{\theta}{2}\right]\right) \end{pmatrix}, \tag{6}$$

and the transfer matrix is written as follows:

$$M(\theta) = D_{4/3}P_3(\theta)D_{3/2}P_2D_{2/1}P_1D_{1/0}. \tag{7}$$

To obtain R and T, it is necessary to average (4) and (5) over θ:

$$R = \frac{1}{2\pi}\int_{-\pi}^{\pi} \left| \frac{M_{21}(\theta)}{M_{22}(\theta)} \right|^2 d\theta, \tag{8}$$

$$T = \frac{1}{2\pi}\int_{-\pi}^{\pi} \left| M_{11}(\theta) - \frac{M_{21}(\theta)M_{12}(\theta)}{M_{22}(\theta)} \right|^2 d\theta. \tag{9}$$

For GaN layers $\tilde{n}$ can be calculated using the Fresnel equation:

$$\tilde{n}^2 = \varepsilon, \tag{10}$$

where ε is the dielectric constant. The dielectric constant contains contributions from the lattice (according to the single-phonon resonance model) and free electrons (according to the Drude model):

$$\varepsilon(\omega) = \varepsilon_\infty \left(1 + \frac{\omega_{LO}^2 - \omega_{TO}^2}{\omega_{TO}^2 - \omega(\omega + i\gamma_q)} - \frac{\omega_{pl}^2}{\omega(\omega + i\gamma_e)}\right), \tag{11}$$

where ε_∞ is the high-frequency dielectric constant, ω_{LO} is the frequency of the longitudinal optical phonon, ω_{TO} is the frequency of the transverse optical phonon, γ_q is the damping constant of the optical phonon, $\omega_{pl} = \sqrt{\frac{4\pi N_e e^2}{\varepsilon_\infty m_e}}$ is the plasma frequency, N_e is the concentration of free electrons, m_e is the effective mass of the electron, $\gamma_e = 1/\tau_e$ is the plasmon damping constant, τ_e is the electron relaxation time determined from expressions for mobility $\mu_e = \frac{e\tau_e}{m_e}$.

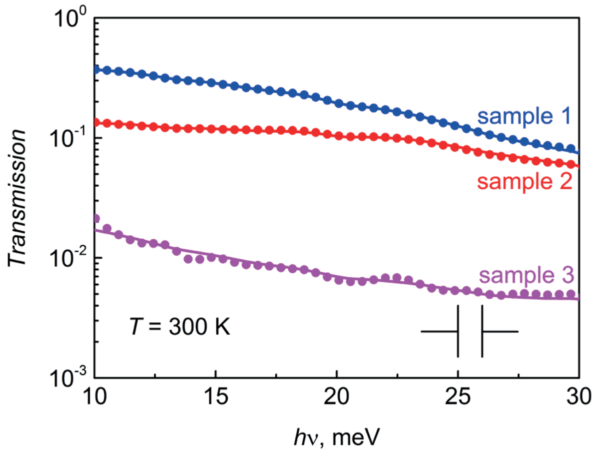

Fig. 1. Experimental (circles) and simulated (lines) transmission spectra in the THz spectral range for sample 1 (blue line and circles), 2 (red line and circles) and 3 (magenta line and circles). The experiment was carried out at room temperature

Using (9), the transmission spectra of the samples under study were simulated. For sapphire, the values n and k from [3, 4] were used, and for GaN layers they were calculated according to (10) and (11). For the buffer layer, characteristic concentration and mobility values for intentionally undoped GaN films were used: $N_e = 4 \cdot 10^{16}$ cm^{-3}, $\mu_e = 200$ cm^2/V·s [5]. The ω_{pl} and γ_e values of the doped GaN layers were used as fitting parameters for the model. For simplicity, the effective electron mass is assumed to be constant for all doping levels and equal to $0.2m_0$. Other necessary parameters of gallium nitride were taken from [6–8]. In Figure 1, solid lines show the results of modeling the transmission of the structures under study at the best-fit parameters. It can be seen that the model calculation well describes the transmission spectrum in the THz spectral range. Table presents the parameters of the doped GaN layers obtained from the study of the Hall effect and electrical conductivity, and the parameters obtained from the simulation of the transmission in the terahertz spectral range. As the doping level increases, the concentration and mobility values obtained from Hall measurements and from transmittance spectrum simulations differ less and less. The concentration values for the least doped GaN film differ the most. Thus, it can be said that the single-phonon resonance model and the Drude model adequately describe the contribution of the lattice and electrons to the dielectric constant of GaN in the terahertz spectral range.

Fig. 2, *a* shows the experimental transmission spectra of the samples in the mid-infrared spectral range. These spectra have several features. Firstly, the spectra exhibit oscillations, the

Table

Parameters of samples obtained by various methods

Sample	Hall and conductivity experiments		Terahertz transmission experiment			
	N_e, cm^{-3}	μ_e, cm^2/V·s	ω_{pl}, meV	γ_e, meV	N_e, cm^{-3}	μ_e, cm^2/V·s
1	$3.1\cdot10^{17}$	246	9	12.1	$6.3\cdot10^{16}$	478
2	$1.4\cdot10^{18}$	231	25.3	18.3	$4.9\cdot10^{17}$	316
3	$3.4\cdot10^{18}$	205	58.6	27.9	$2.7\cdot10^{18}$	207

period of which is almost the same for all the samples under study. These oscillations are caused by the interference of light in the buffer layer and the doped GaN film. At a frequency ω greater than $4.56\cdot10^{14}$ rad/s (photon energy greater than 300 meV), the real refractive index *n* is practically independent of the doping level, and absorption is low (Fig. 3), i.e., *n* is determined by the lattice and can be estimated as $\sqrt{\varepsilon_\infty}$. Knowing the period of oscillations and the refractive index, it is easy to obtain the thickness of the layer in which interference occurs. This thickness was 6.3–6.4 μm, which is consistent with the technologists' data. Secondly, at photon energies less than 170 meV there is no transmission. This is due to absorption in the sapphire substrate [9]

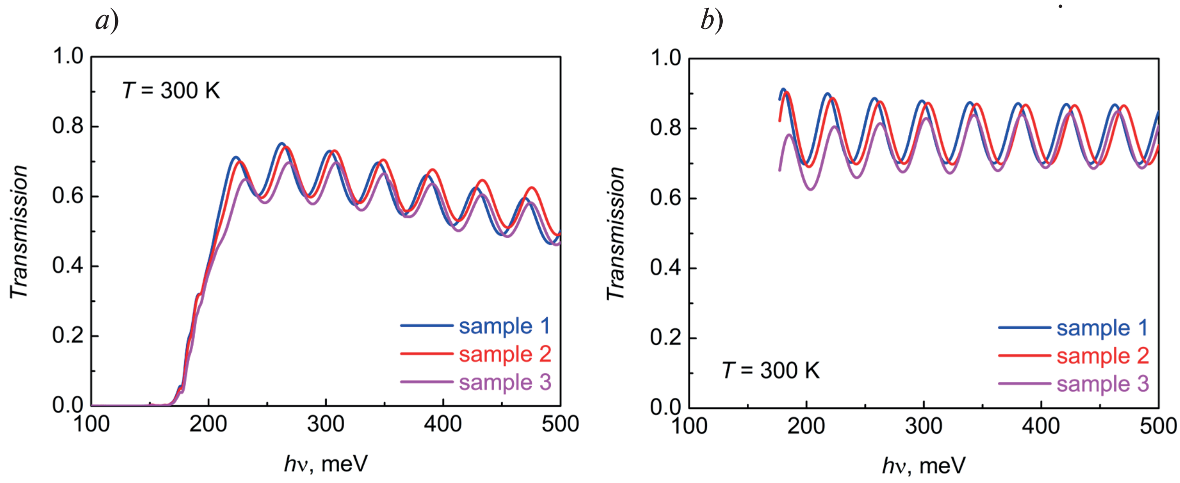

Fig. 2. Experimental (*a*) and simulated (*b*) transmission spectra in the mid-infrared spectral range for sample 1 (blue line), 2 (red line) and 3 (magenta line).
The experiment was carried out at room temperature; resolution is 1 meV

Fig. 2, *b* shows the simulated transmission spectra of the structures under study in the mid-infrared spectral range, calculated using (9). The values of *n* and *k* for sapphire were taken from [9], and for GaN layers were calculated using (10) and (11). In this case, the parameters of the buffer layer remained the same, and for the parameters of the doped GaN films, the values obtained as a result of modeling transmission in the THz region were taken (Table). Fig. 2 demonstrates that the period and amplitude of the calculated transmission oscillations coincide well with the experimental ones. It is also clear that at photon energies less than 300 meV, the transmission of samples decreases with increasing doping level, which is due to absorption by free electrons. At the same time, the experimental and theoretical transmission spectra differ. Firstly, the simulated transmission spectra do not demonstrate sharp monotone increase in range from 170 to 220 meV. Secondly, the theoretical transmittance curves are located slightly higher on the *OY* axis. Thirdly, a decrease in transmission is observed, starting with a photon energy of 300 meV. These differences are explained by ambiguous data for *n* and *k* for sapphire in the mid-infrared spectral range, as well as extra absorption mechanisms in GaN, which are not taken into account in model (11). It can be concluded that the single-phonon resonance model and the

Drude model satisfactorily describe the contribution of the lattice and electrons to the dielectric constant in the mid-infrared range up to photon energies of 300 meV.

Fig. 3 shows the spectra of the real refractive index and extinction coefficient of gallium nitride, calculated on the basis of (10) and (11) for the samples under study. These dependences were also calculated for pure GaN ($N_e = 0$), which makes it possible to identify the contribution of free electrons to n and k. The feature in the region of 100 meV, characteristic of all samples, is due to the Reststrahlen band of GaN. From a comparison with n and k for pure GaN, it is clear that the presence of free electrons greatly modifies the spectra. In this way, in the spectra of the real refractive index in the terahertz region, a minimum appears, which shifts to the high-frequency region with increasing concentration of free electrons. The value of extinction coefficient increases monotonically with N_e growth over the entire range.

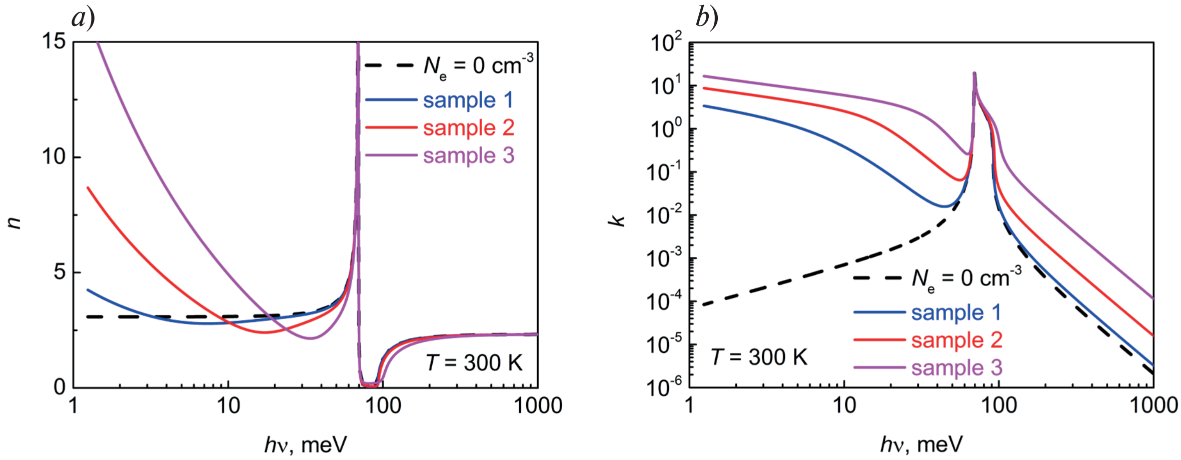

Fig. 3. Spectra of the real refractive index (a) and extinction coefficient (b) for pure GaN (dashed line), sample 1 (blue line), 2 (red line) and 3 (magenta line)

For experimental studies of absorption, including studies under conditions of carrier heating by an external electric field, in the mid-infrared spectral range it is convenient to use a CO_2 laser (radiation wavelength 10.6 μm, photon energy 117 meV). Fig. 4 shows the absorption spectra of the samples under study and pure GaN, calculated in a wide range of photon energies from the relation

$$\alpha = 2\frac{\omega}{c}k. \tag{12}$$

For free electron concentrations of 0, $6.3 \cdot 10^{16}$, $4.9 \cdot 10^{17}$ and $2.7 \cdot 10^{18}$ cm^{-3}, the absorption

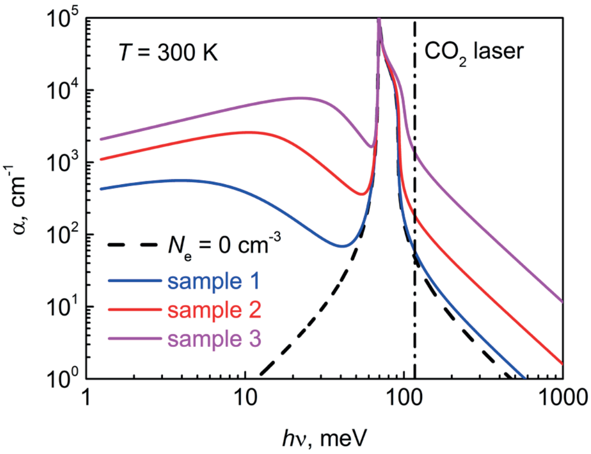

Fig. 4. Absorption coefficient spectra for pure GaN (dashed line), sample 1 (blue line), 2 (red line) and 3 (magenta line). The vertical dash-dotted line corresponds to the energy of the CO_2 laser photon (117 meV)

coefficient at a photon energy of 117 meV is 48, 59, 183 and 1370 cm^{-1}, respectively. Thus, for sample No. 1, the contribution of free electrons to absorption is quite small, therefore, for experimental studies it is necessary to use samples with a concentration noticeably higher than $6\cdot10^{16}$ cm^{-3}. To study the effects of electroabsorption in *n*-GaN epitaxial films at the wavelength of a CO_2 laser radiation, the optimal film thickness decreases with increasing concentration of free electrons. To determine it, equality $\alpha d = 1$ can be used. Thus, for electron concentrations of $4.9\cdot10^{17}$ and $2.7\cdot10^{18}$ cm^{-3}, the optimal film thickness is 55 and 7 μm, respectively. It is advisable to use silicon as a substrate.

Conclusion

In this work, the transmission of GaN-based microstructures in the terahertz and mid-infrared spectral ranges at room temperature was experimentally studied. The transmission of the studied structures was simulated using the transfer matrix method. The dielectric constant of GaN was the sum of the contributions from the lattice (according to the single-phonon resonance model) and free electrons (according to the Drude model). Transmission modeling in the THz range made it possible to obtain refined values of the parameters of doped gallium nitride films, and modeling in the mid-infrared spectral range demonstrated that the single-phonon resonance model and the Drude model in the structures we studied provide adequate results up to photon energies of 300 meV. The absorption coefficient of GaN was also calculated in a wide range of photon energies for different doping levels and the free electrons contribution to the absorption was revealed. In particular, absorption at the photon energy of CO_2 laser radiation is considered. It has been shown that in gallium nitride, absorption on free electrons at a given photon energy can be experimentally observed at an electron concentration exceeding $6\cdot10^{16}$ cm^3. Thus, for free electron concentrations of $4.9\cdot10^{17}$ and $2.7\cdot10^{18}$ cm^{-3}, the optimal thickness for observing the absorption modulation of CO_2 laser radiation in electric field is 55 and 7 μm, respectively.

REFERENCES

1. **Katsidis C.C., Siapkas D.I.,** General transfer-matrix method for optical multilayer systems with coherent, partially coherent, and incoherent interference, Applied Optics. 41 (19) (2002) 3978–3987.

2. **Adamov R.B., Pashnev D., Shalygin V.A., Moldavskaya M.D., Vinnichenko M.Ya., Janonis V., Jorudas J., Tumėnas S., Prystawko P., Krysko M., Sakowicz M., Kašalynas I.,** Optical Performance of Two Dimensional Electron Gas and GaN:C Buffer Layers in AlGaN/AlN/GaN Heterostructures on SiC Substrate, Applied Sciences. 11 (13) (2021) 6053.

3. **Artemyev A.A.,** Opticheskiye svoystva struktur AlGaN/GaN/Al_2O_3 v teragertsovom diapazone chastot. Vypusknaya rabota bakalavra [Optical properties of AlGaN/GaN/Al_2O_3 heterostructures in terahertz range. Bachelor's thesis], St. Petersburg, 2017 (in Russian).

4. **Adamov R.B., Moldavskaya M.D., Shalygin V.A.,** Opticheskiye svoystva sapfira v teragertsovom diapazone chastot [Optical properties of sapphire in terahertz range], Proceedings of the 21st Russian Young Conference on Physics of Semiconductors and Nanostructures, Opto-and Nanoelectronics, Saint Petersburg, Russia, 25 – 29 November 2019. P. 17 (in Russian).

5. **Shalygin V.A., Vorobjev L.E., Firsov D.A., Panevin V.Yu., Sofronov A.N., Melentyev G.A., Antonov A.V., Gavrilenko V.I., Andrianov A.V., Zakharyin A.O., Suihkonen S., Törma P.T., Ali M., Lipsanen H.,** Impurity breakdown and terahertz luminescence in *n*-GaN epilayers under external electric field, Journal of Applied Physics. 106 (12) (2009) 123523.

6. **Barker A.S.Jr., Ilegems M.,** Infrared Lattice Vibrations and Free-Electron Dispersion in GaN, Physical Review B. 7 (2) (1973) 743–750.

7. **Davydov V.Yu., Kitaev Yu.E., Goncharuk I.N., Smirnov A.N., Graul J., Semchinova O., Uffmann D., Smirnov M.B., Mirgorodsky A.P., Evarestov R.A.,** Phonon dispersion and Raman scattering in hexagonal GaN and AlN, Physical Review B. 58 (19) (1998) 12899–12907.

8. **Kuroda N., Kitayama T., Nishi Y., Saiki K., Yokoi H., Watanabe J., Cho M., Egawa T., Ishikawa H.,** Infrared Study on Graded Lattice Quality in Thin GaN Crystals Grown on Sapphire, Japanese Journal of Applied Physics. 45 (2A) (2006) 646–650.

9. **Dobrovinskaya E.R., Lytvynov L.A., Pishchik V.,** Sapphire: Material, Manufacturing, Applications, Chap. 2, Properties of Sapphire, Springer, New York, 2009.

THE AUTHORS

MELENTEV Grigorii A.
gamelen@spbstu.ru
ORCID: 0000-0002-1680-333X

KARAULOV Danila A.
donil793@yandex.ru
ORCID: 0009-0002-1608-3659

KOSTROMIN Nikita A.
kostrominnick1@gmail.com
ORCID: 0009-0006-9763-2830

VINNICHENKO Maksim Ya.
mvin@spbstu.ru
ORCID: 0000-0002-6118-0098

FIRSOV Dmitry A.
dmfir@rphf.spbstu.ru
ORCID: 0000-0003-3947-4994

SHALYGIN Vadim A.
vadim_shalygin@mail.ru
ORCID: 0000-0001-6728-7286

Received 04.12.2023. Approved after reviewing 07.12.2023. Accepted 12.12.2023.

Conference paper
UDC 621.315.592
DOI: https://doi.org/10.18721/JPM.171.103

Features of isovalent doping of gallium arsenide with bismuth ions

D.A. Zdoroveyshchev [1] ✉, O.V. Vikhrova [1], Yu.A. Danilov [1], Yu.A. Dudin [1],
A.V. Zdoroveyshchev [1], A.E. Parafin [2], M.N. Drozdov [2]

[1] Lobachevsky State University of Nizhny Novgorod, Nizhny Novgorod, Russia
[2] Institute for Physics of Microstructures of the RAS, Nizhny Novgorod, Russia
✉ danielzdoroveishev@yandex.ru

Abstract. The work shows the possibility of doping gallium arsenide with bismuth during ion implantation and the effect of rapid thermal and pulsed laser annealing on these structures. The results of a study of bismuth depth distribution profiles are presented in comparison with theoretical calculations. The influence of bismuth on the optical properties of gallium arsenide was investigated using transmittance and reflection spectroscopy methods. It has been shown that the introduction of bismuth leads to a decrease in the band gap of gallium arsenide.

Keywords: gallium arsenide, bismuth doping, ion implantation, pulsed laser annealing, rapid thermal annealing

Funding: This work was supported by the Russian Science Foundation (project No. 23-29-00312).

Citation: Zdoroveyshchev D.A., Vikhrova O.V., Danilov Yu.A., Dudin Yu.A., Zdoroveyshchev A.V., Parafin A.E., Drozdov M.N., Features of isovalent doping of gallium arsenide with bismuth ions, St. Petersburg State Polytechnical University Journal. Physics and Mathematics. 17 (1.1) (2024) 20–24. DOI: https://doi.org/10.18721/JPM.171.103

This is an open access article under the CC BY-NC 4.0 license (https://creativecommons.org/licenses/by-nc/4.0/)

Материалы конференции
УДК 621.315.592
DOI: https://doi.org/10.18721/JPM.171.103

Особенности изовалентного легирования арсенида галлия ионами висмута

Д.А. Здоровейщев [1] ✉, О.В. Вихрова [1], Ю А. Данилов [1], Ю.А. Дудин [1],
А.В. Здоровейщев [1], А.Е. Парафин [2], М.Н. Дроздов [2]

[1] Нижегородский государственный университет им. Н.И. Лобачевского, Нижний Новгород, Россия
[2] Институт физики микроструктур РАН, Нижний Новгород, Россия
✉ danielzdoroveishev@yandex.ru

Аннотация. В работе показана возможность легирования арсенида галлия висмутом методом ионной имплантации, а также влияние быстрого термического и импульсного лазерного отжига на эти структуры. Представлены результаты исследования профилей распределения висмута по глубине в сравнении с теоретическими расчетами. Влияние висмута на оптические свойства арсенида галлия исследовано методами спектроскопии пропускания и отражения. Показано, что введение висмута приводит к уменьшению ширины запрещенной зоны арсенида галлия.

Ключевые слова: арсенид галлия, легирование висмутом, ионная имплантация, импульсный лазерный отжиг, быстрый термический отжиг

© Zdoroveyshchev D.A., Vikhrova O.V., Danilov Yu.A., Dudin Yu.A., Zdoroveyshchev A.V., Parafin A.E., Drozdov M.N., 2024. Published by Peter the Great St. Petersburg Polytechnic University.

Финансирование: Работа поддержана Российским научным фондом (проект № 23-29-00312).

Ссылка при цитировании: Здоровейщев Д.А., Вихрова О.В., Данилов Ю.А., Дудин Ю.А., Здоровейщев А.В., Парафин А.Е., Дроздов М.Н. Особенности изовалентного легирования арсенида галлия ионами висмута // Научно-технические ведомости СПбГПУ. Физико-математические науки. 2024. Т. 17. № 1.1. С. 20–24. DOI: https://doi.org/10.18721/JPM.171.103

Статья открытого доступа, распространяемая по лицензии CC BY-NC 4.0 (https://creativecommons.org/licenses/by-nc/4.0/)

Introduction

Bismuth is an element of Group V of the Periodic Table and, accordingly, is isovalent to arsenic atoms. The introduction of Bi atoms into the crystal lattice of gallium arsenide leads to the formation of a substitutional solid solution $GaAs_{1-x}Bi_x$. Due to the fact that Bi is heavier than arsenic (209 and 75 a.m.u., respectively), doping GaAs with it leads to a significant change in the properties of this semiconductor.

Thus, the introduction of bismuth leads to a decrease in the band gap (Eg) of this material. It was shown in [1] that the value of E_g at room temperature decreases monotonically from 1.42 eV for gallium arsenide to 0.8 eV for GaAs with ≈ 11 at.% of bismuth.

Also, in GaAs:Bi, even at low concentrations of bismuth, the energy of spin-orbit splitting (Δ_{SO}) increases. It was shown in [2] that Δ_{SO} increased from 0.34 eV for GaAs to ≈ 0.46 eV in GaAs:Bi with a bismuth content of about 1.8 at.%.

The influence of bismuth on electric transport properties is also noted in the literature. The addition of bismuth to nominally undoped gallium arsenide leads to the formation of the hole conductivity associated with the appearance of a shallow acceptor level at 26.8 meV, and, as shown in [3] and [4], an increase in the bismuth concentration in the $GaAs_{1-x}Bi_x$ solid solution leads to an increase in the hole concentration. The effect on electric transport in doped GaAs:Bi layers is shown in [5]. Thus, at bismuth concentrations up to 1.6 at.%, the electron mobility changes insignificantly, while the hole mobility decreases by more than an order of magnitude. Moreover, a decrease in the hole concentration in acceptor GaAs:Bi was observed, which the authors associate with the formation of bismuth clusters in GaAs, leading to the appearance of hole trap states.

As an alternative to the epitaxial methods usually described in the literature for obtaining GaAs:Bi, this work uses bismuth doping by ion implantation.

Materials and Methods

Bismuth ions were implanted into i-GaAs(001) substrates at the Raduga-3M accelerator, while the accelerating voltage (30 or 80 kV) and the dose of implanted ions were varied. The main feature of the accelerator is a vacuum arc source, which makes it possible to create intense ion beams using solid precursors. The source operates in a pulse-periodic mode with a pulse duration of ≈ 200 μs and a repetition rate of 50 pulses/s. Another feature of the accelerator is that the ion beam contains several charge fractions, and the distribution among the fractions depends on the specific metal. In particular, for Bi, the beam contains, according to [6], 83% Bi^+ and 17% Bi^{++} fractions. The implantation dose was chosen in such a way that, according to calculations using the SRIM 2013 code, the average bismuth content in the implanted layer varied from 0.5 to 1.0 and 1.5 at. %. For an accelerating voltage of 30 kV, these doses were $7\cdot10^{14}$, $1.4\cdot10^{15}$ and $2.1\cdot10^{15}$ cm^{-2}, respectively. For an accelerating voltage of 80 kV, the implantation doses were $8\cdot10^{14}$, $1.6\cdot10^{15}$ and $2.4\cdot10^{15}$ cm^{-2}. Since the ion mass is large (M_1 = 209 a.m.u.), the large sputtering coefficient (S = 16.0 atoms/ion for a Bi ion energy of 80 keV) must be taken into account when calculating distribution profiles.

After implantation, one part of the samples was subjected to pulsed laser annealing (PLA) with a KrF excimer laser with a pulse duration of 30 ns at different energy densities (P) per pulse (240 mJ/cm^2 for structures irradiated at 30 kV; 250, 300 and 400 mJ/cm^2 for 80 kV), and for

© Здоровейщев Д.А., Вихрова О.В., Данилов Ю.А., Дудин Ю.А., Здоровейщев А.В., Парафин А.Е., Дроздов М.Н., 2024. Издатель: Санкт-Петербургский политехнический университет Петра Великого.

comparison, the other part of the samples was subjected to rapid thermal annealing (RTA) in ultra-pure argon at T_a = 800 °C for 20 s. At this process the working surface of the samples was placed on a Si substrate plate, which prevented the evaporation of As atoms from the surface layer. The distribution of bismuth in the resulting layers was studied using the method of secondary ion mass spectrometry (SIMS) on the TOF.SIMS 5 installation during sputtering of GaAs with a beam of Cs ions. For comparison with experimental profiles, theoretical profiles of bismuth distribution were calculated using the SRIM 2013 code, taking into account ion sputtering of the structure surface in accordance with [7]. The properties of the resulting structures were studied using transmission and reflection spectroscopy in the wavelength range from 0.18 to 1.8 μm using a Cary 6000i dual-beam spectrophotometer (Varian).

Results and Discussion

The profiles of the distribution of bismuth atoms over the depth of the structures obtained by the SIMS method are shown in Fig. 1. For comparison, the calculated profiles are also given there. Note that for the Bi ion energy of 80 keV, the maximum of the distribution is located outside the boundary of the figure (the average projected range was 24 nm). It can be seen that, in comparison with the calculation, the profiles of Bi atoms after implantation are pulled towards the surface (see curves *2* in Fig. 1, *a* and Fig. 1, *b*). After thermal (curve *3* in Fig. 1, *b*) and laser annealing (profile *3* in Fig. 1, *a* and profiles *4* and *5* in Fig. 1, *b*), an increase of the bismuth concentration is observed in the near-surface region and a decrease in deeper regions. This suggests that during annealing, bismuth atoms move from the bulk to the surface. It is interesting that during laser annealing with P < 300 mJ/cm^2 of samples irradiated with both accelerating voltages of 30 and 80 kV, a second maximum is observed at a depth of about 5 nm, which disappears during annealing with a higher PLA energy. The height of the surface peak of bismuth atoms increases with increasing energy density of pulsed laser annealing.

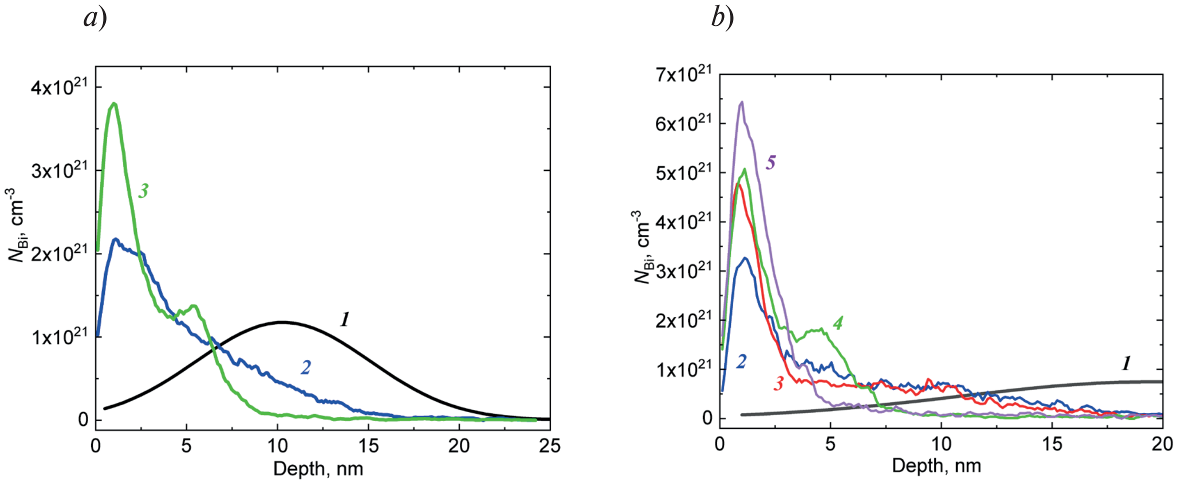

Fig. 1. Calculated (curves *1*) and experimentally determined bismuth depth distribution profiles: (*a*) implantation with an accelerating voltage of 30 kV, a dose of 1.4×10^{15} cm^{-2} before annealing (curve *2*) and after PLA with P = 240 mJ/cm*2* (curve *3*); (*b*) implantation with an accelerating voltage of 80 kV, a dose of 1.6×10^{15} cm^{-2} before annealing (curve *2*), after RTA (curve *3*) and after PLA with an energy density of 250 (curve *4*) and 400 mJ/cm^2 (curve *5*)

The optical properties of GaAs samples irradiated with Bi ions were studied. Reflection spectra for structures implanted at 30 kV are shown in Fig. 2.

The reflection spectra of single-crystal GaAs contain characteristic features in the form of a doublet maximum at photon energies of 2.90 and 3.14 eV and a maximum at ~ 5 eV. After implantation, the reflection spectrum is a structureless dependence on the quantum energy, which indicates a complete loss of long-range order (amorphization) in the near-surface region of irradiated GaAs. After both thermal and laser annealing, the crystal structure is almost restored; only insufficient resolution of peaks near 3 eV indicates residual radiation defects.

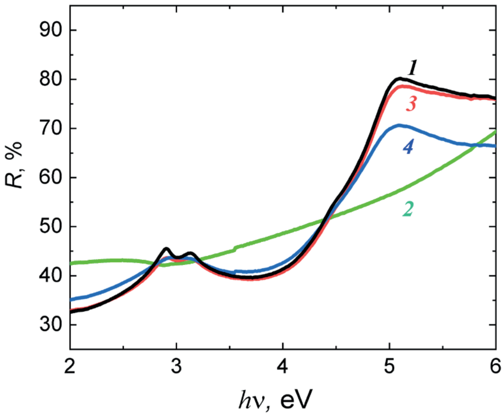

Fig. 2. Reflection spectra: single-crystal GaAs (curve *1*) and GaAs samples irradiated with Bi ions with an accelerating voltage of 30 kV: after ion implantation (curve *2*), RTA (curve *3*) and PLA (curve *4*) with $P = 240$ mJ/cm^2

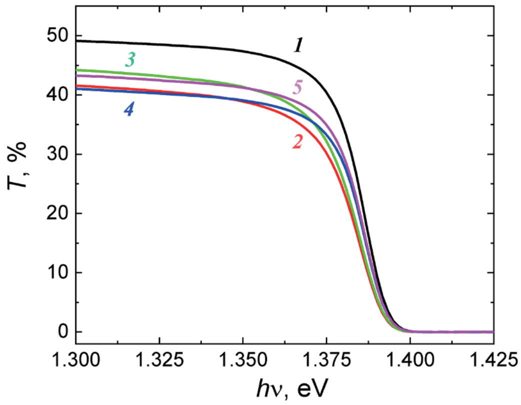

Fig. 3. Transmission spectra of single-crystal GaAs (curve *1*) and GaAs samples irradiated with Bi ions with an accelerating voltage of 80 kV: doses of $8{\cdot}10^{14}$ cm^{-2} (curve *2*) and $2.4{\cdot}10^{15}$ cm^{-2} (curve *3*) after RTA, a dose of $2.4{\cdot}10^{15}$ cm^{-2} after PLA with $P = 250$ mJ/cm^2 (curve *4*) and $P = 400$ mJ/cm^2 (curve *5*)

Fig. 3 shows the transmission spectra of GaAs(001) irradiated with Bi ions. Double-sided polished substrates of GaAs were used in these experiments.

It can be concluded that when bismuth is introduced, the absorption edge shifts to longer wavelengths. The band gap values for GaAs with bismuth estimated from the spectra give $E_g \approx 1.398$ eV at room temperature, which is less than 1.42 eV for single-crystal GaAs. An estimate based on data from [1] of the effective bismuth concentration, which affects the absorption edge, gives a value of ~ 1 at.%. This value coincides well with the average concentration of bismuth atoms in the layer up to approximately 15 nm, excluding the near-surface region with a thickness of 3 nm (see Fig. 1).

When discussing the presented results, it is first necessary to understand the reasons for the deviation of the implanted Bi profiles from the calculated ones. Let us pay attention to the similarity in the behavior of the impurity (pulling the Bi profile to the surface) during annealing and during the implantation process. This may indicate that, during pulsed ion irradiation, melting of the near-surface layer occurs, followed by recrystallization from the single-crystal substrate when the sample is cooled. In this case, the recrystallization front moves from single-crystal GaAs to the surface, leading to segregation and accumulation of bismuth near the surface. A similar process can occur during PLA. It is unlikely that Bi atoms in the subsurface layer 3 nm thick after implantation occupy GaAs lattice sites. Apparently, they enter into a chemical interaction with atmospheric oxygen and are included in the form of oxides in the transparent native oxide GaAs.

Conclusion

The work experimentally demonstrated the possibility of doping gallium arsenide with bismuth in the process of ion implantation. The effectiveness of using pulsed laser and rapid thermal annealing for restoring the crystal structure of the obtained samples has been shown, as evidenced by the reflection spectra. In a study of transmission spectra, it was experimentally shown that bismuth reduces the band gap of GaAs. In this case, the effective concentration of bismuth, which affects the shift of the absorption edge, is about 1 at.%. This may be due to heating processes occurring during implantation, which is a feature of the ion source which we used, as confirmed by secondary ion mass spectrometry data.

REFERENCES

1. **Mohmad A.R., Bastiman F., Hunter C.J., Richards R.D., Sweeney S.J., Ng J.S., David J.P.R., Majlis B.Y.,** Localization effects and band gap of GaAsBi alloys, Phys. Stat. Solidi B. 251 (2014) 1276.
2. **Fluegel B., Francoeur S., Mascarenhas A., Tixier S., Young E.C., TiedjeT.,** Giant Spin-Orbit Bowing in $GaAs_{1-x}Bi_x$, Physical Review Letters. 97 (2006) 067205.
3. **Pettinari G., Engelkamp H., Christianen P.C.M., Maan J.C., Polimeni A., Capizzi M., Tiedje T.,** Compositional evolution of Bi-induced acceptor states in $GaAs_{1-x}Bi_x$ alloy, Physical Review B. 83 (20) (2011) 201201.
4. **Pettinari G., Patanи A., Polimeni A., Capizzi M., Lu X., Tiedje T.,** Bi-induced p-type conductivity in nominally undopedGa(AsBi), Applied Physics Letters. 100 (2012) 092109.
5. **Kini R.N., Mascarenhas A.,** Effect of Bismuth Alloying on the Transport Properties of the Dilute Bismide Alloy, $GaAs_{1-x}Bi_x$, [Springer Series in Materials Science] Bismuth-Containing Compounds. 186 (2013) 181–200.
6. **Brown L.G.,** The Physics and Technology of Ion Sources, Wiley, New York, 1989.
7. **Ryssel H., Ruge I.,** Ion implantation (in Russian), Nauka, Moscow, 1983.

THE AUTHORS

ZDOROVEYSHCHEV Daniil A.
danielzdoroveishev@yandex.ru
ORCID: 0000-0002-2877-4628

ZDOROVEYSHCHEV Anton V.
zdorovei@nifti.unn.ru
ORCID: 0000-0002-8379-2263

VIKHROVA Olga V.
vikhrova@nifti.unn.ru
ORCID: 0000-0002-4804-3216

PARAFIN Alexey E.
parafin@ipmras.ru

DROZDOV Mikhail N.
drm@ipmras.ru

DANILOV Yury A.
danilov@nifti.unn.ru

DUDIN Yury A.
ya-dudin@nifti.unn.ru

Received 10.12.2023. Approved after reviewing 26.02.2024. Accepted 26.02.2024.

St. Petersburg Polytechnic University Journal. Physics and Mathematics. 2024 Vol. 17. No. 1.1
Научно-технические ведомости СПбГПУ. Физико-математические науки. 17 (1.1) 2024

Conference paper
UDC 537.31, 538.913
DOI: https://doi.org/10.18721/JPM.171.104

Destruction of the conducting state by ac electric field in naphthalocyanine complexes

V.A. Pshenichnyi [1] ✉, T.V. Dubinina [1], K.A. Drozdov [1]

[1] Lomonosov Moscow State University, Moscow, Russia

✉ pshenichnyi.va17@physics.msu.ru

Abstract. It is shown that in naphthalocyanine films, conductivity occurs due to electron transport along metal nanowires. In an alternating electric field, reversible partial rupture of nanowires may take place. Active resistance for film with partial nanowire ruptures is frequency dependent and can be more or less than that of film without ruptures. A model for this effect is proposed. The prediction of the response of a system to an external influence simplifies the use of materials for practical applications.

Keywords: nanowires, resistive switching, alternating electric field

Funding: Synthesis of complex was funded by State Assignment of the Lomonosov Moscow State University (topic no. 121021000105-7).

Citation: Pshenichnyi V.A., Dubinina T.V., Drozdov K.A., Destruction of the conducting state by ac electric field in naphthalocyanine complexes, St. Petersburg State Polytechnical University Journal. Physics and Mathematics. 17 (1.1) (2024) 25–30. DOI: https://doi.org/10.18721/JPM.171.104

This is an open access article under the CC BY-NC 4.0 license (https://creativecommons.org/licenses/by-nc/4.0/)

Материалы конференции
УДК 537.31, 538.913
DOI: https://doi.org/10.18721/JPM.171.104

Разрушение проводящего состояния переменным электрическим полем в комплексах нафталоцианинов

В.А. Пшеничный [1] ✉, Т. В. Дубинина [1], К.А. Дроздов [1]

[1] МГУ имени М.В. Ломоносова, Москва, Россия

✉ pshenichnyi.va17@physics.msu.ru

Аннотация. Показано, что в пленках нафталоцианинов проводимость осуществляется за счет транспорта электронов по металлическим нанонитям. В переменном электрическом поле может происходить обратимый частичный разрыв нанонитей. Активное сопротивление пленки с частичным разрывом нанонитей зависит от частоты и может быть больше или меньше, чем у пленки без разрывов. Предложена модель этого эффекта. Прогнозирование реакции системы на внешнее воздействие упрощает использование материалов для практических приложений.

Ключевые слова: нанонити, резистивные переключения, переменное электрическое поле

Финансирование: Синтез комплекса выполнен по Государственному заданию МГУ имени М.В. Ломоносова (тема № 121021000105-7).

Ссылка при цитировании: Пшеничный В.А., Дубинина Т.В., Дроздов К.А. Разрушение проводящего состояния переменным электрическим полем в комплексах

© Pshenichnyi V. A., Dubinina T. V., Drozdov K. A., 2024. Published by Peter the Great St. Petersburg Polytechnic University.

нафталоцианинов // Научно-технические ведомости СПбГПУ. Физико-математические науки. 2024. Т. 17. № 1.1. С. 25–30. DOI: https://doi.org/10.18721/ JPM.171.104

Статья открытого доступа, распространяемая по лицензии CC BY-NC 4.0 (https:// creativecommons.org/licenses/by-nc/4.0/)

Introduction

Low-dimensional semiconductors are actively used for many practical applications [1]. One of promising effects is resistive switching. This effect lies in the possibility of a controlled reversible transition between two states with different electrical resistances (Ron and Roff). One of the variants of the structure with this property is a composite based on organic matrix permeated with metal nanowires [2]. The formation of nanowires can occur in strong electric fields due to the injection of metal ions from the contact and their self-organization. As the field strength increases, nanowire fragments are formed first, with their subsequent integration into full-fledged network, connecting the two electrodes [3]. At the same time, when critical currents are reached, a thermal-induced break in the system occurs. Thus, Ron corresponds to the situation when nanowires connect contacts, and Roff corresponds to multiply non-connected fragments.

The behavior of such system in AC field simultaneously characterizes the speed of switching between states with different nanowire configurations and stability under to external interference.

Materials and Methods

Solutions and films based on naphthalocyaninates with a central magnesium ion (NaPh-Mg) were studied. 3,4,12,13,21,22,30,31-Octa-(2-naphthoxy)-2,3-naphthalocyaninato magnesium complex was obtained starting from 6,7-di(2-naphthoxy)naphthalene-2,3-dicarbonitrile according to the previously described procedure [4]. The NaPh-Mg molecules have planar shape with average size of 21×21×2 Å. Films were obtained by deposition from solution onto glass substrates with ITO conducting layer. 1.5 and 1.0 μm films were obtained by drop-cast, 0.2 μm films by spin coating method. Film thickness was determined by white light interferometry with thickness variation less than 5% for all films. The top contact to the films with an area of 0.4 mm2 was formed using the Kontaktol silver paste.

Optical spectroscopy, DC and AC conductivity measurements were used as experimental methods. All measurements were performed at room temperature. Before conductivity measurements, all sample were shielded from external radiation and kept in dark conditions until complete relaxation. An 1 Ohm load resistor was series-connected to the sample.

Absorption spectra for solutions and films in the range of 300–900 nm were obtained using an Avantes AvaSpec-2048 spectrometer. For films spectral data was obtained before creation of upper contact. The current-voltage characteristics for the films were obtained using a Kietley 2612 instrument. Frequency dependencies of the conductivity in the range of $1-10^6$ Hz were obtained using a QuadTech 1920 Precision LCR Meter. The experimental data was cross-checked based on the coincidence of curves on repeated cycling both at increasing and decreasing voltage (DC mode) and frequency (AC mode).

Results and Discussion

The absorption spectra for solution and films in visible spectral range has a set of local maxima and is formed by various electronic transition between molecular levels in NaPh–Mg (Fig. 1). The absorption for all films varies in intensity, but does not demonstrate any significant differences in the shape and position of local maxima. The solution-film transition is accompanied by a decrease in intensity in the range of 550–800 nm, but the position of local absorption maxima is reproduced well. The latter allows to assert that that no significant distortion of the spatial configuration of NaPh-Mg molecules occurs in the films [5]. Films can be considered as identical media of varying thickness.

The formation of metal nanowires and resistive switching in all the samples was confirmed via I–V characteristics (Fig. 2).

© Пшеничный В.А., Дроздов К.А., Дубинина Т.В., 2024. Издатель: Санкт-Петербургский политехнический университет Петра Великого.

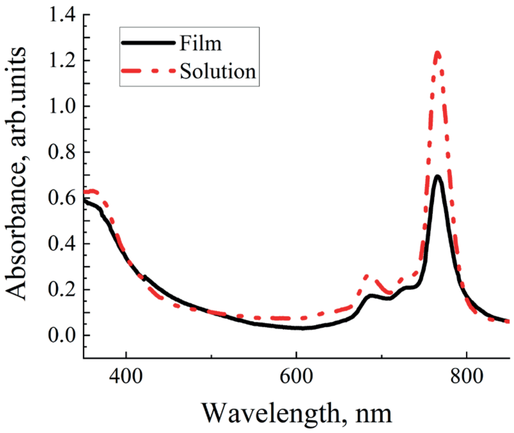

Fig. 1. Optical absorption for NaPh-Mg solution (dashed line) and 1.0 μm film (solid line)

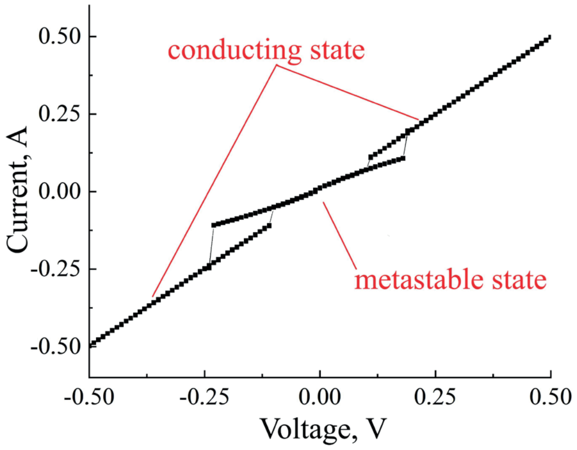

Fig. 2. Typical I—V characteristic for NaPh-Mg films. The specific graph corresponds to 0.2 μm film thickness

In addition to conducting and non-conducting, a set of metastable states also exist for all films. In metastable states, the structure is in dynamic equilibrium. Nanowires are continuously separated into individual fragments, which are joined again not necessarily in the initial configuration. The transport of charge carriers in the metastable state is determined by not only the structure of nanowire network, but also by energy barriers separating fragments. In comparison with the conducting, metastable states are characterized by increased electrical resistance and appearance (or increase) of capacitance [3].

In DC mode with voltage $U > 0.3$ V, all films were in stable conducting state. AC mode experiments were carried with $U = 1.0 + 0.5 \sin(wt)$, which corresponded to voltage range of 0.5—1.5 V. Varying film thickness resulted in varying values of electric field strength E.

In AC mode, the stability of the conducting state was preserved only in the low frequency range (3000, 500, 300 Hz for films with a thickness of 1.5, 1.0 and 0.2 μm, respectively). In this frequency range conducting state was characterized by active resistance Z' (equal to film resistance in DC mode), and reactive resistance Z'' (Z'' was lower than Z' by several orders of magnitude). At higher frequencies, two different behaviors (MI and MII) were observed. Both could take place simultaneously, with MI happening at lower frequencies. The dominance of specific behavior could be enforced by altering the I/U ratio in the film, which was achieved by adding a second load resistor in parallel to the sample (insets in Fig. 3, *a*, *b*).

MI (Fig. 3, *a*) was characterized by a spontaneous reversible transition of the system to a state with increased active resistance Z'. Simultaneously the reactive resistance Z'' decreased to negative values, which indicated appearance of capacitive contribution. Such behavior marks this state as metastable with nanowire fragmentation [3]. For metastable state Z' decreases nearly linearly, while capacity changes very little. A decrease in the film thickness leads to a shift of frequency range towards lower values.

MII (Fig. 3, *b*) was characterized by a decrease of the active resistance Z' to values below those of conducting state. Negative values for Z'' indicated capacity presence and thus, the metastable nature of this state. A decrease in the film thickness leads to an increase in the frequency range at which this effect was observed both towards lower and higher values.

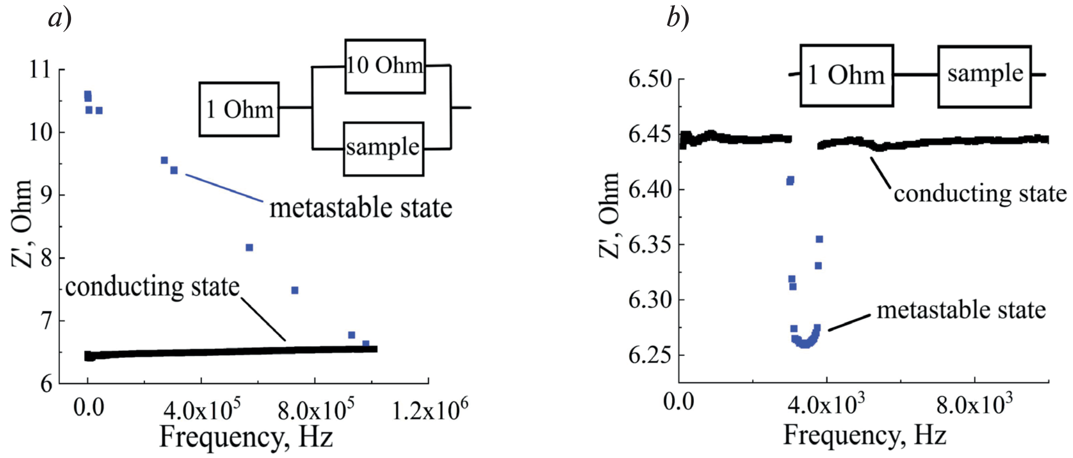

Fig. 3. Frequency dependence for active resistance Z' based on I/U ratio in 1.5 μm film.
The inset schematically demonstrates the load resistors configuration

It is possible not only to observe MI and MII simultaneously, but also to see several configurations for metastable state in each of them (Fig. 4) with indistinguishable reactive resistance Z'' and capacitance values (inset in Fig. 4). This means that both metastable configurations are characterized by the same degree of nanowire fragmentation (number of ruptures the electron must pass to get from one contact to another).

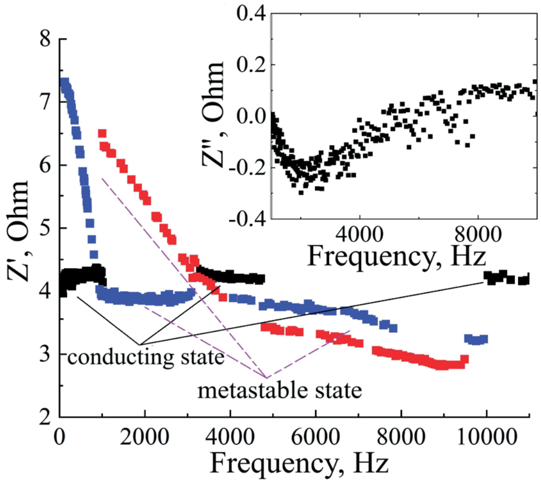

Fig. 4. Frequency dependence for active resistance Z' in 1.0 μm film
The inset demonstrates indistinguishable reactive resistance Z'' for metastable states

In order to explain all of the observed effects, a model of “mobile” nanowire fragments was proposed. The stability of nanowire configuration is determined by the value of applied electric field (stabilizing factor) and heat generation due to current flow (destabilizing factor). In alternating electric field thermal power is proportional to the square of the frequency for low frequencies *w*. When the rupture of a nanowire occurs, the fragments and separate metal ions, that composed said nanowire, have excessive thermal energy. With enough energy, they can instantly reform, either by themselves, or by attaching to non-ruptured nanowire. Compared to initial configuration (Fig. 5, *a*), re-formation can lead to both increase (Fig. 5, *b*) and decrease of active resistance (Fig. 5, *c*). The qualitative resistance value is shown below the corresponding diagrams.

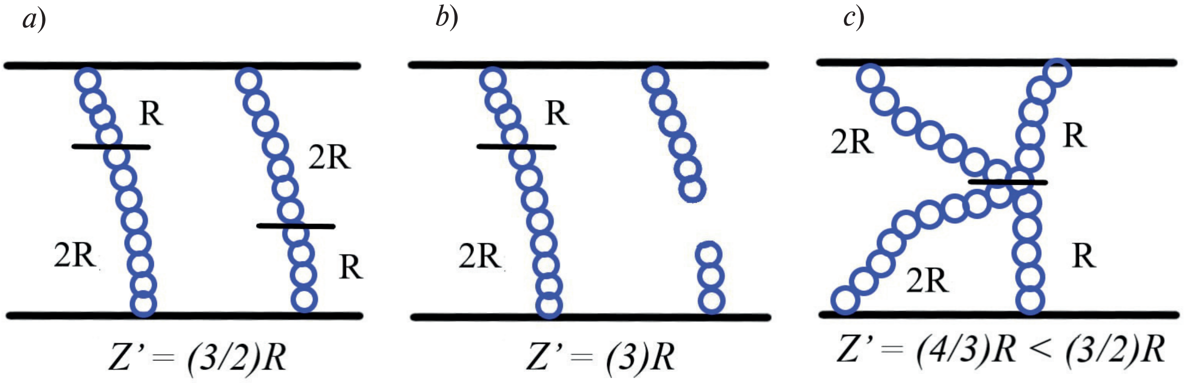

Fig. 5 Schematic illustration for nanowire re-form with change of active resistance Z'

Transition from conducting to metastable state with increased active resistance Z' (Fig. 4) can be associated with fragmentation of nanowires. Such process is always accompanied increase of capacitance and negative impact on Z'', which is inversely proportional to frequency (inset in Fig. 4). The best approximation for $I-V$ curves for metastable state (Fig. 2) is achieved with two parallel conduction mechanisms, namely, drift (unbroken nanowires) and activation (ruptured nanowires). As the frequency increases the re-formation of ruptured nanowires become more intense, resulting in Z' decrease.

After some critical frequencies (~ 2000 Hz on inset in Fig. 4) the degree of fragmentation begins to decrease. This is accompanied by consequent slow decrease of active resistance Z' for metastable state. Such behavior may be explained by ruptured nanowire fragments attaching to non-ruptured nanowires. The difference in active resistance Z' for different configurations of metastable state (Fig. 4) may be due to how the nanowire fragments are attached to the overall system.

The stability of new configuration is determined by the amount of generated heat from current flow and excessive energy that is still present in system after previous rupture. At high frequencies, the decrease of Z' invokes instant overheating, so metastable state cannot exist. This corresponds to system returning to MI on high frequencies (> 10000 Hz in Fig. 4).

Conclusion

It was shown that in naphthalocyanine films, conductivity occurs due to electron transport along metal nanowires. Based on the nanowires configuration, 3 main states of the system can be distinguished: conductive (nanowires are intact), metastable (some of the nanowires are broken) and non-conducting (all nanowires are broken). Switching between states is fully reversible. In DC mode the system state is determined by the values of applied electric field and the magnitude of the flowing current.

AC electric field can induce destruction of conducting state due to additional frequency dependent heat generation. Behavior of ruptured nanowires is frequency dependent. They can exist independently, providing activation contribution to the total conductivity. But within specific frequency range, ruptured fragments attach to non-broken nanowires, lowering overall resistance for the system. The lower frequency of this range is determined by the condition of sufficient energy to ensure mobility of the fragment when initial nanowire rupture occurs. Higher frequency is determined by the ability of a system with reduced resistance to pass currents with high heat generation without nanowires breaking to fragments.

REFERENCES

1. **Fang J., Zhou Z., Xiao M., Lou Z., Wei Z., Shen G.,** Recent Advances in Low-Dimensional Nanomaterials for Photodetectors, InfoMat. 2 (2019) 1–27.

2. **Yang L., Qingyun Q.,** Recent advances in organic-based materials for resistive memory applications, InfoMat. 2 (2020) 995–1033.

3. **Kotova M.S., Drozdov K.A., Dubinina T.V., Kuzmina E.A., Tomilova L.G., Vasiliev R.B., Dudnik A.O., Ryabova L.I., Khokhlov D.R.,** In situ impedance spectroscopy of filament formation by resistive switches in polymer based structures, Sci. Rep. 8, 9080 (2018).

4. **Dubinina T.V., Maklakov S.S., Petrusevich E.F., Borisova N.E.,** Photoactive layers for photovoltaics based on near-infrared absorbing aryl-substituted naphthalocyanine complexes: preparation and investigation of properties, New Journal of Chemistry. 45 (2021) 14815–14821.

5. **Djurovich P.I.,** Measurement of the lowest unoccupied molecular orbital energies of molecular organic semiconductors, Organic Electronics. 10 (2009) 515–520.

THE AUTHORS

PSHENICHNYI Vadim A.
pshenichnyi.va17@physics.msu.ru
ORCID: 0009-0003-0530-066X

DROZDOV Konstantin A.
Drozdov@physics.msu.ru
ORCID: 0000-0001-8600-7761

DUBININA Tatiana V.
DubininaTV@my.msu.ru
ORCID: 0000-0002-9970-7123

Received 14.12.2023. Approved after reviewing 13.02.2024. Accepted 13.02.2024.

St. Petersburg Polytechnic University Journal. Physics and Mathematics. 2024 Vol. 17. No. 1.1
Научно-технические ведомости СПбГПУ. Физико-математические науки. 17 (1.1) 2024

Conference paper
UDC 538.958
DOI: https://doi.org/10.18721/JPM.171.105

Dynamics of electron-nuclear spin system in GaAs:Mn epitaxial layers

V.S. Berdnikov [1] ✉, M.S. Kuznetsova [1], K.V. Kavokin [1], R.I. Dzhioev [2]

[1] St. Petersburg State University, St. Petersburg, Russia;
[2] Ioffe Institute, St. Petersburg, Russia
✉ vladimir.berdnikov.00@mail.ru

Abstract. In this paper we present experimental study of electron-nuclear spin dynamics in GaAs bulk layers doped with Mn ions at temperature 4.2 K. The electron spin dynamics is experimentally investigated by measuring the degree of polarization of photoluminescence in a transverse magnetic field (Hanle effect) and the recovery of the electron spin polarization in a longitudinal magnetic field (polarization recovery curve). To study nuclear spin dynamics, we use two-stage experimental protocol including optical cooling of nuclear spin system and measuring change of the polarisation degree of photoluminescence in different transverse magnetic fields. We show dependence of electron spin relaxation times on excitation power for three samples with different concentrations of shallow donors and acceptors. Electron spin relaxation times have been obtained as at the exciton transition as at the deep acceptor Mn transition. Also we show dependence of nuclear spin-lattice relaxation times T1 on value of external transverse magnetic field.

Keywords: semiconductors, gallium arsenide, spin, spin dynamics, spin relaxation, optical orientation, Hanle effect, polarization

Funding: The study was supported by the St. Petersburg State University grant 94030557.

Citation: Berdnikov V.S., Kuznetsova M.S., Kavokin K.V., Dzhioev R.I., Dynamics of electron-nuclear spin system in GaAs:Mn epitaxial layers, St. Petersburg State Polytechnical University Journal. Physics and Mathematics. 17 (1.1) (2024) 31–36. DOI: https://doi.org/10.18721/JPM.171.105

This is an open access article under the CC BY-NC 4.0 license (https://creativecommons.org/licenses/by-nc/4.0/)

Материалы конференции
УДК 538.958
DOI: https://doi.org/10.18721/JPM.171.105

Динамика электронно-ядерной спиновой системы в эпитаксиальных слоях GaAs:Mn

В.С. Бердников [1] ✉, М.С. Кузнецова [1], К.В. Кавокин [1], Р.И. Джиоев [2]

[1] Санкт-Петербургский государственный университет, Санкт-Петербург, Россия;
[2] Физико-технический институт им. А.Ф. Иоффе РАН, Санкт-Петербург, Россия
✉ vladimir.berdnikov.00@mail.ru

Аннотация. В настоящей работе представлено экспериментальное исследование динамики электронно-ядерной спиновой системы в объемных слоях GaAs, легированного ионами Mn при температуре 4,2 K. Получена зависимость времен электронной спиновой релаксации от мощности оптической накачки для трех образцов с различной концентрацией мелких доноров и акцепторов. Времена электронной спиновой

© Berdnikov V.S., Kuznetsova M.S., Kavokin K.V., Dzhioev R.I., 2024. Published by Peter the Great St. Petersburg Polytechnic University.

релаксации определялись как для экситонного перехода, там и для перехода глубокого акцепторного центра Mn. Получена зависимость времен ядерной спин-решеточной релаксации T1 от величины внешнего поперечного магнитного поля.

Ключевые слова: полупроводники, арсенид галлия, спин, спиновая динамика, спиновая релаксация, оптическая ориентация, эффект Ханле, поляризация

Финансирование: Работа выполнена при финансовой поддержке Санкт-Петербургского государственного университета в рамках гранта № 94030557.

Ссылка при цитировании: Бердников В.С., Кузнецова М.С., Кавокин К.В., Джиоев Р.И. Динамика электронно-ядерной спиновой системы в эпитаксиальных слоях GaAs:MN // Научно-технические ведомости СПбГПУ. Физико-математические науки. 2024. Т. 17. № 1.1. С. 31–36. DOI: https://doi.org/10.18721/ JPM.171.105

Статья открытого доступа, распространяемая по лицензии CC BY-NC 4.0 (https://creativecommons.org/licenses/by-nc/4.0/)

Introduction

The idea of using spin states of carriers for processing and storing information has been actively discussed in recent decades. It is important for spintronics to study the characteristics of an electron-nuclear spin system, such as electron and nuclear spin relaxation times.

GaAs is a well-studied semiconductor, but adding a magnetic impurity of Mn leads to unexpected results. In Mn-doped GaAs one can see suppression of the Bir-Aronov-Pikus spin relaxation mechanism, which is significant in regular *p*-type GaAs [1,2].

In this paper, we present measurements of electron spin relaxation times τ_s as function of excitation power for 3 samples with different concentrations of impurities. Also in this work we have obtained the dependence of the nuclear spin relaxation times T_1 on the external magnetic field.

Structures and Methods

The sample under study consists of 36-μm layers of bulk GaAs:Mn grown by liquid-phase epitaxy on a (001)-oriented GaAs substrate. Samples are doped with Mn ions. Shallow donors and acceptors are also present. Parameters of doping concentrations are shown in Table.

Table

Concentrations of Mn acceptors and the difference in concentrations of shallow donors and acceptors for different samples

Sample	$N_{Mn}\cdot 10^{17}$ cm^{-3}	$N_d - N_a \cdot 10^{15}$ cm^{-3}
Sample 1	2.77	3.44
Sample 2	3.6	–0.33
Sample 3	1.2	0.03

Notations: N_{Mn}, N_d and N_a are the concentrations of Mn and shallow donors and acceptors , respectively.

Electron spin dynamics is experimentally investigated by measuring the degree of polarization of photoluminescence (PL) in a transverse magnetic field (Hanle effect) and the recovery of the electron spin polarization in a longitudinal magnetic field (polarization recovery curve, PRC). Electron spin polarization is created by circularly polarized continuous wave excitation using Ti:Sapphire laser operating at 800 nm. Excitation beam is focused on the sample to the 300-μm diameter spot. To avoid the effect of nuclear spins to electron spin dynamics, the polarization helicity of the excitation has been modulated at the frequency 50 kHz. To create the transverse to optical pump magnetic field we use the electromagnet installed outside the cryostat. Pairs of Helmholtz coils create longitudinal magnetic fields with magnitude up to 30 mT.

© Бердников В.С., Кузнецова М.С., Кавокин К.В., Джиоев Р.И., 2024. Издатель: Санкт-Петербургский политехнический университет Петра Великого.

Spin relaxation time of electron τ_s and lifetime of optically excited electrons τ are obtained by measuring the series of the Hanle curves and polarization recovery curves. The dynamics of the average electron spin in Voigt geometry manifests itself in the magnetic-field dependence of degree of circular polarization of luminescence [1]:

$$\rho_c = \frac{\rho_0}{\left(1+\dfrac{\tau}{\tau_s}\right)} \frac{1}{\left(1+\left(B/B_{1/2}\right)^2\right)}, \tag{1}$$

where $B_{1/2} = \hbar/(g_e\mu_B)T_s^{-1}$ is the characteristic field that gives inverse electron spin lifetime $T_s^{-1} = \tau_s^{-1} + \tau^{-1}$, and B is the value of the external transverse magnetic field.

To get initial polarization ρ_0, we model data from experiments in Faraday geometry with the following expression [3]:

$$\rho_c = \frac{\rho_0}{1+\dfrac{\tau}{\tau_s^*}},\quad \tau_s^* = \tau_s\left[1+\left(B/B_c\right)^2\right], \tag{2}$$

where B_c is the correlation field (fitting parameter), and B is the value of the external longitudinal magnetic field.

Optical orientation and the Hanle effect form the basis for experiments to study electron-nuclear spin dynamics. To investigate the nuclear spin relaxation time, we use two stage experiment. At the first stage the nuclear spin system is cooled due to hyperfine interaction with polarized electron spin and application of the longitudinal magnetic field B_z = 3 mT. At this stage the Overhauser field B_N is generated. At the second stage the field B_z is turned off and certain transverse magnetic field B_x with magnitude range from 0.1 mT to 40 mT is turned on.

Precession of the electron spin in the total effective transverse magnetic field $B_x \pm B_N$ results in the following time dependence of the PL circular polarization degree [4]:

$$\rho_c = \rho_0 \frac{B_{1/2}^2}{B_{1/2}^2 + \left(B_x + b + \left(B_N - b\right)\exp\left(-\dfrac{t}{T_1}\right)\right)^2}, \tag{3}$$

where ρ_0 and $B_{1/2}$ are parameters extracted from the analysis of the 50 kHz modulated Hanle curve at the same excitation power; t is the laboratory time; b is the effective field appeared due to dynamic nuclear polarization during the optical pumping at the second stage.

Results and Discussion

Firstly, we measure photoluminescence spectra at different excitation power from 0.01 mW to 20 mW. For clarity, only spectra for Sample 1 are presented in Fig. 1, *a*. The energy of excitation is 1.55 eV. There are peaks corresponding to energy transitions shown in Fig. 1, *b* with black arrows. We can see a wide Mn-related band with peak at the energy 1.41 eV (labeled as Mn band). The peaks at the 1.51 eV and 1.49 eV correspond to free and donor-bound excitons (labeled as X) and conduction-band-acceptor transitions (labeled as Ac) respectively.

Below a threshold value of excitation power, $P_{th} \approx 1$ mW, the X peak is absent, while the Mn band is still visible in the spectra. It also can be seen in inset of Fig. 1, *a*, which demonstrates the ratio I_X/I_{Mn} of X and Mn intensities.

Fig. 2, *a* demonstrates results of analysis of experimental data of series Hanle curves and PRC, measured for 3 samples from Table. These results are presented for energy of detection 1.41 eV (corresponding to electron recombination with hole at Mn acceptor). In each case the spin relaxation time increases with increasing the excitation power until some value which matches the value P_{th} = 1 mW that we have seen from the analysis of PL spectra. The values of the spin relaxation time in GaAs:Mn are 2 orders of magnitude greater than in p-GaAs, similar to [3].

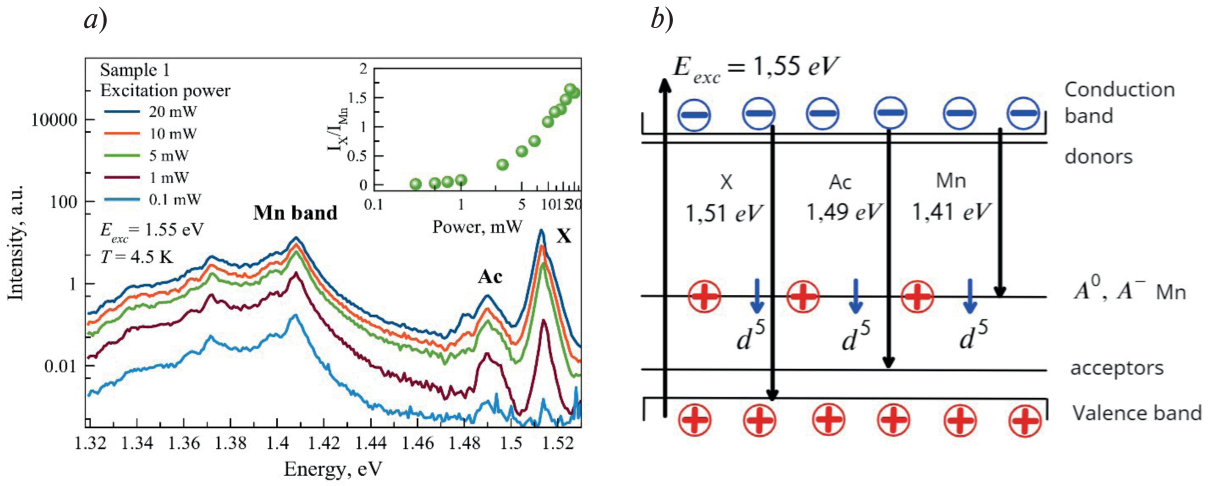

Fig. 1. Photoluminescence spectra of Sample 1 at different excitation powers. Intensity is shown in logarithmic scale. Inset shows the ratio of X and Mn peak intensities depending on excitation power (*a*). Energy diagram of GaAs:Mn (*b*)

All measurements were also performed at the energy of detection 1.51 eV (free and donor bounded excitons). As evident from comparison in Fig. 2, *b*, the behavior of electron spin relaxation time measured at energies 1.41 eV and 1.51 eV is strongly different. The value of electron spin relaxation time measured for energy 1.51 eV monotonously decreases with the increase of excitation power. This difference is a clear indication that it is the Mn impurity which causes such unexpected behavior of spin relaxation time.

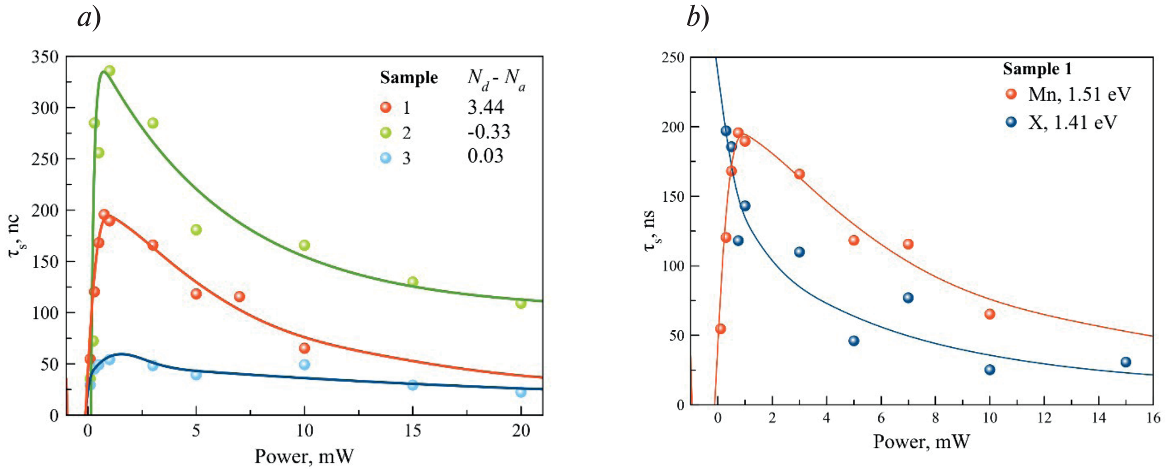

Fig. 2. Spin relaxation time of electrons vs excitation power for 3 samples (*a*). Dependences of spin relaxation time on excitation power at different energy of detection for Sample 1 (red points correspond to at Mn peak, blue points to X peak) (*b*). Solid lines are spline fits plotted as guides to the eye

To study nuclear spin dynamics, we measured the time dependences of the PL polarization in the two-stage experiment at different values of the transverse magnetic field. As seen from Fig. 3. the degree of circular polarization of luminescence drops at the moment of field switching. Then we can see partial recovery of the polarization with time.

Curves were modelled with Eq.3, where B_N and T_1 are fitting parameters. Thus, we obtained the Overhauser field B_N and nuclear spin relaxation time T_1 as functions of external transverse magnetic field. Results are presented in Fig. 4, *a*, *b*, respectively.

The Overhauser field increases with growing external magnetic field from 27 mT to 60 mT.

Spin-lattice relaxation time depends on external field and rises from 3 s at small magnetic field B_x to 20 s in saturation. This value is 2 orders greater than in nonmagnetic doped *p*-GaAs [5].

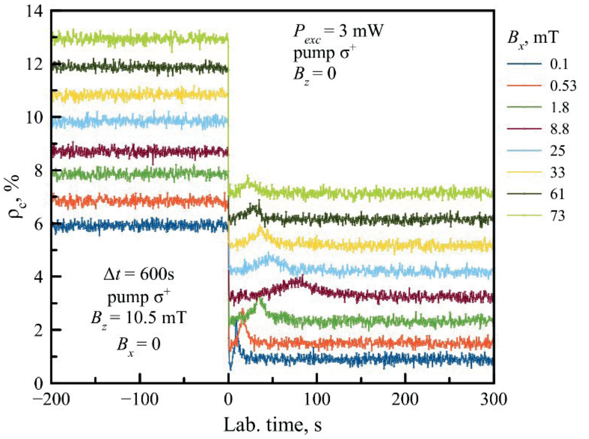

Fig. 3. Degree of circular polarization of luminescence in two-stage experiment for Sample 1. Cooling time Δt = 600 s, excitation power P_{exc} = 3 mW. Curves are presented as waterfall

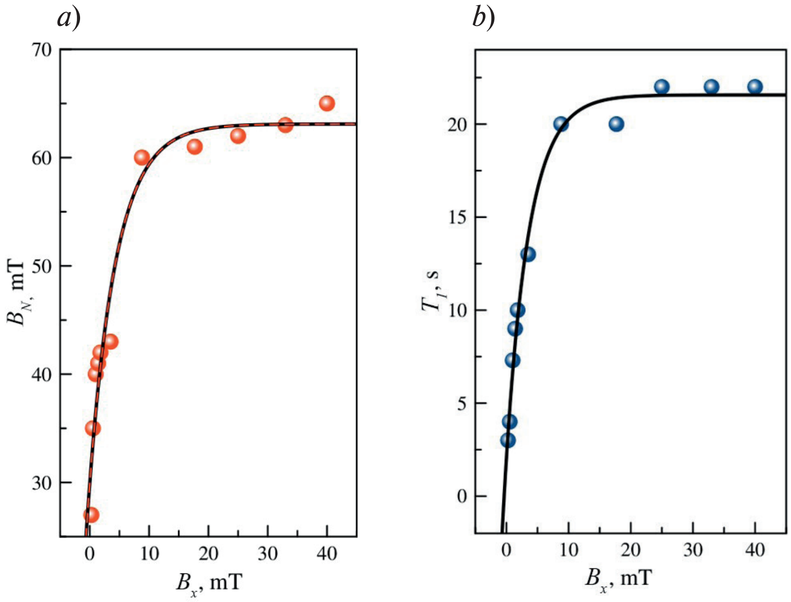

Fig. 4. Dependences of Overhauser field (*a*) and nuclear spin relaxation time (*b*) on the external transverse magnetic field for Sample 1

We suppose that it is related to suppression of quadrupole nuclear relaxation. However the mechanisms of nuclear spin-lattice relaxation in GaAs:Mn requires further investigation.

Conclusion

We have confirmed that electron spin relaxation time in epitaxial layers of GaAs:Mn demonstrate an unusual behavior compared to nonmagnetic doped p-GaAs. It can be explained by suppression of Bir–Aronov–Pikus spin relaxation mechanism.

Spin-lattice relaxation time in GaAs:Mn demonstrates the behavior untypical for p-type GaAs.

A two-stage experiment does not allow us to confidently determine the nuclear spin relaxation time T1 because of the effects of optical pumping during the measurement stage. To verify our results, a three-stage experiment including "dark times" [5] needs to be used. In this experiment, different time periods without optical pump are added between optical cooling and measurement stages.

Acknowledgments

We are grateful to V.M. Litvyak for valuable discussions and support.

REFERENCES

1. ed. by **Meier F., Zakharchenya B.P.,** Optical orientation, Amsterdam: North-Holland, 1984, p. 81.
2. **Bir G.L., Aronov A.G., Pikus G.E.,** Spin relaxation of electrons due to scattering by holes, Zh. Eksp. Teor. Fiz. 69 (1975) 1382–1397.
3. **Astakhov G.V., Dzhioev R.I., Kavokin K.V., Korenev V.L., Lazarev M.V., Tkachuk M.N., Kusrayev Yu.G., Kiessling T., Ossau W., Molenkamp L.W.,** Supression of electron spin relaxation in Mn-doped GaAs, Physical Revive Letters 101 (2008) 0766022.
4. **Litvyak V.M.,** Effects observed in semiconductors during deep cooling of nuclear spins, Candidate's thesis. St. Petersburg, 2022, 64–77.
5. **Kotur M., Dzhioev R.I., Vladimirova M., Cherbunin R.V., Sokolov P.S., Yakovlev D.R., Bayer M., Suter D., Kavokin K.V.,** Spin-lattice relaxation of optically polarized nuclei in p-type GaAs, Physical Reviev B 97 (2018) 165206.

THE AUTHORS

BERDNIKOV Vladimir S.
vladimir.berdnikov.00@mail.ru
ORCID: 0009-0002-1428-3323

KUZNETSOVA Maria S.
mashakuznecova@bk.ru
ORCID: 0000-0003-3836-1250

KAVOKIN Kirill V.
kkavokin@gmail.com
ORCID: 0000-0002-0047-5706

DZHIOEV Roslan I.
Dzhioev@orient.ioffe.ru

Received 14.12.2023. Approved after reviewing 15.01.2024. Accepted 02.02.2024.

St. Petersburg Polytechnic University Journal. Physics and Mathematics. 2024 Vol. 17. No. 1.1
Научно-технические ведомости СПбГПУ. Физико-математические науки. 17 (1.1) 2024

Structure growth, surface, and interfaces

Conference paper
UDC 539.67
DOI: https://doi.org/10.18721/JPM.171.106

Investigation of nanosized structures using internal friction effect

D.A. Kozodaev [1], I.A. Novikov [1, 2] ✉, V.A. Moshnikov [2]

[1] NT-MDT, Zelenograd, Moscow, Russia

[2] Saint-Petersburg State Electrotechnical University ETU "LETI", St. Petersburg, Russia

✉ ianovikov@stud.etu.ru

Abstract. The goal of this work is to study electrically active defects in planar ($Si\text{-}SiO_2$) and isoplanar ($Si\text{-}SiO_2\text{-}Si_3N_4$) silicon electret structures by the internal friction Q^{-1} method. The Q^{-1} set with a reversed pendulum type design is used for research. The activation energies and frequency factors of thermoelastic processes were determined due to the displacement of peaks on the Q^{-1} relaxation spectra. Moreover, additional local maxima formed after electrification of structures were found on the temperature dependence Q^{-1}. It is assumed that this may be due to the interaction of charged particles obtained as a result of irradiation in a corona discharge with capture centers, which are hydride Si-H and hydroxyl Si-OH groups, as well as with deep capture centers at the $SiO_2\text{-}Si_3N_4$ interface. We confirmed that the developed complex research method for determining the main electrophysical parameters of electret structures based on silicon oxide and silicon nitride allows finding optimal approaches to electrifying $Si\text{-}SiO_2$ and $Si\text{-}SiO_2\text{-}Si_3N_4$ structures for their practical application as active elements of electret sensors and actuators.

Keywords: Internal friction, Young's Modulus, electrets, silicon oxide, silicon nitride

Citation: Kozodaev D.A., Novikov I.A., Moshnikov V.A., Investigation of nanosized structures using internal friction effect, St. Petersburg State Polytechnical University Journal. Physics and Mathematics. 17 (1.1) (2024) 37–42. DOI: https://doi.org/10.18721/JPM.171.106

This is an open access article under the CC BY-NC 4.0 license (https://creativecommons.org/licenses/by-nc/4.0/)

Материалы конференции
УДК 539.67
DOI: https://doi.org/10.18721/JPM.171.106

Исследование наноразмерных структур с использованием эффекта внутреннего трения

Д.А. Козодаев [1], И.А. Новиков [1, 2] ✉, В.А. Мошников [2]

[1] ООО «НТ-МДТ», Зеленоград, Москва, Россия

[2] СПбГЭТУ «ЛЭТИ», Санкт-Петербург, Россия

✉ ianovikov@stud.etu.ru

Аннотация. Целью данной работы является исследование электрически активных дефектов в планарных ($Si\text{-}SiO_2$) и изопланарных ($Si\text{-}SiO_2\text{-}Si_3N_4$) кремниевых электретных структурах методом внутреннего трения Q^{-1}. Для проведения исследований использовалась установка Q^{-1}, работающая по принципу обращенного маятника. Благодаря смещению пиков на релаксационных спектрах Q^{-1} были определены энергии активации и частотные факторы термоупругих процессов. Также, на температурной зависимости Q^{-1} были обнаружены дополнительные локальные максимумы, образующиеся после электризации структур. Предполагается, что это может быть связано с взаимодействием заряженных частиц, полученных в результате облучения в коронном разряде, с центрами захвата, которыми являются гидридные Si-H и гидроксильные Si-OH группы,

© Kozodaev D.A., Novikov I.A., Moshnikov V.A., 2024. Published by Peter the Great St. Petersburg Polytechnic University.

а также с глубокими центрами захвата на интерфейсе SiO_2-Si_3N_4. Результаты работы показывают, что разработанный комплексный метод исследования для определения основных электрофизических параметров электретных структур на основе оксида и нитрида кремния позволяет определять оптимальные способы электризации структур Si-SiO_2 и Si-SiO_2-Si_3N_4 для их практического применения в качестве активных элементов электретных сенсоров и актюаторов.

Ключевые слова: внутреннее трение, модуль Юнга, электреты, оксид кремния, нитрид кремния

Ссылка при цитировании: Козодаев Д.А., Новиков И.А., Мошников В.А. Исследование наноразмерных структур с использованием эффекта внутреннего трения // Научно-технические ведомости СПбГПУ. Физико-математические науки. 2024. Т. 17. № 1.1. С. 37–42. DOI: https://doi.org/10.18721/ JPM.171.106

Статья открытого доступа, распространяемая по лицензии CC BY-NC 4.0 (https://creativecommons.org/licenses/by-nc/4.0/)

Introduction

Silicon planar technology in production of microelectronics and microsystem technology allows to create miniature sensors and actuators for various purposes, including based on the electret effect (electret microphones, pressure sensors). Base materials obtained using planar and isoplanar technologies are of particular interest as electret materials in the designs of such devices; these are silicon dioxide SiO_2, silicon nitride Si_3N_4 and their two-layer composition SiO_2-Si_3N_4. There are many ways to obtain such structures, for example, by high-temperature thermal oxidation and nitration of silicon, gas-phase and plasma chemical deposition, ion implantation, and others. At the same time, the whole variety of electronic processes occurring in silicon-based semiconductor structures depends not only on the structure and defectiveness of silicon itself, its oxide and nitride, but also primarily on the Si-SiO_2 and SiO_2-Si_3N_4 interface [1].

The electret materials used in microsystem engineering must meet the following physical requirements. Firstly, it is the temporary stability of the electric field created by electrets, and secondly, the stability of the characteristics to environmental influences.

The miniaturization of modern devices leads to the need to modernize existing methods of control and nanodiagnostics of their parameters. Scanning probe microscopy is a vivid example of a technology allowing to obtain images not only in the traditional concepts of microscopy (roughness), but also as an analytical response to physical parameters distributed over the surface of the analyzed material. Such capabilities are implemented both by creating special techniques for controlling the probe, and by modifying the probe materials.

Among the new parameters that are planned to be transferred to the field of nano- and subnano measurements are the parameters of the so-called internal friction Q^{-1}. At the initial stage of the work, it is necessary to study the features of the nature of the measured phenomena. We selected the methods developed in the dissertation [2] as the basic methods. Internal friction Q^{-1} is the ability of materials to dissipate the energy of mechanical vibrations, converting it through various mechanisms into heat. The internal friction Q^{-1} is the inverse of the Q-factor, which is characterized by the ratio of the energy stored in the oscillatory system to the energy lost during the oscillation period [3, 4].

Let us explain the physical nature of the experimentally observed attenuation of free bending vibrations of the plate by the example of considering the thermoelastic effect. When bending a uniformly heated thin plate made of a material that expands under heating, the stretched sections of the sample cool down, and the compressed ones heat up. Thus, deformation causes a disturbance of thermal equilibrium. Temperature equalization is accompanied by an irreversible transition of elastic energy into thermal energy and is one of the reasons for the damping of vibrations. This process of restoring disturbed equilibrium is called relaxation. If several relaxation processes with different relaxation times τ_i occur simultaneously in a solid, then the totality of all relaxation times forms the so-called relaxation spectrum. At the same time, by changing the frequency of forced oscillations, a sequence of resonant peaks of internal friction Q^{-1} can be distinguished. For

© Козодаев Д.А., Новиков И.А., Мошников В.А., 2024. Издатель: Санкт-Петербургский политехнический университет Петра Великого.

the purposes of analyzing film nanomaterials and technological processes, designs of the reversed pendulum type are the most effective [5, 6]. In such measurement schemes, only the surface layers are subjected to deformation effects of plate samples, and thus the possibility of integrally obtaining information about the properties of the entire coating layer is realized.

The method of analyzing nanomaterials using the internal friction Q^{-1} effect has proven itself in many applications. Among them, determination of the intensity of relaxation internal friction and activation energy in semiconductor compounds before and after electron irradiation [7]. Thus, the aim of the work is to study electrically active defects at the interface of dielectric films of silicon oxide and silicon nitride on a silicon substrate by the internal friction method.

Materials and Methods

The study of relaxation processes makes it possible to obtain information about the electronic structure of solids, electron-phonon interactions, the nature of phase transitions, the anharmonicity of interatomic interaction forces and the properties of various defects in semiconductor and dielectric materials. For Si-SiO_2 and Si-SiO_2-Si_3N_4 electret structures, understanding the nature of the relaxation processes taking place in them makes it possible to predict the charge stability in these materials.

The materials studied were oxide films grown on the silicon surface, as well as composite structures of silicon oxide and nitride on the silicon surface.

Silicon dioxide was obtained by combined thermal oxidation in the dry–wet–dry oxidation mode at a temperature of 1050 °C, a layer of silicon nitride was obtained by chemical deposition from the gas phase in the form of a mixture of silane and ammonia at a temperature of 1000 °C: the samples were rectangular plates measuring 5×15 mm^2. The thicknesses of the SiO_2 and Si_3N_4 layers were ~ 0.7 μm and ~ 0.1 μm, respectively. The plates were divided into two parts, one of which was not charged, and the second was electrified in a corona discharge to a surface potential of 300 V.

The measurements were carried out on the internal friction Q^{-1} set using the reversed pendulum method, shown in Fig. 1 [5], in the temperature range of 20–430 °C and frequencies of 0.5–2 Hz. Relaxation times τ_i depend on temperature and frequency, so it is advisable to go into the infrasound region to work at 'comfortable' temperatures.

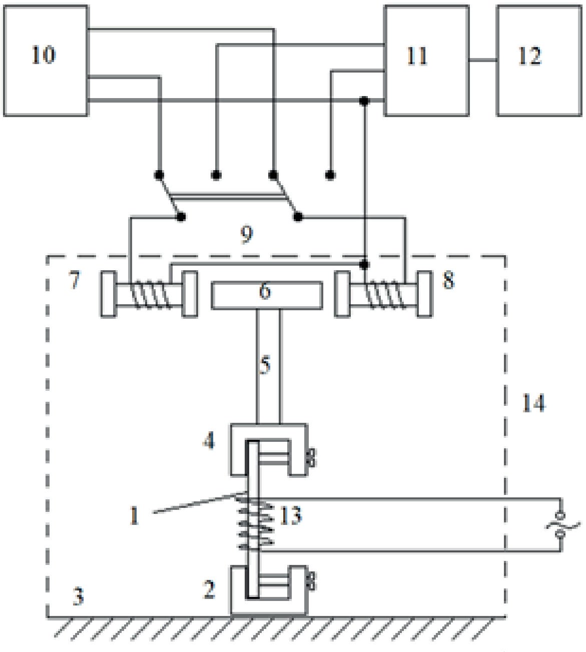

Fig. 1. Scheme of internal friction Q^{-1} set

The principle of operation of the Q^{-1} set is as follows. Sample *1* is fixed on edge using collet *2* to base *3*. Collet *4* with a pendulum *5* is attached to the other edge of sample *1*, in the upper part of which ring *6* of ferromagnetic material is installed. Near ring *6*, coils *7* and *8* are symmetrically arranged, which, using switch 9, are connected either to low frequency generator *10* or to amplitude discriminator *11* connected to electronic counter *12* by an output. In the first case, coils *7* and *8* are used as the exciter of mechanical vibrations of the pendulum *5* due to the interaction of the magnetic field of the coils with ferromagnetic ring *6*, in the second case as a sensor for the movements of ring *6*. Heater *13* is located near sample *1*. Elements *1*, *2*, *4–8*, *13* are placed in airtight container *14*, from which air is pumped out to reduce the damping of the oscillations of pendulum *5*.

To determine the relaxation parameters (activation energy E_A and frequency factor ω_0) of the interphase boundaries, studies were carried out at different oscillation frequencies. This was carried out by changing the geometric sizes of the samples with automatic adjustment of the intrinsic oscillation frequency of the sample. When the frequency changed, the relaxation peaks shifted in temperature upward, which made it possible to determine the activation energies and frequency factors of thermoelastic processes (E_{A1} = 0.28 eV and ω_{01} = $3.2\cdot10^4$ s^{-1}, E_{A2} = 0.39 eV and ω_{01} = $1.0\cdot10^5$ s^{-1}).

The relaxation maxima associated with the excitation of the interface due to thermoelastic vibrations caused by the disordered structure of the Si-SiO_2 and Si-SiO_2-Si_3N_4 transition layers and the difference in the coefficients of thermal expansion were observed on the temperature dependence of the Q^{-1} of electrified samples.

With various methods of producing films, depending on the technological conditions in the structures under study, both tensile and compressive elastic mechanical stresses may be present. A more complex case of joint (and equivalent in magnitude) action of both (tensile and compressive) stresses is relatively rare. The value of elastic stresses is ~ $1-5\cdot10^9$ dyn/cm^2 (on average ~ $3\cdot10^9$ dyn/cm^2). One of the causes of elastic stresses is the difference in the coefficients of thermal expansion Si, SiO_2, Si_3N_4 [8, 9]. Elastic stresses in Si-SiO_2 and Si-SiO_2-Si_3N_4 structures depend on technological conditions: temperature and film deposition rate, characteristics of the annealing process, concentration of impurity defects and porosity of the film.

Results and Discussion

Common to all the uncharged samples studied was the detection of relaxation maxima on the temperature dependence Q^{-1} at a temperature of 180 °C for Si-SiO_2 and 100 °C and ~ 180 °C for Si-SiO_2-Si_3N_4 (Fig. 2).

Additional relaxation peaks were observed on the temperature dependence of the internal friction of electrified samples, which were absent in uncharged structures. Since the internal friction spectra of the studied samples did not change from tempering, it can be assumed that the appearance of an additional peak is due to the action of a charge injected into the sample volume using a corona discharge.

For electrified samples, this technique is informative enough to determine the energy position of the Q^{-1} peak associated with relaxation processes. The most interesting physical result is the ability to track changes in the temperature of the peak maximum, accompanied by a charge drain. Fig. 2 shows the Q^{-1} spectra for charged samples. With each subsequent measurement, the charge decreases, this is accompanied by the movement of the relaxation peak to the region of higher temperatures and, what is especially interesting, by an inflection and an increase in the elastic modulus in the peak region.

Within the framework of the model, it is assumed that during the electrification of a sample in a corona discharge, negatively charged ions are deposited on its free surface. As a result of electronic exchange with structural defects, excess electrons penetrate into the sample volume and are localized at the capture centers in the near-surface layer. Hydrogen-containing complexes, such as Si-H and Si-OH, as well as their own structural defects act as the main capture centers in layers of silicon dioxide and nitride [10]. Electron capture by Si-H and Si-OH groups occurs with electrochemical reactions and delocalization of atomic hydrogen. Under the action of an external or intrinsic electric field of the electret structure, charge carriers are released from the capture centers and flow deep into the sample until they are localized on the capture traps. In addition, charge carriers may be intercepted at deep capture centers concentrated at the SiO_2-Si_3N_4 phase interface.

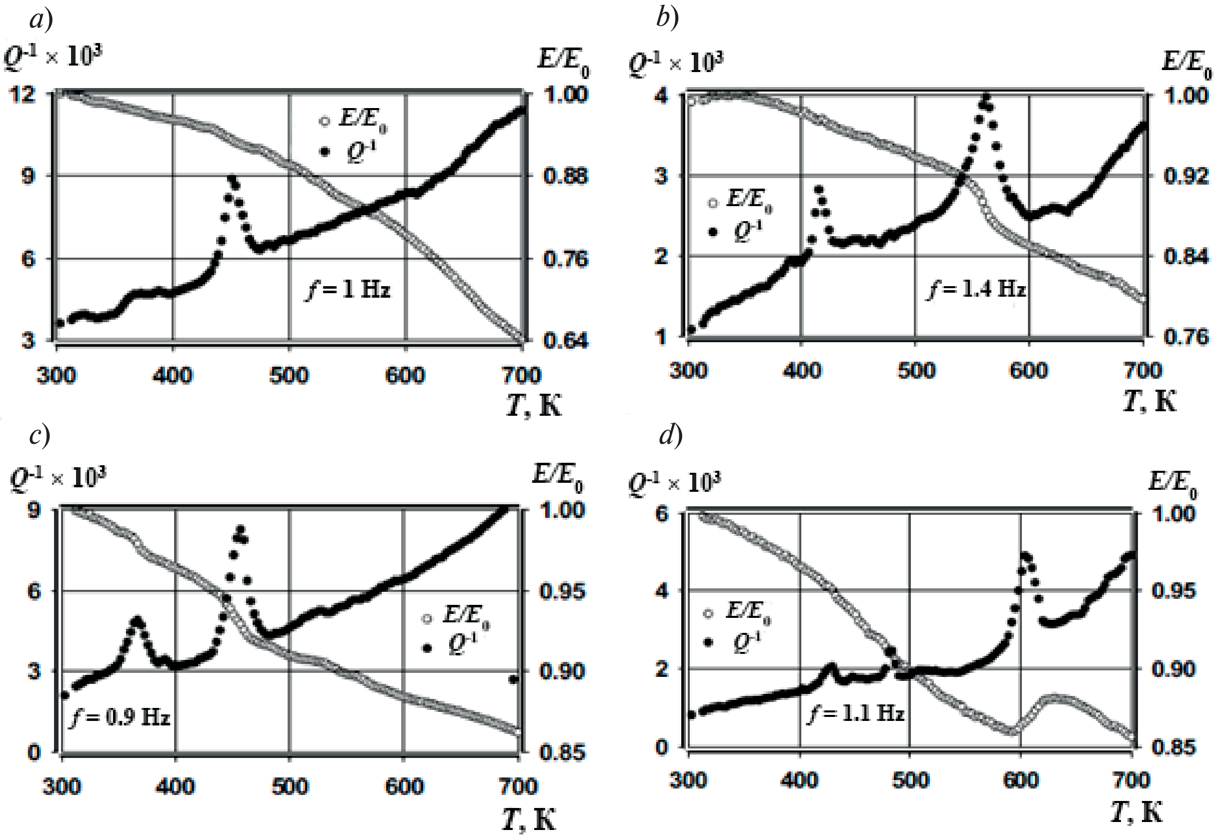

Fig. 2. Temperature dependence of Q^{-1} and change in Young's modulus of uncharged Si-SiO$_2$ (*a*), Si-SiO$_2$-Si$_3$N$_4$ (*c*) samples and negatively charged Si-SiO$_2$ (*b*), Si-SiO$_2$-Si$_3$N$_4$ (*d*) samples

Conclusion

It is shown that additional peaks associated with the excitation of new defects appear on the temperature dependence Q^{-1} of charged samples, which are absent in uncharged structures. This indicates that the charge carriers injected into the volume have a sufficiently strong effect on the defects in the structure of the materials under study. It is assumed that atomic hydrogen, delocalized during electrification during electron capture and decomposition of the impurity capture center, is responsible for these peaks.

A new method was proposed for studying relaxation processes in electrified samples, in which the dynamics of changes in the internal friction and Young's modulus of charged samples during sequential heating-cooling cycles was tracked. Under the influence of temperature, the charge carriers are activated, shifted deep into the sample and re-localized at the capture centers, thereby releasing more and more hydrogen.

REFERENCES

1. **Belonogov E.K., Darinsky B.M., Il'in A.S., Mitrokhin V.I., Kharin A.N., Yaroslavtsev N.P., Moshnikov V.A.,** Internal friction in films based on Si3N4 and Cu-Se. Bulletin of the Russian Academy of Sciences: Physics. 69 (8) (2005) 1306–1309.

2. **Kozodaev D.A.,** Elektretniy effekt v strukturah Si-SiO$_2$ i Si-SiO$_2$ – Si$_3$N$_4$ [Electret effect in Si-SiO$_2$ and Si-SiO$_2$ – Si$_3$N$_4$ structures]. PhD thesis. Saint-Petersburg Electrotechnical University ETU "LETI" (In Russian) (2002).

3. **Nowick A.S., Berry B.S.,** Anelastic Relaxation in Crystalline Solids. New York: Academic Press, 1972.

4. **Blanter M.S., Golovin I.S., Neuhдuser H., Sinning H.-R.,** Introduction to Internal Friction: Terms and Definitions. In: Internal Friction in Metallic Materials. Springer Series in Materials Science Vol. 90. Springer, Berlin, Heidelberg.

5. **Rembeza S.I., Mitrokhin V.I.,** From internal friction to optoelectronics. International Scientific Journal for Alternative Energy and Ecology© Scientific Technical Centre «TATA». 3 (167) (2015) 150–157.

6. **Smirnova I.V., Shilova O.A., Moshnikov V.A., Panov M.F., Shevchenko V.V., Klimenko N.,** Investigation of the physicochemical properties, structure, and composition of nanosized borosilicate films prepared by the sol-gel method. Glass Physics and Chemistry 32 (2006) 460–470.

7. **Kurashvili I., Darsavelidze G., Kimeridze T., Tabatadze I., Melashvili T., Sichinava A., Archuadze G.,** Internal friction temperature spectra in electron-irradiated SiGe alloys. Bulletin of the Georgian National Academy of Sciences. 13 (3) (2019) 43–49.

8. **EerNisse E.P.,** Viscous flow of thermal SiO_2. Appl. Phys. Lett. 30(6) (1977) 290–293.

9. Hu S. M., Temperature dependence of critical stress in oxygen-free silicon. Journal of Applied Physics 49 (11) (1978) 5678–5679.

10. **Lin H., Xia Z., Shen S.,** The study of the intrinsic charges in SiO electrets, Proceedings of 8th International Symposium on Electrets (ISE 8), Paris, France. (1994) 107–112.

THE AUTHORS

KOZODAEV Dmitriy A.
kozodaev@ntmdt.nl

NOVIKOV Ivan A.
ianovikov@stud.etu.ru
ORCID: 0009-0003-0155-4208

MOSHNIKOV Vyacheslav A.
vamoshnikov@mail.ru
ORCID: 0000-0001-6500-5492

Received 14.12.2023. Approved after reviewing 05.03.2024. Accepted 11.03.2024.

Conference paper
UDC 535.37
DOI: https://doi.org/10.18721/JPM.171.107

Effect of growth temperature on photoluminescence properties of NH_3-MBE grown GaN-on-Si layers

I.V. Osinnykh [1, 2] ✉, T.V. Malin [1], D.S. Milakhin [1, 3], K.S. Zhuravlev [1]

[1] Rzhanov Institute of Semiconductor Physics Siberian Branch of RAS, Novosibirsk, Russia;
[2] Novosibirsk StateUniversity, Novosibirsk, Russia;
[3] Novosibirsk State Technical University, Novosibirsk, Russia
✉ igor-osinnykh@isp.nsc.ru

Abstract. In this paper, we present the results of the investigation of GaN-on-Si layers grown by the ammonia MBE technique within the technologically acceptable temperature range (775 °C–825 °C) by photoluminescence technique. The lowest value of the concentration of defects was obtained at a growth temperature of 825 °C. The increase in the concentration of defects in the film with decreasing growth temperature can be explained by the deviation from the optimum growth temperature and consequently by the deterioration of the crystalline perfection of the GaN layers.

Keywords: GaN, ammonia-MBE, photoluminescence, heterostructures, point defects

Citation: Osinnykh I.V., Malin T.V., Milakhin D.S, Zhuravlev K.S., Effect of growth temperature on photoluminescence properties of NH_3-MBE grown GaN-on-Si layers, St. Petersburg State Polytechnical University Journal. Physics and Mathematics. 17 (1.1) (2024) 43–48. DOI: https://doi.org/10.18721/JPM.171.107

This is an open access article under the CC BY-NC 4.0 license (https://creativecommons.org/licenses/by-nc/4.0/)

Материалы конференции
УДК 535.37
DOI: https://doi.org/10.18721/JPM.171.107

Влияние температуры роста на фотолюминесцентные свойства слоев GaN-on-Si, выращенных методом NH_3-МЛЭ

И.В. Осинных [1, 2] ✉,Т.В. Малин [1], Д.С. Милахин [1, 3], К.С. Журавлев [1]

[1] Институт физики полупроводников им. А.В. Ржанова СО РАН, Новосибирск, Россия;
[2] Новосибирский государственный университет, Новосибирск, Россия;
[3] Новосибирский государственный технический университет, Новосибирск, Россия
✉ igor-osinnykh@isp.nsc.ru

Аннотация. В данной работе представлены результаты исследования слоев GaN-on-Si, выращенных методом аммиачной МЛЭ в диапазоне температур 775–825 °C методом фотолюминесценции. Наименьшее значение концентрации дефектов было получено при температуре роста 825 °C. Увеличение концентрации дефектов в пленке с понижением температуры роста можно объяснить отклонением от оптимальной температуры роста и, как следствие, ухудшением кристаллического совершенства слоев GaN.

Ключевые слова: GaN, аммиачная МЛЭ, фотолюминесценция, гетероструктуры, точечные дефекты

Ссылка при цитировании: Осинных И.В., Малин Т.В., Милахин Д.С., Журавлев К.С. Влияние температуры роста на фотолюминесцентные свойства слоев GaN-on-Si,

© Osinnykh I.V., Malin T.V., Milakhin D.S, Zhuravlev K. S., 2024. Published by Peter the Great St. Petersburg Polytechnic University.

выращенных методом NH_3-МЛЭ // Научно-технические ведомости СПбГПУ. Физико-математические науки. 2024. Т. 17. № 1.1. С. 43–48. DOI: https://doi.org/10.18721/JPM.171.107

Статья открытого доступа, распространяемая по лицензии CC BY-NC 4.0 (https://creativecommons.org/licenses/by-nc/4.0/)

Introduction

In recent years, the market for high-power, ultrahigh-frequency electronics has seen an increase in the proportion of high electron mobility transistors (HEMTs) based on AlGaN/GaN heterostructures, which are successfully competing with similar devices based on Si and GaAs due to the large band gap [1]. High values of spontaneous and piezoelectric polarization in AlGaN/GaN heterostructures provide a high concentration of two-dimensional electron gas (2DEG) near the heterojunction $n_e > 10^{13}$ cm^{-2}. The high carrier density in HEMTs enables high current densities, which in combination with high breakdown voltage and high thermal conductivity contribute to increased device performance. In addition, AlGaN/GaN HEMTs can operate at higher temperatures, and the high binding energy of the gallium and nitrogen atoms significantly increases resistance to ionizing radiation. Despite the significant achievements of III-nitride technology, it should be noted that the problems of reducing power dissipation and improving the stability and reliability of devices are still relevant. High parameters of devices based on III-nitride materials have been predicted theoretically, but the practical implementation of AlGaN/GaN transistor and diode structures reveals a number of problems: high threshold voltage, current non-linearity, the manifestation of current saturation at unexpectedly low voltages and the limitation of the voltage variation range, the effect of current collapse. In particular, the problems of increasing breakdown voltages and reducing various types of leakage currents are acute [2, 3], so the possibilities of overcoming them are being actively investigated.

It is well known that leakage currents in the undoped GaN layer are caused by a high background concentration of free carriers (mainly electrons). The main background impurities from the residual atmosphere are oxygen and carbon, which lead to unintentional doping of the GaN buffer layer and the appearance of n-type and p-type conductivity, respectively [4] Intentional doping of GaN with acceptors (C, Fe) is a common method to compensate for the uncontrolled incorporation of donors to obtain high resistivity GaN layers [5, 6]. However, donor compensation with carbon significantly degrades the structural properties of GaN, in particular the surface morphology of GaN layers [7], which negatively affects the electrophysical parameters of 2DEG. When GaN buffer layers are doped with iron, a ‘memory effect’ is observed [8]. This effect leads to unintentional doping of all layers of the heterostructure, including the channel of the transistor structure. Another ambiguous approach, often implemented in the metal organic chemical vapor deposition (MOCVD) technique, is based on the intentional reduction of the structural perfection of the initial GaN buffer layers. On the one hand, this approach leads to an increase in the number of edge dislocations in the GaN layers, which results in an increase in the number of deep acceptor levels [9] to which electrons from donor levels are trapped. However, an increase in dislocation density inevitably leads to deterioration in the electrophysical properties of 2DEG and, as mentioned above, threading dislocations can be sources of electrons [10]. A number of papers report the possibility of controlling the background doping with carbon and oxygen [11, 12] by changing the growth conditions. Obviously, the growth conditions also influence both the concentration of point defects in the GaN layers and the dislocation density in the grown heterostructures. From a technological perspective, it is important to achieve a high resistivity of the GaN buffer layer in order to reduce leakage currents. Ammonia molecular beam epitaxy (NH_3-MBE) technique is characterized by lower growth temperatures compared MOCVD and allows obtaining sharp heterojunctions that is important at growth of heterostructures with binary AlGaN barrier [13, 14]. Plasma MBE technique needs to maintain a slight metal enrichment (2 monolayers) on the surface of the growing film during the growth, which inevitably leads to a local violation of the stoichiometric conditions and formation of metal drops on the surface, this effect is not present during ammonia MBE growth.The aim of this work is to investigate the

© Осинных И.В., Малин Т.В., Милахин Д.С., Журавлев К.С., 2024. Издатель: Санкт-Петербургский политехнический университет Петра Великого.

effect of growth temperature on the concentration of defects, including background impurities and donor-like defects, in GaN-on-Si layers grown by NH_3-MBE technique.

Materials and Methods

The investigated samples were grown on the NH_3-MBE Compact-21N machine on two-inch high-resistance Si (111) wafers. After the nitridation process, a 50 nm thick AlN nucleation layer was grown, followed by a buffer layer consisting of 160 nm AlN, 160 nm $Al_{0.6}Ga_{0.4}N$ and 160 nm $Al_{0.3}Ga_{0.7}N$. In the final stage of growth of GaN-on-Si heterostructures, 1000 nm thick GaN layers were grown at selected temperatures (775 °C, 800 °C and 825 °C) in a 200 sccm ammonia flow at a growth rate of about 600 nm/h (*BEEP*(Ga) = $1.3 \cdot 10^{-6}$ Torr). In the following text the samples of the investigated series are referred to as ‘GaN-775’, ‘GaN-800’, ‘GaN-825’. For steady-state PL excitation, the He-Cd laser with λ_{las} = 325 nm was used. The output excitation power of the He-Cd laser was about of 10 mW. The N_2 laser with λ_{las} = 337 nm, the repetition frequency 1 kHz and the pulse duration 7 ns was used to measure PL decay curves. The output average excitation power of the N_2 laser was about of 27 mW. PL was investigated by double monochromator SDL-1 with a cooled FEU-79 multiplier operating in photon counting mode. The time-correlated photon counting method was used to measure the PL decay curves in the range of delay times 0—100 μs. The measurements were performed at room temperature.

Results and Discussion

Fig. 1, *a* shows the steady-state photoluminescence spectra of GaN layers at room temperature. For GaN-on-Si, due to the large difference between the refractive indices of GaN and Si, the effect of light interference on the recorded spectrum leads to a periodic modulation of the emission intensity. The measured PL spectra consist of two bands: thenear-band-edge PL band in the UV spectral region with an intensity maximum position of about 3.4 eV (NBE) and the yellow defect-related band (YB) with an intensity maximum position of about 2.2 eV. In the spectra, there is a weak blue band at 2.8—3.0 eV, also due to defects. Lateral tensile stresses of GaN-on-Si thin epitaxial layers in the (0001) plane leads to a decrease of the band gap and as a consequence to the NBE redshift compared to undeformed GaN. TheNBE band for GaN-800 has the highest red shift that indicates the largest value of tensile stresses in this structure. The shape of the edge PL band of the studied structures is asymmetric, and contains two additional peaks at a distance of ~70 meV and ~140 from the main peak, which are associated with LO phonon replicas of the free exciton (FE) band [15]. For all investigated structures, the intensities of the first and second LO phonon replicas are 5 and 20 times lower than the intensity of the FE peak, respectively. The presence of lines associated with LO phonon replicas shows crystalline perfection of GaN-on-Si layers [16]. Fig. 1, *b* shows the decay curves of the yellow PL band after pulse excitation, measured at room temperature at registration energy of 2.175 eV, close to the position of the yellow PL band intensity maximum. The intense peak in the 0.12—0.2 μs time range corresponds to the registration of the laser pulse. Therefore, t_0 = 0.2 μs should be taken as the starting point of the decay time. The peak in the 25—40 μs time range is due to inductions in the PL photon registration system. The PL intensity of all structures is decreased for more than 100 μs, approximation by the function $I(t) \sim t^{\gamma}$ gives an exponent of degree $\gamma < 1$. The value of $\gamma = 0.55$ is highest for the GaN-775 structure, average $\gamma = 0.46$ for the GaN-825 structure and lowest $\gamma = 0.35$ for the GaN-800 structure. Exponential PL decay law is expected for the electron transition from the conduction band to the acceptor level, while long non-exponential PL decay is indicative of donor-acceptor type transitions.

The yellow and blue bands are usually associated with the carbon impurity (C_N) [17, 18]: the yellow YL_1 band with a maximum position at 2.17 eV is due to the electron transition from the conduction band to the (−1/0) CN level, the blue BLC band with a maximum position at 2.85 eV is due to the electron transition from the conduction band to the (0/+1) C_N level. It is believed that PL bands caused by defects provide information about crystal defects and are actively used to improve the technology of their growth. Since the ratio of the intensities of these bands to the intensity of the NBE in the PL spectrum of GaN can be proportional to the defect concentration, it can be used as a criterion for the crystalline quality of the GaN. The intensity of the yellow band is approximately the same for all structures of the investigated series, with the maximum value of the yellow band intensity for the structure GaN-775 and the minimum value for the

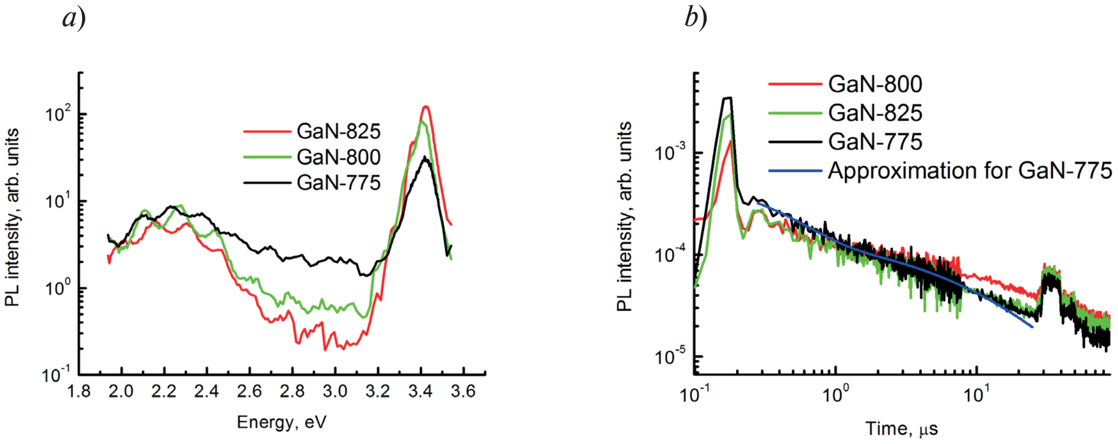

Fig. 1. Photoluminescence spectra (*a*) and decay curves at registration energy of 2.175 eV with the example of approximation (see the text for details) (*b*) of GaN layers measured at room temperature

structure GaN-825. A similar ratio is observed for the blue band: the GaN-775 structure has the maximum intensity of the blue band; the GaN-800 structure has a much lower intensity of the blue band, and in the spectrum of the GaN-825 structure the blue band almost merges with the background. The intensity of the NBE band is inversely correlated with the intensity of the defect bands: it is minimal for the GaN-775 structure and maximal for the GaN-825 structure. However the intensity of the NBE photoluminescence at a given temperature and excitation power depends on the concentrations and capture cross sections not only of the radiative recombination centers but also on the different centers of non-radiative recombination and their charge states, which are determined by the position of the Fermi level. In other words, at high acceptor doping levels, the ratio of defect PL band intensities to NBE PL intensities is very low, which is explained by the low concentration of non-radiative recombination centers. Consequently, among the structures studied in this work, the GaN-825 structure has the lowest concentration of non-radiative recombination centers, while the GaN-775 structure has the highest concentration of non-radiative recombination centers.

The dependence of the non-exponential PL intensity on time (*t*) and radiation energy (*E*) is well described by the deep center donor-acceptor recombination model developed in [19]:

$$I(E,t)=\int_0^\infty I_E(t)\exp\left(\frac{E'-E-E_{em}}{2\Delta^2}\right)dE', \tag{1}$$

$$\begin{aligned}I_E(t)={}&\frac{4\pi N_D}{E^4}\left(\frac{e^2}{\varepsilon}\right)^3 W_{\max}\exp\left(-\frac{2e^2}{\varepsilon E a_d}-W_{\max}t\exp\left(-\frac{2e^2}{\varepsilon E a_d}\right)\right)\times\\&\times\exp\left(4\pi N_D\int_0^\infty\left(\exp\left(-W(r)t\right)-1\right)r^2dr\right),\end{aligned} \tag{2}$$

$$W_R(r)=W_{\max}\exp\left(-2\frac{r}{a_d}\right), \tag{3}$$

here the shape of the PL band of a single donor-acceptor pair is assumed to be Gaussian which is true for the configuration coordinate model for values of the Huang-Rhys parameter $S >> 1$, ad is the donor’s Bohr radius, the value of the effective electron mass in GaN is $m^* = 0.2$ and the dielectric permittivity is $\varepsilon = 9.5$, r is the distance between donor and acceptor, $W_R(r)$ is the probability of radiative transition per unit time, W_{max} is the pre-exponential factor, N_D is the concentration of the neutral donors (the dominant defect component).

The approximation of the experimentally measured decay curves by the theoretical dependence at a fixed value $W_{max} = 2\cdot10^6$ s^{-1} [20] allows to estimate the N_D values for all the structures studied. The concentration of neutral donors of about $6\cdot10^{17}$ cm^{-3} is highest for the GaN-775 structure, average of about $3\cdot10^{17}$ cm^{-3} for the GaN-825 structure and lowest for the GaN-800 structure of about $1 \cdot 10^{17}$ cm^{-3}. Since the grown structures are significantly compensated by radiative and non-radiative defects, the obtained value is much lower than the total donor concentration (N_D^{total}). According to the well-known expression

$$N_D / N_D^{total} = \left[1 + \frac{g_1}{g_0} \exp\left(-\frac{F - E_d}{kT}\right)\right]^{-1}, \tag{7}$$

Here F is the position of the Fermi level below the conduction band, g_0 and g_1 are degeneracy multiplicities of empty and filled charge states. At sufficiently high temperature and high defect concentration, the Fermi level is below the donor level, so the ratio is $N_D/N_D^{total} << 1$. Since the GaN-775 structureis characterized by a highest defect concentration, and consequently the lowest F the ratio N_D/N_D^{total} is expected to be the smallest for this structure. Therefore, the highest N_D value means the highest N_D^{total} value for the GaN-775 structure. At the same time, it cannot be stated that the GaN-800 structure has the lowest donor concentration since the GaN-825 structure is characterized by a lowest defect concentration and has the highest ratio N_D/N_D^{total}. So the lowest N_D^{total} can be in the GaN-825 structure.

Conclusion

Based on the above results of the study by the PL method of a series of GaN-on-Si samples grown by the NH$_3$-MBE technique at different growth temperatures a number of conclusions can be drawn. The growth of GaN-on-Si layers at 825 °C allows obtaining GaN layers with the lowest concentration of non-radiative defects as evidenced by the lowest intensity of the defect-related PL bands, the concentration of donors is also low. Decreasing the growth temperature of GaN-on-Si layers leads to an increase in the concentration of non-radiative defects. The increase in the number of defects in the film with decreasing growth temperature can be explained by the deviation from the optimum growth temperature and consequently by the deterioration of the crystalline perfection of the GaN layers. The growth of GaN-on-Si layers at 775 °C is characterizes by the highest concentration of donors.

REFERENCES

1. **Chen K.J., Haberlen O., Lidow A., Tsai C. lin, Ueda T., Uemoto Y., Wu Y.,** GaN-on-Si Power Technology Devices and Applications. IEEE Transactions on Electron Devices. 64 (3) (2017) 779–795.

2. **Miller E.J., Dang X.Z. and Yu E.T.,** Gate leakage current mechanisms in AlGaN/GaN heterostructure field-effect transistors. Journal of Applied Physics 88 (2000) 5951–5958.

3. **Hashizume T., Kotani J., Hasegawa H.,** Leakage mechanism in GaN and AlGaN Schottky interfaces. Applied Physics Letters 84 (2004) 4884–4886.

4. **Murthy M., Freitas Jr.J.A., Kim J., Glaser E.R., Storm D.,** Residual impurities in GaN substrates and epitaxial layers grown by various techniques. Journal of Crystal Growth 305 (2007) 393–398.

5. **Van de Walle C.G., Stampfl C., Neugebauer J.,** Theory of doping and defects in III-V nitrides. Journal of Crystal Growth 189–190 (1998) 505–510.

6. **Bougrioua Z., Azize M., Jimenez A., Brana A-F., Lorenzini P., Beaumont B., Munoz E., Gibart P.,** Fe doping for making resistive GaN layers with low dislocation density; consequence on HEMTs. Physica Status Solidi C 2 (7) (2005) 2424–2428.

7. **Lundin W.V., Sakharov A.V., Zavarin E.E., Kazantsev D.Yu., Ber B.Ya., Yagovkina M.A., Brunkov P.N., Tsatsulnikov A.F.,** Study of GaN doping with carbon from propane in a wide range of MOVPE conditions. Journal of Crystal Growth 449 (2016) 108–113.

8. **Rudziński M., Desmaris V., van Hal P.A., Weyher J.L., Hageman P.R., Dynefors K., Rodle T.C., Jos H.F.F., Zirath H., Larsen P.K.,** Growth of Fe doped semi-insulating GaN on sapphire and 4H-SiC by MOCVD. Physica Status Solidi C 3 (6) (2006) 2231–2236.

9. **Weimann N.G., Eastman L.F., Doppalapudi D., Ng H.M., Moustakas T.D.,** Scattering of electrons at threading dislocations in GaN. Journal of Applied Physics 83 (7) (1998) 3656–3659.

10. **Reynolds Jr.C.L., Reynolds J.G., Crespo A., Gillespie J.K., Chabak K.D., Davis R.F.,** Dislocations as quantum wires: Buffer leakage in AlGaN/GaN Heterostructures. Journal of Materials Research 28(13) (2013) 1687–1691.

11. **Gamarra P., Lacam C., Tordjman M., Splettstosser J., Schauwecker B., di Forte-Poisson M.-A.,** Optimisation of a carbon doped buffer layer for AlGaN/GaN HEMT devices. Journal of Crystal Growth 414 (2015) 232–236.

12. **Schubert F., Wirth S., Zimmermann F., Heitmann J., Mikolajick T., Schmult S.,** Growth condition dependence of unintentional oxygen incorporation in epitaxial GaN. Science and Technology of Advanced Materials 17(1) (2016) 239–243.

13. **Zhuravlev K.S., Malin T.V., Mansurov V.G., Zemlyakov V.E., Egorkin V.I., Parnes Ya.M.,** Normally off transistors based on in situ passivated AlN/GaN heterostructures. Tech. Phys. Lett. 42 (2016) 750–753.

14. **Aleksandrov I.A., Malin T.V., Zhuravlev K.S., Trubina S.V., Erenburg S.B., Pecz B., Lebiadok Y.V.,** Diffusion in GaN/AlN superlattices: DFT and EXAFS study. Applied Surface Science 515 (2020) 146001.

15. **Leroux M., Grandjean N., Beaumont B., Nataf G., Semond F., Massies J., Gibart P.,** Temperature quenching of photoluminescence intensities in undoped and doped GaN. Journal of Applied Physics 86 (7) (1999) 3721–3728.

16. **Kung P., Saxler A., Zhang X., Walker D., Wang T. C., Ferguson I., Razeghi M.,** High quality AIN and GaN epilayers grown on (001) sapphire, (100), and (111) silicon substrates. Applied Physics Letters 66 (1995) 2958–2960.

17. **Reshchikov M.A.,** Measurement and analysis of photoluminescence in GaN. Journal of Applied Physics 129 (2021) 121101.

18. **Schmult S., Schürmann H., Schmidt G., Veit P., Bertram F., Christen J., Großer A., Mikolajick T.,** Correlating yellow and blue luminescence with carbon doping in GaN. Journal of Crystal Grows 586 (2022) 126634.

19. **Goldys E.M., Godlewski M., Langer R., Barski A., Bergman P., Monemar B.,** Analysis of the red optical emission in cubic GaN grown by molecular-beam epitaxy. Physical Review B 60 (8) (1999) 5464–5469.

20. **Reshchikov M.A., Shahedipour F., Korotkov R.Y., Ulmer M.P., Wessels B.W.,** Deep acceptors in undoped GaN. Physica B: Condensed Matter 273–274 (1999) 105–108.

THE AUTHORS

OSINNYKH Igor V.
igor-osinnykh@isp.nsc.ru
ORCID: 0000-0002-3165-7027

MILAKHIN Denis S.
dmilakhin@isp.nsc.ru
ORCID: 0000-0002-9042-8929

MALIN Timur V.
mal-tv@isp.nsc.ru
ORCID: 0000-0001-6015-0631

ZHURAVLEV Konstantin S.
zhur@isp.nsc.ru
ORCID: 0000-0002-3171-5098

Received 14.12.2023. Approved after reviewing 23.01.2024. Accepted 05.02.2024.

St. Petersburg Polytechnic University Journal. Physics and Mathematics. 2024 Vol. 17. No. 1.1
Научно-технические ведомости СПбГПУ. Физико-математические науки. 17 (1.1) 2024

Conference paper
UDC 538.958
DOI: https://doi.org/10.18721/JPM.171.108

Electron irradiation as a method for controlling luminescence of hexagonal boron nitride

O.A. Gogina [1] ✉, Yu.V. Petrov [1], O.F. Vyvenko [1], S. Kovalchuk [2], K. Bolotin [2]

[1] Saint-Petersburg State University, St. Petersburg, Russia;
[2] Free University of Berlin, Berlin, Germany
✉ o_gogina@mail.ru

Abstract. Hexagonal boron nitride (hBN) is characterized by two main point defect-related luminescence bands with the peaks in visible, at 650 nm (1.9 eV), and UV, 320 nm (4 eV) spectral regions, which possess the properties of single photon emitters (SPE). We demonstrate that sufficiently long irradiation of thin hBN flakes in a scanning electron microscope with electron beam with energies from 5 keV to 20 keV and the flux equal or more than 10^{15} cm^{-2}s^{-1} resulted in a drastic increase in the integral intensity of the 4 eV band previously associated with carbon-related defects. The effect of the irradiation induced luminescence enhancement increases with the decrease of the electron beam energy that corresponds well with the calculated energy losses in thin samples. An increase in the concentration of carbon-related defects introduced into the sample from surface carbon contaminated layer via recombination-enhanced migration or changes of the charge state of existing defects could be supposed to be mechanisms of the observed effect. The obtained results demonstrate the possibility of local control of UV SPE concentration in hBN.

Keywords: point defects, cathodoluminescence, scanning electron microscopy

Funding: The research was supported by Russian Science Foundation (project 23-22-00067, https://rscf.ru/project/23-22-00067/).

Citation: Gogina O.A., Petrov Yu.V., Vyvenko O.F., Kovalchuk S., Bolotin K., Electron irradiation as a method for controlling luminescence of hexagonal boron nitride, St. Petersburg State Polytechnical University Journal. Physics and Mathematics. 17 (1.1) (2024) 49–54. DOI: https://doi.org/10.18721/JPM.171.108

This is an open access article under the CC BY-NC 4.0 license (https://creativecommons.org/licenses/by-nc/4.0/)

Материалы конференции
УДК 538.958
DOI: https://doi.org/10.18721/JPM.171.108

Электронное облучение как метод управления люминесценцией в гексагональном нитриде бора

О.А. Гогина [1] ✉, Ю.В. Петров [1], О.Ф. Вывенко [1], С. Ковальчук [2], К. Болотин [2]

[1] Санкт-Петербургский государственный университет, Санкт-Петербург, Россия;
[2] Свободный университет Берлина, Берлин, Германия
✉ o_gogina@mail.ru

Аннотация. Точечные дефекты в монокристаллическом гексагональном нитриде бора (h-BN), являющиеся центрами люминесценции, рассматриваются как потенциальные источники одиночных фотонов. В работе продемонстрировано, что облучение электронным пучком в сканирующем электронном микроскопе может приводить к увеличению интенсивности люминесценции в ультрафиолетовой части спектра, что

© Gogina O.A., Petrov Yu.V., Vyvenko O.F., Kovalchuk S., Bolotin K., 2024. Published by Peter the Great St. Petersburg Polytechnic University.

может служить перспективным методом для контролируемого локального управления люминесценцией дефектов в гексагональном нитриде бора при правильном выборе энергии и плотности потока электронов.

Ключевые слова: точечные дефекты, катодолюминесценция, сканирующая электронная микроскопия

Финансирование: Исследование выполнено за счет средств гранта Российского научного фонда № 23-22-00067, https://rscf.ru/project/23-22-00067/.

Ссылка при цитировании: Гогина О.А., Петров Ю.В., Вывенко О.Ф., Ковальчук С., Болотин К. Электронное облучение как метод управления люминесценцией в гексагональном нитриде бора // Научно-технические ведомости СПбГПУ. Физико-математические науки. 2024. Т. 17. № 1.1. С. 49–54. DOI: https://doi.org/10.18721/JPM.171.108

Статья открытого доступа, распространяемая по лицензии CC BY-NC 4.0 (https://creativecommons.org/licenses/by-nc/4.0/)

Introduction

Modern quantum computer technologies, including quantum cryptography, require new materials for the fabrication of single photon emitters (SPE) [1–3]. It was recently reported that some point defects in hexagonal boron nitride (hBN) can serve as SPE working at room temperature with characteristic luminescence bands within a wide wavelength range from 200 nm to 700 nm [4, 5]. The most pronounced SPE luminescence bands are characterized with the main peak positions at approximately 650 nm (1.9 eV) and 320 nm (4 eV) [6] (denoted further as 1.9 eV band and 4 eV band).

Previous investigations showed that the defects responsible for the 4 eV luminescence band could be formed already during the growth of large single crystals. Though the exact nature of these defects remained unknown [1, 7], it was tentatively ascribed to a carbon-related defect such as carbon at the nitrogen atom site or a composite complex of oxygen and carbon impurities [8]. The luminescence center responsible to the 1.9 eV band was attributed to boron dangling bonds [9], vacancy-related defects or an anti-site defect where the nitrogen occupies the boron site with missing atom at the nitrogen site (N_BV_N) [10].

To create quantum communication devices utilizing the usage of SPE, it is necessary to develop experimental methods for the local tuning of the concentration of the desirable luminescence centers. In our previous paper, we demonstrated that subsequent irradiation of hBN with focused He^+ and electron beams can be used to control the intensity of the 1.9 eV luminescence band [6]. In this paper, we investigated in more details the changes in the intensity of the 4 eV luminescence band produced by the electron irradiation with various fluxes and electron beam energies.

Materials and Methods

The starting material in our experiments was hBN crystal with a declared purity of 99.99% produced by the Ossila company. The samples for the investigations were prepared by peeling from hBN single crystal the flakes of a thickness of about 200 nm then transferred onto silicon substrate.

Electron irradiations and cathodoluminescence (CL) measurements were performed using a Zeiss SUPRA 40VP scanning electron microscope (SEM) equipped with the Gatan Mono CL3+ registration system.

The experiments were carried out at room temperature with the electron irradiation in continuous scanning mode. During the irradiation, repetitive wavelength increasing-decreasing CL spectra scans were performed, and the data arrays containing the luminescence intensity, wavelength and detection time were collected with the help of specially developed software package. The electron beam energy and the irradiation flux density were varied between 5 and 20 keV and between 10^{14} and 10^{16} cm^{-2}s^{-1}, respectively.

© Гогина О.А., Петров Ю.В., Вывенко О.Ф., Ковальчук С., Болотин К., 2024. Издатель: Санкт-Петербургский политехнический университет Петра Великого.

Results and Discussion

Fig. 1, *a* represents the color map of the CL intensity in the spectral region of 3.1–4.9 eV (4 eV band) as a function of the duration of the electron beam exposure. The map was composed from the data of 90 CL spectra recorded subsequently during electron beam exposure for 10,000 seconds. It is clear from the map in Fig. 1, *a* that the 4 eV band contains several peaks and the overall intensity of CL increases with the electron irradiation time.

The acquired spectral band could be decomposed into six separate Gaussian-like components: three relatively broad (3.4, 4.1, 4.8 eV) and three more narrow (3.7, 3.9, 4.05 eV) bands. An example of the experimental CL spectrum, the components of its deconvolution and their sum are drawn over the CL map in Fig. 1, *a*. According to data presented in literature [8], three narrow bands can be attributed to one luminescence center with zero phonon line at 4.05 eV and two phonon replicas.

Fig. 1, *b* depicts CL intensity map of the investigated hBN flake at a wavelength of 320 nm acquired after 10,000 seconds of electron irradiation. Bright rectangular area of the enhanced luminescence corresponds to the region where the scans with the electron beam was performed indicating a substantial increase of the intensity at such wavelength with respect to the initial state.

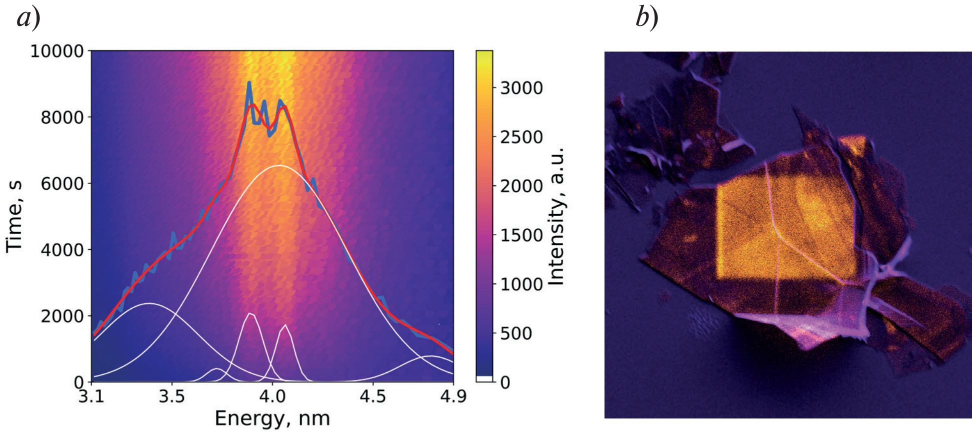

Fig. 1. Color map of temporal luminescence intensity changes of the 4 eV band with overlaid example of the experimental CL spectrum (blue line) and its decomposition into Gaussian-like components (*a*). White and red lines represent the components and their sum, respectively. CL map at a wavelength of 320 nm after the irradiation with electron irradiation dose of 10^{19} cm^{-2} (*b*). The map is semi-transparently overlaid with secondary electrons SEM image of the hBN flake to make its borders visible

It was found that the temporal evolution of luminescence intensity differs for the different spectral components. The variation of the magnitude of each of six bands obtained from spectrum decomposition with the electron irradiation duration is presented in Fig. 2, where the band peak energy is shown in the legend. The most pronounced luminescence enhancement by a factor of about 4–4.5 was observed for bands at 3.4, 4.05 and 4.1 eV, while the effect was noticeably less for their neighbors at 3.7 and 3.9 eV and small or negligible for band at 4.8 eV.

The impact of the electron irradiation on the 4 eV band luminescence intensity was found to be very sensitive to the electron beam energy. For the energy of 5 keV the intensity increases by 9 times, whereas for 20 keV it increases by approximately 3 times after the same irradiation time, that can be well recognized from Fig. 3, *a* obtained with an order of magnitude larger electron flux than one presented in Fig. 1 and Fig. 2.

Using the CASINO program [11], we performed calculations of the depth dependence of the total energy losses (dE/dx) in hBN for the electron energies of 5, 10 and 20 keV, which is presented in Fig. 3, *b*. From the energy loss profile data (Fig. 3, *b*) and the thickness of the samples (of about 200 nm), we calculated the total deposited energy (ΔE) and total number of electron-hole (e–h) pairs generated within the flake:

$$N_{\text{pairs}} = \Delta E \big/ \left(3 \cdot E_g\right), \tag{1}$$

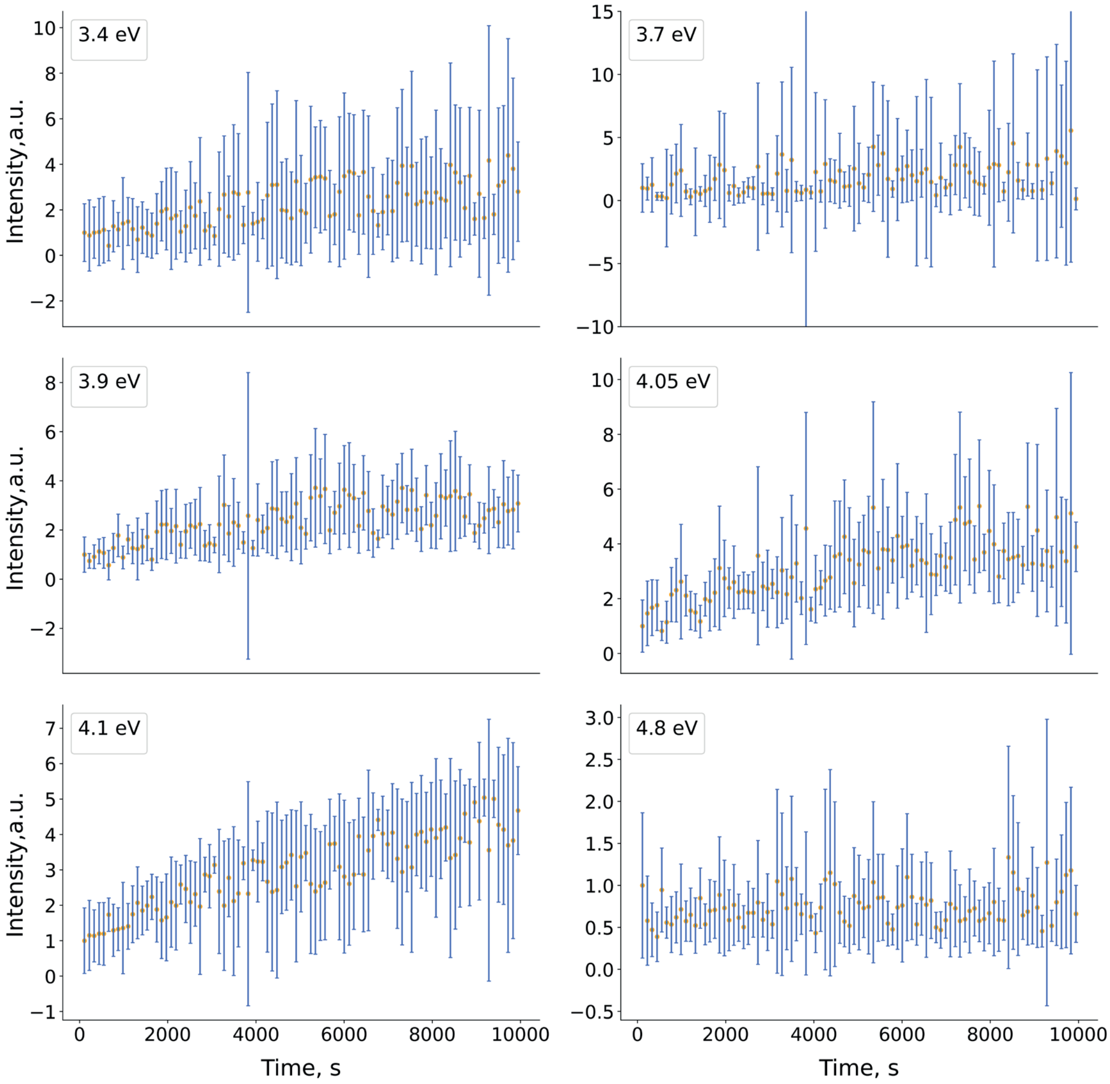

Fig. 2. Temporal variation of the normalized to the initial intensity magnitude of the six spectral components of the 4eV hBN luminescent band under the irradiation with an electron beam with an energy of 5 keV and the electron flux density of about 10^{15} cm^{-2} s^{-1}.

where E_g is the band gap of the hBN of 6.08 eV [12]. The calculation results of ΔE and N_{pairs} are presented in Table.

We can conclude from the calculated and presented dE/dx, ΔE and N_{pairs} data that the electrons of all used energies penetrate through the entire volume of hBN into the substrate transmitting to the sample the less energy the higher is their energy. Thus, the observed enhancement of the luminescence might be caused by the electron beam induced generation of emitting defects or by the change in the charge state of existing defects accompanied by the recombination of generated electron-hole pairs.

Table

Results of numerical simulation in CASINO software

E, keV	ΔE, keV	N_{pairs}
5	2.9	158
10	1.3	71
20	0.626	34

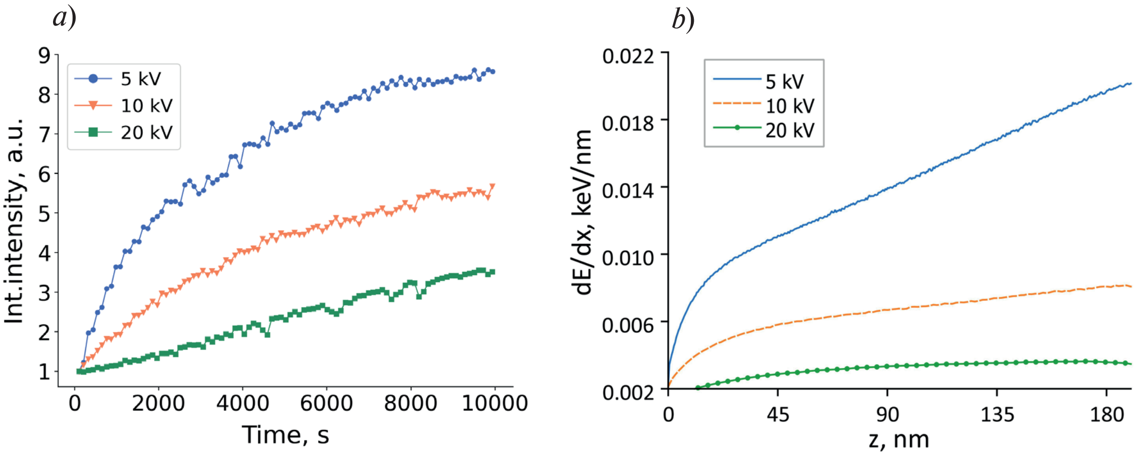

Fig. 3. Dependences of the integral intensity of the 4 eV band on the time of electron irradiation with different electron beam energies, and electron irradiation flux of 10^{16} cm^{-2}s^{-1} (*a*). Each line is normalized by the intensity at the initial time point. Dependence of electron energy losses on depth obtained from numerical simulation using CASINO program (*b*)

Conclusion

It was established that the intensity of luminescence band in the 3.1–4.9 eV energy range in hBN increases drastically under the sufficiently long electron irradiation making it possible to use conventional SEM technique to control the density and spatial design of SPE in UV spectral region.

As pointed out in the introduction, 4 eV luminescent band is attributed to a defect somehow related to the carbon impurity. The luminescent peaks at 3.4, 3.7, 3.9, 4.05, 4.1 eV are sensitive to electron beam irradiation. That could indicate that these lines are sensitive to new carbon impurities introduced by electron irradiation.

Theoretical calculations show that the carbon dimers C_BC_N are responsible for the luminescent source with energy of 4.1 eV [13]. Similarly, earlier experimental studies have demonstrated that this line is associated with another carbon defect, a substitutional impurity at a nitrogen site C_N [1, 5, 7, 13]. In another paper this lines are associated with impurity complex C_NO_N [8].

In turn, the carbon impurity contamination under the electron beam action may be due to the deposition of hydrocarbons from the residual gases in the chamber with their subsequent decomposition on the sample surface. The formation of a carbon-rich layer on the surface can serve as a source of carbon-containing defects in the bulk. Obviously, carbon diffusion in the bulk material is negligible at room temperature, but it could be drastically accelerated in the presence of non-equilibrium free charge carriers, due to the phenomenon that is known as ‘recombination-enhanced defect migration’.

Acknowledgments

The research was supported by Russian Science Foundation (project 23-22-00067, https://rscf.ru/project/23-22-00067/). The results were obtained using the equipment of the Interdisciplinary Resource Center for Nanotechnology of St. Petersburg State University Research Park.

REFERENCES

1. **Bourrellier R., Meuret S., Tararan A. et al.,** Bright UV single photon emission at point defects in h-BN, Nano letters. 16 (7) (2016) 4317–4321.

2. **Castelletto S., Inam F.A., Sato S. and Boretti A.,** Hexagonal boron nitride: a review of the emerging material platform for single-photon sources and the spin–photon interface, Beilstein Journal of Nanotechnology. 11 (1) (2020) 740–769.

3. **Beveratos A., et al.,** Single photon quantum cryptography, Physical review letters. 89 (18) (2002) 187901.

4. **Korona T., Chojecki M.,** Exploring point defects in hexagonal boron-nitrogen monolayers, International Journal of Quantum Chemistry. 119 (14) (2019) e25925.

5. **Weston L., Wickramaratne D., Mackoit M., et al.,** Native point defects and impurities in hexagonal boron nitride, Physical Review B. 97(21) (2018) 214104.

6. **Petrov Y.V., Vyvenko O.F., Gogina O.A., et al.,** Electron Beam-Stimulated Luminescence of Helium Ion-Irradiated Hexagonal Boron Nitride, Bulletin of the Russian Academy of Sciences: Physics. 87(10) (2023) 1455–1461.

7. **Pelini T., Elias C., Page R., et al.,** Shallow and deep levels in carbon-doped hexagonal boron nitride crystals, Physical Review Materials. 3 (9) (2019) 094001.

8. **Vokhmintsev A., Weinstein I., Zamyatin D.,** Electron-phonon interactions in subband excited photoluminescence of hexagonal boron nitride, Journal of Luminescence. 208 (2019) 363–370.

9. **Turiansky M.E., Alkauskas A., Bassett L.C., Van de Walle C.G.,** Dangling bonds in hexagonal boron nitride as single-photon emitters, Physical review letters. 123 (12) (2019) 127401.

10. **Tran T.T., Bray K., Ford M.J., et al.,** Quantum emission from hexagonal boron nitride monolayers, Nature nanotechnology. 1 1(1) (2016) 37–41.

11. **Drouin D., Couture A. R., Joly D., et al.,** CASINO V2. 42—a fast and easy-to-use modeling tool for scanning electron microscopy and microanalysis users, Scanning: The Journal of Scanning Microscopies. 29 (3) (2007) 92–101.

12. **Cassabois G., Valvin P., Gil B.,** Hexagonal boron nitride is an indirect bandgap semiconductor, Nature photonics. 10 (4) (2016) 262–266.

13. **Mackoit-Sinkevičienė M., Maciaszek M., Van de Walle C.G., Alkauskas A.,** Carbon dimer defect as a source of the 4.1 eV luminescence in hexagonal boron nitride, Applied Physics Letters. 115 (21) (2019) 212101.

THE AUTHORS

GOGINA Olga A.
o_gogina@mail.ru
ORCID: 0009-0006-6658-0601

PETROV Yurii V.
y.petrov@spbu.ru
ORCID: 0000-0003-3084-3677

VYVENKO Oleg F.
vyvenko@gmail.com
ORCID: 0000-0001-6077-3679

KOVALCHUK Sviatoslav
kovalchook@gmail.com
ORCID: 0000-0002-4817-1939

BOLOTIN Kirill
bolotin@gmail.com
ORCID: 0000-0003-1821-3429

Received 14.12.2023. Approved after reviewing 05.03.2024. Accepted 06.03.2024.

St. Petersburg Polytechnic University Journal. Physics and Mathematics. 2024 Vol. 17. No. 1.1
Научно-технические ведомости СПбГПУ. Физико-математические науки. 17 (1.1) 2024

Heterostructures, superlattices, quantum wells

Conference paper
UDC 538.915
DOI: https://doi.org/10.18721/JPM.171.109

Effects of resonant tunneling in GaAs/AlAs heterostructure

E.V. Domoratsky [1] ✉, M.V. Zakharchenko [1], G.F. Glinskii [1]

[1] St. Petersburg Electrotechnical University "LETI", St. Petersburg, Russia

✉ egor.domorackiy@mail.ru

Abstract. We investigate the effects of resonant tunneling of the charge carriers of the Γ_8 zone in the GaAs/AlAs heterostructure within the framework of the effective mass method, taking into account complex character of the valence band dispersion law. The problem is solved by introducing Green's function with parametric dependence on energy within the biorthogonal formalism of quantum theory. The effects imposed by the spin state of holes, as well as the effect of short-range interface corrections, are investigated.

Keywords: heterostructures, hole tunneling, resonant tunneling

Citation: Domoratsky E.V., Zakharchenko M.V.,Glinskii G.F., Effects of resonant tunneling in GaAs/AlAs heterostructure, St. Petersburg State Polytechnical University Journal. Physics and Mathematics. 17 (1.1) (2024) 55–61. DOI: https://doi.org/10.18721/JPM.171.109

This is an open access article under the CC BY-NC 4.0 license (https://creativecommons.org/licenses/by-nc/4.0/)

Материалы конференции
УДК 538.915
DOI: https://doi.org/10.18721/JPM.171.109

Эффекты резонансного туннелирования в гетероструктуре GaAs/AlAs

Е.В. Доморацкий [1] ✉, М.В. Захарченко [1], Г.Ф. Глинский [1]

[1] Санкт-Петербургский государственный электротехнический университет «ЛЭТИ»
им. В. И. Ульянова (Ленина), Санкт-Петербург, Россия

✉ egor.domorackiy@mail.ru

Аннотация. В работе исследуются эффекты резонансного туннелирования носителей заряда зоны Γ_8 в гетероструктуре GaAs/AlAs в рамках метода эффективной массы с учетом сложного характера закона дисперсии валентной зоны. Задача решается с помощью введения функции Грина с параметрической зависимостью от энергии в рамках биортогонального формализма квантовой теории. Исследованы эффекты, накладываемые спиновым состоянием дырок, а также влиянием короткодействующих интерфейсных поправок.

Ключевые слова: гетероструктуры, туннелирование дырок, резонансное туннелирование

Ссылка при цитировании: Доморацкий Е.В., Захарченко М.В., Глинский Г.Ф. Эффекты резонансного туннелирования в гетероструктуре GaAs/AlAs // Научно-технические ведомости СПбГПУ. Физико-математические науки. 2024. Т. 17. № 1.1. С. 55–61. DOI: https://doi.org/10.18721/ JPM.171.109

Статья открытого доступа, распространяемая по лицензии CC BY-NC 4.0 (https://creativecommons.org/licenses/by-nc/4.0/)

© Domoratsky E. V., Zakharchenko M. V., Glinskii G. F., 2024. Published by Peter the Great St. Petersburg Polytechnic University.

Introduction

Resonant tunneling in quantum-dimensional structures is the charge carrier transfer through potential barriers of finite height when its energy is equal to the resonance energy of the quantum system. This phenomenon is used in the design of a variety of electronic devices working at high frequency and terahertz range: semiconductor optic amplifiers and modulators, quantum-cascade structures and others [1–5]. Another field of application is spintronics where polarization effects are used to separate charge carriers with various effective spin momentum projections. It makes it possible to design different spintronic devices like spin filters and spin injectors [6, 7].

Theoretically, tunneling processes are described by the transmission coefficient which is equal to the relation of probability flow densities. To find probability flow, we need to solve the stationary inhomogeneous Schrodinger equation. In general case, it has the following operator form

$$\left[\hat{H}-E\right]\left|\psi\left(E\right)\right\rangle=\left|\rho\right\rangle, \tag{1}$$

where $\hat{H}$ is the Hamiltonian of the quantum system, $|\psi\,(E)\rangle$ is vector, which describes the stationary state of the quantum system with energy E and $|\rho\rangle$ is vector characterizing the particle source in the quantum system.

The Schrodinger equation is generally solved by the transfer matrix method. This approach has a high calculation precision, however, it requires large software capacities and is also associated with the need to satisfy a large number of boundary conditions in the case of multi-barrier structures and the complex structure of the energy zones of the materials [8, 9].

In the present work, effects of resonant tunneling in heterostructures are investigated using Green's function method which can be formulated within the framework of the biorthogonal approach to the analysis of quantum systems described by non-Hermitian operators [10, 11]. The problem is reduced to a solution of the inhomogeneous Schrodinger equation in the k-representation using the corresponding Green's function, parametrically dependent on energy. In the case of the open unlimited space, the particle wave function amplitude is not equal to zero at infinity. Accordingly, the system Hamiltonian is non-Hermitian. Within the framework of the developed approach, a finite space is considered and a method of smoothly changing dissipative potential barriers near the boundaries of the structure into the system is applied. In the region of this dissipative potential, the amplitude of the wave function of the particle fades. The presence of a potential of this kind leads to the fact that the Hamiltonian of a particle in a limited region also becomes non-Hermitian. Consequently, the solution of the problem with the escape of a particle to infinity can be replaced by the solution of the problem in a finite-size space with the analogous non-Hermitian Hamiltonian [12].

Theory

The mathematical formulation of the biorthogonal theory is based on the search for two sets of eigenvectors and eigenvalues of a given non-Hermitian Hamiltonian and its conjugate operator. The problems of finding eigenvalues and eigenvectors have the form

$$\begin{gathered}\hat{H}\left|\psi_n^r\right\rangle=E_n\left|\psi_n^r\right\rangle,\\ \hat{H}^\dagger\left|\psi_n^l\right\rangle=E_n^\dagger\left|\psi_n^l\right\rangle,\end{gathered} \tag{2}$$

where $\left|\psi_n^r\right\rangle$ and $\left|\psi_n^l\right\rangle$ are 'right' and 'left' eigenvectors respectively, related by the biorthonormality and completeness conditions

$$\begin{gathered}\left\langle\psi_n^l\middle|\psi_{n'}^r\right\rangle=\delta_{nn'},\\ \sum_n\left|\psi_n^r\right\rangle\left\langle\psi_n^l\right|=1.\end{gathered} \tag{3}$$

© Доморацкий Е.В., Захарченко М.В., Глинский Г.Ф., 2024. Издатель: Санкт-Петербургский политехнический университет Петра Великого.

The tunneling problem is considered within the framework of Green's function method, which is convenient for analyzing a continuous energy spectrum. Green's function for the Schrodinger equation, parametrically dependent on the energy of a particle, has the operator form

$$\hat{G}(E) = \left(\hat{H} - E\right)^{-1}. \tag{4}$$

Using the Kohn–Luttinger basis, we can solve the Schrodinger equation (1) within the framework of the effective mass method [13]. The effective Hamiltonian of Γ_8 zone in k-representation has the form

$$H^{(\Gamma_8)} = \frac{\hbar^2}{2m_0}\begin{bmatrix} P+Q & W & V & 0 \\ W^{\dagger}+ & P-Q & 0 & V \\ V^{\dagger} & 0 & P-Q & -W \\ 0 & V^{\dagger} & -W^{\dagger} & P+Q \end{bmatrix}, \tag{5}$$

where $P = \gamma_1\left(k_x^2 + k_y^2 + k_z^2\right)$, $Q = \gamma_2\left(k_x^2 + k_y^2 - 2k_z^2\right)$, $V = -\sqrt{3}\gamma_2\left(k_x^2 - k_y^2\right) + i2\sqrt{3}\gamma_3 k_x k_y$, $W = -2\sqrt{3}\gamma_3\left(k_x - ik_y\right)k_z$, γ_1, γ_2, γ_3 are Luttinger parameters characterizing structure of the valence band. For a finite volume of the system, wave vector k is taking discrete values.

Thus, we can determine the solution of Eq. (1) with the Γ_8 effective Hamiltonian using the corresponding Green's function

$$\langle k|\psi(E)\rangle = \sum_{k'}\langle k|\hat{G}(E)|k'\rangle\langle k'|\rho\rangle. \tag{6}$$

Results and Discussion

In this work, tunneling of holes in a one-dimensional double barrier heterostructure GaAs/AlAs is investigated. The system has the following parameters: width of quantum well $d_w = 20$ nm, width of quantum barriers $d_b = 30$ nm, the energy gap between two materials is 0.46 eV. The k_y and k_z components of wavevector k are equal to zero. Luttinger parameters for GaAs: $\gamma_1 = 6.98$, $\gamma_2 = 2.06$, $\gamma_3 = 2.93$. Luttinger parameters for AlAs: $\gamma_1 = 3.76$, $\gamma_2 = 0.82$, $\gamma_3 = 1.42$ [14]. The characteristic functions of the potentials and energy dependence of the tunneling coefficient are shown in Figs. 1 and 2, respectively.

Quantum barriers are formed by AlAs atoms and quantum well potential is formed by GaAs atoms. The dissipative potentials at the boundaries of the region are located at some distance from the quantum barriers and are set smoothly enough so that their effect on tunneling is excluded. Source of particles is set on the left side in front of the first barrier.

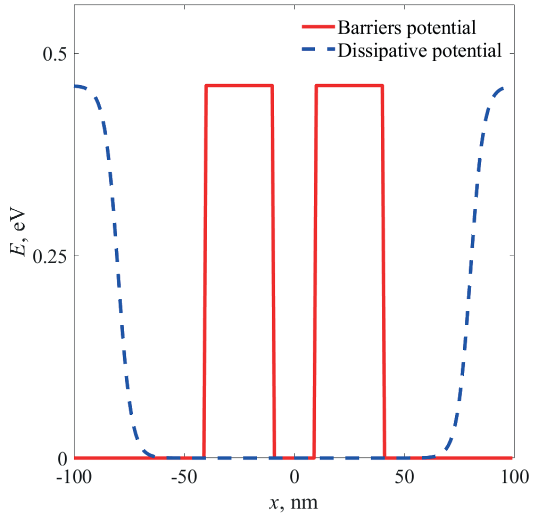

Fig. 1. Double barrier structure (red solid line) with dissipative potential (blue dotted line) near the boundaries

As shown in Fig. 2, the energy dependence of transmission coefficient has several resonant peaks. The first of them are low-intensity resonant peaks located before the energy of the quantum barrier. They correspond to the tunneling of holes with energy below the height of the barrier. It is possible due to the existence of quasi-resonant energy levels in quantum well between two barriers. The last peak in this energy range is located after the energy of quantum barriers and corresponds to the transition of holes with energy higher than the height of quantum barriers. The width of these peaks is related to the lifetime of charge carriers in the quantum system – a smaller width corresponds to a longer lifetime of charge carriers.

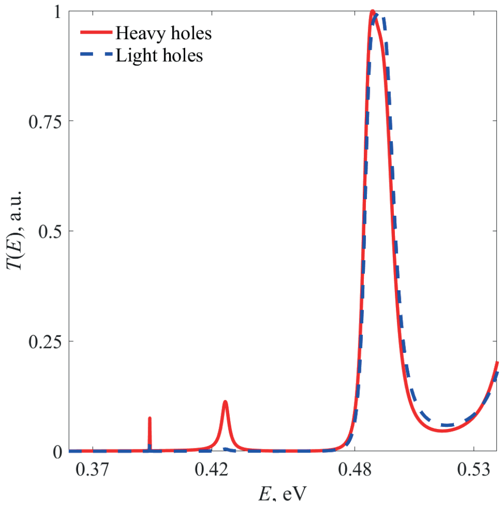

Fig. 2. Tunneling ration depending on the energyfor heavy (solid red line) and light (dashed blue line) holes

Let us consider the structure with non-zero k_y and k_z components of wavevector $\mathbf{k}$. Energy dependence of the transmission coefficient in such system is shown in Fig. 3.

In this case, energy dependence of the transmission coefficient is different for holes with all spin projections. The shift of the second series of resonant peaks is approximately 20 meV. As illustrated in Fig. 3, holes with different spin projections have their own resonant energies: at the first resonant peak heavy holes with both spin projections are tunneling with the same probability and with the same energy. However, light holes have different tunneling probabilities and resonant energies. At the next resonant peak, there is increasing intensity of the second resonant peak. The shift of this series is too small.

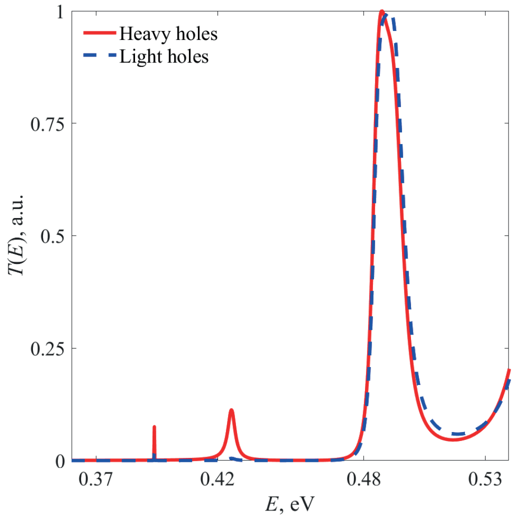

Fig. 3. Tunneling ratio depending on the energy for holes with different effective spin projections ($m_S = +3/2$ is marked by the solid red line, $m_S = +1/2$ by the solid blue line, $m_S = -1/2$ by the dashed blue line, $m_S = -3/2$ by the dashed red line)

Since the heterostructure consists of two different materials, we need to consider the influence on resonant tunneling from both of them. GaAs and AlAs have different dispersion laws, so we need to include in our model the changing of Luttinger parameters and thus take into account the effect of the interface on the holes with a certain spin projection: $\gamma^i_{\mathbf{kk}'} = \gamma^i \delta_{\mathbf{kk}'} + \Delta\gamma^i f_{\mathbf{kk}'}$, where $\Delta\gamma^i = \gamma^i_1 - \gamma^i_2$. Tunneling coefficient dependent on energy for heavy holes with spin projection +3/2 is shown in Fig. 4. The k_y and k_z components of wavevector **k** are equal to zero.

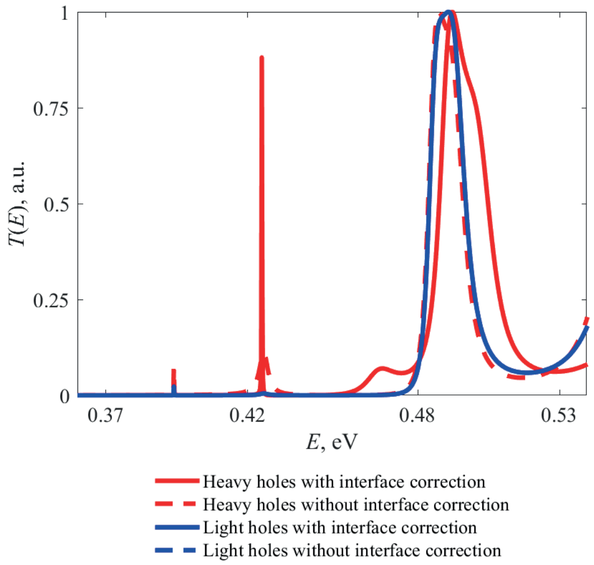

Fig. 4. Difference between tunneling ratio depending on the energy for two cases (the case with interface correction corresponds to the solid red line, the case without interface correction to the dashed blue line)

We can observe increasing intensity of the first resonant peaks and shift of the second series of peaks. The shift is approximately 15 meV. There are two different peaks for independent tunneling of heavy holes and light holes because these interface corrections including change of Luttinger parameters do not influence light hole tunneling.

Finally, we investigate the Rashba effect of the interaction of a heavy hole with effective spin projection +3/2 and the interface of the quantum structure. To introduce these corrections, we need to use the effective Hamiltonian. Its kinetic energy is the sum of Hamiltonian (5) and Rashba Hamiltonian (6). The dependences of the tunneling coefficient are compared in Fig. 5 taking into account the Rashba effect and without it.

$$\Delta H^{(\Gamma_8)} = i\frac{\hbar^2}{2m_0}\Delta R\begin{bmatrix} R_1 & R_3^\dagger & 0 & 0 \\ R_3 & R_2 & R_4^\dagger & 0 \\ 0 & R_4 & -R_2 & R_3^\dagger \\ 0 & 0 & R_3 & -R_1 \end{bmatrix}, \tag{6}$$

where $R_1 = \frac{3}{2}\left(k_x k'_y - k_y k'_x\right)$, $R_2 = \frac{1}{2}\left(k_x k'_y - k_y k'_x\right)$, $R_3 = \frac{\sqrt{3}}{2}\left[\left(k_y k'_z - k_z k'_y\right) + i\left(k_z k'_x - k_x k'_z\right)\right]$, $R_4 = 2\left[\left(k_y k'_z - k_z k'_y\right) + i\left(k_z k'_x - k_x k'_z\right)\right]$, ΔR is interface correction amplitude.

It can be seen from Fig. 5 that there is the shift of resonant peaks for heavy holes with spin projection +3/2 with energy more than the height of the quantum barrier. It is approximately 20 meV. Additionally, there is another shift of the peak in the low-energy range, which is approximately 10 meV.

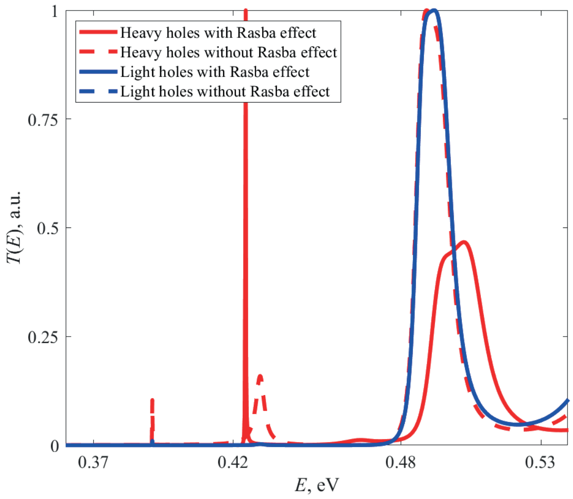

Fig.5. Difference between tunneling ratio depending on the energy for two cases (solid red line corresponds to the case with the Rashba effect, dashed blue line to the case without the Rashba effect)

Conclusion

The effects of resonant tunneling of charge carriers in a GaAs/AlAs heterostructure with a system of two potential barriers are investigated. The tunneling of holes in the Γ_8 zone is considered, where a significant role is played by the difference in the dispersion of particles corresponding to different spin projections. The influence of short-range interface corrections related to the difference in the dispersion law in the materials forming the heterostructure is also considered. In particular, the change in the transmission coefficient is shown when taking into account the interface effect of Rashba. Shifts of tunneling ratio resonant peaks are shown and estimated. The investigated heterostructure can be used to design spintronics devices.

REFERENCES

1. **Galeti H.V.A., Bezerra A.T., Galvao Gobato Y., Brasil M.J.S.P., Taylor D., Henini M.,** Optical and electrical control of spin polarization of two-dimensional hole gases in p-type resonant tunnelling devices. Journal of Physics D: Applied Physics. 50 (46) (2013) 505313.

2. **Lin S., Wang D., Tong Y., Wang X.,** III-nitrides based resonant tunneling diodes. Journal of Physics D: Applied Physics. 25 (53) (2020) 253002.

3. **Huang X., Qin C., Yu Y., Zhang X.,** Acceleration of carrier recovery in a quantum well semiconductor optical amplifier due to the tunneling effect. JOSA B. 10 (29) (2012) 2990–2994.

4. **Bhouri A., Rached A., Lazzari J. L.,** Resonant tunneling transport in $Al_zGa_{1-z}N/In_xGa_{1-x}N/Al_zGa_{1-z}N/In_yGa_{1-y}N$ quantum structures. Journal of Physics D: Applied Physics. 38 (48) (2015) 385102.

5. **Zhao L., Gao L., Reno J. R., Kumar S.,** Resonant-tunneling Transport of Holes in Terahertz GaAs/AlGaAs Quantum Cascade Superlattices. Advanced Solid State Lasers. 2016.

6. **Chandrasekar L.B., Karunakaran M., Gnanasekar K.,** Spin-Dependent Electron Tunneling in $ZnSe/Zn_{1-x}Mn_xSe$ Heterostructures with Double δ-Potentials. Communications in Theoretical Physics. 3 (71) (2019) 339.

7. **Chandrasekar L. B., Karunakaran M., Gnanasekar K.,** Spin-dependent tunneling of light and heavy holes with electric and magnetic fields. Journal of Semiconductors. 11 (39) (2018) 112001.

8. **Davidovich M.V.,** Features of vacuum resonant tunneling at one- and two-well barrier potentials. Journal of Technical Physics. 9 (92) (2022) 1387–1401.

9. **Bhouri A., Rached A., Lazzari J.L.,** Resonant tunneling transport in $Al_zGa_{1-z}N/In_xGa_{1-x}N/Al_zGa_{1-z}N/In_yGa_{1-y}N$ quantum structures. Journal of Physics D: Applied Physics. 38 (48) (2015) 385102.

10. **Brody D.C.,** Biorthogonal quantum mechanics. Journal of Physics A: Mathematical and Theoretical. 3 (47) (2013) 035305.

11. **Mostafazadeh A.,** Pseudo-Hermitian representation of quantum mechanics. International Journal of Geometric Methods in Modern Physics. 7 (7) (2010) 1191–1306.

12. **Zakharchenko M.V., Glinskii G.F.,** The theory of resonant tunneling of charge carriers within the framework of the Green's function method and biorthogonal formalism. Journal of Technical Physics. 10 (93) (2023) 1396–1400.

13. **Glinskii G.F.,** A simple numerical method for determining the energy spectrum of charge carriers in semiconductor heterostructures. Technical Physics Letters. 3 (44) (2018) 232–234.

14. **Vurgaftman I., Meyer J.R., Ram-Mohan L.R.,** Band parameters for III–V compound semiconductors and their alloys. Journal of applied physics. 11 (89) (2001) 5815–5875.

THE AUTHORS

DOMORATSKY Egor V.
egor.domorackiy@mail.ru

GLINSKII Gennadii F.
genaglinskii@mail.ru

ZAKHARCHENKO Mikhail V.
mikhailvzakh@gmail.com

Received 13.12.2023. Approved after reviewing 29.02.2024. Accepted 29.02.2024.

St. Petersburg Polytechnic University Journal. Physics and Mathematics. 2024 Vol. 17. No. 1.1
Научно-технические ведомости СПбГПУ. Физико-математические науки. 17 (1.1) 2024

Conference paper
UDC 538.958
DOI: https://doi.org/10.18721/ JPM.171.110

Study of the band structure of GeSiSn/Ge/Si heterostructures by FTIR photoreflectance spectroscopy

I.V. Chumanov [1] ✉, D.D. Firsov [1], D.V. Kolyada [1], O.S. Komkov [1], I.V. Skvortsov [2],
V.I. Mashanov [2], V.A. Timofeev [2]

[1] St. Petersburg Electrotechnical University "LETI", St. Petersburg, Russia;
[2] A.V. Rzhanov Institute of Semiconductor Physics SB RAS, Novosibirsk, Russia
✉ chumanov2000@yandex.ru

Abstract. The work demonstrates the use of photomodulation FTIR spectroscopy to study structures containing epitaxial layers of GeSn and GeSiSn in the temperature range of 79–180 K. The photoreflectance method has enabled observation of direct interband transitions, and evaluation of the impact of temperature variation and mechanical strain on their energy values.

Keywords: semiconductors, solid solutions, FTIR spectroscopy, photoreflectance method, heterostructures, silicon, epitaxy

Funding: The study was funded by the Russian Science Foundation grant 20-79-10092.

Citation: Chumanov I.V., Firsov D.D., Kolyada D.V., Komkov O.S., Skvortsov I.V, Mashanov V.I., Timofeev V.A., Study of the band structure of GeSiSn/Ge/Si heterostructures by FTIR photoreflectance spectroscopy, St. Petersburg State Polytechnical University Journal. Physics and Mathematics. 17 (1.1) (2024) 62–67. DOI: https://doi.org/10.18721/JPM.171.110

This is an open access article under the CC BY-NC 4.0 license (https://creativecommons.org/licenses/by-nc/4.0/)

Материалы конференции
УДК 538.958
DOI: https://doi.org/10.18721/JPM.171.110

Исследование зонной структуры гетероструктур GeSiSn/Ge/Si методом инфракрасной фурье-спектроскопии фотоотражения

И.В. Чуманов [1] ✉, Д.Д. Фирсов [1], Д.В. Коляда [1], О.С. Комков [1], И.В. Скворцов [2],
В.И. Машанов [2], В.А. Тимофеев [2]

[1] Санкт-Петербургский электротехнический университет «ЛЭТИ», Санкт-Петербург, Россия;
[2] Институт физики полупроводников им. А.В. Ржанова СО РАН, Новосибирск, Россия
✉ chumanov2000@yandex.ru

Аннотация. В работе продемонстрировано применение метода фотомодуляционной ИК фурье-спектроскопии для исследования структур, содержащих слои GeSn и GeSiSn в диапазоне температур 79–180 K. Метод фотоотражения позволил наблюдать прямые межзонные переходы, оценить влияние температуры и механических напряжений в структуре.

Ключевые слова: полупроводники, твердые растворы, фурье-спектроскопия, метод фотоотражения, гетероструктуры, кремний, эпитаксия

Финансирование: Работа выполнена при поддержке Российского научного фонда (грант № 20-79-10092).

© Chumanov I.V., Firsov D.D., Kolyada D.V., Komkov O.S., Skvortsov I.V, Mashanov V.I., Timofeev V.A., 2024. Published by Peter the Great St. Petersburg Polytechnic University.

Ссылка при цитировании: Чуманов И.В., Фирсов Д.Д., Коляда Д.В., Комков О.С., Скворцов И.В., Машанов В.И., Тимофеев В.А. Исследование зонной структуры гетероструктур GeSiSn/Ge/Si методом инфракрасной фурье-спектроскопии фотоотражения // Научно-технические ведомости СПбГПУ. Физико-математические науки. 2024. Т. 17. № 1.1. С. 62–67. DOI: https://doi.org/10.18721/ JPM.171.110

Статья открытого доступа, распространяемая по лицензии CC BY-NC 4.0 (https://creativecommons.org/licenses/by-nc/4.0/)

Introduction

Presently there is an active interest in research on the development of semiconductor devices based on group IV compounds of the periodic table (Si, Ge and Sn). Such compounds can have a direct band structure, which makes it possible to create light-emitting devices on their basis. Another important advantage is its good compatibility with silicon technology [1, 2]. One promising alloy is $Ge_{1-x}Sn_x$, which has a direct band structure at a certain tin content (from about 6.5–8.6 % [3, 4]). This makes it possible to manufacture photodetectors and light-emitting devices, such as lasers and LEDs, in the mid-infrared wavelength range based on this compound. Studies [5, 6] have attempted to create a photodiode and an LED based on such an alloy. Another promising compound for these purposes is the $Ge_{1-x-y}Si_xSn_y$ alloy, which enables band engineering through the adjustment of the Sn content [3]. The possibility of obtaining emitting and photodiode structures based on this alloy has also been demonstrated [7–9].

The goal of the current work is to obtain information about the band structure of the $Ge_{1-x-y}Si_xSn_y$ alloy using the FTIR photoreflectance spectroscopy method. Knowledge of the band structure parameters of $Ge_{1-x-y}Si_xSn_y$ can be used for the development of new optoelectronic devices.

Materials and Methods

In this study, the optical properties of heterostructure samples containing $Ge_{0.918}Sn_{0.082}$ and $Ge_{0.923}Si_{0.025}Sn_{0.052}$ alloys were investigated. The samples were grown via molecular beam epitaxy on (100) silicon substrates. The studies were performed using two series of structures. As the base of the samples of each series, a 100 nm silicon buffer layer was grown on a silicon substrate, on top of which, after a 10 nm $Ge_{0.3}Sn_{0.7}$ insert, a 200 nm thick Ge virtual substrate layer was formed. The final layer, 200 nm thick, was different for each series of samples: $Ge_{0.918}Sn_{0.082}$ for series A; $Ge_{0.923}Si_{0.025}Sn_{0.052}$ for series B. For each series, the samples were annealed in an argon atmosphere at different temperatures (see Table).

Table

Description of the studied samples

Annealing temperature	Non-annealed	125 °C	300 °C	350 °C
Series A	A0	A1	A2	A3
Series B	B0	B1	B2	B3

To study the optical properties of the samples described above, the method of photomodulation Fourier-transform infrared (FTIR) spectroscopy was used. The photoreflectance method is based on measuring the changes in the intensity of the probe beam as a result of the periodic action of the modulating beam ($\hbar\omega > E_g$) on the electric field within the sample. Photoinjected electron-hole pairs are separated under the influence of this field and partially compensate for the surface charged states. This causes a change in the optical characteristics of the structure and, consequently, leads to modulation of the reflectance. Using phase-sensitive detection, a change in the reflection coefficient is recorded, which can be either positive or negative, depending on the phase of the reflectance modulation [10].

The experimental setup was based on a Vertex 80 FTIR spectrometer equipped with CdHgTe and InSb photodetectors cooled by liquid nitrogen. Synchronous detection was performed by

© Чуманов И.В., Фирсов Д.Д., Коляда Д.В., Комков О.С., Скворцов И.В., Машанов В.И., Тимофеев В.А., 2024.
Издатель: Санкт-Петербургский политехнический университет Петра Великого.

using an SR-830 lock-in amplifier. Light from an incandescent lamp with a quartz bulb was used as a probe beam, and modulation was carried out by a laser with a wavelength of 405 nm, which was mechanically chopped at a frequency of 2.3 kHz. To cool the samples, a liquid-nitrogen-cooled cryostat and a closed-cycle helium cryostat were used, allowing a cooling temperature down to 11 K to be achieved.

During the preparation of the spectra for analysis, a phase-correction technique was used to restore the modulation phase [11]. The photoreflectance spectra were analyzed using the method described previously [12].

Results and Discussion

For the first series of samples containing a $Ge_{0.918}Sn_{0.082}$ layer, the photoreflectance spectra measured in the temperature range of 79–180 K are presented in Fig. 1. For all the samples a photoreflectance signal in the form of a double peak is present on the left side of the spectrum. The left maximum corresponds to a direct interband transition in the $Ge_{0.918}Sn_{0.082}$ compound. The nature of the right extremum at the time of writing the work is not clear, but we assume that the double peak may appear because of the presence of mechanical strain in the structure. Such strain can cause a splitting in energy between the subbands of heavy and light holes. This assumption correlates with the results of X-ray diffraction measurements, which have given the strain relaxation degree of only 72% for the $Ge_{0.918}Sn_{0.082}$ epitaxial layer.

For the A0 and A1 samples, additional photoreflectance signals in the spectra were observed at energies above 800 meV. These evidently belong to the germanium virtual substrate layer, as their energy corresponds to the direct interband transition in this material.

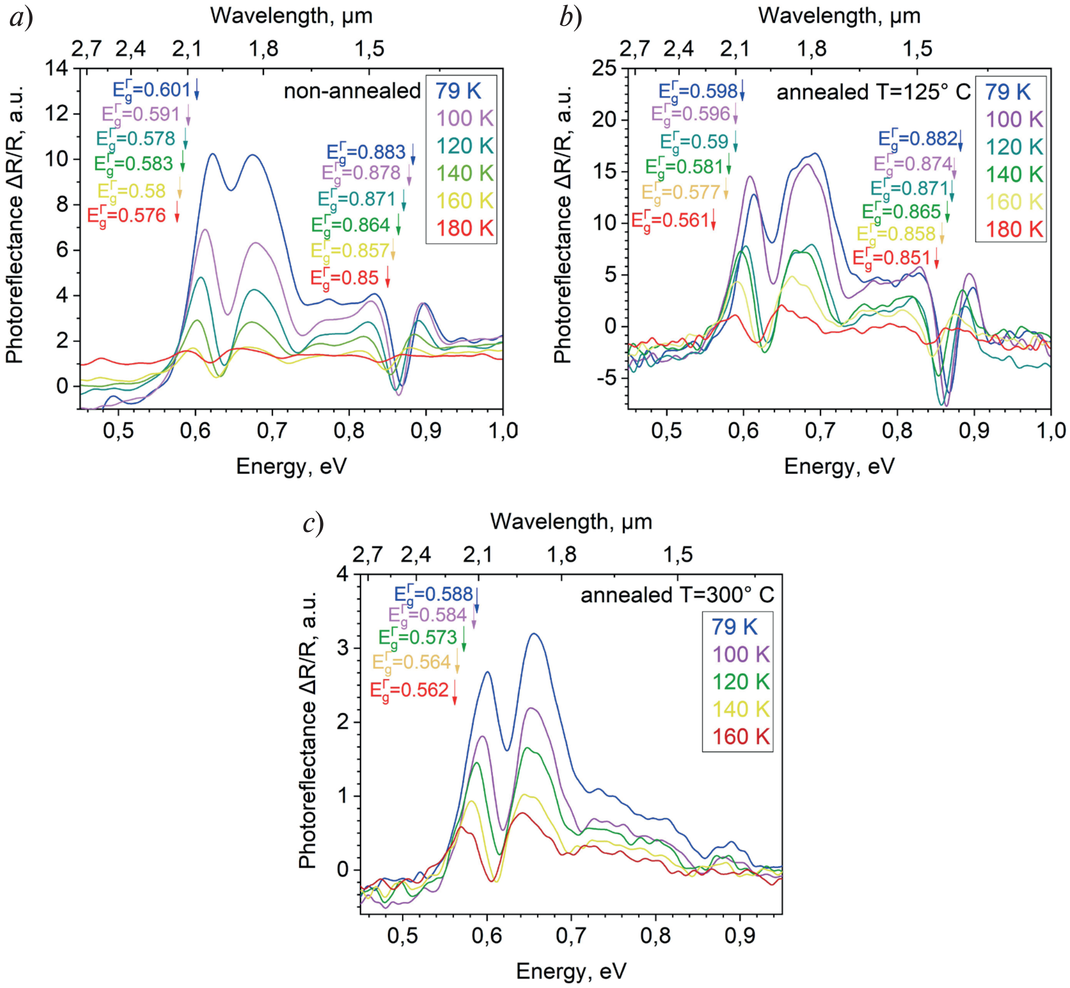

Fig. 1. Photoreflectance spectra for samples of series A: non-annealed, A0 (*a*); annealed at 125 °C, A1 (*b*) and annealed at 300 °C, A2 (*c*)

From the spectra of the Series A samples, one can also evaluate the effect of annealing on the photoreflectance signal. For example, it can be noted that the signal from sample A1 is increased compared to non-annealed one (A0). With further annealing, the signal began to weaken and was not observed for sample A3. Presumably, the annealing changes the concentration of defects and therefore the equilibrium concentration of charge carriers, which affects the built-in electric field of the sample, resulting in a weaker reflectance modulation.

Fig. 2 shows the temperature dependences of the energy of the direct transitions in the $Ge_{0.918}Sn_{0.082}$ layer (*a*) and germanium layer (*b*), obtained from the analysis of the spectra using the techniques described in [12]. The experimental results were approximated by the empirical Varshni equation, and the fitting parameters for each sample are shown as insets in the corresponding figures. In comparison, the corresponding dependences were plotted based on the available literature [13–16]. By comparing the experimental results for Ge with the literature data in Fig. 2, *b*, a good accuracy of the photoreflectance method for studying such structures is shown.

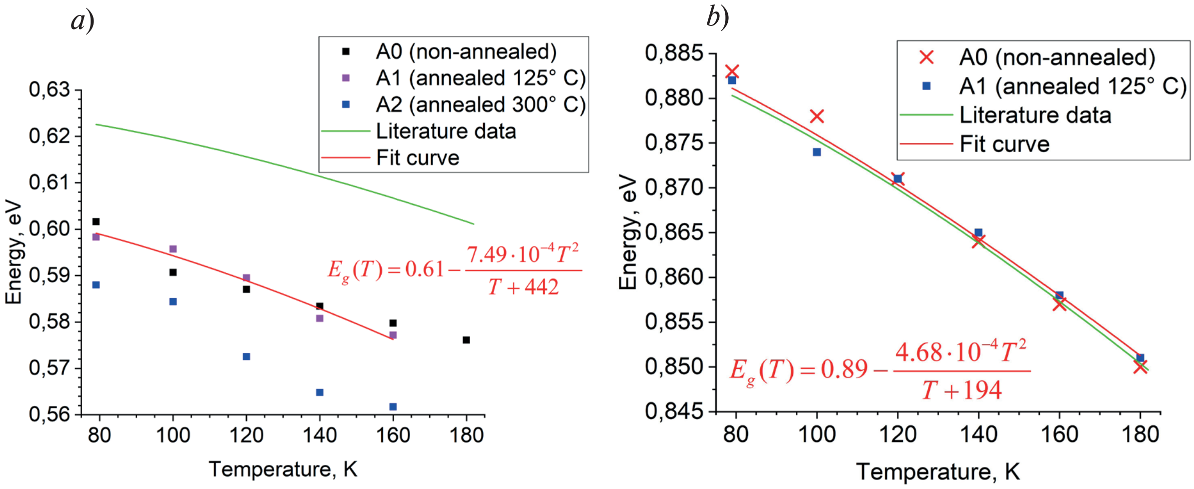

Fig. 2. Temperature dependence of the energy of direct transitions in the $Ge_{0.918}Sn_{0.082}$ (*a*) and Ge (*b*) layers

According to the dependencies in Fig. 2, *a*, it can also be noted that the experimentally obtained energy values for $Ge_{0.918}Sn_{0.082}$ do not precisely coincide with the calculations based on literature data. This discrepancy can be explained by the presence of mechanical strain in the structure. In addition, for the sample A2 annealed at 300 °C, the energy value at 79 K was lower by ~12 meV relative to A0 and A1. Along with the observed greater splitting of the photoreflectance peak, this may imply a change in the strain values in the case of annealing at a relatively high temperature.

The photoreflectance spectra of the sample series with the $Ge_{0.923}Si_{0.025}Sn_{0.052}$ epitaxial layer are shown in Fig. 3, *a*. The spectra exhibited a broadened and asymmetrical (relative to the maximum) peak, which can be represented as a combination of two signals. Indeed, at energies less than 770 meV, signals from the $Ge_{0.923}Si_{0.025}Sn_{0.052}$ alloy are observed, from which the values of the energy gap at the Γ point are determined. The broad shoulder to the right of the maximum is likely caused by the signal from the Ge virtual substrate, which was observed in the samples of series A.

The dots in Fig. 3, *b* indicate the temperature dependence of the value of the direct transition energy in $Ge_{0.923}Si_{0.025}Sn_{0.052}$ obtained from the analysis of the photoreflectance spectra. The red curve approximates the experimental data using the Varshni equation, and the green curve is a dependence constructed on the base of literature data [13–16]. Notably, in this series of samples, the photoreflectance signal was observed only for the non-annealed sample. The absence of the signal in the annealed samples can be caused by a decrease in the modulation of the built-in electric field. Additional research would be necessary to determine the reason behind this effect.

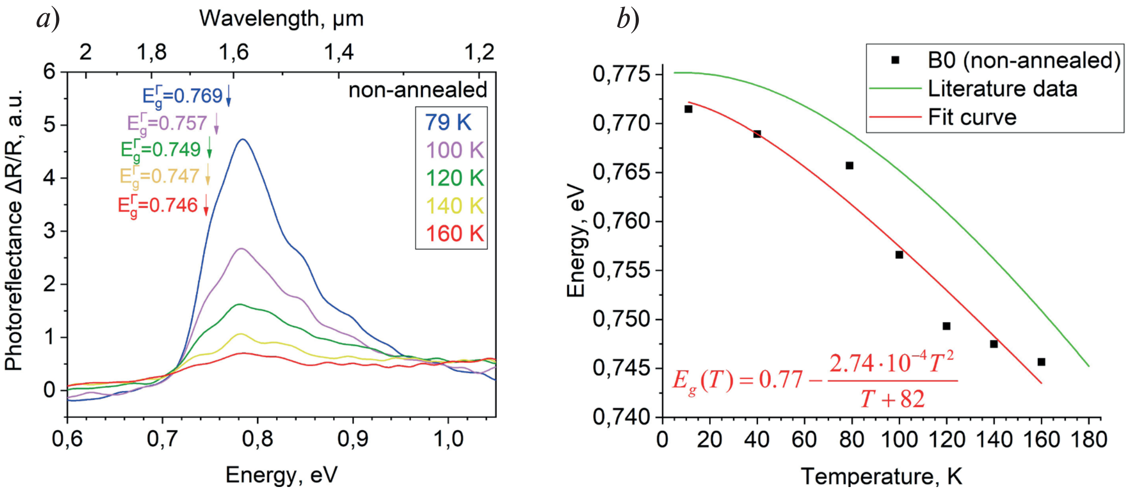

Fig. 3. Photoreflectance spectra for the sample B0 (*a*) and temperature dependence of the obtained energy of direct transitions in the $Ge_{0.923}Si_{0.025}Sn_{0.052}$ layer (*b*)

Conclusion

The FTIR photoreflectance spectroscopy method was employed to study the band structure of $Ge_{0.918}Sn_{0.082}$ and $Ge_{0.923}Si_{0.025}Sn_{0.052}$ epitaxial layers. The photoreflectance spectra of $Ge_{0.923}Si_{0.025}Sn_{0.052}$ were detected for the first time. An analyzis of the spectra made it possible to study the energy gap at the Γ point in the $Ge_{0.918}Sn_{0.082}$ and $Ge_{0.923}Si_{0.025}Sn_{0.052}$ alloys. For the non-annealed samples, the energy values of direct transitions at a temperature of 79 K were 801 meV for $Ge_{0.918}Sn_{0.082}$, and 769 meV for $Ge_{0.923}Si_{0.025}Sn_{0.052}$. Based on the temperature dependence of photoreflectance, the change in the energy values of interband transitions was estimated, and an increase in mechanical stress with increasing temperature was shown. The information obtained about the samples demonstrates the good applicability of the photoreflectance FTIR spectroscopy as a method of investigating the band structure of epitaxial $Ge_{1-x-y}Si_xSn_y$ alloys.

REFERENCES

1. **Soref R.,** Mid-infrared photonics in silicon and germanium. Nature photonics, 4 (8) (2010) 495–497.

2. **Kolyada D.V., Firsov D.D., Timofeev V.A., Mashanov V.I., Karaborchev A.A., Komkov O.S.,** Investigation of the effect of annealing and composition on infrared photoluminescence of GeSiSn/Si multiple quantum well nanoheterostructures. Semiconductors, 56 (8) (2022).

3. **Timofeev V.A., Mashanov V.I., Nikiforov A.I., Skvortsov I.V., Gayduk A.E., Bloshkin A.A., Loshkarev I.D., Kirienko V.V., Kolyada D.V., Firsov D.D., Komkov O.S.,** Tuning the structural and optical properties of GeSiSn/Si multiple quantum wells and GeSn nanostructures using annealing and a faceted surface as a substrate. Applied Surface Science, 593 153421 (2022).

4. **Chen R., Lin H., Huo Y., Hitzman C., Kamins T.I., Harris J.S.,** Increased photoluminescence of strain-reduced, high-Sn composition $Ge_{1-x}Sn_x$ alloys grown by molecular beam epitaxy. Applied physics letters, 99 (18) (2011).

5. **Oehme M., Schmid M., Kaschel M., Gollhofer M., Widmann D., Kasper E., Schulze J.,** GeSn pin detectors integrated on Si with up to 4% Sn. Applied Physics Letters, 101 (14) (2012).

6. **Zhou Y., Dou W., Du W., Pham T., Ghetmiri S. A., Al-Kabi S., Mosleh A., Alher M., Margetis J., Tolle J., Sun G., Soref R. A., Li B., Mortazavi M., Naseem H., Yu S. Q.,** Systematic study of GeSn heterostructure-based light-emitting diodes towards mid-infrared applications. Journal of Applied Physics, 120 (2) (2016).

7. **Gallagher J.D., Xu C., Senaratne C.L., Aoki T., Wallace P.M., Kouvetakis J., Menendez J.,** $Ge_{1-x-y}Si_xSn_y$ light emitting diodes on silicon for mid-infrared photonic applications. Journal of Applied Physics, 118 (13) (2015).

8. **Timofeev V.A., Mashanov V.I., Nikiforov A.I., Loshkarev I.D., Gulyaev D.V., Volodin V.A., Kozhukhov A.S., Komkov O.S., Firsov D.D., Korolkov I.V.,** Study of structural and optical properties of a dual-band material based on tin oxides and GeSiSn compounds. Applied Surface Science, 573 151615 (2022).

9. **Fischer I. A., Wendav T., Augel L., Jitpakdeebodin S., Oliveira F., Benedetti A., Stefanov S., Chiussi S., Capellini G., Busch K., Schulze J.,** Growth and characterization of SiGeSn quantum well photodiodes. Optics Express, 23 (19) (2015) 25048–25057.

10. **Komkov O.S.,** Infrared photoreflectance of III–V semiconductor materials. Physics of the Solid State, (2021) 1–24.

11. **Firsov D.D., Komkov O.S.,** Photomodulation Fourier transform infrared spectroscopy of semiconductor structures: features of phase correction and application of method. Technical Physics Letters, 39 (2013) 1071–1073.

12. **Hosea T.J.C.,** Estimating Critical-Point Parameters of Modulated Reflectance Spectra. physica status solidi (b), 189 (2) (1995) 531–542.

13. **Wasa K., Kitabatake M., Adachi H.,** Thin film materials technology: sputtering of control compound materials. Springer Science & Business Media. (2004).

14. **Bertrand M., Thai Q., Chrйtien J., Pauc N., Aubin J., Milord L., Gassenq A., Hartmann J., Chelnokov A., Calvo V., Reboud V.,** Experimental Calibration of Sn-Related Varshni Parameters for High Sn Content GeSn Layers. Annalen der Physik, 531 (6) (2019) 1800396.

15. **Gupta S., Magyari-Köpe B., Nishi Y., Saraswat K.C.,** Achieving direct band gap in germanium through integration of Sn alloying and external strain. Journal of Applied Physics, 113 (7) (2013).

16. **D'Costa V.R., Fang Y.Y., Tolle J., Kouvetakis J., Menendez J.,** Tunable optical gap at a fixed lattice constant in group-IV semiconductor alloys. Physical Review Letters, 102 (10) (2009) 107403.

THE AUTHORS

CHUMANOV Ivan V.
chumanov2000@yandex.ru
ORCID: 0009-0009-2564-6100

FIRSOV Dmitrii D.
d.d.firsov@gmail.com
ORCID: 0000-0001-7608-9580

KOLYADA Dmitry V.
kolyada.dima94@mail.ru

KOMKOV Oleg S.
okomkov@yahoo.com
ORCID: 0000-0002-8999-1175

SKVORTSOV Ilya V.
i.skvortsov@isp.nsc.ru
ORCID: 0000-0002-2153-1615

MASHANOV Vladimir I.
mash@isp.nsc.ru
ORCID: 0000-0003-4420-6695

TIMOFEEV Vyacheslav A.
Vyacheslav.t@isp.nsc.ru
ORCID: 0000-0003-4093-7802

Received 14.12.2023. Approved after reviewing 05.02.2024. Accepted 06.02.2024.

Conference paper
UDC 535.3, 535.4
DOI: https://doi.org/10.18721/JPM.171.111

Luminescence in nanostructures with compensated quantum wells under optical and electrical pumping

R.B. Adamov [1], G.A. Melentev [1], A.A. Podoskin [2], S.O. Slipchenko [2],
I.V. Sedova [2], S.V. Sorokin [2], I.S. Makhov [3], D.A. Firsov [1], V.A. Shalygin [1]✉

[1] Peter the Great St. Petersburg Polytechnic University, St. Petersburg, Russia;
[2] Ioffe Institute, St. Petersburg, Russia;
[3] National Research University "Higher School of Economics", St. Petersburg, Russia
✉ shalygin@rphf.spbstu.ru

Abstract. Comprehensive studies of the luminescence of *p–i–n* structures with 10 compensated GaAs/AlGaAs quantum wells have been performed. The studies were carried out in the terahertz (THz) and near-infrared (NIR) spectral ranges with both optical and electrical pumping of nonequilibrium charge carriers. The THz photoluminescence spectra revealed an emission line caused by electron transitions from the first size-quantization subband *e*1 to the ground levels of donors *D*1*s*. The photo- and electroluminescence spectra in the NIR range revealed an emission line caused by electron transitions from the *D*1*s* levels to the first subband of heavy holes *hh*1. These transitions provide effective depletion of the *D*1*s* levels and are therefore relevant for creating a THz emitter operating at *e*1–*D*1*s* transitions. At high injection currents in the *p–i–n* diode, lasing occurs at the *D*1*s*–*hh*1 transitions, which increases the efficiency of depletion of the *D*1*s* levels. It is shown that for a given optical pump power or injection current density, the overall rate of the *D*1*s*–*hh*1 transitions in the *p–i–n* structure with 10 QWs is significantly higher than in similar structure with 50 QWs.

Keywords: quantum wells, *p–i–n*-structures, gallium arsenide, aluminum arsenide, impurities, photoluminescence, electroluminescence

Funding: The work of the authors R.B.A., G.A.M. and V.A.S. was supported by the Russian Science Foundation (Grant No. 22-22-00103, https://rscf.ru/project/22-22-00103/).

Citation: Adamov R.B., Melentev G.A., Podoskin A.A., Slipchenko S.O., Sedova I.V., Sorokin S.V., Makhov I.S., Firsov D.A., Shalygin V.A., Luminescence in nanostructures with compensated quantum wells under optical and electrical pumping, St. Petersburg State Polytechnical University Journal. Physics and Mathematics. 17 (1.1) (2024) 68–76. DOI: https://doi.org/10.18721/JPM.171.111

This is an open access article under the CC BY-NC 4.0 license (https://creativecommons.org/licenses/by-nc/4.0/)

Материалы конференции
УДК 535.3, 535.4
DOI: https://doi.org/10.18721/JPM.171.111

Люминесценция наноструктур с компенсированными квантовыми ямами при оптической и электрической накачке

Р.Б. Адамов [1], Г.А. Мелентьев [1], А.А. Подоскин [2], С.О. Слипченко [2],
И.В. Седова [2], С.В. Сорокин [2], И.С. Махов [3], Д.А. Фирсов [1], В.А. Шалыгин [1]✉

[1] Санкт-Петербургский политехнический университет Петра Великого, Санкт-Петербург, Россия;
[2] Физико-технический институт им. А.Ф. Иоффе РАН, Санкт-Петербург, Россия;

© Adamov R.B., Melentev G.A., Podoskin A.A., Slipchenko S.O., Sedova I.V., Sorokin S.V., Makhov I.S., Firsov D.A., Shalygin V.A., 2024. Published by Peter the Great St. Petersburg Polytechnic University.

[3] Национальный исследовательский университет «Высшая школа экономики», Санкт-Петербург, Россия
✉ shalygin@rphf.spbstu.ru

Аннотация. Проведены комплексные исследования люминесценции *p–i–n* структур с 10 компенсированными квантовыми ямами GaAs/AlGaAs. Исследования выполнены в терагерцовом (ТГц) и ближнем инфракрасном (БИК) спектральных диапазонах как при оптической, так и при электрической накачке неравновесных носителей заряда. На спектрах ТГц фотолюминесценции выявлена линия излучения, обусловленная переходами электронов из первой подзоны размерного квантования *e*1 на основные уровни доноров *D*1*s*. На спектрах фото- и электролюминесценции в БИК диапазоне выявлена линия излучения, обусловленная переходами электронов с уровней *D*1*s* в первую подзону размерного квантования тяжелых дырок *hh*1. Эти переходы обеспечивают эффективное опустошение уровней *D*1*s* и потому актуальны для создания ТГц эмиттера, работающего на переходах *e*1–*D*1*s*. При больших токах инжекции в *p–i–n* диоде возникает лазерная генерация на переходах *D*1*s*–*hh*1, что повышает эффективность опустошения уровней *D*1*s*. Показано, что при заданной мощности оптической накачки или плотности инжекционного тока общая скорость переходов *D*1*s*–*hh*1 в *p–i–n*-структуре с 10 КЯ значительно выше, чем в аналогичной структуре с 50 КЯ.

Ключевые слова: квантовые ямы, *p–i–n*-структуры, арсенид галлия, арсенид алюминия, примеси, фотолюминесценция, электролюминесценция

Финансирование: Работа авторов Р.Б.А., Г.А.М. и В.А.Ш. выполнена при финансовой поддержке Российского научного фонда (грант № 22-22-00103, https://rscf.ru/project/22-22-00103/).

Ссылка при цитировании: Адамов Р.Б., Мелентьев Г.А., Подоскин А.А., Слипченко С.О., Седова И.В., Сорокин С.В., Махов И.С., Фирсов Д.А., Шалыгин В.А. Люминесценция наноструктур с компенсированными квантовыми ямами при оптической и электрической накачке // Научно-технические ведомости СПбГПУ. Физико-математические науки. 2024. Т. 17. № 1.1. С. 68–76. DOI: https://doi.org/10.18721/ JPM.171.111

Статья открытого доступа, распространяемая по лицензии CC BY-NC 4.0 (https:// creativecommons.org/licenses/by-nc/4.0/)

Introduction

In recent decades, electrically pumped terahertz radiation sources are actively developed. One of the promising research directions in this field is related to impurity-assisted transitions of nonequilibrium charge carriers in semiconductors and semiconductor nanostructures. Terahertz radiation emission under current injection in *p–n* junctions fabricated from bulk silicon carbide and silicon has been experimentally observed in [1, 2]. Terahertz electroluminescence has been also studied in Be-doped GaAs/AlAs quantum wells sandwiched between two p^+-GaAs:Be layers [3].

Using *compensated* GaAs/AlGaAs quantum wells to create terahertz emitters with electrical pumping seems to be promising. It has already been shown experimentally that such nanostructures allow to obtain the emission of terahertz radiation under *optical pumping* [4, 5]. The experiments were performed on compensated quantum wells with different doping profiles. In some nanostructures, compensation was carried out directly in each quantum well by introducing donors and acceptors with the same concentration. In others, donors and compensating acceptors were spatially separated, namely, donors were located in quantum wells, while acceptors were embedded in barriers forming the quantum wells. Under interband optical pumping conditions, all studied structures exhibited terahertz radiation emission. The origin of the observed terahertz emission has been attributed to transitions of nonequilibrium electrons from the first size-quantization subband (*e*1) to the ground donor levels (*D*1*s*), as well as to intracenter electron transitions ($D2p_{xy}$–*D*1*s*). It has been found that the spatial separation of donors and acceptors provides an approximately twofold increase in the integral intensity of THz emission. This is directly related to the fact that the spatial separation of donors and acceptors in structures with compensated quantum wells increases the rate of radiative electronic transitions *D*1*s*–*hh*1 by a factor of 2.4–3.3 compared to the structure without the spatial separation, which has been confirmed by photoluminescence

© Адамов Р.Б., Мелентьев Г.А., Подоскин А.А., Слипченко С.О., Седова И.В., Сорокин С.В., Махов И.С., Фирсов Д.А., Шалыгин В.А., 2024. Издатель: Санкт-Петербургский политехнический университет Петра Великого.

studies in the near-infrared (NIR) spectral range [5]. Indeed, the electron transitions *D*1*s*–*hh*1 provide dynamic depletion of *D*1*s* levels, which are the final states for terahertz radiative transitions *e*1–*D*1*s*; therefore, an increase in the rate of *D*1*s*–*hh*1 transitions is accompanied by an increase in the intensity of terahertz emission at *e*1–*D*1*s* transitions.

Luminescence in the NIR spectral range was studied in [6] in *p*–*i*–*n* structures with 50 compensated GaAs/AlGaAs quantum wells under conditions of *electrical pumping* of nonequilibrium charge carriers. At sufficiently high injection currents, stimulated emission at the *D*1*s*–*hh*1 transitions was observed in the electroluminescence spectra, associated with the generation of closed modes in the cavity formed due to total internal reflection by four cleaved edges of the *p*–*i*–*n* diode. It has been found that the structure with compensated quantum wells without spatial separation of donors and acceptors provides a fivefold increase in the integral intensity of stimulated NIR emission at the *D*1*s*–*hh*1 transitions compared to the structure with spatial separation of donors and acceptors (when donors are located in quantum wells, while acceptors are embedded in barriers). In this regard, to develop electrically-pumped terahertz emitters operating at the *e*1–*D*1*s* transitions under conditions of lasing at *D*1*s*–*hh*1 transitions, it is more expedient to use structures with the compensated GaAs/AlGaAs quantum wells without spatial separation of donors and acceptors.

Obviously, for a given injection current, it is possible to increase the concentrations of nonequilibrium electrons and holes in each quantum well if the total number of quantum wells in the structure is reduced. In this case, the choice of the optimal number of quantum wells must take into account the losses of electrons and holes injected from the emitters due to their recombination in the waveguide layers.

The present work is dedicated to the experimental study of these issues. The *p*–*i*–*n* structures with compensated GaAs/AlGaAs quantum wells have been grown without spatial separation of donors and acceptors, since, as noted above, such a doping profile provides high integral intensity of stimulated NIR emission at the *D*1*s*–*hh*1 transitions. To significantly increase the level of excitation of nonequilibrium electrons in each quantum well compared to [6], the number of quantum wells in the structure was reduced to 10 (i.e., it lowered by 5 times). We study NIR luminescence in these structures at a temperature of 10 K. The studies are carried out under both optical and electrical pumping. The main channels of radiative recombination are determined under various experimental conditions. In addition, the current-voltage characteristics (CVC) of *p*–*i*–*n* diodes made from these structures are studied. Terahertz luminescence in the *p*–*i*–*n* structures is investigated at optical pumping. The possibility of observing the emission of terahertz radiation from forward-biased *p*–*i*–*n* diodes under conditions of generation of stimulated emission in the NIR range is discussed.

Experimental Technique

The *p*–*i*–*n* heterostructure with selectively doped GaAs/AlGaAs multiple quantum wells (MQWs) was grown by molecular beam epitaxy on epi-ready Si-doped n^+-GaAs (001) substrate at ~580 °C. The heterostructure contains the following layers (in the direction from the substrate to the surface): *n*-GaAs buffer layer with a thickness of ~ 0.5 μm ($n \sim 10^{18}$ cm^{-3}), bottom 1-μm thick *n*-$Al_{0.9}Ga_{0.1}As$ cladding layer ($n \sim 2\cdot10^{18}$ cm^{-3}), undoped 0.3-μm thick $Al_{0.3}Ga_{0.7}As$ waveguide layer, MQW region consisted of ten 6.9 nm thick GaAs QWs separated by 7.6 nm $Al_{0.3}Ga_{0.7}As$ barriers, undoped 0.3-μm thick $Al_{0.3}Ga_{0.7}As$ waveguide layer, top 1-μm thick *p*-$Al_{0.9}Ga_{0.1}As$ cladding layer ($p \sim 5\cdot10^{17}$ cm^{-3}), and 0.4-μm thick p^{++}-GaAs contact layer ($p \sim 10^{19}$ cm^{-3}). The MQW region was selectively doped, namely, the central part (about 2.6 nm) of each GaAs quantum well was doped simultaneously with Si and Be at a nearly equal concentration of ~ $1.2\cdot10^{17}$ cm^{-3} (the surface density of both donors and acceptors is ~ $3\cdot10^{10}$ cm^{-2}), while the $Al_{0.3}Ga_{0.7}As$ barriers remained undoped.

Samples for luminescence studies were prepared by cleaving the heterostructure into square and rectangular pieces. Photoluminescence (PL) studies were carried out with the samples of 3×3 mm size. For electroluminescence (EL) studies, two-terminal sample devices with lateral sizes of 0.5×2 mm were fabricated. Au-Ge/Au contact was evaporated on the *n*-GaAs substrate and Ti/Pt/Au contact was made on the p^{++}-GaAs layer. Each device represents a *p*–*i*–*n* diode since MQWs have intrinsic conductivity due to compensation of donors by acceptors. The diodes were soldered *p*-side down to copper heatsinks.

The samples were mounted on cold finger of a closed cycle cryostat. The experiments were carried out at a temperature of 10 K. Optical pumping of the sample was provided by means of a continuous-wave solid-state laser at a wavelength of 532 nm. The laser beam was focused into a spot of 510 μm in diameter at the center of the sample. Photoexcitation power varied in the range of 0.1–100 mW.

Near-infrared photoluminescence studies were conducted by means of a grating monochromator Horiba Jobin Yvon FHR-640 with silicon CCD camera. Optical path between the sample and the monochromator contained a window and a lens fabricated from silica glass.

Experiments on terahertz photoluminescence were performed using a Fourier spectrometer Bruker Vertex 80v operating in step-scan mode. Terahertz radiation emitted from the sample was detected using a liquid helium-cooled silicon bolometer and a lock-in amplifier. Photoresponse was measured at the frequency of a chopper modulating the pumping laser beam (87 Hz). For more details see [5].

Electroluminescence studies were also conducted using the grating spectrometer (in NIR spectral range) and the Fourier spectrometer (in THz spectral range). The measurements were carried out under forward bias of the *p–i–n* diodes. At weak injection currents ($J < 10$ mA), measurements were carried out in DC mode by using a Keithley 2601A System SourceMeter. Measurements at higher currents were carried out in pulsed mode (pulse duration of 1 μs, repetition frequency of 87 Hz) using self-made pulse generator. In parallel with the study of NIR electroluminescence, the current-voltage characteristics of the diodes were obtained. Oscillograms of current and voltage pulses were recorded using a Tektronix TDS2024B oscilloscope.

Results and Discussion

Near-infrared photoluminescence spectra of the *p–i–n* structure with ten compensated QWs are presented in Fig. 1. The identification of the main spectral lines can be carried out using the results of our previous papers [5–7]. At a low pumping powers ($P = 0.1$–1 mW), there are two PL lines in the spectra. The wide asymmetric line with the maximum at a photon energy of $\hbar\omega = E_M(p^{++}) \cong 1480$ meV is associated with the p^{++}-GaAs contact layer and can be attributed to radiative electron transitions from the conduction band to merged acceptor/valence band [6]. Other asymmetric line with maximum at 1536 meV (for $P = 0.1$ mW), which undergoes a blue shift under increasing pumping power, can be attributed to the impurity-assisted electron transitions in the quantum wells. These are the radiative transitions from *e*1 subband to the ground acceptor state *A*1*s* which play negative role from the point of view of the THz radiation emission at *e*1–*D*1*s* transitions [5, 6]. But at pump power of 10 mW and higher, a hump due to the *D*1*s*–*hh*1 transitions emerges on the high-frequency side of the *e*1–*A*1*s* line. Let us emphasize once again that the *D*1*s*–*hh*1 transitions play a positive role from the point of view of the THz emission mechanism we are considering. At powers exceeding 30 mW, the line *D*1*s*–*hh*1 dominates over

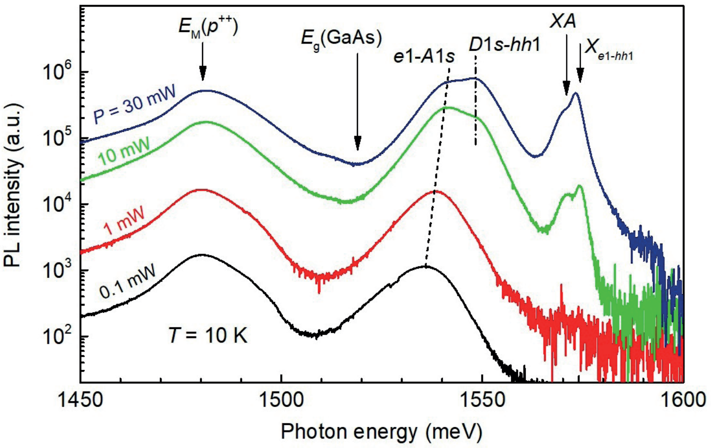

Fig. 1. Near-infrared photoluminescence spectra for *p-i-n* structure with 10 compensated QWs. Here E_g(GaAs) denotes the forbidden gap of GaAs. Dashed and dash-dotted lines point out the maximum positions of the impurity-assisted recombination lines for various pump powers

the line *e*1—*A*1*s*. It should be emphasized that the *p*—*i*—*n* structure with 10 quantum wells provides an advantage in the efficiency of optical excitation of the *D*1*s*—*hh*1 PL line in comparison with the 50-QW structure studied in [6]. Namely, the structure with 10 QWs, when it is pumped at power of 10 mW, provides the same magnitude of the *D*1*s*—*hh*1 line (per quantum well) that the structure with 50 QWs gives at pumping power of ~ 100 mW. As a result, at a given pumping power, the total rate of *D*1*s*—*hh*1 transitions in the structure with 10 QWs is twice as high as in the structure with 50 QWs.

Besides, one can also reveal two sharp PL peaks related to the radiative recombination of the acceptor-bound exciton *XA* (at $\hbar\omega$ = 1571 meV) and of free excitons formed from electrons of the *e*1 subband and holes of the *hh*1 subband, $X_{e1\text{-}hh1}$, at 1574.3 meV (see Fig. 1).

Before we move on to the analysis of the electroluminescence spectra, it is reasonable to discuss the current-voltage characteristics of the studied diodes. We measured CVC for the *p*—*i*—*n* diode with 10 compensated QWs at a temperature of 10 K and compared it with the experimental data for a similar diode of the same lateral sizes with 50 compensated QWs from [6], see Fig. 2. As can be seen from the figure, a fivefold reduction in the number of QWs drastically changes the behavior of CVC at forward bias. First, the region of negative differential conductivity disappears (in 50-QW diode the negative differential conductivity is observed in the voltage range of 5.0—8.5 V). Second, to provide the same electric current in the 10-QW diode it is necessary to apply significantly larger voltage compared to the 50-QW diode. The first factor can be considered as positive, but the second one is certainly negative. Experiments have shown that at forward voltage on the diode exceeding 15 V, when the electric field strength in the *i*-layer of the diode exceeds $1.5\cdot10^5$ V/cm, an electrical breakdown occurs in this layer, and the diode is destroyed. For this reason, 10-QW diodes cannot pass a current of more than *J* = 1.3 A (with a pulse duration of 1 μs or less), while 50-QW diodes could withstand pulse currents of up to *J* = 6 A. The above increase in the effective resistance of the *i*-layer is due to a 3-fold increase in the total thickness of the $Al_{0.3}Ga_{0.7}As$ waveguide layers (from 200 to 600 nm), which is required to provide a sufficient total width of the NIR waveguide layer (~ 730 nm).

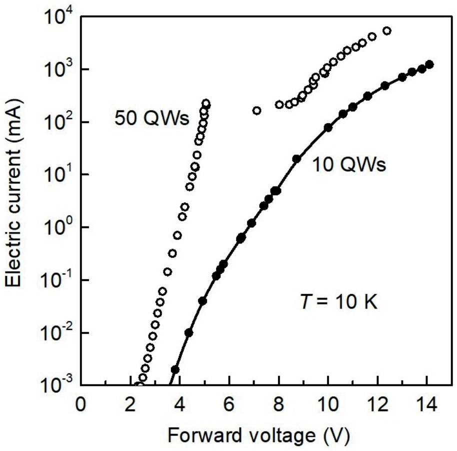

Fig. 2. Comparison of the current-voltage characteristics for *p-i-n* diodes of the same lateral sizes with 10 and 50 compensated QWs (solid and empty circles, respectively). Line is a guide for the eye

Near-infrared electroluminescence spectra of the *p*—*i*—*n* diode with ten compensated QWs at various injection currents are presented in Fig. 3. Note, that the EL line due to radiative recombination of the acceptor-bound exciton (*XA*) is significantly broaden. The broadening is caused by a rather high electric field in the *i*-layer of the diode even at the lowest injection current used in the EL experiment. Using the *i*-layer thickness of 730 nm and the CVC data from Fig. 2, one can estimate the electric field strength of about $5\cdot10^4$ V/cm. At injection current of 5 mA and less the position of the *XA* peak is almost unchanged (~ 1572 meV). As the current increases from 5 mA to 1230 mA, the exciton peak experiences a red shift of about 4 meV, which is caused by an increase in the voltage drop across the MQW layers. Microscopic mechanism of a red shift of the excitonic peak in electric field was considered in [8] and was called as the quantum-confined Stark effect.

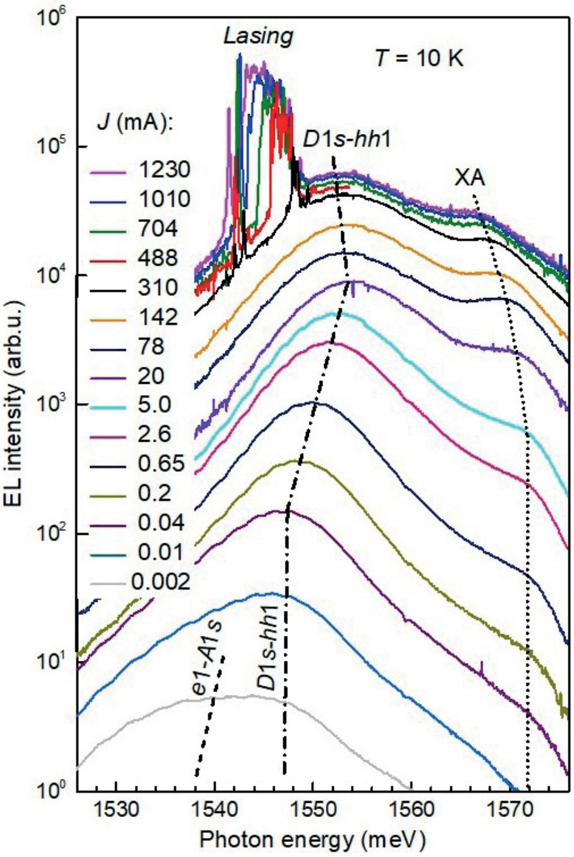

Fig. 3. Near-infrared electroluminescence spectra for *p-i-n* diode with 10 compensated QWs at various values of the injection current *J*. Dashed and dash-dotted lines point out the maximum positions of the impurity-assisted EL lines. Dotted line demonstrates the maximum positions of the acceptor-bound exciton line on the EL spectra

Let us consider the behavior of the donor-assisted recombination line *D*1*s*—*hh*1. As mentioned above, in the PL spectrum at a power of 30 mW, this line is slightly dominant over the acceptor-assisted recombination line *e*1—*A*1*s* (see Fig. 1). The same situation is observed in the EL spectra at the intermediate injection current between 0.002 and 0.01 mA (see Fig. 3). Under increase in the current up to 20 mA, the *D*1*s*—*hh*1 line begins to dominate significantly over the line *e*1—*A*1*s*, and superposition of these lines undergoes a blue shift of about +8 meV. With a further increase in the injection current to 1230 mA, a red shift of the *D*1*s*—*hh*1 line (of about −4 meV) is observed, which we associate with the quantum-confined Stark effect [9]. Previously, a similar transition from blue shift to red was also observed in *p*—*i*—*n* diodes with 50 compensated QWs [6]. A notable feature of the EL spectra at high injection currents (310—1230 mA) is the appearance of narrow emission lines on the low-frequency wing of the broad spontaneous EL line *D*1*s*—*hh*1, which merge into a single band several meV wide as the current increases. These lines represent high Q-factor closed modes of stimulated emission arising due to total internal reflection at the cleaved sample edges [10, 11].

The lasing threshold current for the 10-QW *p*—*i*—*n* diode is about 300 mA, which is 7 times less than the threshold current in the 50-QW diode [6]. This is an important advantage. Another advantage is that at a given injection current, the overall rate of *D*1*s*—*hh*1 transitions in the structure with 10 QWs is significantly higher than in the structure with 50 QWs. Indeed, comparing the spectral position of the *D*1*s*—*hh*1 line relative to the exciton peak of *XA* for *p*—*i*—*n* diodes with different numbers of quantum wells (see Fig. 3 here and Fig. 6 in [6]), one can, for example, notice that a current of 0.2 mA in the diode with 10 QWs provides the same level of nonequilibrium charge carrier excitation per QW as is achieved at a current of ~ 3 mA in the diode with 50 QWs. This means that increasing the current in the 10-QW diode by 5 times (up to 1 mA) one can achieve the same overall rate of *D*1*s*—*hh*1 transitions as in the 50-QW diode at 3 mA, and further increase in the current up to 3 mA will provide a threefold improvement compared to the 50-QW diode. Thus, we can conclude that 10-QW diodes are more promising for creating electrically pumped THz emitters based on $e1$-$D1s$ transitions in comparison with 50-QW diodes.

Then we studied THz luminescence. First, experiments were carried out under optical pumping. Spectra of the THz PL photoresponse are presented in Fig. 4. There are three pronounced peaks in the spectra. The low-frequency peak at $\hbar\omega$ = 18 meV can be attributed $e1$–$D1s$ transitions. In the limits of experimental accuracy its position corresponds to the $e1$–$D1s$ peak previously observed in similar MQW structure but without conducting cladding layers and p^{++}-GaAs top layer [5]. Two other peaks (centered at ~ 28 meV and ~ 38 meV) have not been observed in Ref. [5]. It is reasonable to associate them with highly doped p^{++}-GaAs layer. Both peaks can arise due to photorefractive effect in p^{++}-GaAs layer associated with the room-temperature background radiation and optical pumping. Note, that high-frequency peak at ~ 38 meV can be also associated with THz emission at the $A1s$–$hh1$ transitions (see Ref. [4]).

At the final stage of these investigations, we made an attempt to explore THz luminescence under electrical pumping. Since during optical pumping of the p–i–n structures under study we have already observed the emission of THz radiation at the $e1$–$D1s$ transitions (see Fig. 4), and in diodes made from this structure we observed NIR lasing at the $e1$–$D1s$ transitions (see Fig. 3), we also expected to detect the emission of THz radiation from the p–i–n diodes under NIR lasing conditions. Unfortunately, our expectations were not met. We did not observe measurable THz emission from the edges of the diodes.

Apparently, this is due to the fact that the area of the diode edge from which we tried to collect THz EL radiation is almost 3 orders of magnitude smaller than the surface area from which THz PL radiation was collected. A possible solution to this problem is to use metal grating as a semi-transparent electrical contact to the p-side of the diode, which will allow collecting THz EL radiation from a large area (even larger than in THz PL studies).

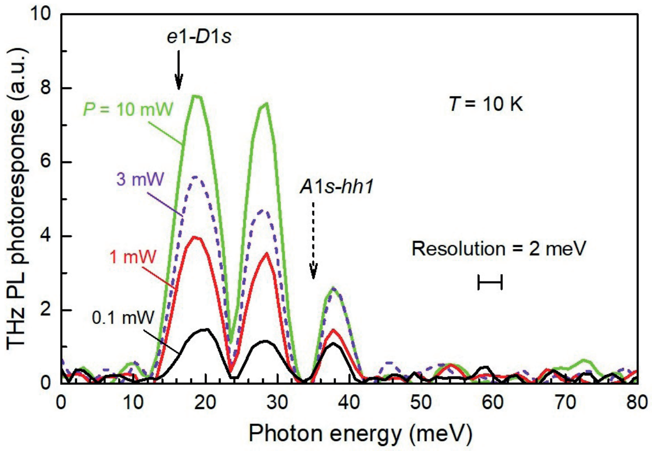

Fig. 4. Terahertz photoluminescence spectra for the p–i–n structure with 10 compensated QWs at various pump power P. Solid arrow shows the peak position for the $e1$–$D1s$ transitions after [5]. Dashed arrow points out the peak position for the $A1s$–$hh1$ transitions after [4]

Conclusion

The impurity-assisted NIR and THz photoluminescence have been studied in the p–i–n structure with 10 compensated GaAs/AlGaAs quantum wells. The compensation was carried out directly in each quantum well by introducing donors and acceptors with the same concentration. In the p–i–n diodes fabricated from the structure, the current-voltage characteristic and impurity-assisted NIR electroluminescence have been studied as well. Behavior of the $D1s$–$hh1$ emission line (which plays a positive role in the THz emission at the $e1$–$D1s$ transitions) has been analyzed in the NIR photo- and electroluminescence spectra. It has been shown, that at given power of optical pumping or density of injection current, the overall rate of $D1s$–$hh1$ transitions in the p–i–n structure with 10 QWs is significantly higher than in the similar structure with 50 QWs.

NIR stimulated emission at the *D*1*s*—*hh*1 transitions has been observed in the electroluminescence spectra. It has been established that reducing the number of quantum wells from 50 to 10 leads to a 7-fold decrease in the lasing threshold current. THz emission line due to electron transitions *e*1—*D*1*s* has been revealed in the THz photoluminescence spectra. To obtain THz radiation from forward-biased *p*—*i*—*n* structures with compensated GaAs/AlGaAs quantum wells, it is proposed to use metal grating as a semi-transparent electrical contact to the *p*—*i*—*n* diode.

REFERENCES

1. **Andrianov A.V., Gupta J.P., Kolodzey J., Sankin V.I., Zakhar'in A.O., Vasil'ev Yu.B.,** Current injection induced terahertz emission from 4H-SiC *p-n* junctions, Applied Physics Letters. 103 (22) (2013) 221101.

2. **Zakhar'in A.O., Vasilyev Yu.B., Sobolev N.A., Zabrodskii V.V., Egorov S.V., Andrianov A.V.,** Injection-induced terahertz electroluminescence from silicon *p*—*n* structures, Semiconductors. 51 (5) (2017) 604—607.

3. **Li S.M., Zheng W.M., Wu A.L., Cong W.Y., Liu J., Chu N.N., Song Y.X.,** Terahertz electroluminescence from Be δ-doped GaAs/AlAs quantum well, Applied Physics Letters. 97 (2) (2010) 023507.

4. **Makhov I.S., Panevin V.Yu., Firsov D.A., Vorobjev L.E., Klimko G.V.,** Impurity-assisted terahertz photoluminescence in compensated quantum wells, Journal of Applied Physics. 126 (17) (2019) 175702.

5. **Adamov R.B., Melentev G.A., Sedova I.V., Sorokin S.V., Klimko G.V., Makhov I.S., Firsov D.A., Shalygin V.A.,** Terahertz photoluminescence in doped nanostructures with spatial separation of donors and acceptors, Journal of Luminescence. 266 (2024) 120302.

6. **Adamov R.B., Melentev G.A., Podoskin A.A., Kondratov M.I., Grishin A.E., Slipchenko S.O., Sedova I.V., Sorokin S.V., Klimko G.V., Makhov I.S., Firsov D.A., Shalygin V.A.,** Luminescence in *p-i-n* structures with compensated quantum wells, Semiconductors. 57 (8) (2023) 643—652.

7. **Adamov R.B., Petruk A.D., Melentev G.A., Sedova I.V., Sorokin S.V., Makhov I.S., Firsov D.A., Shalygin V.A.,** Near-infrared photoluminescence in n GaAs/AlGaAs quantum wells with different locations of compensating acceptor impurity, St. Petersburg Polytechnic University Journal: Physics and Mathematics. 15 (4) (2022) 32—43.

8. **Miller D.A.B., Chemla D.S., Damen T.C., Gossard A.C., Wiegmann W., Wood T.H., Burrus C.A.,** Electric field dependence of optical absorption near the band gap of quantum-well structures, Physical Review B. 32 (2) (1985) 1043—1060.

9. **Bastard G., Brum J.A., Ferreira R.,** Electronic States in Semiconductor Heterostructures, Solid State Physics. 44 (1991) 229—415.

10. **Podoskin A.A., Romanovich D.N., Shashkin I.S., Gavrina P.S., Sokolova Z.N., Slipchenko S.O., Pikhtin N.A.,** Specific Features of Closed-Mode Formation in Rectangular Resonators Based on InGaAs/AlGaAs/GaAs Heterostructures for High-Power Semiconductor Lasers, Semiconductors. 53 (6) (2019) 828—832.

11. **Podoskin A.A., Romanovich D.N., Shashkin I.S., Gavrina P.S., Sokolova Z.N., Slipchenko S.O., Pikhtin N.A.,** Switching Control Model of Closed-Mode Structures in Large Rectangular Cavities Based on AlGaAs/InGaAs/GaAs Laser Heterostructures, Semiconductors. 54 (5) (2020) 581—586.

THE AUTHORS

ADAMOV Roman B.
roma.adamow@gmail.com
ORCID: 0000-0002-7731-349X

MELENTEV Grigorii A.
gamelen@spbstu.ru
ORCID: 0000-0002-1680-333X

PODOSKIN Aleksandr A.
podoskin@mail.ioffe.ru
ORCID: 0000-0002-8819-844X

SLIPCHENKO Sergey O.
serghpl@mail.ioffe.ru
ORCID: 0000-0003-4851-3641

SEDOVA Irina V.
irina@beam.ioffe.ru
ORCID: 0000-0002-9540-0933

SOROKIN Sergey V.
sorokin@beam.ioffe.ru
ORCID: 0000-0003-0320-2233

MAKHOV Ivan S.
imahov@hse.ru
ORCID: 0000-0003-4527-1958

FIRSOV Dmitry A.
dmfir@rphf.spbstu.ru
ORCID: 0000-0003-3947-4994

SHALYGIN Vadim A.
vadim_shalygin@mail.ru
ORCID: 0000-0001-6728-7286

Received 05.12.2023. Approved after reviewing 07.12.2023. Accepted 12.12.2023.

St. Petersburg Polytechnic University Journal. Physics and Mathematics. 2024 Vol. 17. No. 1.1
Научно-технические ведомости СПбГПУ. Физико-математические науки. 17 (1.1) 2024

Conference paper
UDC 551.510.411
DOI: https://doi.org/10.18721/JPM.171.112

Electroluminescence of narrow-gap InAs/InAs$_{1-y}$Sb$_y$/InAsSbP heterostructures with y = 0.07–0.12

M.S. Ruzhevich [1] ✉, K.D. Mynbaev [2], N.L. Bazhenov [2], V.V. Romanov [2], K.D. Moiseev [2]

[1] ITMO University, St. Petersburg, Russia;

[2] Ioffe Institute, St. Petersburg, Russia

✉ max.ruzhevich@niuitmo.ru

Abstract. Electroluminescence of narrow-gap n-InAs/InAs$_{1-y}$Sb$_y$/p-InAsSbP heterostructures with the indium antimonide content in the active region y = 0.07—0.12 has been studied. A radiative recombination channel associated with the InAsSb/InAsSbP heterointerface has been discovered. The dependence of the type of this heterointerface on the actual composition of the barrier layer near the interface has been established.

Keywords: solid solutions, InAsSb, electroluminescence, heterostructures

Citation: Ruzhevich M.S., Mynbaev K.D., Bazhenov N.L., Romanov V.V., Moiseev K.D., Electroluminescence of narrow-gap InAs/InAs$_{1-y}$Sb$_y$/InAsSbP heterostructures with y = 0.07—0.12, St. Petersburg State Polytechnical University Journal. Physics and Mathematics. 17 (1.1) (2024) 77—82. DOI: https://doi.org/10.18721/JPM.171.112

This is an open access article under the CC BY-NC 4.0 license (https://creativecommons.org/licenses/by-nc/4.0/)

Материалы конференции
УДК 551.510.411
DOI: https://doi.org/10.18721/JPM

Электролюминесценция узкозонных гетероструктур InAs/InAs$_{1-y}$Sb$_y$/InAsSbP с y = 0,07–0,12

М.С. Ружевич [1] ✉, К.Д. Мынбаев [2], Н.Л. Баженов [2], В.В. Романов [2], К.Д. Моисеев [2]

[1] Университет ИТМО, Санкт-Петербург, Россия;

[2] ФТИ им. А.Ф. Иоффе, Санкт-Петербург, Россия

✉ max.ruzhevich@niuitmo.ru

Аннотация. Исследована электролюминесценция узкозонных гетероструктур n-InAs/InAs$_{1-y}$Sb$_y$/p-InAsSbP с содержанием антимонида индия в активной области y = 0,07—0,12. Обнаружен канал интерфейсной излучательной рекомбинации, связанный с гетерограницей InAsSb/InAsSbP. Установлена зависимость типа этой гетерограницы от фактического состава барьерного слоя вблизи границы.

Ключевые слова: твердые растворы, InAsSb, электролюминесценция, гетероструктуры

Ссылка при цитировании: Ружевич М.С., Мынбаев К.Д., Баженов Н.Л., Романов В.В., Моисеев К.Д. Электролюминесценция узкозонных гетероструктур InAs/InAs$_{1-y}$Sb$_y$/InAsSbP с y = 0,07—0,12 // Научно-технические ведомости СПбГПУ. Физико-математические науки. 2024. Т. 17. № 1.1. С. 77—82. DOI: https://doi.org/10.18721/JPM.171.112

Статья открытого доступа, распространяемая по лицензии CC BY-NC 4.0 (https://creativecommons.org/licenses/by-nc/4.0/)

© Ruzhevich M.S., Mynbaev K.D., Bazhenov N.L., Romanov V.V., Moiseev K.D., 2024. Published by Peter the Great St. Petersburg Polytechnic University.

Introduction

Heterostructures (HSs) based on InAs(Sb,P) solid solutions are promising for creating emission sources operating in the mid-infrared (IR) spectral range. Light-emitting diodes (LEDs) based on these HSs are the main components in optoelectronic devices intended for spectroscopy of gases and molecules, environmental monitoring, medical diagnostics, etc. [1–3]. Changing the mole fraction y of InSb in the $InAs_{1-y}Sb_y$ solid solution used as the active region of these HSs makes it possible to cover a wide spectral range from 3.4 to 11.0 μm. However, shifting to the long-wavelength boundary of this range, which requires an increase in y, leads to an increase in the mismatch in the crystal lattice parameter of the InAsSb epitaxial layer relative to the binary InAs substrate and to the covering barrier layer. This hinders practical implementation of the HSs; however, the relative ease of their manufacture and low price compared to other types of mid-IR radiation sources continue to attract attention to this material.

This work presents results of studying electroluminescence (EL) of narrow-gap n-InAs/$InAs_{1-y}Sb_y$/p-InAsSbP HSs with $y = 0.07–0.12$, and compares these results with the features of the band diagram of the structures. Experimental studies were conducted in a wide temperature range $T = 4.2–300$ K.

Materials and Methods

HSs were grown by metal-organic vapor phase epitaxy (MOVPE) in a horizontal reactor at atmospheric pressure; details of the process were reported elsewhere [4]. Undoped (001)InAs wafers with the electron concentration $n = 3\cdot10^{16}$ cm^{-3} ($T = 300$ K) were used as substrates. The active region of HSs with the thickness of 3.0 μm represented an epitaxial layer of $InAs_{1-y}Sb_y$ with $y = 0.07$, 0.09, $y = 0.10$, or $y = 0.12$, and was not doped either. To create a 1.2 μm-thick covering barrier layer, a quaternary InAsSbP solid solution was used. The p-type conductivity in the barrier layer was obtained by doping the layer with zinc during the growth.

Based on the HSs, 400×400 μm LED chips were manufactured and mounted on TO-18-type housings. The emission was registered from the side of the barrier layer. EL spectra were recorded using a cooled InSb-based photodiode under pulsed excitation with a frequency 1 kHz and pulse duration 2 μs.

Results and Discussion

Figure 1 shows a full EL spectrum of the HS with $y = 0.07$, recorded at $T = 4.2$ K and injection current per pulse $i = 1$ A. At low temperatures, in the range from 4.2 to 150 K, in addition to the low-energy emission band with photon energy $h\nu \sim 0.3$ eV, the EL spectra of all structures contained a high-energy band with a spectral maximum near $h\nu \sim 0.4$ eV and a full width at half-maximum (FWHM) at $T = 4.2$ K, ~ 12 meV. We observed this feature earlier when studying EL of HSs with an active region based on $InAs_{1-y}Sb_y$ with $0.14 < y \le 0.16$. In particular, in Ref. [5], the results of the detailed studies of the nature of this EL band were presented and it was determined that this band was related to the recombination of donor-acceptor pairs in the InAs substrate. The low-energy band of the spectrum corresponds to the emission associated with the narrow-gap active region. In our studies, the spectra of this emission were recorded separately; the inset in Fig. 1 shows the spectrum for the sample with $y = 0.07$, recorded at $T = 4.2$ K and $i = 4$ A. The emission band has the maximum at 0.335 eV, a symmetrical Gaussian shape and a FWHM of 20 meV.

Fig. 2 shows a change in the position of the spectral maxima of the EL bands with temperature for four HSs, as well as the corresponding temperature dependences of the bandgap E_g of the active region material. For each HS, the EL spectra were recorded for several (2–3) experimental samples cut from different parts of the wafer, and the results were close. Calculation of the $E_g(T)$ dependence for the $InAs_{1-y}Sb_y$ solid solution was carried out according to the Varshni relation:

$$E_g = E^0 - \alpha\cdot T^2\cdot(T+\beta)^{-1},$$

© Ружевич М.С., Мынбаев К.Д., Баженов Н.Л., Романов В.В., Моисеев К.Д., 2024. Издатель: Санкт-Петербургский политехнический университет Петра Великого.

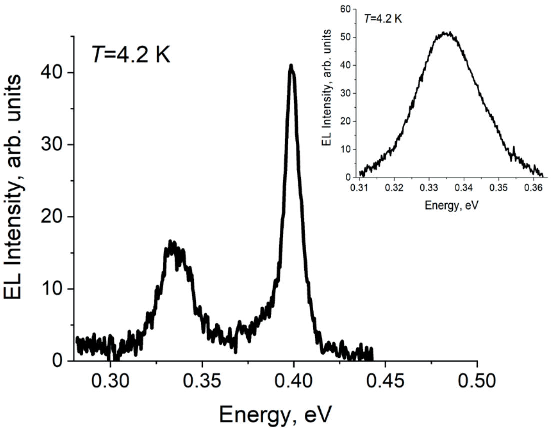

Fig. 1. EL spectrum of the HS with $y = 0.07$ at $T = 4.2$ K.
The inset shows the emission spectrum associated with the active region

Here, the band gap parameter for a solid solution, $E^0(y)$, was calculated at 0 K as

$$E^0(y) = (1-y)E^0_{InAs} + yE^0_{InSb} - y(1-y)C_{InAsSb},$$

where $E^0_{InAs} = 0.417$ eV, $E^0_{InSb} = 0.24$ eV, the bowing parameter $C_{InAsSb} = 0.61$ eV. The parameters α and β were taken as those for matrix material InAs: $\alpha = 2.76 \cdot 10^{-4}$ eV/K and $\beta = 93$ K.

As can be seen in Fig. 2, in the low-temperature region (from 4.2 to ~ 140 K), there is a significant difference between the energies of the spectral maximum of the emission band and the calculated values of E_g of the active region material for all HSs. At 4.2 K, the energy discrepancy δE between the calculated values of E_g and the position of the spectral maximum mounted up to 50 meV. At temperatures above 200 K the energies of the spectral maximum approached the calculated values of E_g, and for all studied samples at the room temperature, the energy of the EL peak was close to E_g of the corresponding $InAs_{1-y}Sb_y$ solid solution. We observed a similar behavior of EL maxima earlier for HSs with $0.14 < y \leq 0.16$ [5]. At the same time, HSs of similar design with $y = 0$–0.09 grown by a different MOVPE technique demonstrated a good agreement between the energy of the spectral maximum and calculated E_g values of the active region material with $\delta E \approx 0$ in the entire temperature range $T = 4.2$–300 K [6].

To interpret the results obtained in this work, the HS band diagrams were analyzed. Figs. 3, *a*, *b* show variants of the band diagram of the HS with $y = 0.09$ without electric bias. The diagram in Fig. 3, *a* was drawn under assumption that the chemical composition of the barrier layer corresponded to the technological parameters specified during its growth, i.e., $x = 0.41$ and $y = 0.19$ for $InAs_{1-x-y}Sb_yP_x$. As can be seen, in this case, an InAsSb/InAsSbP type I heterointerface and a classical heterojunction with asymmetric carrier confinement for electrons and holes at the opposite boundaries of the active region should be formed. However, as has been shown for HSs of various designs and with different InSb contents in the active region, the chemical composition of the InAsSbP quaternary solid solution deposited by MOVPE on a lattice-mismatched narrow-gap layer of the InAsSb ternary solid solution does not correspond to the specified composition near the heterointerface [7]. In particular, for a HS with $y = 0.09$, in the active region for the $InAs_{1-x-y}Sb_yP_x$ solid solution near the interface, interpolation of the data from [7] gives the values $x = 0.375$ and $y = 0.21$. The corresponding band diagram is shown in Fig. 3, *b*. As can be seen, in this case, an InAsSb/InAsSbP heterointerface of type II is formed. Fig. 3, *c* shows the same band diagram at a forward bias of 0.3 V. It can be seen that potential wells for electrons and holes are formed at the heterointerface; under these conditions, there is a high probability of interface recombination of electrons from the well at the side of the active layer with holes in the well at the side of the barrier layer.

In the case under consideration, the energy of the photon emitted as a result of interface recombination at a type II heterointerface depends mainly on the valence band offset ΔE_V. Figure 3, *d* shows results of the calculations of ΔE_V for HSs under consideration; the calculations took into account the established changes in the composition of the InAsSbP quaternary solid solution isomorphous to the narrow-gap ternary InAsSb solid solution. As can be seen, with a

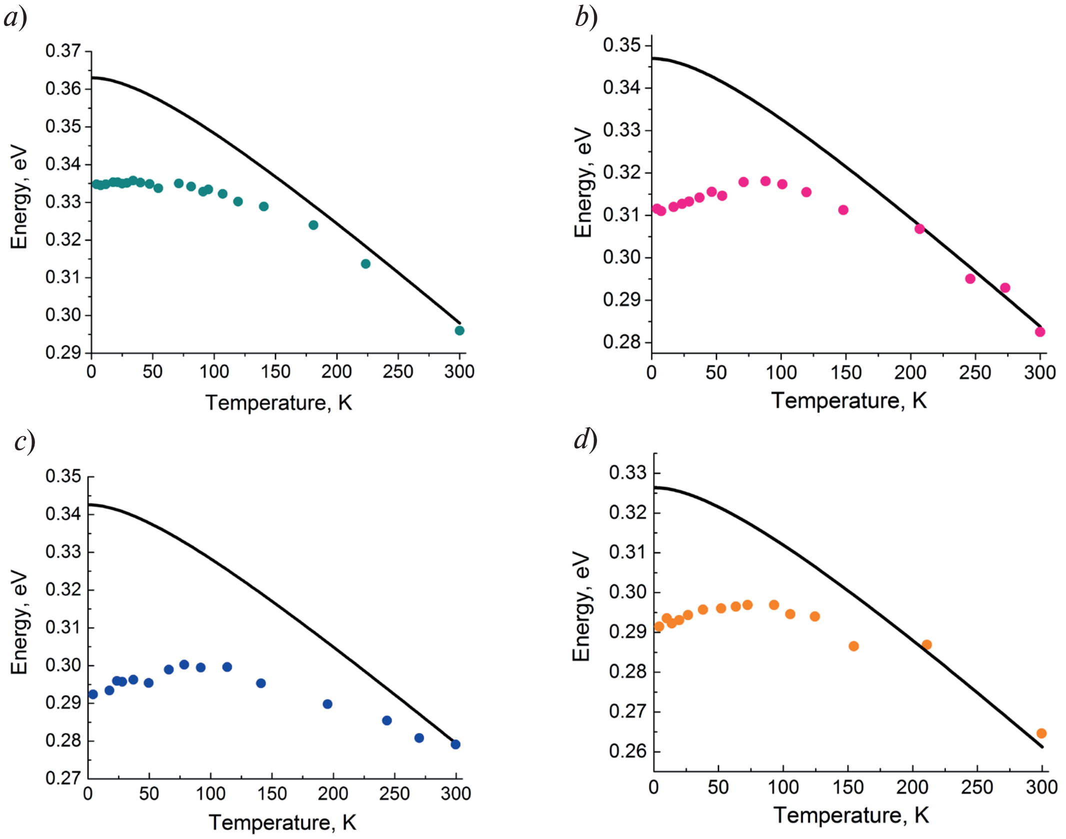

Fig. 2. Calculated temperature dependences of E_g for the active region of the HSs (solid lines) and experimental data of the positions of spectral maxima of EL (symbols): y = 0.07 (*a*); 0.09 (*b*), 0.10 (*c*), and 0.12 (*d*)

change in the composition of the active layer, the ΔE_V changes very little, which is explained by the "tuning" of the InAsSbP composition at the heterointerface in order to compensate for the mismatch of the crystal lattice parameter. The estimated average ΔE_V value 16 meV (shown in Fig. 3, *d* by dashed line) was obtained from calculations according to expressions from [7].

The values of δE obtained from the experiment, however, demonstrated a certain dependence on y in the active layer (Fig. 3, *d*) and were actually greater than the calculated values of ΔE_V. However, as was demonstrated in [8], structural defects in InAs-based compounds can generate deep acceptor states on the surface of the semiconductor. With increasing the InSb content in the solid solution, generation of surface states at the InAsSb/InAsSbP heterointerface should be expected as a result of the growth of internal strain in the epitaxial layer of the active region. Thus, we can suggest that at low temperatures, EL in the HSs was related to interface recombination near the type II InAsSb/InAsSbP heterointerface with the participation of the interface states. With temperature increasing, band-to-band transitions begin to dominate. This explains the temperature dependence of δE shown in Fig. 2. The extremum appearing on $\delta E(y)$ dependence at y = 0.10 in Fig. 3, *d* is caused by the relaxation of an epitaxial layer as a result of the generation of a grid of dislocations, as at this point, the lattice mismatch becomes greater than 1%.

We explain the difference between the data obtained in this work and the data in [6] by the difference in the types of InAsSb/InAsSbP heterointerfaces. Barrier layers with significantly lower Sb and P contents were used in [6]. Band diagrams calculated for HSs used in [6] were of type I even when calculations were performed with consideration for possible variations in the P and Sb content in the barrier layer due to the changes in its chemical composition as a result of lattice mismatch. Thus, in the HSs studied in [6], the EL spectra in the entire temperature range T = 4.2–300 K were related to interband transitions in the active region. The switching of recombination mechanisms with changes in the temperature, as was observed in this work, makes it possible to suppress the temperature dependence of the HS emission wavelength, which is very important for the operation of mid-IR radiation sources [1,2].

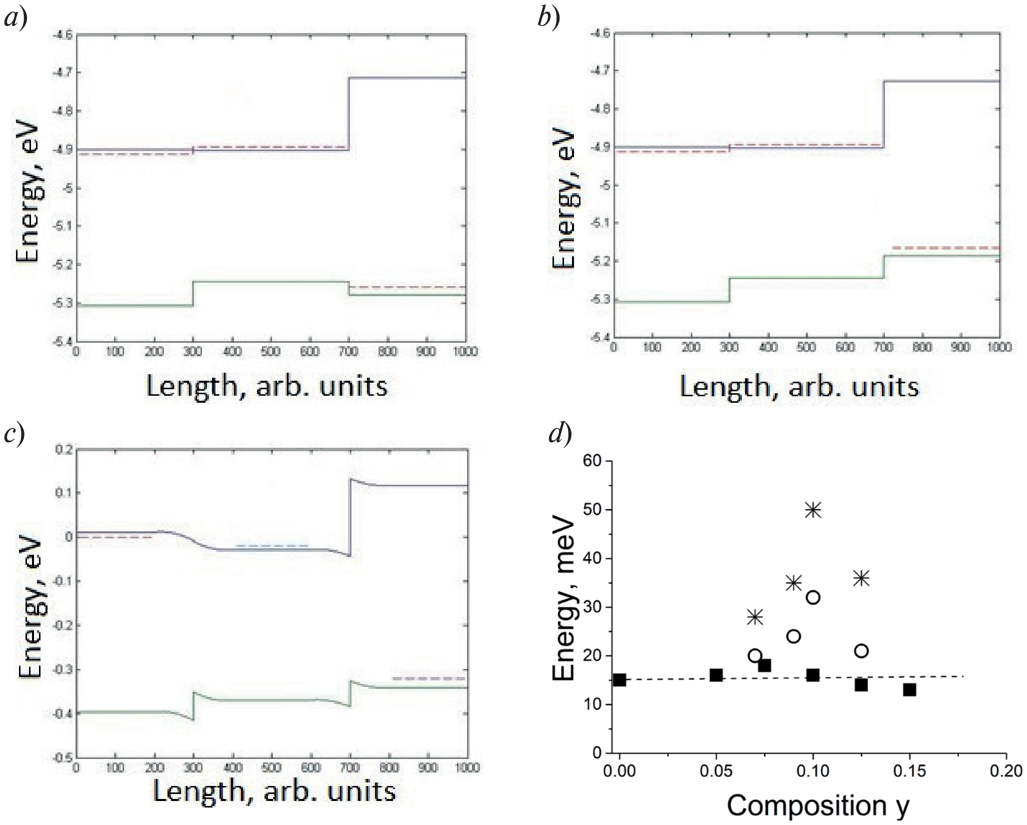

Fig. 3. Band diagram of *n*-InAs/InAs$_{1-y}$Sb$_y$/*p*-InAsSbP HS with $y = 0.09$ for calculated (*a*) and actual (*b*) compositions of the barrier layer without bias and at a forward bias of 0.3 V (*c*). Fig. 3, *d* shows δE values observed at $T = 4.2$ K (stars) and $T = 77$ K (circles) and the results of calculating ΔE_V at the heterointerface for various y taking into account changes in the composition of the InAsSbP solid solution (squares)

Conclusion

The paper presents the results of the study of electroluminescence of narrow-gap *n*-InAs/InAs$_{1-y}$Sb$_y$/*p*-InAsSbP heterostructures with $y = 0.07$–0.12 in the temperature range 4.2–300 K. It is shown that from 4.2 to ~ 140 K, interface radiative recombination at the InAsSb/InAsSbP heterointerface dominates. This is due to the formation of a type II heterointerface, caused by the change in the chemical composition of the InAsSbP quaternary solid solution that is deposited on a layer of a lattice-mismatched InAsSb ternary solid solution, which leads to a difference between the specified and actual composition of the InAsSbP barrier layer. An increase in the temperature above 140 K leads to switching of the recombination channel to the interband one in the active region. The resulting weak temperature dependence of the emission wavelength of the heterostructures can be used in practical applications.

REFERENCES

1. **Ting D., Soibel A., Khoshakhlagh A., Keo S., Rafol B., Fisher A., Pepper B., Luong E., Hill C., Guhapala S.,** Advances in III-V semiconductor infrared absorbers and detectors, Inf. Phys. Technol. 97 (2019) 210–216.

2. **Jung D., Bank S., Lee M. L., Wasserman D.,** Next-generation mid-infrared sources, J. Opt. 19 (2017) 123001–123031.

3. **Smith S.D., Crowder J.G., Hardaway H.R.,** Recent developments in the applications of mid-infrared lasers, LEDs, and other solid state sources to gas detection, Proceed. SPIE 4651 (1) (2002) 157–172.

4. **Romanov V. V., Ivanov E. V., Moiseev K. D.,** $InAs_{1-y}Sb_y$/InAsSbP Narrow-gap heterostructures ($y = 0.09$–0.16) grown by metalorganic vapor phase epitaxy for the spectral range of 4–6 μm, Phys. Sol. State 61 (10) (2019) 1699–1706.

5. **Semakova A.A., Romanov V.V., Bazhenov N.L., Mynbaev K.D., Moiseev K.D.,** Suppressing the temperature dependence of the wavelength in heterostructures with a staggered type-II InAsSb/InAsSbP heterojunction, Semiconductors 55 (3) (2021) 354–358.

6. **Mynbaev K.D., Bazhenov N.L., Semakova A.A., Chernyaev A.V., Kizhaev S.S., Stoyanov N.D., Bougrov V.E., Lipsanen H., Salikhov Kh.M.,** Spontaneous and stimulated emission in InAsSb-based LED heterostructures, Infr. Phys. Technol. 85 (2017) 246–250.

7. **Romanov V.V., Moiseev K.D.,** Peculiarities of the electronic structure of epitaxial InAsSbP layer deposited on the surface of $InAs_{1-y}Sb_y$ solid solution, Phys. Solid State 65 (10) (2023) 1707–1714.

8. **Smołka T., Motyka M., Romanov V.V., Moiseev K.D.,** Photoluminescence spectroscopy of the InAsSb-based *p-i-n* heterostructure, Materials 15 (2022) 1419 (11 p.).

THE AUTHORS

RUZHEVICH Maxim S.
max.ruzhevich@niuitmo.ru
ORCID: 0000-0002-4513-6345

MYNBAEV Karim D.
mynkad@mail.ioffe.ru
ORCID: 0000-0002-9853-8874

BAZHENOV Nikolay L.
bazhnil.ivom@mail.ioffe.ru
ORCID: 0000-0002-3019-2280

ROMANOV Vyacheslav V.
romanovvv@mail.ioffe.ru
ORCID: 0000-0002-9989-3843

MOISEEV Konstantin D.
mkd@iropt2.ioffe.ru
ORCID: 0000-0002-6306-0129

Received 13.01.2024. Approved after reviewing 26.01.2024. Accepted 26.01.2024.

St. Petersburg Polytechnic University Journal. Physics and Mathematics. 2024 Vol. 17. No. 1.1
Научно-технические ведомости СПбГПУ. Физико-математические науки. 17 (1.1) 2024

Conference paper
UDC 538.958
DOI: https://doi.org/10.18721/JPM.171.113

Polarized reflectance spectroscopy of aluminum nanoantennas on the surface of emitting GeSiSn/Si heterostructures

S.A. Khakhulin [1] ✉, D.D. Firsov [1], O.S. Komkov [1], V.A. Timofeev [2], I.V. Skvortsov [2], V.I. Mashanov [2], D.E. Utkin [3]

[1] Saint Petersburg Electrotechnical University "LETI", St. Petersburg, Russia;
[2] Rzhanov Institute of Semiconductor Physics, Novosibirsk, Russia;
[3] Novosibirsk State University, Novosibirsk, Russia
✉ khsmn@ya.ru

Abstract. The study presents an investigation of the optical properties of rectangular-shaped aluminum nanoantenna arrays formed on the surface of an emitting GeSiSn/Si heterostructure with multiple quantum wells. The positions of the localized surface plasmon resonance modes excited along the long (L) and short (S) sides of the examined nanoantennas are determined utilizing the technique of Fourier-transform infrared reflectance anisotropy spectroscopy. Experimental results demonstrate that both L- and S-modes are located in the near-infrared range, and as the lateral dimensions of the nanoantennas increase, the modes' positions shift towards lower energies with an increase in the intensity of the resonance. The S-mode appears in the spectra as an overlay on the more pronounced L-mode with an intensity an order of magnitude lower. The geometry of the nanoantennas arrays with the resonance position near the photoluminescence peak of $Ge_{0.84}Si_{0.076}Sn_{0.084}/Si$ heterostructures ($E \approx 0.65$ eV) is characterized.

Keywords: polarized reflectance, reflectance anisotropy spectroscopy, RAS, aluminum nanoantennas, localized surface plasmon resonance, LSPR

Funding: The study was funded by the Russian Science Foundation grant No. 20-79-10092.

Citation: Khakhulin S.A., Firsov D.D., Komkov O.S., Timofeev V.A., Skvortsov I.V., Mashanov V.I., Utkin D.E., Polarized reflectance spectroscopy of aluminum nanoantennas on the surface of emitting GeSiSn/Si heterostructures, St. Petersburg State Polytechnical University Journal. Physics and Mathematics. 17 (1.1) (2024) 83–88. DOI: https://doi.org/10.18721/JPM.171.113

This is an open access article under the CC BY-NC 4.0 license (https://creativecommons.org/licenses/by-nc/4.0/)

Материалы конференции
УДК 538.958
DOI: https://doi.org/10.18721/JPM.171.113

Поляризационная спектроскопия отражения алюминиевых наноантенн на поверхности излучающих гетероструктур GeSiSn/Si

С.А. Хахулин [1] ✉, Д.Д. Фирсов [1], О.С. Комков [1], В.А. Тимофеев [2], И.В. Скворцов [2], В.И. Машанов [2], Д.Е. Уткин [3]

[1] Санкт-Петербургский государственный электротехнический университет «ЛЭТИ», Санкт-Петербург, Россия;
[2] Институт физики полупроводников им. А.В. Ржанова, Новосибирск, Россия;
[3] Новосибирский государственный университет, Новосибирск, Россия
✉ khsmn@ya.ru

© Khakhulin S.A., Firsov D.D., Komkov O.S., Timofeev V.A., Skvortsov I.V., Mashanov V.I., Utkin D.E., 2024. Published by Peter the Great St. Petersburg Polytechnic University.

Аннотация. В работе представлены результаты исследования оптических свойств массивов алюминиевых наноантенн прямоугольной формы, сформированных на поверхности гетероструктуры GeSiSn/Si с множественными квантовыми ямами. По спектрам ИК фурье-спектроскопии анизотропного отражения определены положения мод локализованного поверхностного плазмонного резонанса, возникающего вдоль длинной (*L*) и короткой (*S*) сторон рассматриваемых наноантенн. Экспериментально показано, что обе моды расположены в ближнем ИК-диапазоне и при увеличении латеральных размеров наноантенн смещаются в сторону меньших энергий с увеличением интенсивности резонанса. *S*-мода проявляется в спектрах в виде наложения на более интенсивную *L*-моду и имеет интенсивность на порядок меньше. Среди исследованных образцов определена геометрия массивов наноантенн с резонансом вблизи энергии пика фотолюминесценции гетероструктур $Ge_{0.84}Si_{0.076}Sn_{0.084}/Si$ $E \approx 0.65$ эВ.

Ключевые слова: поляризационная спектроскопия отражения, спектроскопия анизотропного отражения, алюминиевые наноантенны, локализованный поверхностный плазмонный резонанс

Финансирование: Работа выполнена при поддержке Российского научного фонда (грант № 20-79-10092).

Ссылка при цитировании: Хахулин С.А., Фирсов Д.Д., Комков О.С., Тимофеев В.А., Скворцов И.В., Машанов В.И., Уткин Д.Е. Поляризационная спектроскопия отражения алюминиевых наноантенн на поверхности излучающих гетероструктур GeSiSn/Si // Научно-технические ведомости СПбГПУ. Физико-математические науки. 2024. Т. 17. № 1.1. С. 83–88. DOI: https://doi.org/10.18721/ JPM.171.113

Статья открытого доступа, распространяемая по лицензии CC BY-NC 4.0 (https://creativecommons.org/licenses/by-nc/4.0/)

Introduction

The integration of photonic devices into silicon electronics is possible through the development of light detectors and emitters based on GeSiSn alloy nanoheterostructures. Such semiconductor structures achieve operating range in the near and mid-infrared (IR) spectrum down to 8 microns. This characteristic renders them highly promising for use in fiber-optic systems, photonic integrated circuits and sensors made on a single silicon chip [1]. The sensitivity and emission properties of these heterostructures can be controlled and enhanced through the creation of hybrid systems involving plasmonic metal nanoparticles on the surface of GeSiSn/Si heterostructures.

The interaction between electromagnetic radiation and metal nanoparticles induces the oscillation of free electrons within the metal, resulting in localized surface plasmon resonance (LSPR) [2]. The outcome of this resonance is a pronounced amplification of the electric field in the vicinity of the surface by several hundred times. The confinement of electromagnetic radiation energy within a nanovolume, owing to the LSPR phenomenon, finds broad applications predominantly associated with the enhancement of luminescence in various emissive structures [3].

The frequency and intensity of LSPR depend on the size, shape and dielectric environment of metal nanoparticles [2]. In practice, this renders them a universally applicable physical system for manipulating emissive structures across a broad optical spectrum. Typically, silver or gold is employed as the material for plasmonic nanoparticle production, owing to their strong interaction with light and lower losses [4]. As an alternative, aluminum can be used in a wider optical range with plasmon resonance in nanoparticles varied from ultraviolet to mid-infrared with limitations in a narrow part of the optical spectrum around 800 nm caused by interband transitions [5].

To investigate the formed metal nanoparticles, one can employ polarized reflectance spectroscopy, specifically utilizing its variant, the Fourier-transform infrared (FTIR) reflectance anisotropy (RA) spectroscopy method [6]. This optical technique has demonstrated its efficiency as a robust tool for examining plasmon resonances in metal nanoparticles [7].

Thus, the purpose of this work is to study the optical properties of aluminum nanoantenna arrays formed on the surface of an emitting GeSiSn/Si nanoheterostructure using methods of polarized reflectance spectroscopy.

© Хахулин С.А., Фирсов Д.Д., Комков О.С., Тимофеев В.А., Скворцов И.В., Машанов В.И., Уткин Д.Е., 2024.
Издатель: Санкт-Петербургский политехнический университет Петра Великого.

Materials and Methods

Arrays of aluminum nanoantennas were formed through electron nanolithography on the surface of a heterostructure with multiple $Ge_{0.84}Si_{0.076}Sn_{0.084}/Si$ quantum wells, where the well and barrier widths are 1 nm and 7 nm, respectively. The growth of the heterostructure was carried out using molecular beam epitaxy [1]. The nanoantennas were deposited on an area of 500×500 μm^2.

Figure 1 illustrates the geometry of the arrays structure, exemplified by an image of array #3 captured through scanning electron microscopy (SEM). The designations of the lateral dimensions of the nanoantennas, which distinguish each array structure from one another, are provided in the figure. These dimensions are detailed in Table.

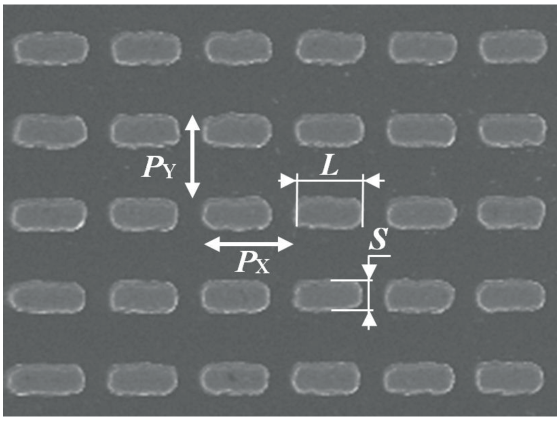

Fig. 1. Image of the nanoantenna structure array #3 obtained by scanning electron microscopy. The nominal height H of all nanoantennas is 50 nm

Table

Parameters of the studied aluminum nanoantennas arrays formed on the surface of the $Ge_{0.84}Si_{0.076}Sn_{0.084}/Si$ radiating heterostructure with multiple quantum wells

sample	L, nm	S, nm	H, nm	P_x, nm	P_y, nm
#1	200	140	50	485	435
#2	265	147		478	435
#3	360	157		485	435

Polarized reflectance spectra were measured using a Vertex 80 Fourier-transform infrared (FTIR) spectrometer with radiation linearly polarized along the long L and short S sides of the nanoantennas. The modulation spectra of reflectance anisotropy were measured using an original setup, implemented on the basis of the same FTIR spectrometer and described in detail in [6]. The essence of the latter method is to modulate the direction of linear polarization of the probe radiation along two perpendicular directions x and y lying in the plane of the samples surface. The value being measured synchronously corresponds to the normalized difference in reflectance coefficients:

$$\frac{\Delta R}{R} = 2\frac{R_x - R_y}{R_x + R_y},$$

where R_x and R_y represent the reflectance coefficients when the plane of the incident radiation linear polarization is aligned along the corresponding direction in the surface plane. In this study, the x and y directions coincide with the long (L) and short (S) sides of the aluminum nanoantennas, respectively (see Fig. 1).

Results and Discussion

From each of the presented nanoantenna arrays, an ordinary reflectance spectrum R was obtained with probe radiation linearly polarized along the L and S sides. The reference reflectance spectrum was measured from a gold-coated mirror, exhibiting a high reflectance range from 2.3 eV to mid-IR energies. A typical reflectance spectrum is shown in Fig. 2 (top) utilizing array #3 as an example. Analyzing ordinary reflectance spectra proves challenging due to the difficulty in identification of areas where the differences in reflectance spectra with linear polarization direction **E** along *L* (**E**//*L*) and *S* (**E**//*S*) are marginal against the general background of the total reflected radiation. In such cases, the modulation method of reflectance anisotropy spectroscopy is advantageous, wherein only the polarization-dependent component of the reflectance spectra is detected. Fig. 2 (bottom) illustrates the resulting reflectance anisotropy spectrum from array #3.

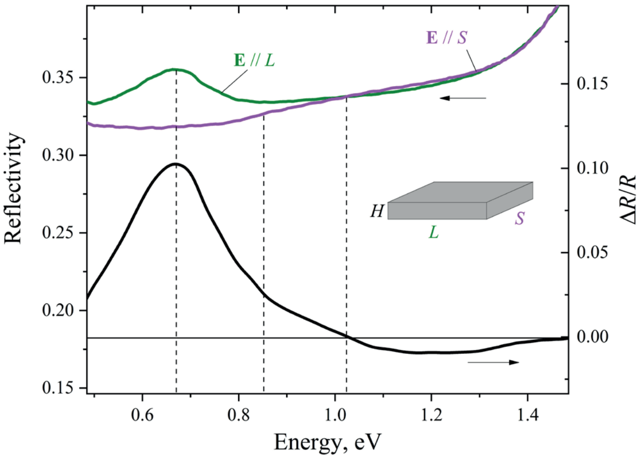

Fig. 2. Polarized reflectance spectrum (top) of nanoantenna array #3 with linear polarization of the probe radiation parallel to the *L* side (green curve) and *S* side (purple curve). Bottom – modulation reflectance anisotropy spectrum of the same structure

Upon comparison of the RA spectra with ordinary reflectance spectra, it becomes evident that, in addition to the prominent peak associated with plasmon resonance along *L* side, a distinct resonance also emerges in the structure along the *S* side. This resonance spans a broad energy range of 0.82–1.4 eV and differs in intensity from the *L*-mode by almost an order of magnitude. The energy range where the S mode appears partially overlaps with the similar range of the *L*-mode, causing the resonance along the *S* side to manifest as an overlap with the intense peak excited along *L* in the reflectance anisotropy spectra. The inflection in the RA spectrum corresponds to the initiation of *S*-modes in its low-energy region. It is worth noting that in the case of the nanoantenna array #3, the resonance excited along the *S* side is relatively discernible in the polarized reflectance spectra. This distinction arises because structure #3 comprises relatively large nanoparticles among the nanoantenna arrays presented in the study and the resonance intensity is proportionate to the volume of such particles [5].

Hence, to ascertain the spectral position of the resonant modes across all nanoantenna arrays, reflectance anisotropy spectra were measured. The resultant curves are depicted in Fig. 3. As the lateral dimensions of nanoantennas increase, the resonant *L*- and *S*-modes are predictably shifted towards lower energies. This shift is anticipated as the effective cross section of the metal plane, wherein plasmonic oscillations occur, expands [3, 5]. It is important to note that in the case of arrays #2 and #1 the *S*-mode in ordinary polarized reflectance spectra becomes visually indistinguishable against the background of the entire spectrum. However, in the reflectance anisotropy spectra, the *S*-mode manifests as an overlay on the intense *L*-mode, evident from the inflections of the corresponding curves in the high-energy regions of the whole RA spectrum. Additionally, it is appropriate to mention that the RA spectra of the GeSiSn/Si heterostructure surface without plasmonic nanoantennas exhibit a zero signal, indicating optical isotropy in the specified energy range.

The photoluminescence spectrum of a heterostructure with multiple $Ge_{0.84}Si_{0.076}Sn_{0.084}$/Si quantum wells, on the surface of which arrays of nanoantennas are formed, exhibits a signal peak near 0.65 eV. Consequently, among the presented arrays, the most pronounced plasmonic enhancement of the radiation from such a heterostructure is expected through the interaction of

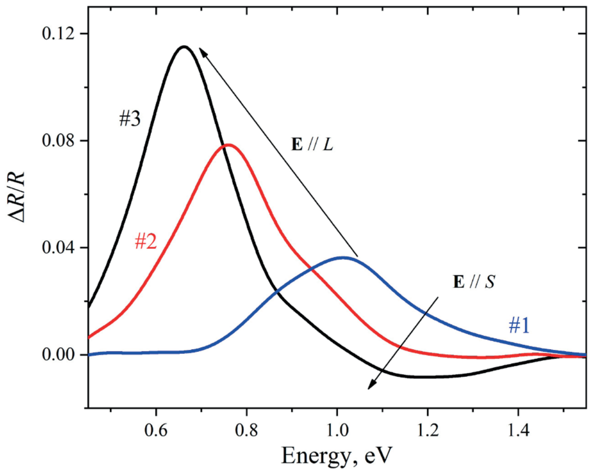

Fig.3. Reflectance anisotropy spectra for each of the nanoantenna arrays. The arrows indicate the dynamics of the resonance energy position with increasing lateral dimensions of the nanoantennas

$Ge_{0.84}Si_{0.076}Sn_{0.084}/Si$ with array #3. This expectation arises from the fact that array #3 showcases a maximum of localized surface plasmon resonance at 0.66 eV, while the resonance of structure #1 at 0.65 eV holds a null value.

Conclusion

Thus, we have studied the optical properties of arrays of aluminum nanoantennas formed on a GeSiSn/Si emitting heterostructure using polarized reflectance spectroscopy methods. To control the emission properties of GeSiSn/Si heterostructures, an array of nanoantennas with geometry #3 can be used, since it has an intense resonance at an energy of 0.66 eV, which is located near the photoluminescence peak of the heterostructure ≈ 0.65 eV.

The ability to create nanoparticles with a localized surface plasmon resonance in the near-IR range makes aluminum a suitable material for creating interacting plasmonic and emissive structures in this range.

Acknowledgments

The authors thank M.V. Zakharchenko for useful discussions. The authors also thank the Shared Equipment Centers CKP “NANOSTRUCTURY” of the Rzhanov Institute of Semiconductor Physics SB RAS and CKP “VTAN” (ATRC) of the NSU Physics Department for the technical and instrumental support.

REFERENCES

1. **Timofeev V.A., Mashanov V.I., Nikiforov A.I., Skvortsov I.V., Gayduk A.E., Bloshkin A.A., Kirienko V.V., Utkin D.E., Kolyada D.V., Firsov D.D., Komkov O.S.,** Remarkable enhancement of photoluminescence and photoresponse due to photonic crystal structures based on GeSiSn/Si multiple quantum wells. Materials Today Physics. 33 (2023) 101052.

2. **Hutter E., Fendler J.H.,** Exploitation of localized surface plasmon resonance, Advanced materials. 16 (19) (2004) 1685–1706.

3. **Giannini V., Fernбndez-Domнnguez A.I., Heck S.C., Maier S.A.,** Plasmonic nanoantennas: fundamentals and their use in controlling the radiative properties of nanoemitters. Chemical reviews. 111 (6) (2011) 3888–3912.

4. **Ekinci Y., Solak H.H., Lцffler J.F.,** Plasmon resonances of aluminum nanoparticles and nanorods. Journal of Applied Physics. 104 (8) (2008) 083107.

5. **Lecarme O., Sun Q., Ueno K., Misawa H.,** Robust and versatile light absorption at near-infrared wavelengths by plasmonic aluminum nanorods, ACS Photonics. 1 (2014) 538–546.

6. **Firsov D.D., Khakhulin S.A., Komkov O.S.,** Fourier-Transform Infrared Reflection Anisotropy Spectroscopy of Semiconductor Crystals and Structures: Development and Application in the Mid-Infrared, Applied Spectroscopy. 77 (5) (2023) 470–481.

7. **Berkovits V.L., Kosobukin V.A., Ulin V.P., Alekseev P.A., Soldatenkov F.Yu., Nashchekin A.V., Khakhulin S.A., Komkov O.S.,** Finding the wedge-shaped Au nanoclusters at the surface of GaAs and investigating them with the polarization spectroscopy of plasmons. Semiconductors. 57 (6) (2023) 478–483.

THE AUTHORS

KHAKHULIN Semyon A.
khsmn@ya.ru
ORCID: 0000-0002-1780-2013

FIRSOV Dmitrii D.
d.d.firsov@gmail.com
ORCID: 0000-0001-7608-9580

KOMKOV Oleg S.
okomkov@yahoo.com
ORCID: 0000-0002-8999-1175

TIMOFEEV Vyacheslav A.
Vyacheslav.t@isp.nsc.ru
ORCID: 0000-0003-4093-7802

SKVORTSOV Ilya V.
i.skvortsov@isp.nsc.ru
ORCID: 0000-0002-2153-1615

MASHANOV Vladimir I.
mash@isp.nsc.ru
ORCID: 0000-0003-4420-6695

UTKIN Dmitry E.
utkinde@isp.nsc.ru
ORCID: 0000-0001-9510-5427

Received 13.12.2023. Approved after reviewing 31.01.2024. Accepted 05.02.2024.

St. Petersburg Polytechnic University Journal. Physics and Mathematics. 2024 Vol. 17. No. 1.1
Научно-технические ведомости СПбГПУ. Физико-математические науки. 17 (1.1) 2024

Conference paper
UDC 538.9
DOI: https://doi.org/10.18721/JPM.171.114

Gurzhi effect in point contacts in GaAs

D.I. Sarypov [1, 2] ✉, D.A. Pokhabov [1, 2], A.G. Pogosov [1, 2],
D.A. Egorov [1, 2], E.Yu. Zhdanov [1, 2], A.K. Bakarov [1, 2]

[1] Rzhanov Institute of Semiconductor Physics, SB RAS, Novosibirsk, Russia;
[2] Novosibirsk State University, Novosibirsk, Russia
✉ d.sarypov@g.nsu.ru

Abstract. Hydrodynamic electron transport through point contacts of different widths in two-dimensional electron gas in GaAs/AlGaAs heterostructure is studied. Effect Gurzhi, i.e., minimum in the temperature dependence of the point contact resistance, corresponding to the conductance exceeding the ballistic limit, is experimentally observed. The minimum is shown to be observed in case when electron-electron scattering length is comparable with the point contact width. Under this condition, electrons act as viscous fluid, that leads to the resistance reduction. The experimental data including the width dependence are consistent with the theoretical prediction of the viscous contribution to the point contact conductance.

Keywords: electron-electron scattering, electron hydrodynamics, viscous electron fluid

Funding: The study was funded by the Russian Science Foundation (project 22-12-00343).

Citation: Sarypov D.I., Pokhabov D.A., Pogosov A.G., Egorov D.A., Zhdanov E.Yu., Bakarov A.K., Gurzhi effect in point contacts in GaAs, St. Petersburg State Polytechnical University Journal. Physics and Mathematics. 17 (1.1) (2024) 89–94. DOI: https://doi.org/10.18721/JPM.171.114

This is an open access article under the CC BY-NC 4.0 license (https://creativecommons.org/licenses/by-nc/4.0/)

Материалы конференции
УДК 538.9
DOI: https://doi.org/10.18721/JPM.171.114

Эффект Гуржи в точечных контактах в арсениде галлия

Д.И. Сарыпов [1, 2] ✉, Д.А. Похабов [1, 2], А.Г. Погосов [1, 2],
Д.А. Егоров [1, 2], Е.Ю. Жданов [1, 2], А.К. Бакаров [1, 2]

[1] Институт физики полупроводников им. А.В. Ржанова СО РАН, Новосибирск, Россия;
[2] Новосибирский государственный университет, Новосибирск, Россия
✉ d.sarypov@g.nsu.ru

Аннотация. Исследован гидродинамический электронный транспорт через точечные контакты различной ширины в двумерном электронном газе в гетероструктуре GaAs/AlGaAs. В температурной зависимости сопротивления точечного контакта наблюдается минимум, соответствующий кондактансу, превышающему баллистический предел. Экспериментальные данные согласуются с теоретическим предсказанием вязкостного вклада в кондактанс точечного сужения.

Ключевые слова: электрон-электронное рассеяние, гидродинамика электронов, вязкая электронная жидкость

Финансирование: Работа выполнена при финансовой поддержке РНФ (проект № 22-12-00343).

© Sarypov D.I., Pokhabov D.A., Pogosov A.G., Egorov D.A., Zhdanov E.Yu., Bakarov A.K., 2024. Published by Peter the Great St. Petersburg Polytechnic University.

Ссылка при цитировании: Сарыпов Д.И., Похабов Д.А., Погосов А.Г., Егоров Д.А., Жданов Е.Ю., Бакаров А.К. Эффект Гуржи в точечных контактах в арсениде галлия // Научно-технические ведомости СПбГПУ. Физико-математические науки. 2024. Т. 17. № 1.1. С. 89–94. DOI: https://doi.org/10.18721/ JPM.171.114

Статья открытого доступа, распространяемая по лицензии CC BY-NC 4.0 (https://creativecommons.org/licenses/by-nc/4.0/)

Introduction

Electron-electron (*e–e*) interaction is shown to have significant impact on mesoscopic electron transport in case when *e–e* scattering length lee is comparable with characteristic size of the system w [1–12]. At the same time, the effects associated with e–e interaction, because of their many-body origin, are difficult to describe. Hydrodynamic approach can simplify the *e–e* interaction description by considering electrons as viscous fluid [13–15]. Hydrodynamic electron transport is overviewed in details in [16,17].

Due to total momentum conservation during *e–e* collisions, specific conditions are required for the hydrodynamic effects to be observed. Gurzhi showed [18] that, in case of ballistic conductors with long momentum relaxing length $l >> w$, when $l_{ee} \lesssim w$ correlations in the electrons motion act as a lubricant and prevent the momentum loss on the boundary roughness – the main momentum dissipation place. This effect leads to the resistance reduction, which has been experimentally proven in graphene [19] and GaAs [20].

In this work we present the experimental study of the hydrodynamic electron transport in the point contacts (PCs) based on the GaAs/AlGaAs heterostructure with an emphasis on the width dependence. We studied the temperature dependence of the resistance of 7 PC of different width. In the experiment we observe the PC resistance reduction below the ballistic limit with increasing temperature up to a certain value of about 20 K. For quantitative description of this effect, we employ the recent theory [21] predicting that the PC conductance enhancement due to the lubricant effect $\Delta G = G_{\text{vis}}$ is defined by the formula:

$$G_{\text{vis}} = \frac{\pi}{32}\frac{n^2e^2w^2}{\eta} = \frac{\pi}{8}\frac{e^2}{h}\left(k_F w\right)\frac{w}{l_{ee}}, \tag{1}$$

where $n = k_F^2/2\pi$ is the electrons density, k_F is Fermi quasiwavevector, e, h are the elementary charge and Planck’s constant, respectively and the electron liquid viscosity expressed as $\eta = hk_F n l_{ee} / 8\pi$ [21]. The result of the measurements confirms this prediction.

Materials and Methods

Experimental samples are created from GaAs/AlGaAs heterostructure grown by molecular beam epitaxy on a GaAs substrate (Fig. 1, *a*). Doping the heterostructure with Si δ-layers allow electrons to fill the quantum well at the heterointerface and form two-dimensional electron gas (2DEG). The mobility and concentration of electrons at $T = 4.2$ K are $\mu = 0.8 \cdot 10^6$ cm²/(V·s) and $n = 2 \cdot 10^{11}$ cm^{-2}, respectively. Momentum relaxing length at this temperature is $l = 5.9$ µm. The quality of 2DEG in this structure is also confirmed by the observation of the quantum Hall effect [24].

Seven PCs of different lithographic width wlith, changing from 0.7 to 1.3 µm with the step of 0.1 µm, are created using e-beam lithography. The effective PC width $w = w_{\text{lith}} - w_0$, with the depletion layer thickness w_0 considered, is lower than wlith. We defined w_0 for all PCs from the resistance measurements at low temperature and relations (2–3) in the “Discussion” section. It was found out, that w_0 is universal for all PCs and equal 0.4 µm. Hereby, the PC effective width $w = w_{\text{lith}} - w_0$ varies from 0.3 to 0.9 µm. PCs are located on the Hall bar in series (Fig. 1, *b*). All PCs have a length of 0.6 µm. Both width and length of PCs are smaller than l, so all PCs can be considered ballistic.

Resistance measurements were performed in the cryostat in the temperature range from 4 to 65 K by means of lock-in technique at frequency of 7 Hz and the excitation current amplitude of 100 nA (Fig. 1, *b*).

© Сарыпов Д.И., Похабов Д.А., Погосов А.Г., Егоров Д.А., Жданов Е.Ю., Бакаров А.К., 2024. Издатель: Санкт-Петербургский политехнический университет Петра Великого.

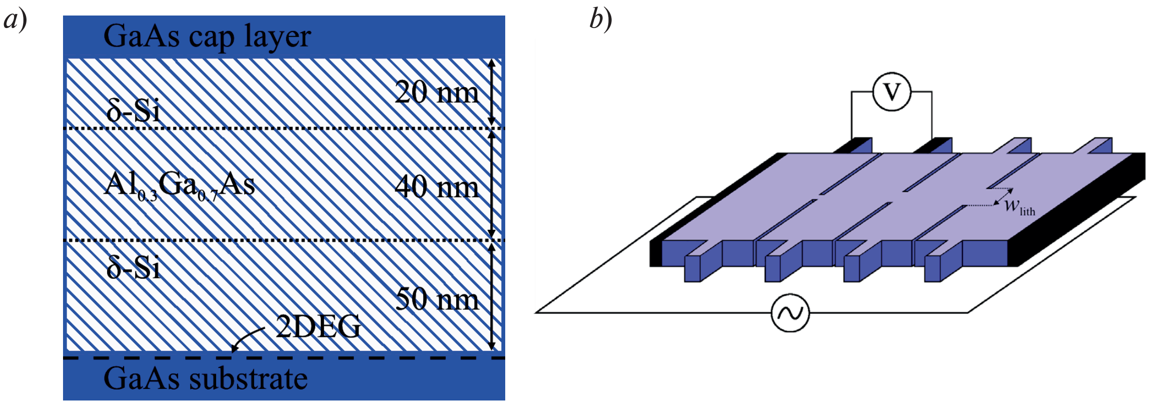

Fig. 1. Schematic images of heterostructure with 2DEG doped with Si δ-layers (*a*) and experimental sample with point contacts (*b*). Point contact lithographic width wlith varies from 0.7 to 1.3 μm

Results

Fig. 2, *a* shows the temperature dependence of the PC resistance. It is clearly seen, that, for all PCs, the resistance first falls at temperatures $\lesssim 20$ K and then monotonically increases, demonstrating the minimum. We attribute the observed resistance reduction to Gurzhi effect [18]. The minimal resistance is lower than the low-temperature ballistic PC resistance due to the momentum loss suppression at the PC boundary, induced by the lubricant effect [21]. This effect is expected under the condition $l_{ee} \lesssim w << l$ [18]. As will be shown below, this condition is fulfilled for studied PCs in the resistance minimum.

Dotted line in Fig. 2, *a* shows that the resistance minimum position depends on the PC width *w*. The minimum shifts to the higher temperatures for smaller *w*. This trend is shown in details on the dependence of the resistance minimum position $T_{\min}$ on the w on a quadratic scale (Fig. 2, *b*).

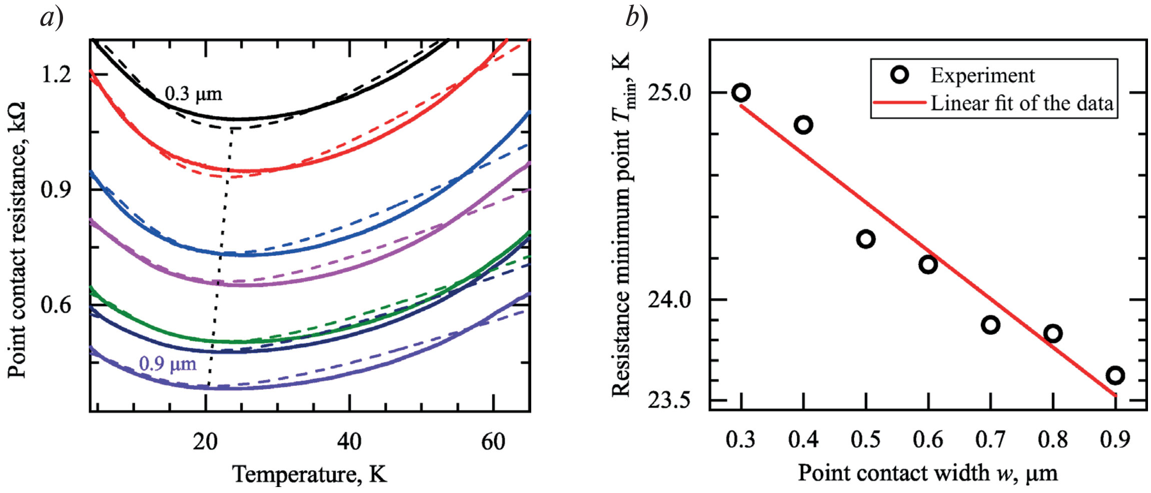

Fig. 2. Temperature dependence of PC resistance of different width *w* (*a*). Solid lines show experimental data and dashed lines show approximation by model (4). Dotted line shows that resistance minimum shifts to lower temperature as *w* increases. Resistance minimum point Tmin in quadratic scale as function of *w* (*b*). Experimental data are shown by circles. Linear approximation is shown by line

Discussion

A solid line in Fig. 2, *b* points to the linear relation between $T^2_{\min}$ and *w* that can be explained by the temperature dependence of l_{ee}. The minimal resistance is achieved when the *e*–*e* scattering rate is comparable with the rate of the momentum relaxation scattering [18]. In our case it means that $l_{ee} \sim w$. Since $l_{ee} \infty T^{-2}$ [22, 23] we have the dependence $w \infty T^{-2}_{\min}$.

The resistance measurements $R(T)$ accounting viscous contribution Gvis can be presented as:

$$R(T) = R_{2\text{DEG}}(T) + \left(G_{\text{ball}} + G_{\text{vis}}\right)^{-1}, \tag{2}$$

where the first term $R_{2\text{DEG}}$ is the resistance of the macrocsopic 2DEG regions adjacent to the constrictions, and the second is the PC resistance including viscous G_{vis} and the ballistic G_{ball} PC conductance at zero temperature. The additive form of G_{ball} and G_{vis} in (2) is applicable for the entire temperature range studied [21]. At low temperature, when electron transport is ballistic, the PC conductance is defined by the formula:

$$G_{\text{ball}} = \frac{2e^2}{h}\frac{k_F(w_{\text{lith}} - w_0)}{\pi} \equiv \frac{2e^2}{h}\frac{k_F w}{\pi}. \tag{3}$$

To describe the viscous contribution to the PC conductance, the formula (1) can be rewritten with fitting parameter T_0:

$$G_{\text{vis}} = \frac{2e^2}{h}\left(k_{\text{F}} w\right)^2 \left(\frac{T}{T_0}\right)^2. \tag{4}$$

We use the following form of the temperature dependence of R2DEG:

$$R_{2\text{DEG}} = R_0\left(1 + \frac{T}{T_{\text{ph}}}\right), \tag{5}$$

where R_0, Tph are fitting parameters. Here $R_{2\text{DEG}}$ is defined by impurity scattering R_0 and phonon scattering $R_0(T/T_{\text{ph}})$. Quadratic temperature dependence of G_{vis} follows from G_{vis} dependence on l_{ee}: $G_{\text{vis}} \infty l_{\text{ee}}^{-1}$ and $l_{\text{ee}} \infty T^{-2}$. The result of the approximation (4–5) is in acceptable agreement with experimental data (see dashed curves in Fig. 2, *a*).

Further, the results of the approximation (4) were used to obtain G_{vis}, which is shown in Fig. 3, *a* as the function of temperature. It is noteworthy, that in case when G_{vis} is divided by w^2 all the curves corresponding to different w collapse into one. This means, that the fitting parameter T_0 is universal for all PCs and G_{vis} scales as $G_{\text{vis}} \infty w^2$.

The experimentally obtained dependence $G_{\text{vis}}(T)$ allowed us to extract l_{ee}. As follows from (1) and (4), l_{ee} equals:

$$l_{\text{ee}} = \frac{\pi}{16}\frac{1}{k_{\text{F}}}\left(\frac{T_0}{T}\right)^2. \tag{6}$$

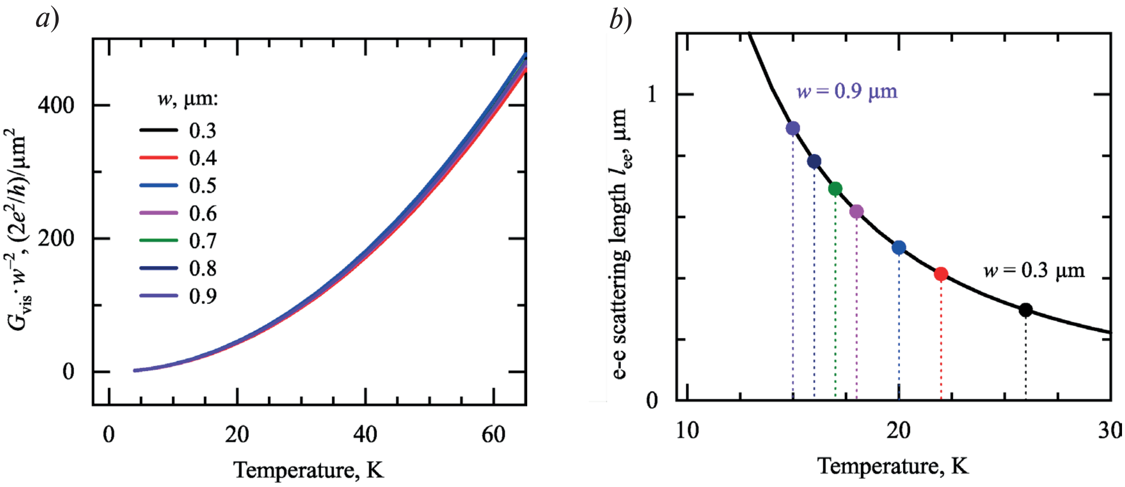

Fig. 3. (*a*) Temperature dependence of viscous contribution to conductance G_{vis} taken with weight w^2 for different PCs widths *w*. (*b*) Electron-electron scattering length lee as function of temperature. Circles correspond to experimentally studied *w*

Fig. 3, *b* shows *e*—*e* scattering length lee as the function of temperature obtained by Eq. (6) with T_0 as the fitting parameter. Vertical dotted lines in Fig. 3, *b* show the temperature range (15—25 K) in which l_{ee} lies in the actual range of *w* (0.3—0.9 μm). Thus, at the temperature range corresponding to the resistance minima (23—25 K) the condition $l_{ee} < w$ is satisfied. This inequality corresponds to the resistance minimum observation condition. Therefore, the Gurzhi requirement for the resistance minimum observation is achieved in our case.

Conclusion

We study electron transport in hydrodynamic regime through PC in 2DEG in GaAs/AlGaAs heterostructure. Gurzhi effect, consisting in the resistance reduction with increasing temperature is experimentally observed. It corresponds to the conductance exceeding the ballistic limit. The observed effect can be explained by the momentum loss suppression at the PC boundary due to the lubricant effect caused by *e*—*e* interaction. Viscous contribution to the PC resistance, attributable to the lubricant effect is extracted from the experiment. The obtained viscous contribution confirms the theoretical prediction.

REFERENCES

1. **de Jong M.J.M., Molenkamp L.W.,** Hydrodynamic electron flow in high-mobility wires. Phys. Rev. B 51 (1995) 13389—13402.
2. **Melnikov M.Yu., Kotthaus J.P., Pellegrini V., Sorba L., Biasol G., Khrapai V.S.,** Influence of e - e scattering on the temperature dependence of the resistance of a classical ballistic point contact in a two-dimensional electron system. Phys. Rev. B 86 (2012) 075425.
3. **Narozhny B.N., Gornyi I.V., Titov M., Schütt M., Mirlin A.D.,** Hydrodynamics in graphene: Linear-response transport. Phys. Rev. B 91 (2015) 035414.
4. **Alekseev P.S.,** Negative Magnetoresistance in Viscous Flow of Two-Dimensional Electrons. Phys. Rev. Lett. 117 (2016) 166601.
5. **Gusev G.M., Levin A.D., Levinson E.V., Bakarov A.K.,** Viscous electron flow in mesoscopic two-dimensional electron gas. AIP Advances 8 (2018) 025318.
6. **Levin A.D., Gusev G.M., Levinson E.V., Kvon Z.D., Bakarov A.K.,** Vorticity-induced negative nonlocal resistance in a viscous two-dimensional electron system. Phys. Rev. B 97 (2018) 245308.
7. **Narozhny B. N., Schütt M.,** Magnetohydrodynamics in graphene: Shear and Hall viscosities. Phys. Rev. B 100 (2019) 035125.
8. **Raichev O.E., Gusev G.M., Levin A.D., Bakarov A.K.,** Manifestations of classical size effect and electronic viscosity in the magnetoresistance of narrow two-dimensional conductors: Theory and experiment. Phys. Rev. B 101 (2020) 235314.
9. **Keser A.C., Wang D.Q., Klochan O., Ho D., Tkachenko O.A., Tkachenko V.A., Culcer D., Adam S., Farrer I., Ritchie D.A., Suchkov O.P., Hamilton A.R.,** Geometric Control of Universal Hydrodynamic Flow in a Two-Dimensional Electron Fluid. Phys. Rev. X 11 (2021) 031030.
10. **Khudaiberdiev D.A., Gusev G.M., Olshanetsky E.B., Kvon Z.D., Mikhailov N.N.,** Magnetohydrodynamics and electron-electron interaction of massless Dirac fermions. Phys. Rev. Res. 3 (2021) L032031.
11. **Levin A.D., Gusev G.M., Yaroshevich A.S., Kvon Z.D., Bakarov A.K.,** Geometric engineering of viscous magnetotransport in a two-dimensional electron system. Phys. Rev. B 108 (2023) 115310.
12. **Ginzburg L.V., Wu Y., Röösli M.P., Gome P.R., Garreis R., Tong C., Stará V., Gold C., Nazaryan K., Kryhin S., Overweg H., Reichl C., Berl M., Taniguchi T., Watanabe K., Wegscheider W., Ihn T., Ensslin K.,** Long distance electron-electron scattering detected with point contacts. Phys. Rev. Res. 5 (2023) 043088.
13. **Andreev A.V., Kivelson S.A., Spivak B.,** Hydrodynamic Description of Transport in Strongly Correlated Electron Systems. Phys. Rev. Lett. 106 (2011) 256804.
14. **Principi A., Vignale G., Carrega M., Polini M.,** Bulk and shear viscosities of the two-dimensional electron liquid in a doped graphene sheet. Phys. Rev. B 93 (2016) 125410.
15. **Gurzhi R.N.,** Hydrodynamic effects in solids at low temperature. Sov. Phys. Usp. 11, 255 (1968).
16. **Polini M., Geim A.K.,** Viscous electron fluids. Physics Today 73 (2020) 28—34.

17. **Narozhny B.N.,** Hydrodynamic approach to two-dimensional electron systems. Riv. Nuovo Cim. 45 (2022) 661–736.

18. **Gurzhi. R.N.,** Minimum of resistance in impurity-free conductors. Sov. Phys. JETP. 44 (1962) 771–772.

19. **Krishna Kumar R., Bandurin D.A., Pellegrino F.M.D., Cao Y., Principi A., Guo H., Auton G.H., Ben Shalom M., Ponomarenko L.A., Falkovich G., Watanabe K., Taniguchi T., Grigorieva I.V., Levitov L.S., Polini M., Geim A.K.,** Superballistic flow of viscous electron fluid through graphene constrictions. Nature Phys 13 (2017) 1182–1185.

20. **Ginzburg L.V., Gold C., Röösli M.P., Reichl C., Berl M., Wegscheider W., Ihn T., Ensslin K.,** Superballistic electron flow through a point contact in a Ga[Al]As heterostructure. Phys. Rev. Res. 3 (2021) 023033.

21. **Guo H., Ilseven E., Falkovich G., Levitov L.S.,** Higher-than-ballistic conduction of viscous electron flows. Proceedings of the National Academy of Sciences 114 (2017) 3068–3073.

22. **Chaplik A.V.,** Energy spectrum and electron scattering processes in inversion layers. Zh. Eksp. Teor. Fiz. 60 (1971) 1845–1852.

23. **Giuliani G.F., Quinn, J.J.,** Lifetime of a quasiparticle in a two-dimensional electron gas. Phys. Rev. B 26 (1982) 4421–4428.

24. **Budantsev M.V., Pokhabov D.A., Pogosov A.G., Zhdanov E.Yu., Bakarov A.K., Toropov A.I.,** Hysteretic phenomena in a 2DEG in the quantum Hall effect regime, studied in a transport experiment. Semiconductors 48 (2014) 1423–1431.

THE AUTHORS

SARYPOV Daniil I.
d.sarypov@g.nsu.ru
ORCID: 0000-0003-1056-5235

EGOROV Dmitriy A.
d.egorov@g.nsu.ru
ORCID: 0000-0001-5668-7284

POKHABOV Dmitriy A.
pokhabov@isp.nsc.ru
ORCID: 0000-0002-8747-0261

ZHDANOV Evgeniy Yu.
zhdanov@isp.nsc.ru
ORCID: 0000-0002-7173-6213

POGOSOV Arthur G.
pogosov@isp.nsc.ru
ORCID: 0000-0001-5310-4231

BAKAROV Askhat K.
bakarov@isp.nsc.ru
ORCID: 0000-0002-0572-9648

Received 14.12.2023. Approved after reviewing 06.01.2024. Accepted 07.01.2024.

Quantum wires, quantum dots, and other low-dimensional systems

Conference paper
UDC 621.315.592
DOI: https://doi.org/10.18721/JPM.171.115

Excitation of plasmon modes localized at the edge of a graphene rectangle by teraherz wave

K.V. Mashinsky [1] ✉, V.V. Popov [1], D.V. Fateev [1, 2]

[1] Kotelnikov Institute of Radio Engineering and Electronics (Saratov Branch), RAS, Saratov, Russia;

[2] Saratov State University, Saratov, Russia

✉ konstantin-m92@yandex.ru

Abstract. Excitation of edge plasmon modes in a graphene rectangle by an incident electromagnetic wave is predicted. The problem is solved using a self-consistent electromagnetic approach based on the method of integral equations developed by the authors. It is found that the frequencies of edge plasmon resonances depend on both the width and length of graphene rectangle. For a graphene rectangle having the aspect ratio of 1 micron by 200 microns, the frequencies of edge plasmon resonances lie in terahertz frequency range

Keywords: edge plasmon, terahertz, graphene

Funding: Russian Science Foundation grant 22-19-00611 “Terahertz resonant edge effects in 3D plasmonic structures with 2D electron gas”.

Citation: Mashinsky K.V., Popov V.V., Fateev D.V., Excitation of plasmon modes localized at the edge of a graphene rectangle by teraherz wave, St. Petersburg State Polytechnical University Journal. Physics and Mathematics. 17 (1.1) (2024) 95–99. DOI: https://doi.org/10.18721/JPM.171.115

This is an open access article under the CC BY-NC 4.0 license (https://creativecommons.org/licenses/by-nc/4.0/)

Материалы конференции
УДК 621.315.592
DOI: https://doi.org/10.18721/JPM.171.115

Возбуждение терагерцовой волной плазмонных мод, локализованных на краю графенового прямоугольника

К.В. Машинский [1] ✉, В.В. Попов [1], Д.В. Фатеев [1, 2]

[1] Саратовский филиал Института радиотехники и электроники
им. В.А. Котельникова РАН, г. Саратов, Россия;

[2] Саратовский национальный исследовательский государственный
университет им. Н.Г. Чернышевского, г. Саратов, Россия

✉ konstantin-m92@yandex.ru

Аннотация. Предсказано возбуждение падающей электромагнитной волной краевых плазмонных мод в графеновом прямоугольнике. Задача о возбуждении плазмонов решена с помощью разработанного авторами самосогласованного электродинамического подхода, основанного на методе интегральных уравнений. Обнаружено, что частоты краевых плазмонов зависят как от ширины графенового прямоугольника, так и от его длины. Для прямоугольника с аспектным соотношением сторон 1 микрон на 200 микрон частоты резонансов краевых плазмонов лежат в терагерцовом диапазоне частот.

Ключевые слова: краевой плазмон, терагерц, графен

© Mashinsky K.V., Popov V.V., Fateev D.V., 2024. Published by Peter the Great St. Petersburg Polytechnic University.

Финансирование: РНФ 22-19-00611 «Терагерцовые резонансные краевые эффекты в трехмерных плазмонных структурах с двумерным электронным газом».

Ссылка при цитировании: Машинский К.В., Попов В.В., Фатеев Д.В. Возбуждение терагерцовой волной плазмонных мод, локализованных на краю графенового прямоугольника // Научно-технические ведомости СПбГПУ. Физико-математические науки. 2024. Т. 17. № 1.1. С. 95–99. DOI: https://doi.org/10.18721/ JPM.171.115

Статья открытого доступа, распространяемая по лицензии CC BY-NC 4.0 (https:// creativecommons.org/licenses/by-nc/4.0/)

Introduction

Plasmons in graphene structures are considered as promising platform for planar terahertz optoelectronics [1,2]. Advantages of plasmons in graphene include field localization at lengths shorter than the electromagnetic wavelength [3], nonlinear properties useful for terahertz detection [4, 5], as well as the possibility of their amplification [6, 7].

Theoretical studies of plasmon effects are commonly conducted in the assumption that the graphene structure is uniform and infinitely long in the direction perpendicular to the plasmon wave vector [8, 9]. Different types of plasmon modes in two-dimensional (2D) electron systems have been studied under this assumption: single-layer plasmons [10], screened plasmons [11, 12], “gate proximity” plasmons [11], and oblique plasmons in graphene nanoribbon array [13].

Consideration of full three-dimensional plasmonic problems, in which a 2D plasmonic cavity is confined in two perpendicular directions, made it possible to reveal edge plasmon modes [14]. Using the near-field optical microscopy for excitation and imaging plasmons in disk-shaped and rectangular graphene nanocavities, strong interaction of edge [15, 16] and sheet plasmon modes [14] was experimentally observed. Edge plasmon is viewed as a tool for stronger localization of terahertz (THz) field below the diffraction limit [17].

In this work, we predict the excitation of plasmonic modes localized near the edge of a graphene rectangle by a normally incident THz electromagnetic wave.

Structure and Methods

We solve the problem of the incidence of an electromagnetic wave on a rectangular graphene cavity (Fig. 1, *a*). A graphene rectangle lies on a flat interface between two media with different dielectric constants; the length of the rectangle is $l = 200$ μm, and its width is $w = 1$ μm. A linearly polarized wave of THz frequency is normally incident on the plane of the interface between two media, scatters by a graphene rectangle and excites plasmon modes in it. The electric field vector of the incident wave is polarized along the short side of the rectangle w.

The problem is solved using a rigorous electromagnetic approach based on the integral equation method [18]. The main steps of the electromagnetic approach include:

(i) Fourier transformation of the Maxwell equations and electromagnetic boundary conditions;

(ii) formulation of the integral equations for the components of oscillating current densities in graphene;

(iii) solving the integral equations using the Galerkin procedure by expanding the current density components into series over the orthogonal Legendre polynomials;

(iv) transforming the system of integral equations into an infinite system of linear algebraic equations for the expansion coefficients of current densities;

(v) truncating the infinite system of linear algebraic equations for reaching the desired convergence of its solution and then solving it numerically.

The calculated expansion coefficients of current densities make it possible to determine the electromagnetic fields at any point of the structure under consideration, calculate the absorption cross section of the structure, and find the spatial distributions of charge density oscillations over the graphene rectangle.

© Машинский К.В., Попов В.В., Фатеев Д.В., 2024. Издатель: Санкт-Петербургский политехнический университет Петра Великого.

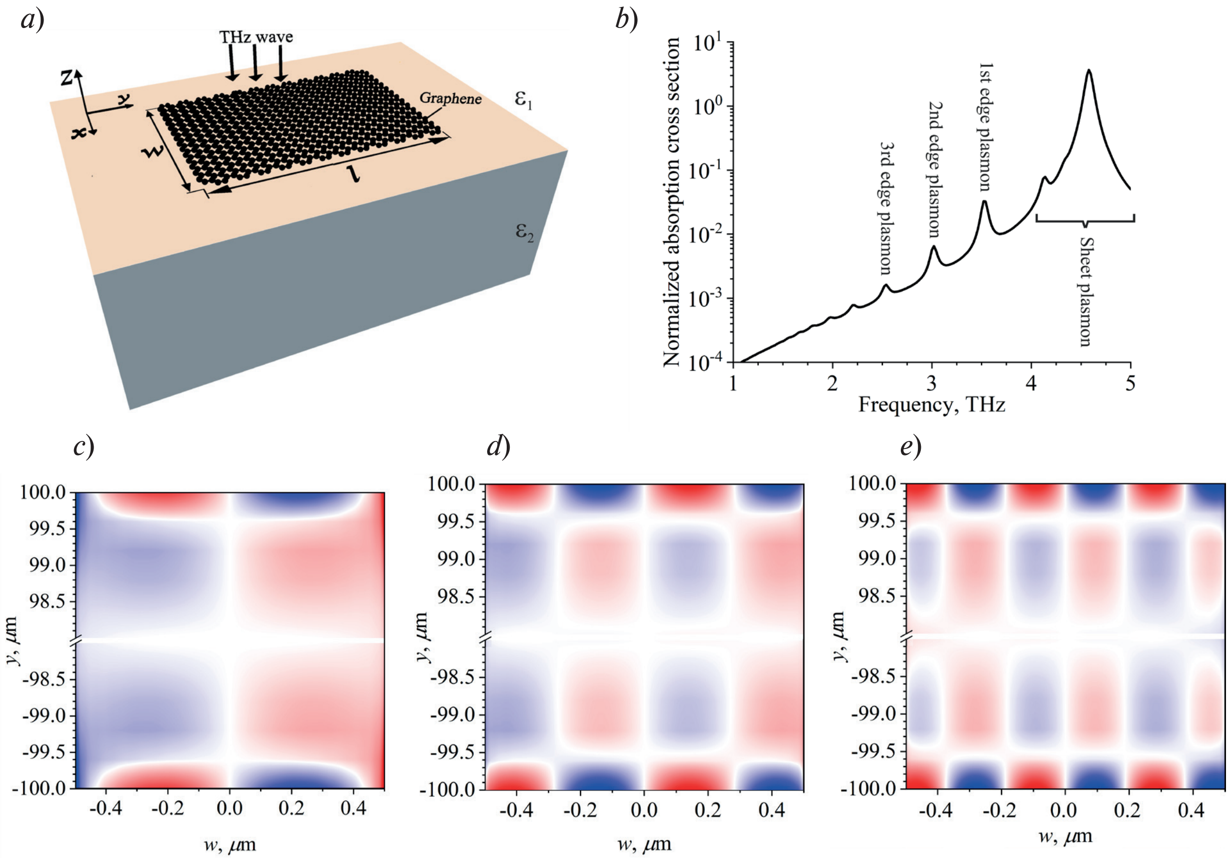

Fig. 1. Schematic view of the studied structure (*a*). Spectrum of absorption cross-section normalized to the geometric area of graphene rectangle for $w = 1$ μm and $l = 200$ μm (*b*). The instantaneous spatial distributions of the oscillating charge density over the area of graphene rectangle in the plasmon resonances excited at frequencies of 3.6 THz (*c*), 3.1 THz (*d*), and 2.5 THz (*e*). Red color in panels (*c*), (*d*), and (*e*) indicates a positive sign of the oscillating charge density, and blue indicates a negative sign. Considerable middle parts of the vertical axes *y* in panels *c*, *d*, and *e* are omitted to visually show the effects at the edges of graphene rectangle. Parameters of graphene: Fermi energy of charge carries is 150 meV and the momentum relaxation time of charge carriers in graphene is 2 ps

Results and Discussion

The calculated spectrum of the absorption cross section of graphene rectangle demonstrates a series of different resonances (Fig. 1, *b*). Resonance at frequency 4.6. THz corresponds to the excitation of the fundamental *sheet* dipole plasmon mode with charge density oscillations across the length of the graphene rectangle. This fundamental plasmon mode is distributed almost homogeneously along the length of graphene rectangle. For long rectangles with length $l > 50w$, additional resonances are revealed at frequencies below the fundamental *sheet* plasmon mode frequency (Fig. 1, *b*). Instantaneous spatial distributions of the oscillating charge density in these plasmon modes in graphene rectangle are plotted in Figs. 1, *c*, *d*, *e*. As seen in Figs. 1, *c*, *d*, and *e*, the charge oscillations in these plasmon modes are strongly localized near the longitudinal edges of graphene rectangle in crucial contrast from the well-known fundamental *sheet* plasmon mode in which the charge oscillations exist over the entire area of graphene cavity. The profiles of the charge carrier distributions in these modes correspond to the bright plasmon modes because have strong dipole moments due to odd numbers of nodes across the length of graphene rectangle. The wave number of the *edge* plasmon mode excited at frequency 3.6 THz is close to the value of $k_x = \pi/w$, the wave number of the *edge* plasmon mode excited at frequency 3.1 THz is close to $3\pi/w$, and for the *edge* plasmon mode excited at frequency 2.5 THz its wave number corresponds to $5\pi/w$. The dependence of the resonance frequencies these *edge* plasmon modes on their wave numbers are typical for the backward waves characterized by anomalous dispersion.

Conclusion

In this work, we predict the *edge* plasmon modes in graphene rectangular cavity which can be excited by incident THz electromagnetic wave. The frequencies of *edge* plasmon modes fall within THz frequency range in elongate graphene rectangles with micron width. The frequencies of the *edge* plasmon modes reside below the frequency of the fundamental *sheet* dipole plasmon mode in long graphene rectangles with a length approximately 50 times longer than the width of graphene rectangle.

REFERENCES

1. **Huang S., Song C., Zhang G., Yan H.,** Graphene plasmonics: physics and potential applications, Nanophotonics. 6 (2017) 1191.
2. **Cox J. D., Garcнa De Abajo F. J.,** Nonlinear graphene nanoplasmonics, Acc. Chem. Res. 52 (2019) 2536.
3. **Zheng Z.B., Li J.T., Ma T., Fang H.L., Ren W.C., Chen J., She J.C., Zhang Y., Liu F., Chen H.J., Deng S.Z., Xu N.S.,** Tailoring of electromagnetic field localizations by two-dimensional graphene nanostructures, Light Sci. Appl. 6 (2017) e17057.
4. **Spirito D., Coquillat D., De Bonis S.L., Lombardo A., Bruna M., Ferrari A.C., Pellegrini V., Tredicucci A., Knap W., Vitiello M.S.,** High performance bilayer-graphene terahertz detectors, Appl. Phys. Lett. 104 (2014) 061111.
5. **Fateev D.V., Mashinsky K.V., Popov V.V.,** Terahertz plasmonic rectification in a spatially periodic graphene, Appl. Phys. Lett. 110 (2017) 061106.
6. **Dubinov A.A., Aleshkin V.Y., Mitin V., Otsuji T., Ryzhii V.,** Terahertz surface plasmons in optically pumped graphene structures, J. Phys. Condens. Matter. 23 (2011) 145302.
7. **Moiseenko I.M., Popov V.V., Fateev D.V.,** Terahertz plasmon amplification in a double-layer graphene structure with direct electric current in hydrodynamic regime, Phys. Rev. B. 103 (2021) 195430.
8. **Mikhailov S.A., Savostianova N.A.,** Microwave Response of a Two-Dimensional Electron Stripe, Phys. Rev. B. 71 (2005) 035320.
9. **Popov V.V., Tsymbalov G.M., Shur M.S., Knap W.,** The resonant terahertz response of a slot diode with a two-dimensional electron channel, Semiconductors. 39 (2005) 142.
10. **Hwang E.H.,** Das Sarma S., Dielectric function, screening, and plasmons in two-dimensional graphene, Phys. Rev. B. 75 (2007) 205418.
11. **Zabolotnykh A.A., Volkov V.A.,** Interaction of gated and ungated plasmons in two-dimensional electron systems, Phys. Rev. B. 99 (2019) 165304.
12. **Alonso-González P., Nikitin A.Y., Gao Y., Woessner A., Lundeberg M. B., Principi A., Forcellini N., Yan W., Vélez S., Huber A.J., Watanabe K., Taniguchi T., Casanova Hueso F.L.E., Polini M., Hone J., Koppens F.H.L., Hillenbrand R.,** Acoustic terahertz graphene plasmons revealed by photocurrent nanoscopy, Nat. Nanotechnol. 12 (2017) 31.
13. **Popov V.V., Bagaeva T.Y., Otsuji T., Ryzhii V.,** Oblique terahertz plasmons in graphene nanoribbon arrays, Phys. Rev. B. 81. (2010) 073404.
14. **Nikitin A.Y., Alonso-González P., Vélez S., Mastel S., Centeno A., Pesquera A., Zurutuza A., Casanova F., Hueso L.E., Koppens F.H.L., Hillenbrand R.,** Real-space mapping of tailored sheet and edge plasmons in graphene nanoresonators, Nat. Photonics. 10 (2016) 239.
15. **Margetis D.,** Edge plasmon-polaritons on isotropic semi-infinite conducting sheets, J. Math. Phys. 61 (2020) 062901.
16. **Fei Z., Goldflam M.D., Wu J.S., Dai S., Wagner M., McLeod A.S., Liu M.K., Post K.W., Zhu S., Janssen G.C.A.M., Fogler M.M., Basov D.N.,** Edge and Surface Plasmons in Graphene Nanoribbons, Nano Lett. 15 (2015) 8271.
17. **Nikitin A.Y., Guinea F., Garcнa-Vidal F.J., Martнn-Moreno L.,** Edge and waveguide terahertz surface plasmon modes in graphene microribbons, Phys. Rev. B. 84 (2011) 161407(R).
18. **Mashinsky K.V., Popov V.V., Fateev D.V.,** Complete electromagnetic consideration of plasmon mode excitation in graphene rectangles by incident terahertz wave, Sci. Rep. 14 (2024) 7546.

THE AUTHORS

MASHINSKY Konstantin V.
konstantin-m92@yandex.ru
ORCID: 0000-0002-0724-6391

FATEEV Denis V.
fateevdv@yandex.ru
ORCID: 0000-0003-1406-5385

POPOV Vyacheslav V.
popov_slava@yahoo.co.uk
ORCID: 0000-0003-1303-6443

Received 01.12.2023. Approved after reviewing 07.02.2024. Accepted 13.02.2024.

St. Petersburg Polytechnic University Journal. Physics and Mathematics. 2024 Vol. 17. No. 1.1
Научно-технические ведомости СПбГПУ. Физико-математические науки. 17 (1.1) 2024

Conference paper
UDC 535-4
DOI: https://doi.org/10.18721/JPM.171.116

Single photon emission of "silicon-vacancy" centers in nanodiamonds placed in cylindrical pits on a gold film

A.A. Zhivopistsev [1] ✉, A.M. Romshin [2], A.V. Gritsienko [3], P.V. Lega [4],
R.K. Bagramov [5], V.P. Filonenko [5], A.G. Vitukhnovsky [3], I.I. Vlasov [2]

[1] National Research University Higher School of Economics, Moscow, Russia;
[2] Prokhorov General Physics Institute RAS, Moscow, Russia;
[3] Moscow Institute of Physics and Technology (State University), Dolgoprudny, Moscow Region, Russia;
[4] Kotel'nikov Institute of Radioengineering and Electronics, Fryazino, Moscow Region, Russia;
[5] Vereshchagin Institute of High Pressure Physics RAS, Troitsk, Moscow Region, Russia
✉ azh253@gmail.com

Abstract. In this paper, we study photon emission of single "silicon-vacancy" centers in HPHT-nanodiamonds on 1) a gold surface and 2) inside nanophotonic cavity which is cylindrical nanopit on a gold film. It was found that the saturation intensity of single SiV centers in the nanocavity increases by up to 3 times compared to similar diamonds on the gold surface, along with a twofold decrease in saturation power and a 15% reduction in lifetime. The obtained results are explained by the interaction of SiV centers with the surface plasmons in cylindrical nanopit in gold film, as well as by the narrow directivity of the emitter related to geometry factor of the plasmonic nanocavity.

Keywords: nanodiamonds, color centers, microcavities, single photon emitters

Funding: The study was supported by the Russian Science Foundation (Project № 22-19-00324, https://rscf.ru/project/22-19-00324/).

Citation: Zhivopistsev A.A., Romshin A.M., Gritsienko A.V., Lega P.V., Bagramov R.K., Filonenko V.P., Vitukhnovsky A.G., Vlasov I.I., Single photon emission of "silicon-vacancy" centers in nanodiamonds placed in cylindrical pits on a gold film, St. Petersburg State Polytechnical University Journal. Physics and Mathematics. 17 (1.1) (2024) 100–104. DOI: https://doi.org/10.18721/JPM.171.116

This is an open access article under the CC BY-NC 4.0 license (https://creativecommons.org/licenses/by-nc/4.0/)

Материалы конференции
УДК 535-4
DOI: https://doi.org/10.18721/JPM.171.116

Флуоресценция одиночных центров окраски «кремний-вакансия» в наноалмазах в цилиндрических углублениях на золотой пленке

А.А. Живописцев [1] ✉, А.М. Ромшин [2], А.В. Грициенко [3], П.В. Лега [4],
Р.Х. Баграмов [5], В.П. Филоненко [5], А.Г. Витухновский [3], И.И. Власов [2]

[1] Национальный исследовательский университет "Высшая школа экономики", Москва, Россия;
[2] Институт общей физики им. А.М. Прохорова РАН, Москва, Россия;
[3] Московский физико-технический институт (государственный университет), г. Долгопрудный, Московская обл., Россия;
[4] Институт радиотехники и электроники им. В.А. Котельникова РАН, г. Фрязино, Московская обл., Россия;

© Zhivopistsev A.A., Romshin A.M., Gritsienko A.V., Lega P.V., Bagramov R.K., Filonenko V.P., Vitukhnovsky A.G., Vlasov I.I., 2024. Published by Peter the Great St. Petersburg Polytechnic University.

[5] Институт физики высоких давлений им. Л.Ф. Верещагина РАН, г. Троицк, Московская обл., Россия
✉ azh253@gmail.com

Аннотация. В настоящей работе изучалась однофотонная эмиссия центров окраски «кремний-вакансия» в HPHT-наноалмазах 1) на поверхности золота и 2) в цилиндрическом углублении (ЦУ) на золотой пленке. Было обнаружено, что интенсивность насыщения одиночных центров SiV в ЦУ увеличивается до 3 раз по сравнению с аналогичными алмазами на поверхности кремния, наряду с двукратным снижением мощности насыщения и сокращением времени жизни на 15%. Полученные результаты объясняются взаимодействием SiV-центров с поверхностными плазмонами в микрорезонаторе, а также узкой направленностью излучения в виду геометрического фактора плазмонного ЦУ.

Ключевые слова: наноалмазы, центры окраски, микрорезонаторы, однофотонные эмиттеры

Финансирование: Работа поддержана грантом РНФ № 22-19-00324 (https://rscf.ru/project/22-19-00324/).

Ссылка при цитировании: Живописцев А.А., Ромшин А.М., Грициенко А.В., Лега П.В., Баграмов Р.Х., Филоненко В.П., Витухновский А.Г., Власов И.И. Флуоресценция одиночных центров окраски «кремний-вакансия» в наноалмазах в цилиндрических углублениях на золотой пленке // Научно-технические ведомости СПбГПУ. Физико-математические науки. 2024. Т. 17. № 1.1. С. 100–104. DOI: https://doi.org/10.18721/JPM.171.116

Статья открытого доступа, распространяемая по лицензии CC BY-NC 4.0 (https://creativecommons.org/licenses/by-nc/4.0/)

Introduction

The single photon source (SPS) is cornerstone in quantum information transmission and processing protocols [1–3]. Such a source must possess high photostability, brightness and emit photons in a narrow spectral range and solid angle [4]. The "silicon-vacancy" color centers (SiV) in nanodiamonds (NDs), having a bright and narrow (~ 6 nm) zero-phonon line (ZPL) in the near IR region (738 nm), are promising candidates for this role [5, 6]. The emission properties of SiV centers benefit significantly from placing NDs in microresonators [7–10] due to enhancing the rate of spontaneous transitions and increasing the radiation directivity. Moreover, the rate of quantum emitter photoexcitation can be significantly enhanced, which is most clearly manifested in the case of plasmonic nanoantennas [10].

In this work, the fluorescence properties of single SiV centers in HPHT nanodiamonds placed 1) on a gold film and 2) in cylindrical nanopits on a gold film were studied. At the first stage, saturation curves, spectra and decay times of fluorescence were measured for the particles on the gold film. Next, the "pick-and-place" method we developed was used to move the selected nanodiamonds to the cylindrical nanopits on a gold surface, where similar measurements were carried out. Finally, we provide a comparison of optical properties before/after ND moving and discuss the mechanisms contributing to the fluorescent enhancement.

Materials and Methods

The NDs under study were synthesized by the High-Pressure High-Temperature (HPHT) method from a mixture of adamantane ($C_{10}H_{16}$) and detonation nanodiamonds at a pressure ~ 7.5 GPa, temperatures 1500–1600 °C and time exposition 20 s. To form SiV-centers in diamond matrix, a small amount of tetrakis(trimethylsilyl)silane ($C_{12}H_{36}Si_5$) was added to the initial growth mixture with the ratio Si/(Si + C) = 0.01%. The 0.1 mg of output ND-powder was diluted in 2 ml of ethanol and then sonicated in the ultrasonic bath for 30 min to form a homogeneous suspension of NDs. Eventually, 2 μl of the resulting suspension was applied to the gold film with cylindrical pits. A pre-characterization in Scanning Electron Microscope (SEM) revealed the ND size distribution between 150 nm and 500 nm.

© Живописцев А.А., Ромшин А.М., Грициенко А.В., Лега П.В., Баграмов Р.Х., Филоненко В.П., Витухновский А.Г., Власов И.И., 2024. Издатель: Санкт-Петербургский политехнический университет Петра Великого.

The process of cylindrical pit fabrication on a gold film was described in detail in our previous work [10]. The diameter and height of such nanopits are 500 nm and 300 nm, respectively. To transfer NDs to the surface of the gold film and then inside the cylindrical nanopit, we used a “pick-and-place” technique we developed earlier, described in [10].

Optical properties of NDs were studied in home-built confocal microscope equipped with two sources: a continuous laser at 660 nm and pulsed one at 630 nm ($\tau_{pulse} \approx 80$ ps). To confirm the single photon emission from selected ND, we used a Hanbury–Brown–Twiss (HBT) interferometer with two avalanche photodiodes (APDs, Excelitas SPCMA–QRH–14–FC). The fluorescence spectra were recorded with Ocean Insight QEPro spectrometer, and for saturation measurements, the APDs with band pass filter (728–749 nm) were employed. A long–distance objective Mitutoyo ×100, NA = 0.7 was used in all these measurements. The fluorescence decay rates were analyzed with Time-Correlated Single Photon Counting (TC SPC) module Picoquant MicroTime 200 and objective Olympus (×100, NA = 0.95).

Results and Discussion

We started by choosing three random NDs on the gold surface whose emission satisfies to criteria of single photon statistics. In order to reveal such sources, we performed precise confocal mapping and measured the second-order autocorrelation function $g^{(2)}(\tau)$ of SiV fluorescence. Fig. 1, *a* demonstrates an example of $g^{(2)}(\tau)$ functions for NDs on the gold surface (NG–G). The dip at zero time–delay ($\tau = 0$) is less than 0.5 indicating a subpoissonian statistics of light and consequently its single-photon nature. Fluorescence spectra, saturation curves and decay times were measured for selected NDs. After characterization of the ND emitters on the gold surface, we moved the NDs to pre-defined cylindrical pits by the “pick-and-place” method and performed similar measurements. A SEM image for ND1–GNP (Fig. 1, *c*) reveals the geometry of the nanophotonic interface and the size of the diamond particle (~ 350 nm).

Fig. 1, *b* illustrates the background-corrected fluorescence spectra recorded for ND1–G and ND1 inside the microcavity (ND1–GNP) at 30 mW excitation. A bright zero-phonon line (ZPL) at 738 nm and a sharp diamond Raman peak are observed in both spectra. For ND1–GNP the peak intensity of ZPL slightly increases by 30% relative to diamond Raman. The spectral position of ZPL is shifted to the IR region by 0.2 nm, while the full width at half maximum (FWHM) is reduced by ~ 10% in comparison to ND1–G. This behavior could be a product of enhanced interaction between the emitter and plasmon in microcavity.

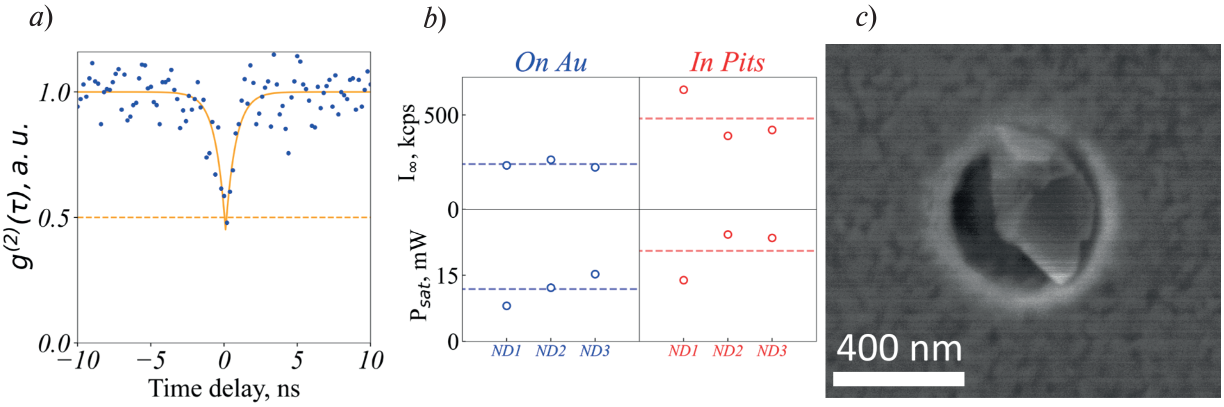

Fig. 1. Second-order autocorrelation function $g^{(2)}(\tau)$ for ND on the surface of the gold film (*a*); Fluorescence spectra of single SiV–centers in NDs on gold film (blue) and in cylindrical pits (red) (*b*); SEM–image of ND1–GNP (*c*)

For quantitative analysis of the fluorescence enhancement factor, the saturation measurements were carried out. Fig. 2, *a* shows the fluorescence intensity of a single SiV as a function of excitation power for ND1–G (blue) and ND1–GNP (red). The data was approximated by the curve

$$I(P) = I_\infty \frac{P}{P_{sat}+P} + c_{bg}\cdot P,$$

where I is the fluorescence intensity, P is the excitation power, I_∞ is the count rate in the limit of large P, P_{sat} is the saturation power, c_{bg} is the coefficient of linear background. The values I_∞ and P_{sat} extracted for three NDs in different photonic environments are presented in Fig. 2, *b*. One can see that emission rates of NDs in nanopits on average exceeds the similar parameter for NDs–G by an enhancement factor $EF = 2$ with the maximum value for ND1 $EF_{\max} = 3$ corresponding to $I^{\infty}_{ND1\text{-}GNP} = 634$ kHz. The saturation power on average also increases from $P^{sat}_{NDs-G} = 11.8$ mW to $P^{sat}_{NDs-GNP} = 20.5$ mW which probably takes explanation from additional absorption by void plasmons [11].

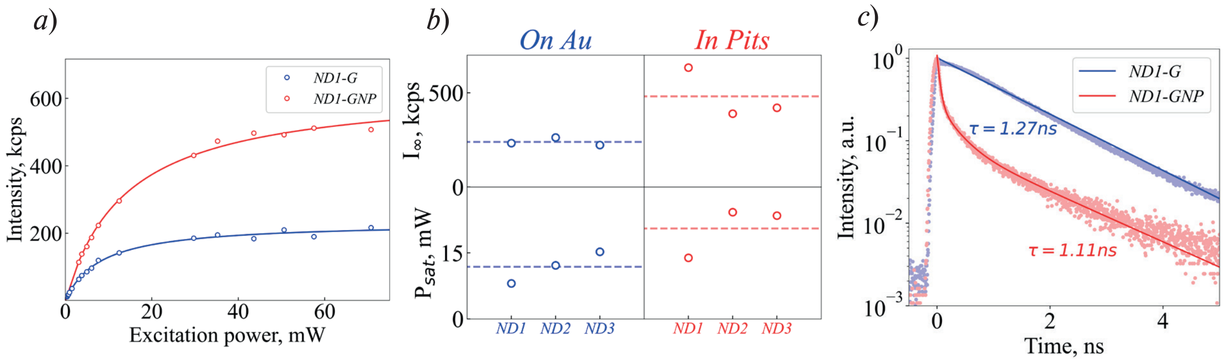

Fig. 2. Saturation curves measured for ND1 on gold surface (blue) and in nanopit (red) (*a*). Extracted I_∞ (top) and P_{sat} (bottom) for three NDs SiV luminescence on gold surface (blue) and in nanopits (red) (*b*). Fluorescent decays for ND on surface (blue) and in nanocavity (red) (*c*)

Finally, we performed time-resolved fluorescence intensity measurements for the NDs both on a gold surface and in a nanophotonic cavity. The SiV-fluorescence decay times extracted from the decay curves were averaged over three NDs and compared between each other. The relaxation time reduces by ~ 15% on average for emitters inside a nanophotonic cavity which can be a sign of effective coupling with void plasmons in a near–surface gold layer. The fluorescence decays for ND1–G demonstrate mono–exponential behavior (Fig. 2, *c*)). In contrast, for ND1–GNP deeply sub-ns component was revealed which we believe is not related to SiV-fluorescence, but rather to an enhanced background fluorescence originating from the gold nanopit [12].

An observed enhancement of the single photon emission can be explained by analyzing contributions from major mechanisms. First, the emitter–plasmon interaction increases in nanophotonic cavity which is confirmed by a slight reduction of the fluorescent lifetime. Second, ND-in-pit interface changes the geometrical factor of the fluorescence, resulting in enhanced directivity of the SiV-center and its extracted emission rate. Third, the small heterogeneity in enhancement factor from particle to particle can be related to inaccuracies in nanomanipulations with diamonds. During the “pick-and-place” operation ND accidently change its spatial position losing the initial orientation of the dipole moment of the emitter relative to the normal of the gold surface. Nevertheless, we believe changes in dipole orientation play a non-primary role in observed enhancement since for all accidentally transferred diamond particles the increase of the emission rate was detected which excludes the factor of accident orientation.

Conclusion

In summary, we investigated single photon emission of SiV-centers in nanodiamonds placed 1) on a gold surface and 2) in plasmonic nanocavity and provided a comparative study of optical properties for these two cases. A nanophotonic structure nanodiamond-in-pit exhibits a 3-fold enhancement of fluorescence intensity with reduced by 15% fluorescent lifetime and narrowed by 10% spectral range of the emission. Such a structure demonstrates promising potential for state-of-the-art quantum applications giving rise to scalable photonic interfaces.

REFERENCES

1. **Awschalom D.D., Hanson R., Wrachtrup J., Zhou B.B.,** Quantum technologies with optically interfaced solid-state spins. Nature Photonics, 12 (9) (2018) 516–527.

2. **Acín A., Bloch I., Buhrman H., Calarco T., Eichler C., Eisert J., Wilhelm F.K.,** The quantum technologies roadmap: a European community view. New Journal of Physics, 20 (8) (2018) 080201.

3. **O'brien J.L., Furusawa A., Vučković J.,** Photonic quantum technologies. Nature Photonics, 3 (12) (2009) 687–695.

4. **Castelletto S.A., Scholten R.E.,** Heralded single photon sources: a route towards quantum communication technology and photon standards. The European Physical Journal-Applied Physics, 41 (3) (2008) 181–194.

5. **Neu E., Hepp C., Hauschild M., Gsell S., Fischer M., Sternschulte H., Becher C.,** Low-temperature investigations of single silicon vacancy colour centres in diamond. New Journal of Physics, 15 (4) (2013) 043005.

6. **Pasternak D.G., Dai J., Kalashnikov D.A., Sedov V.S., Martyanov A.K., Ralchenko V.G., Vlasov I.I.,** Low-Temperature Silicon-Vacancy Luminescence of Individual Chemical Vapor Deposition Nanodiamonds Grown by Seeding and Spontaneous Nucleation. physica status solidi (a), 218 (5) (2021) 2000274.

7. **Radulaski M., Zhang J.L., Tzeng Y.K., Lagoudakis K.G., Ishiwata H., Dory C., Vučković J.,** Nanodiamond integration with photonic devices. Laser & Photonics Reviews, 13 (8) (2019) 1800316.

8. **Szenes A., Bánhelyi B., Szaby L.Z., Szaby G., Csendes T., Csete M.,** Improved emission of SiV diamond color centers embedded into concave plasmonic core-shell nanoresonators. Scientific Reports, 7 (1) (2017) 13845.

9. **Romshin A.M., Gritsienko A.V., Ilin A.S., Bagramov R.K., Filonenko V.P., Vitukhnovsky A.G., Vlasov I.I.,** Enhancing single-photon emission of silicon-vacancy centers in nanodiamonds by a gold film.

10. **Romshin A.M., Gritsienko A.V., Lega P.V., Orlov A.P., Ilin A.S., Martyanov A.K., Vitukhnovsky A.G.,** Effectively enhancing silicon-vacancy emission in a hybrid diamond-in-pit microstructure. Laser Physics Letters, 20 (1) (2022) 015206.

11. **Teperik T.V., Popov V.V., De Abajo F.G.,** Void plasmons and total absorption of light in nanoporous metallic films. Physical review B, 71 (8) (2005) 085408.

12. **Hugall J.T., Baumberg J.J.,** Demonstrating photoluminescence from Au is electronic inelastic light scattering of a plasmonic metal: the origin of SERS backgrounds. Nano letters, 15 (4) (2015) 2600–2604.

THE AUTHORS

ZHIVOPISTSEV Alexander A.
azh253@gmail.com
ORCID: 0009-0008-1846-1979

ROMSHIN Alexey M.
alex_31r@mail.ru
ORCID: 0000-0001-9278-6765

GRITSIENKO Alexander V.
grits_alex@rambler.ru

LEGA Peter V.
lega_peter@list.ru

BAGRAMOV Rustem K.
bagramov@mail.ru

FILONENKO Vladimir P.
vpfil@mail.ru

VITUKHNOVSKY Alexey G.
alexei@sci.lebedev.ru

VLASOV Igor I.
vlasov@nsc.gpi.ru

Received 14.12.2023. Approved after reviewing 28.02.2024. Accepted 16.04.2024.

Conference paper
UDC 535.3
DOI: https://doi.org/10.18721/JPM.171.117

Photoinduced light absorption in Ge/Si quantum dots

R.V. Ustimenko [1] ✉, D.A. Karaulov [1], M.Ya. Vinnichenko [1], I.S. Makhov [2], D.A. Firsov [1],
H.A. Sarkisyan [3], T.A. Sargsian [3, 4], D.B. Hayrapetyan [3, 4]

[1] Peter the Great St. Petersburg Polytechnic University, St. Petersburg, Russia;
[2] HSE University, St. Petersburg, Russia;
[3] Russian-Armenian University, Yerevan, Armenia;
[4] Institute of Chemical Physics after A.B. Nalbandyan of NAS RA, Yerevan, Armenia
✉ ratmirustimenko@yandex.ru

Abstract. Photoinduced absorption in nanostructures with doped Ge/Si quantum dots as well as in undoped structures, was studied. Spectra of photoinduced absorption at cryogenic temperatures under direct and indirect in real space resonant interband pumping, as well as time-resolved spectra were obtained. Two high-energy peaks detected in the absorption spectra may be associated with intraband hole transitions from the ground and excited states of quantum dots to the continuous spectrum. The low-energy peak corresponds to interlevel transitions of holes between the ground and excited states. The dynamics of the decay of high-energy peaks can be described in terms of fast and slow components associated with the capture of photoexcited carriers on the levels in a quantum dot. Structures with Ge/Si quantum dots can be used to develop mid-infrared detectors.

Keywords: quantum dots, GeSi, absorption, time-resolved spectra

Funding: DAF acknowledges a financial support from the Russian Centre for Science Information (RCSI) 20-52-05004. HAS and DBH acknowledge a financial support from the RA Science Committee (grant SCS 20RF-041). RVU and MYV also acknowledge a support from the Ministry of Science and Higher Education of the Russian Federation (state assignment FSEG-2023-0016). ISM also acknowledges a support from the Basic Research Program of the National Research University Higher School of Economics.

Citation: Ustimenko R.V., Karaulov D.A., Vinnichenko M.Ya., Makhov I.S., Firsov D.A., Sarkisyan H.A., Sargsian T.A., Hayrapetyan D.B., Photoinduced light absorption in Ge/Si quantum dots, St. Petersburg State Polytechnical University Journal. Physics and Mathematics. 17 (1.1) (2024) 105–112. DOI: https://doi.org/10.18721/JPM.171.117

This is an open access article under the CC BY-NC 4.0 license (https://creativecommons.org/licenses/by-nc/4.0/)

Материалы конференции
УДК 535.3
DOI: https://doi.org/10.18721/JPM.171.117

Фотоиндуцированное поглощение света в квантовых точках Ge/Si

Р.В. Устименко [1] ✉, Д.А. Караулов [1], М.Я. Винниченко [1], И.С. Махов [2], Д.А. Фирсов [1],
А.А. Саркисян [3], Т.А. Саргсян [3, 4], Д.Б. Айрапетян [3, 4]

[1] Санкт-Петербургский политехнический университет Петра Великого, Санкт-Петербург, Россия;
[2] Национальный исследовательский университет «Высшая школа экономики», Санкт-Петербург, Россия;
[3] Российско-Армянский университет, Ереван, Армения;

© Ustimenko R.V., Karaulov D.A., Vinnichenko M.Ya., Makhov I.S., Firsov D.A., Sarkisyan H.A., Sargsian T.A., Hayrapetyan D.B., 2024. Published by Peter the Great St. Petersburg Polytechnic University.

[4] Институт химической физики НАН РА, Ереван, Армения;
✉ ratmirustimenko@yandex.ru

Аннотация. Исследовано фотоиндуцированное поглощение света в наноструктурах с легированными квантовыми точками Ge/Si, а также в нелегированных структурах. Получены спектры фотоиндуцированного поглощения при криогенных температурах при прямой и непрямой в реальном пространстве резонансной межзонной накачке, а также их временная динамика. Два высокоэнергетичных пика в спектрах можно связать с межуровневыми дырочными переходами из основного и возбужденного состояний квантовых точек в непрерывный спектр. Низкоэнергетичный пик соответствует межуровневым переходам дырок между основным и возбужденным состояниями точек. Временная динамика затухания высокоэнергетичных пиков может быть описана через быструю и медленную компоненты, связанные с особенностями захвата фотовозбужденных носителей на уровни в квантовой точке. Возможным применением структур с квантовыми точками Ge/Si могут быть детекторы среднего инфракрасного диапазона.

Ключевые слова: квантовые точки, GeSi, поглощение, спектры с временным разрешением

Финансирование: ДАФ благодарит за финансовую поддержку Российский центр научной информации (грант РЦНИ № 20-52-05004). ААС и ДБА благодарят за финансовую поддержку комитет по науке Республики Армения (грант SCS 20RF-041). РВУ и МЯВ благодарят за финансовую поддержку Минобрнауки РФ (гос. задание № FSEG-2023-0016). ИСМ благодарит за финансовую поддержку программу фундаментальных исследований НИУ ВШЭ.

Ссылка при цитировании: Устименко Р.В., Караулов Д.А., Винниченко М.Я., Махов И.С., Фирсов Д.А., Саркисян А.А., Саргсян Т.А., Айрапетян Д.Б. Фотоиндуцированное поглощение света в квантовых точках Ge/Si // Научно-технические ведомости СПбГПУ. Физико-математические науки. 2024. Т. 17. № 1.1. С. 105–112. DOI: https://doi.org/10.18721/ JPM.171.117

Статья открытого доступа, распространяемая по лицензии CC BY-NC 4.0 (https://creativecommons.org/licenses/by-nc/4.0/)

Introduction

The study of the properties of quantum dots (QDs) is one of the promising directions in the development of optoelectronic devices [1, 2] for applications in various fields from medicine and energetics to electronics and astrophysics. QDs have certain advantages over quantum wells and bulk materials. Three-dimensional confinement of electrons and holes leads to a discrete spectrum of quantized states inside the QD. By controlling the size and composition of QDs, it is possible to obtain the necessary energies of interlevel, intraband and interband transitions of charge carriers, i.e., control the spectral range in which the structure can operate. Various devices can be created based on QDs, in particular photodetectors [3] or lasers with optical and electric pumping at room temperature [4, 5].

Photodetectors based on Ge/Si QDs operating in the mid and far (terahertz) infrared spectral ranges offer several advantages and features compared to quantum well detectors. Among them, for example, the ability to use normal radiation incidence, facilitating the creation of matrix photodetectors [6], high surface density of dots, long lifetime of nonequilibrium charge carriers, compatibility with silicon electronics, enabling the implementation of silicon-based integrated electronic devices [7]. Silicon is widely used in electronics due to its ability to form transistor structures and thin insulator layers. However, unlike QD nanostructures, it is not well-suited for creating light-emitting structures due to its indirect gap of the bulk material. The interband photoluminescence (PL) spectrum of Ge/Si QDs lies in the region of photon energies lower than the band gap of silicon. In CMOS technology [8], this is fundamentally important, both for the development of new devices such as integrated photosensitive arrays in the near and mid-IR

© Устименко Р.В., Караулов Д.А., Винниченко М.Я., Махов И.С., Фирсов Д.А., Саркисян А.А., Саргсян Т.А., Айрапетян Д.Б., 2024. Издатель: Санкт-Петербургский политехнический университет Петра Великого.

spectral ranges, and for the development of a fundamentally new architecture of integrated optical micro- and nanoelectronics based on silicon. Therefore, the urgent task is to find ways to integrate QDs with silicon technology to fully exploit the advantages of optical information transmission in transistor chips. However, on the way to achieving this goal, the problem arises of the insufficiency of the fundamental basis describing the levels and states of charge carriers in Ge/Si QDs.

In addition, QDs can be used to confirm the fundamental principles of quantum theory of particle interactions. The ability to change the number of charge carriers localized in QDs by adjusting the doping level or through the interband optical pumping makes it possible to study many-particle interactions, including the applicability of the generalized Kohn theorem [9, 10].

The objective of this work is to study the dynamic characteristics of photoinduced light absorption in Ge/Si QDs. This study aims to provide information on the distribution of equilibrium and nonequilibrium charge carriers across states inside the QD.

Samples and experimental setup

Nanostructures with QDs were grown using molecular beam epitaxy on a Si(100) substrate. These nanostructures consisted of 10 layers of Ge/Si QDs, which were separated by 15 nm thick Si layers. The QDs were obtained by deposition of 7 monolayers of Ge. In order to prevent mixing of the wetting layer and the resulting islands, Ge/Si QDs were formed using the method of deposition of a surfactant (Sb) before deposition of Ge [11, 12]. This method leads to a decrease in the size of Ge islands, sharpening of their boundaries [13] and an increase in the density of the QD array. As a result, QDs were formed by a Ge_xSi_{1-x} solid solution with an average germanium content of $x \sim 60–65\%$. The surface density of the QD islands was about $2 \cdot 10^{11}$ cm^{-2}. Doping with an acceptor boron impurity was carried out by introducing a δ-layer in each silicon layer at a distance of 5 nm from each Ge layer. In this work, samples with an impurity concentration of $8 \cdot 10^{11}$ cm^{-2}, as well as undoped structures, were studied. The dimensions of the QDs were determined using transmission electron microscopy. It was found that the QD islands had an average base size of 14 nm and an average height of 2.7 nm.

The minimum of the conduction band of silicon lies in the <100> direction of the Brillouin zone between Γ and *X* points at point Δ. In Ge the conduction band minimum is located at point *L* at the band boundary in the <111> direction [14]. Thus, the position of the minimum of the conduction band changes from Δ to *L* depending on the concentration of germanium in the GeSi solid solution. It is known that at a Ge concentration of less than 80%, the band structure of the GeSi solid solution is similar to Si. The conduction band profile of a structure with Ge/Si QDs, formed by sixfold degenerate Δ-valleys, depends on the direction due to the splitting of the valleys by compressive and tensile stresses arising during the growth of the structure. In the <001> growth direction, this leads to the formation of a type-II heterointerface with a double Δ-valley (see Fig. 1, solid lines). In the plane of the QD layers in the <100> and <010> directions, four Δ-valleys form a type-I heterointerface (see Fig. 1, dashed lines) [15, 16].

After growing the samples were manufactured in multi-pass geometry. The input and output edges of the sample were grinded at an angle of 45° in order to increase the optical path for probing radiation in the sample due to total internal reflection. This sample geometry also made it possible to measure absorption for *s*- and *p*-polarized light.

Previously, we estimated the energy of hole states in a quantum dot using a simple "quantum box" model [17]. The solution was obtained for a constant potential inside a dot, which was represented in the form of a rectangular parallelepiped with dimensions corresponding to the real sizes of quantum dots. This model took into account the finite height of the confining potential and the difference in effective masses. The schematic band diagram of Ge/Si QDs in Fig. 1 illustrates some energy levels of holes and electrons. Additionally, the figure also includes scheme of charge carrier transitions during interband optical pumping (arrows).

Photoinduced intraband absorption spectra for stationary and time-resolved conditions were obtained using a Bruker Vertex 80v Fourier transform spectrometer with a KBr beamsplitter and a HgCdTe photovoltaic detector cooled to liquid nitrogen temperature with a Ge entrance window. Optical pumping was carried out using continuous-wave Nd:YAG solid-state laser (modulation 600 Hz) with radiation wavelengths of 532 nm or 1064 nm, and pulsed Nd:YAG solid-state laser (pulse duration 10 ns, repetition frequency 20 Hz) with radiation wavelength of 532 nm. The sample was placed in a Janis PTCM-4-7 closed-cycle cryostat with an operating temperature of

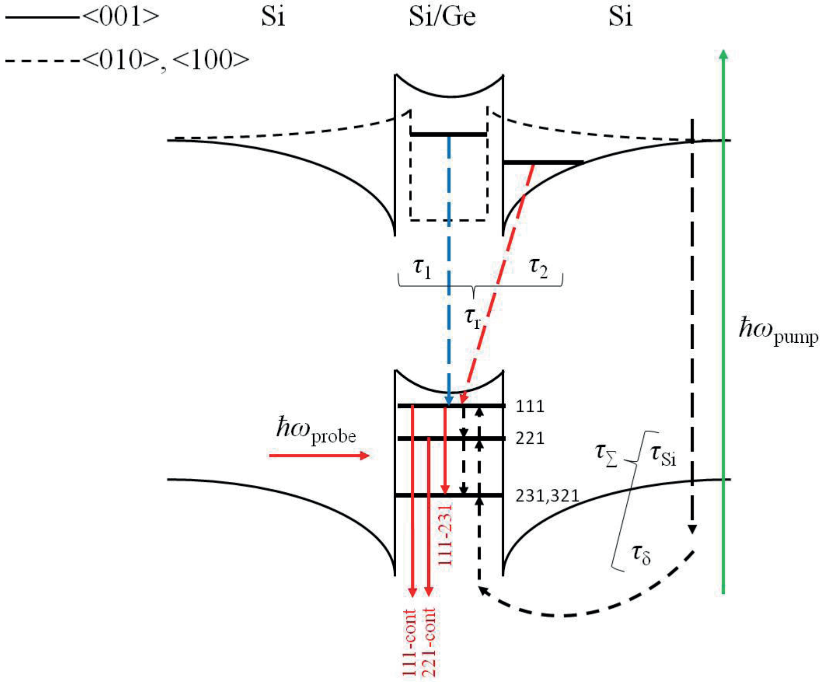

Fig. 1. Schematic representation of the band diagram of Ge/Si QDs in a silicon matrix. Optical transitions within QD states, processes of interband pumping and recombination of photoexcited charge carriers are shown by arrows

4.2–300 K. The globar radiation was directed to the sample through a ZnSe window, optical pumping was carried out through a fused silica window.

Experimental results

The spectra of changes in the intensity of light $|\Delta I|$ transmitted through an undoped sample were obtained using continuous-wave laser (see Fig. 2) at different pump powers and different wavelengths. Excitation of nonequilibrium charge carriers was carried out in two different ways. In the first case, direct in real-space interband optical pumping with a wavelength of 532 nm was used (see green arrow in Fig. 1). In the second case, indirect real-space resonant (1064 nm) pumping was realized from the hole levels in a potential well in a QD to an electron level in a potential well at the heterointerface between the type-II potential barrier of a QD and silicon, arising in the growth direction in the silicon matrix. The obtained absorption spectra of *p*-polarized radiation revealed peaks corresponding to hole transitions from the ground level 111 to the continuous spectrum with a photon energy of 280 meV (arrow 111 → cont), from the excited level 221 to the continuum above the QD with a photon energy of 230 meV (arrow 221 → cont) and peak with a photon energy of 130 meV (arrow 111 → 231), associated with absorption of hole from the ground level 111 to the degenerate excited level 321, 231. These peaks were discovered earlier when measuring equilibrium absorption in QDs [18]. Peak 111 → 321, 231 also manifests itself in the photoinduced absorption spectra for *s*-polarized radiation. This is due to the fact that absorption at these interlevel transitions, according to the polarization selection rules, should occur only for light polarized perpendicular to the growth axis of the structure, and such a polarization component in the geometry of our experiment present in both *s*- and *p*-polarized radiation. A comparison of non-resonant and resonant in real-space pumping showed that the capture time of charge carriers from the barrier to the QD does not affect the photoinduced absorption spectra.

Fig. 3 shows the spectra of transmission changes observed when the undoped sample was pumped with 532 nm continuous-wave radiation at different temperatures. These spectra were obtained by normalizing spectra plotted in Fig. 2 to the equilibrium spectra $\Delta T = |\Delta I| / I_{\text{equilibrium}}$. The spectra contain the previously described peaks for p-polarized light. As the temperature increases, the intensity of 111 → cont peak decreases at slower rate compared to the 221 → cont peak.

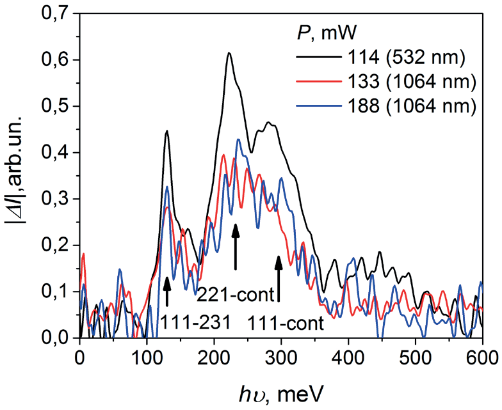

Fig. 2. Photoinduced change in the intensity of p-polarized radiation in undoped QDs for wavelength of pumping light $\lambda = 523$ nm (black curve) and $\lambda = 1064$ nm (blue and red curves) at $T = 4.2$ K

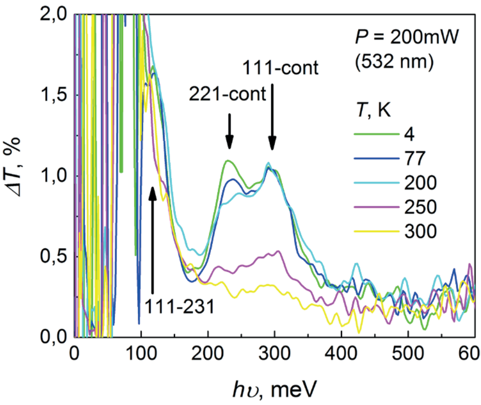

Fig. 3. Spectra of p-polarized transmission changes of undoped QDs under $\lambda = 523$ nm pumping at different temperatures

This behavior is associated with the temperature broadening of the excited level. As mentioned above, interlevel transitions 111 → 321, 231 contribute to the absorption spectra of light of both p- and s-polarization and are weakly identified in the equilibrium absorption spectra. Consequently, during the normalization the peak 111 → 321, 231 becomes indistinguishable in the noise. Similar measurements were carried out in a doped sample, i.e. at an initially higher concentration of holes in the QD. The obtained results demonstrate that at a given doping level, the peak corresponding to the transition from the ground state begins to dominate, while the peak corresponding to transitions from the excited state to the continuous spectrum is lost against its background.

The influence of pumping intensity on the photoinduced absorption spectra was also analyzed. All photoinduced absorption spectra were decomposed into three Gaussian contours. From a comparison of the dependences of the peak areas on the optical pump power, it is clear that the peak associated with transitions from the ground state to the continuous spectrum, with a photon energy of 280 meV, grows faster than the peak corresponding to the transitions from the excited state to the continuous spectrum with an energy of 230 meV. The peak 111 → 321, 231, with a photon energy of about 130 meV, remained virtually unchanged with increasing optical pump power. This is due to the fact that additional optical pumping uniformly increases the concentration of charge carriers at the 111 and 321, 231 levels, while only slightly increasing the number of charge carriers in the continuous spectrum above the QD.

Furthermore, time-resolved spectra of photoinduced absorption were obtained using direct interband high-power pulse pumping at a wavelength of 532 nm with a pulse duration of 10 ns (see Fig. 4). The time slice at the moment of laser radiation arrival corresponds to the previously mentioned spectra.

Based on the previously studied dynamics of photoinduced absorption with a fixed probe radiation energy of 300 meV, which corresponds to the 111 → cont transitions [19, 20], the dynamics of absorption decay can be described in terms of fast and slow components. In the present work, contrary to [19, 20], we studied the time dynamic features of the entire absorption spectrum. Fig. 1 schematically illustrates several relaxation paths of photoexcited charge carriers. The fast component τ_r is associated with the probability of direct τ_1 and indirect τ_2 interband transitions in real space, while the slow component τ_Σ is determined by the probability of charge carrier recombination τ_{Si} in Si and the probability of carrier capture in QDs τ_δ.

The dynamics of charge carriers in Ge/Si QDs under optical pumping with 532 nm radiation wavelength is described taking into account recombination in the QDs, capture of charge carriers from the bulk Si matrix, and ejection of carriers into the bulk from the QDs. The kinetic equation can be expressed as follows [20]:

$$\frac{dp}{dt} = -\frac{p}{\tau_r} + \gamma p_b(t)\left(N_{QD} - p\right) - \alpha p, \qquad (1)$$

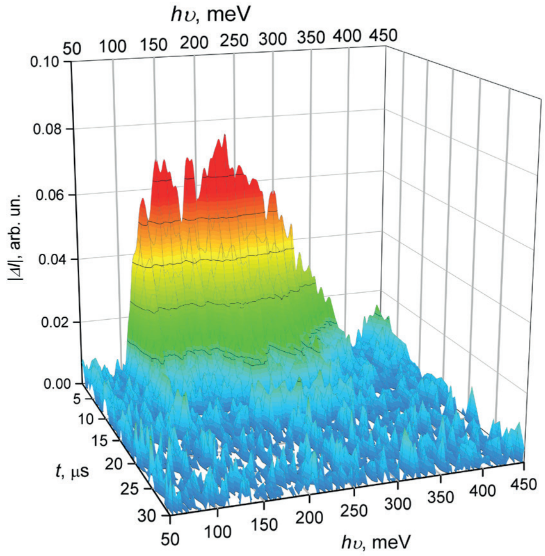

Fig. 1. Schematic representation of the band diagram of Ge/Si QDs in a silicon matrix. Optical transitions within QD states, processes of interband pumping and recombination of photoexcited charge carriers are shown by arrows

where p is the surface density of holes inside QDs, NQD is the number of localized states per unit area of the QD layer, $p_b(t)$ is the concentration of holes in the bulk Si, γ is the capture rate coefficient of holes in QD, α is the coefficient of thermal rate ejection of holes from QD.

This equation does not have an analytical solution in the general case, however, the rate of decay of photoinduced absorption can be empirically described by the sum of two exponential functions [20]:

$$p(t,T)=C_1\exp\left(-\frac{t}{\tau_r(T)}\right)+C_2\exp\left(-\frac{t}{\tau_\Sigma(T)}\right). \tag{2}$$

The fast τ_r and slow τ_Σ components of charge carrier relaxation were determined by approximating the time dependences of the photoinduced absorption decay using expression (2) at different temperatures of the sample with undoped QDs and a time resolution of 200 ns. From the obtained temperature dependences of $\tau_r(T)$ and $\tau_\Sigma(T)$, the amplitude of the peaks associated with transitions from the first and second states to the continuum with energies of 280 and 230 meV, respectively, decreases in accordance with expression (2) and can be described by two components. At $T = 4$ K, the times of the slow and fast components for the 111 → cont peak are 28 and 1.8 μs, respectively. For the 221 → cont peak, the component times are 2.7 and 0.2 μs, respectively. It is worth noting that the peak associated with the interlevel transition 111 → 321, 231 has a time component τ_Σ that, in this case could not be described by the used model. This prevents us to reliably determine the corresponding time. The fast decay time τ_r for interlevel transitions is 2.5 μs at 4 K, which corresponded to the same component in intraband transitions from ground 111 level.

Conclusions

Spectra of photoinduced absorption and transmission of polarized radiation were experimentally obtained in the mid-infrared spectral range for Ge/Si QDs. The measurements were conducted under direct (532 nm) and indirect in real-space resonant (1064 nm) interband optical pumping. Peaks associated with hole transitions from the ground and excited states to the continuous spectrum as well as a peak associated with interlevel hole transitions between the ground and excited states were detected.

A study of the dynamics of the decay of photoinduced absorption during pulsed interband pumping showed that the time dependence of high-energy peaks in the spectrum can be approximated by a biexponential function. The fast decay time of the relaxation curve is associated with the probability of interband recombination in the QD, while the slow time is associated with the capture and ejection of holes in the QD. Analysis of the time dependence of the low-energy peak indicated that recombination processes associated with interlevel transitions occur much slower than processes with transitions to a continuous spectrum above the QD.

Acknowledgments

DAF acknowledges a financial support from the Russian Centre for Science Information (RCSI) 20-52-05004. HAS and DBH acknowledge a financial support from the RA Science Committee (grant SCS 20RF-041). RVU and MYV also acknowledges a support from the Ministry of Science and Higher Education of the Russian Federation (state assignment FSEG-2023-0016). ISM also acknowledges a support from the Basic Research Program of the National Research University Higher School of Economics.

REFERENCES

1. **Bimberg D., Pohl U.W.,** Quantum dots: promises and accomplishments, Materials Today, 14 (9) (2011) 388–397.

2. **García de Arquer F.P. Talapin D.V., Klimov V.I., Arakawa Y., Bayer M., Sargent E.H.,** Semiconductor quantum dots: Technological progress and future challenges, Science. 373 (2021) eaaz8541.

3. **Lim H., Tsao S., Zhang W., Razeghi M.,** High-performance InAs quantum-dot infrared photodetectors grown on InP substrate operating at room temperature, Applied physics letters, 90 (13) (2007) 131112.

4. **Anantathanasarn S., Nötzel R., van Veldhoven P.J.,van Otten F.W.M., Barbarin Y., Servanton G., de Vries T., Smalbrugge E., Geluk E.J., Eijkemans T.J., Bente E.A.J. M., Oei Y.S., Smit M.K., Wolter J.H.,** Wavelength controlled InAs/InP quantum dots for telecom laser applications, Microelectronics journal, 37(12) (2006) 1461–1467.

5. **Chen S., Li W., Wu J., Jiang Qi, Tang M., Shutts S., Elliott S.N., Sobiesierski A., Seeds A.J., Ross I., Smowton P.M., Liu H.,** Electrically pumped continuous-wave III–V quantum dot lasers on silicon, Nature Photonics. 10 (2016) 307–311.

6. **Rappaport N., Finkman E., Brunhes T., Boucaud P., Sauvage S., Yam N., Le Thanh V., Bouchier D.,** Midinfrared photoconductivity of Ge/Si self-assembled quantum dots, Applied Physics Letters. 77 (20) (2000) 3224–3226.

7. **Krasilnik Z.F., Novikov A.V., Lobanov D.N., Kudryavtsev K.E., Antonov A.V., Obolenskiy S.V., Zakharov N.D., Werner P.,** SiGe nanostructures with self-assembled islands for Si-based optoelectronics, Semiconductor science and technology, 26 (2011) 014029.

8. **Le Royer C.,** Interfaces and performance: What future for nanoscale Ge and SiGe based CMOS, Microelectronic engineering. 88 (7) (2011) 1541–1548.

9. **Hayrapetyan D.B., Kazaryan E.M., Sarkisyan H.A.,** On the possibility of implementation of Kohn's theorem in the case of ellipsoidal quantum dots, Journal of Contemporary Physics (Armenian Academy of Sciences). 48 (2013) 32–36.

10. **Sarkisyan H.A., Hayrapetyan D.B., Petrosyan L.S., Kazaryan E.M., Sofronov A.N., Balagula R.M., Firsov D.A., Vorobjev L.E., Tonkikh A.A.,** Realization of the Kohn's theorem in Ge/Si quantum dots with hole gas: Theory and experiment, Nanomaterials. 9 (1) (2019) 56.

11. **Tonkikh A., Zakharov N., Talalaev V., Werner P.,** Ge/Si (100) quantum dots grown via a thin Sb layer, Physica status solidi RRL. 4 (8-9) (2010) 224–226.

12. **Tonkikh A.A., Zakharov N.D., Pippel E., Werner P.,** Sb-modified growth of stacked Ge/Si (100) quantum dots, Thin Solid Films. 519(11) (2011) 3669–3673.

13. **Tonkikh A.A., Zakharov N.D., Novikov A.V., Kudryavtsev K.E., Talalaev V.G., Fuhrmann B., Leipner H.S., Werner P.,** Sb mediated formation of Ge/Si quantum dots: Growth and properties, Thin Solid Films, 520 (8) (2012) 3322–3325.

14. **Kasper E., Lyutovich K.,** Properties of silicon germanium and SiGe: carbon, IET: Edison, NJ. (2000).

15. **El Kurdi M., Sauvage S., Fishman G., Boucaud P.,** Band-edge alignment of SiGe/Si quantum wells and SiGe/Si self-assembled islands, Physical Review B. 73 (2006) 195327.

16. **Schmidt O.G., Eberl K., Rau Y.,** Strain and band-edge alignment in single and multiple layers of self-assembled Ge/Si and GeSi/Si islands, Physical Review B. 62 (24) (2000) 16715.

17. **Anikeeva M.S., Vinnichenko M.Ya., Firsov D.A., Vorobjev L.E., Tonkikh A.A.,** Optical absorption in quantum dots Ge/Si at different population densities of the dots states, St. Petersburg State Polytechnical University Journal: Physics and Mathematics. 4 (158) (2012) 9–15.

18. **Vinnichenko M.Y., Makhov I.S., Ustimenko R.V., Sargsian T.A., Sarkisyan H.A., Hayrapetyan D.B., Firsov D.A.,** Doping effect on the light absorption and photoluminescence of Ge/Si quantum dots in the infrared spectral range, Micro and Nanostructures. 169 (2022) 207339.

19. **Sofronov A.N., Vorobjev L.E., Firsov D.A., Panevin V.Yu., Balagula R.M., Werner P., Tonkikh A.A.,** Photoinduced mid-infrared intraband light absorption and photoconductivity in Ge/Si quantum dots, Superlattices and Microstructures, 87 (2015) 53–57.

20. **Balagula R.M., Sofronov A.N., Vorobjev L.E., Firsov D.A., Tonkikh A.A.,** Temperature evolution of the photoexcited charge carriers dynamics in Ge/Si quantum dots, Physica E: Low-dimensional Systems and Nanostructures, 106 (2019) 85–89.

THE AUTHORS

USTIMENKO Ratmir V.
ratmirustimenko@yandex.ru
ORCID: 0000-0003-4123-4375

KARAULOV Danila A.
donil793@yandex.ru
ORCID: 0009-0002-1608-3659

VINNICHENKO Maksim Ya.
mvin@spbstu.ru
ORCID: 0000-0002-6118-0098

MAKHOV Ivan S.
imahov@hse.ru
ORCID: 0000-0003-4527-1958

FIRSOV Dmitry A.
dmfir@rphf.spbstu.ru
ORCID: 0000-0003-3947-4994

SARKISYAN Hayk A.
hayk.sarkisyan@rau.am
ORCID: 0000-0002-3739-6171

SARGSIAN Tigran A.
tigran.sargsian@rau.am
ORCID: 0000-0001-6594-6460

HAYRAPETYAN David B.
david.hayrapetyan@rau.am
ORCID: 0000-0001-6461-072X

Received 13.12.2023. Approved after reviewing 30.01.2024. Accepted 26.02.2024.

St. Petersburg Polytechnic University Journal. Physics and Mathematics. 2024 Vol. 17. No. 1.1
Научно-технические ведомости СПбГПУ. Физико-математические науки. 17 (1.1) 2024

Conference paper
UDC 538.94
DOI: https://doi.org/10.18721/JPM.171.118

Photosensitive nanostructures based on gallium phosphide nanowires and carbon dots

I.A Kozko [1, 2] ✉, E.P. Karaseva [2], Z.F. Sosnovitskaia [2], M.S. Istomina [4, 5],
V.V. Fedorov [1, 2], S.V. Shmakov [2], V.M. Kondratev [2, 3], A.D. Bolshakov [2, 3, 6, 7]

[1] Peter the Great St. Petersburg Polytechnic University, St. Petersburg, Russia;
[2] Alferov University, St. Petersburg, Russia;
[3] Moscow Institute of Physics and Technology (State University), Dolgoprudny, Moscow Region, Russia;
[4] Almazov National Medical Research Centre, St. Petersburg, Russia;
[5] St. Petersburg Electrotechnical University "LETI", St. Petersburg, Russia
[6] Yerevan State University, Yerevan, Armenia
[7] St. Petersburg State University, St. Petersburg, Russia
✉ ivkozko@gmail.com

Abstract. This research is devoted to study of the photosensitive properties of gallium phosphide epitaxial nanowires (NWs) decorated with carbon dots (CDs). The deposition of CDs facilitates the development of a new functional GaP/CDs material with electronic and optical characteristics distinct from those of the original pristine NWs. The photosensitivity of GaP NWs, both before and after the decoration, was assessed by analyzing their I-V characteristics and impedance spectra when subjected to light irradiation of ultraviolet (UV), visible, and infrared (IR) ranges. The findings reveal a significant photoresistive response of pristine GaP NWs when exposed to UV and blue light (390 nm and 470 nm wavelengths, correspondingly). In contrast, GaP NWs / CDs heterostructures exhibit a spectrally broader photoresistive response to light irradiation within the wavelength range of 390 to 850 nm. The results of this study highlight the potential use of the developed functional nanomaterial for fabricating photodetectors capable of operating across a wide spectral range, utilizing a relatively simple fabrication protocol.

Keywords: GaP, nanowires, carbon dots, photodetector

Funding: This study was funded by Ministry of Science and Higher Education of the Russian Federation (Agreement 075-03-2023-106, project FSMG-2021-0005).

Citation: Kozko I.A., Karaseva E.P., Sosnovitskaia Z.F., Istomina M.S., Fedorov V.V., Shmakov S.V., Kondratev V.M., Bolshakov A.D., Photosensitive nanostructures based on gallium phosphide nanowires and carbon dots, St. Petersburg State Polytechnical University Journal. Physics and Mathematics. 17 (1.1) (2024) 113–118. DOI: https://doi.org/10.18721/JPM.171.118

This is an open access article under the CC BY-NC 4.0 license (https://creativecommons.org/licenses/by-nc/4.0/)

Материалы конференции
УДК 538.94
DOI: https://doi.org/10.18721/JPM.171.118

Фоточувствительные наноструктуры на основе нитевидных нанокристаллов фосфида галлия и углеродных точек

И.А. Козко [1, 2] ✉, Е.П. Карасева [2], З.Ф. Сосновицкая [2], М.С. Истомина [4, 5],
В.В. Фёдоров [1, 2], С.В. Шмаков [2], В.М. Кондратьев [2, 3], А.Д. Большаков [2, 3, 6, 7]

© Kozko I.A., Karaseva E.P., Sosnovitskaia Z.F., Istomina M.S., Fedorov V.V., Shmakov S.V., Kondratev V.M., Bolshakov A.D., 2024. Published by Peter the Great St. Petersburg Polytechnic University.

[1] Санкт-Петербургский политехнический университет Петра Великого, Санкт-Петербург, Россия;
[2] Академический университет им. Ж.И. Алфёрова РАН, Санкт-Петербург, Россия;
[3] Московский физико-технический институт (государственный университет),
г. Долгопрудный, Московская обл., Россия;
[4] Национальный медицинский исследовательский центр им. В. А. Алмазова, Санкт-Петербург, Россия
[5] Санкт-Петербургский государственный электротехнический
университет «ЛЭТИ», Санкт-Петербург, Россия;
[6] Ереванский государственный университет, Ереван, Армения
[7] Санкт-Петербургский государственный университет, Санкт-Петербург, Россия
✉ ivkozko@gmail.com

Аннотация. В данной работе исследуются фоточувствительные свойства эпитаксиальных нитевидных нанокристаллов (ННК) фосфида галлия, а также пути их модификации углеродными точками (УТ). ННК GaP демонстрируют выраженный фоторезистивный отклик при облучении светом УФ и синего диапазона (390 нм и 470 нм, соответственно). Гибридные стуктуры GaP/УТ демонстрируют спектрально широкий фоторезистивный отклик к световому излучению в диапазоне от 390 до 850 нм. Результаты данной работы интересны, в первую очередь, с точки зрения возможности использования разработанного функционального наноматериала для создания фотодетекторов широкого спектрального диапазона согласно простому и технологичному протоколу.

Ключевые слова: фосфид галлия, нитевидный нанокристалл, углеродные точки, фотодетектор, детектор видимого света

Финансирование: Министерство науки и высшего образования Российской Федерации (соглашение 075-03-2023-106, грант FSMG-2021-0005).

Ссылка при цитировании: Козко И.А., Карасева Е.П., Сосновицкая З.Ф., Истомина М.С., Фёдоров В.В., Шмаков С.В., Кондратьев В.М., Большаков А.Д. Фоточувствительные наноструктуры на основе нитевидных нанокристаллов фосфида галлия и углеродных точек // Научно-технические ведомости СПбГПУ. Физико-математические науки. 2024. Т. 17. № 1.1. С. 113–118. DOI: https://doi.org/10.18721/ JPM.171.118

Статья открытого доступа, распространяемая по лицензии CC BY-NC 4.0 (https://creativecommons.org/licenses/by-nc/4.0/)

Introduction

The advancement of nanophotonics and quantum nanotechnologies has sparked significant demand for a new elemental and component base within quantum devices, encompassing light sources [1], waveguides [2], resonators [3], photodetectors [4], and sensors [5, 6]. Notably, semiconductor nanowires (NWs) obtained with molecular beam epitaxy, exhibiting a typical cross-sectional size of 50–300 nm and lengths ranging from hundreds of nanometers to several millimeters, present a promising avenue for leveraging their unique light absorption properties. Owing to their nanometer-scale cross-section, NWs manifest discernible differences in electronic and optical properties relative to bulk materials, while retaining a certain ease of post-growth processing due to their micrometer length. Additionally, NWs boast a substantial surface area to volume ratio, making it feasible to modify their surface with a range of nanostructures [7, 8]. These attributes render NWs highly versatile for fabricating memory elements, photodiodes, and photodetectors spanning various optical ranges, alongside their application in solar cells [9].

Semiconductor materials like gallium phosphide (GaP) can be synthesized in a NW geometry, offering both feasibility and efficient integration of III-V materials on silicon [10]. GaP NWs exhibit significant photoabsorption in the UV and blue light spectral ranges. However, their photosensitive characteristics can be effectively altered by applying coatings with altered absorption spectra. Such hybrid functional nanomaterials can be actively used to fabricate efficient detectors for visible light [11] and UV radiation [12].

This study introduces a novel approach for decoration of GaP NWs with carbon dots (CDs). Carbon dots (CDs) represent an advanced and distinctive class of modern nanomaterials that were

© Козко И.А., Карасева Е.П., Сосновицкая З.Ф., Истомина М.С., Фёдоров В.В., Шмаков С.В., Кондратьев В.М., Большаков А.Д., 2024. Издатель: Санкт-Петербургский политехнический университет Петра Великого.

initially derived by purifying single-walled carbon nanotubes in 2004 [13]. Since their inception, CDs have garnered considerable interest owing to their promising optoelectronic features properties, including adjustable absorption and emission. The photoluminescent characteristics of CDs present new opportunities for the processing of photosensitive nanomaterials, such as the hybrid nanostructure we are developing in this study.

Materials and Methods

The GaP NWs used in this work were synthesized with molecular beam epitaxy through a self-catalytic mechanism on a Si substrate with (111) orientation [10] using Veeco Gen-III machine (Veeco, St. Paul, USA). The morphology of the vertical arrays of GaP NWs was examined by scanning electron microscopy (SEM) (Zeiss Supra25, Carl Zeiss, Germany). The grown NWs exhibited a length of 25–30 μm and a typical cross-sectional size of approximately 200 nm (Fig. 1, *a*).

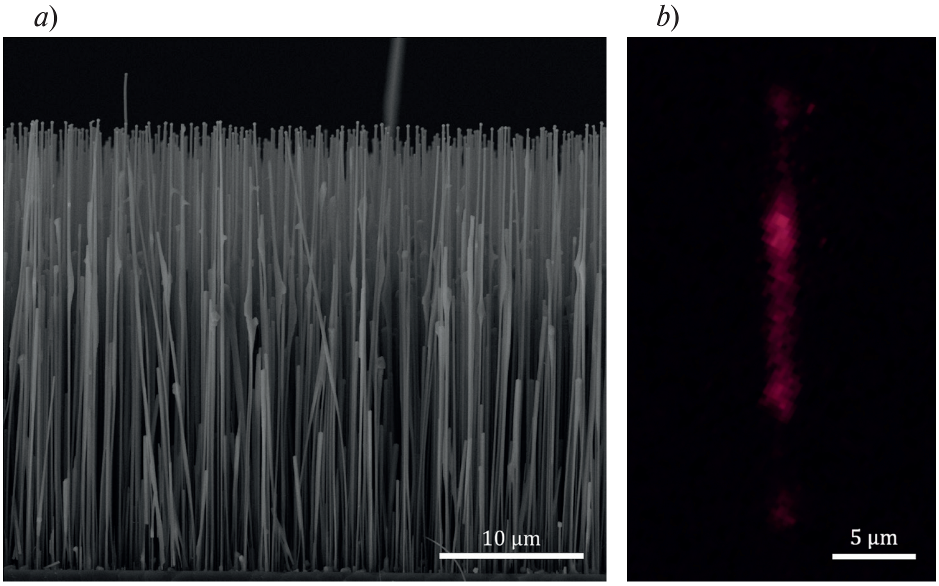

Fig. 1. SEM image of the as-synthesized vertical GaP NWs (*a*) and confocal image of the GaP NW/CDs on the measuring platform with interdigital gold contacts (laser wavelength: 561 nm; optical filter used for obtained image was set for central wavelength at 629 nm and a bandwidth of 62 nm) (*b*)

Carbon dots were derived from L-Lysine using a microwave-assisted technique [7]. The carbon precursors were diluted in water to achieve a homogeneous solution. Subsequently, the solution was transferred to a round bottom flask. Porous silicon plates were then added, initiating the microwave pyrolysis process. As the synthesis progressed, the color of the solution changed from colorless to dark brown, that indicated the carbonization reaction. Afterwards, the flask was cooled down to room temperature, and the silicon wafers were then removed.

To alter the photoresistive properties of the NWs, the synthesized vertical GaP NW array was transferred from a growth silicon substrate into an aqueous solution of CDs using an ultrasonic bath.

The photoresistive properties of the synthesized nanostructures were analyzed by examining their I-V characteristics using the SMU Keithley 2401 (Keithley Instruments, Solon, USA) and by performing electrical impedance spectroscopy using the impedancemeter TETRON-RLC501 (TETRON, Moscow, Russia). To fabricate the sensitive device, the GaP NWs, both pristine and modified, were placed on auxiliary platforms with interdigital gold contacts. The distribution of the NWs on the platform surface was studied using confocal microscopy with an AxioObserver Z1 microscope (Carl Zeiss, Oberkochen, Germany), as depicted in Fig. 1, *b*.

The photosensitive properties of GaP NWs before and after the modification were examined through the analysis of the I-V curves and impedance spectra under light irradiation with wavelengths of 390 nm, 470 nm, 570 nm, 622 nm, and 850 nm.

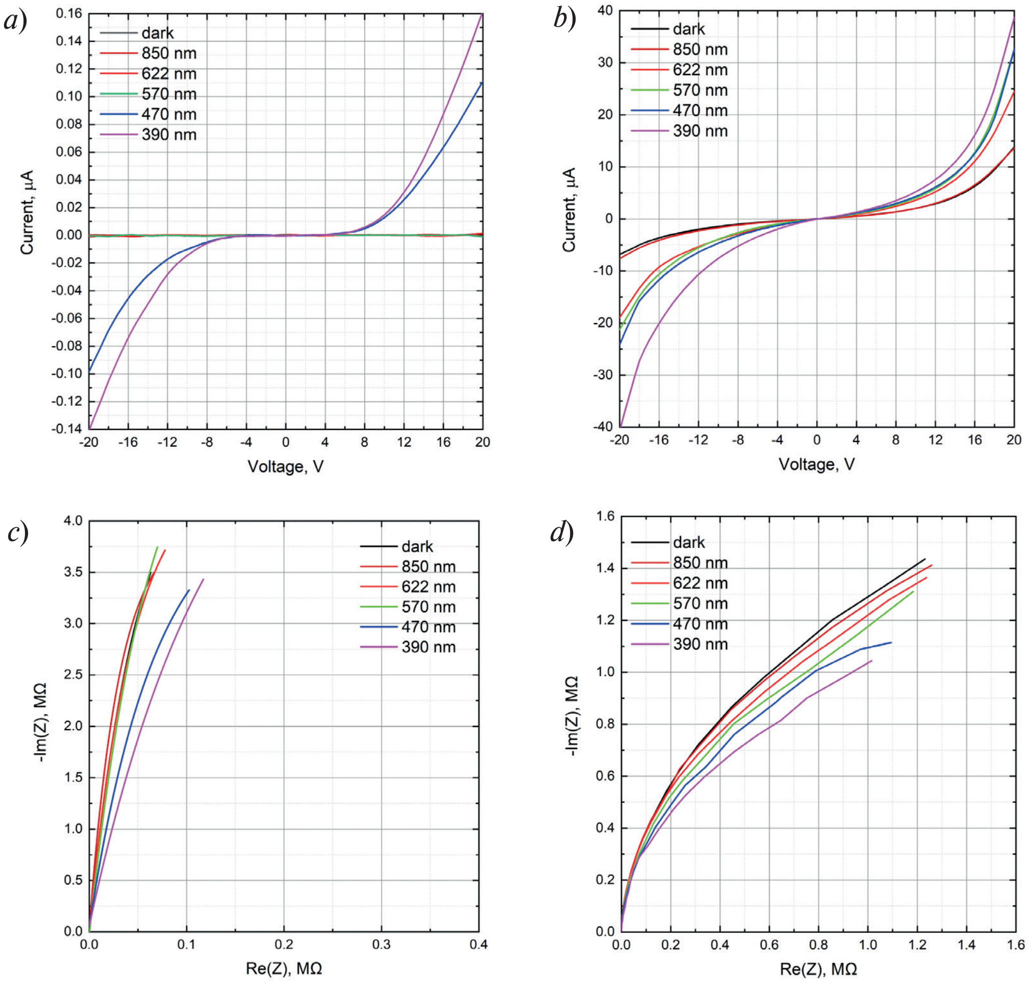

Fig. 2. Current–voltage characteristic demonstrating photoresponses of the non-modified GaP NWs (*a*) and GaP NWs/CDs (*b*), electrochemical impedance (Z) spectroscopy curves demonstrating photoresponses of the non-modified GaP NWs (*c*) and GaP NWs+CDs (*d*)

Results and Discussion

The confocal microscopy images revealed the fluorescence of GaP/CDs NWs under 561 nm laser illumination, and the spectral position of the observed fluorescence was estimated using an optical filter with a bandwidth of 598–660 nm (Fig. 1, *b*). Given the indirect GaP band structure, the observed fluorescence can be attributed solely to the CDs coating on the NW surface.

The CDs used in our study exhibit significant absorption in the visible range when in an aqueous solution [7]. Nonetheless, their photoabsorption undergoes considerable change after deposition, attributed to the agglomeration of the dots on the surface of the NWs. This effect is evident from the results of the performed electrophysical measurements (Fig. 2, *b*, Fig. 2, *d*).

The results depicted in Fig. 2, *b* and Fig. 2, *d* can be attributed to the effective transfer of charge carriers generated under light irradiation in the carbon coating into the conductive channel of the NWs. This process alters the electrical resistance of the NWs. Measurements of such resistance in both a DC and AC circuit can be used for detecting blue and UV light by unmodified NWs (Fig. 2, *a*, Fig. 2, *c*), and for detecting UV, visible, and near-IR light by GaP/CDs (Fig. 2, *b*, Fig. 2, *d*). Analysis of the I-V curves reveals the presence of a Schottky-type potential barrier at the NW-gold interface, which is responsive to changes in external conditions, akin to other semiconductor sensors and photodiodes featuring a Schottky barrier [5, 6].

The unmodified GaP NWs exhibited notable photoresponse exclusively under the blue and UV illumination (Fig. 2, *a*), in agreement with the optical absorption spectra of GaP [14]. Following modification with the CDs, the photosensitivity range of GaP extended to the visible optical range up to specific wavelengths (470, 570, 622, and 850 nm), accompanied by a significant increase in photocurrents, reaching tens of microamperes (Fig. 2, *b*).

Conclusion

In this study, we explore the photosensitive properties of GaP NWs modified by CD coating. Electrophysical measurements reveal a substantial extension of the photoabsorption range of GaP, that was optically transparent for visible light detection prior to the described modification. Our findings highlight the potential use of the synthesized GaP/CDs nanostructures for developing photodetectors with a broad spectral range. The obtained functional nanomaterial is of significant interest for advancing the nanophotonics and quantum nanodevices based on GaP [15-17].

Acknowledgments

A.D.B. and V.M.K. thanks the Ministry of Science and Higher Education of the Russian Federation (Agreement 075-03-2023-106, project FSMG-2021-0005) for support of experiments.

REFERENCES

1. **Kadinskaya S.A., Kondratev V.M., Kindyushov I.K., Koval O.Y., Yakubovsky D.I., Kusnetsov A., Lihachev A.I., Nashchekin A.V., Akopyan I.K., Serov A.Y., Labzovskaya M.E., Mikushev S.V., Novikov B.V., Shtrom I.V., Bolshakov A.D.,** Deep-Level Emission Tailoring in ZnO Nanostructures Grown via Hydrothermal Synthesis, Nanomaterials 13 (2023) 58.
2. **Kuznetsov A., Moiseev E., Abramov A.N., Fominykh N., Sharov V.A., Kondratev V. M., Shishkin I.I., Kotlyar K.P., Kirilenko D.A., Fedorov V.V., Kadinskaya S.A., Vorobyev A.A., Mukhin I.S., Arsenin A.V., Volkov V.S., Kravtsov V., Bolshakov A.D.,** Elastic Gallium Phosphide Nanowire Optical Waveguides – Versatile Subwavelength Platform for Integrated Photonics. Small, 19 (2023) 2301660.
3. **Molina J., E. Escobar J., Ramos D., Gil-Santos E., Ruz J.J., Tamayo J., San Paulo Á., Calleja M.,** High Dynamic Range Nanowire Resonators, Nano Lett. 21(15) (2021) 6617—24.
4. **Mauthe S., Baumgartner Y., Sousa M., Ding Q., Rossell M.D., Schenk A., Czornomaz L., Moselund K.E.,** High-speed III-V nanowire photodetector monolithically integrated on Si, Nat Commun, 11 (2020) 4565.
5. **Kondratev V.M., Vyacheslavova E.A., Shugabaev T., Kirilenko D.A., Kuznetsov A., Kadinskaya S.A., Shomakhov Z.V., Baranov A.I., Nalimova S.S., Moshnikov V.A., Gudovskikh A.S., Bolshakov A.D.,** Si Nanowire-Based Schottky Sensors for Selective Sensing of NH_3 and HCl via Impedance Spectroscopy, ACS Applied Nano Materials, 6 (13) (2023) 11513-11523.
6. **Aubekerov K., Punegova K. N., Sergeenko R., Kuznetsov A., Kondratev V.M., Kadinskaya S.A., Nalimova S.S., Moshnikov V.A.,** Synthesis and study of gas sensitive $ZnFe_2O_4$-modified ZnO nanowires, J. Phys.: Conf. Ser. 2227 (2022) 012014.
7. **Nenashev G.V., Istomina M.S., Kryukov R.S., Kondratev V.M., Shcherbakov I.P., Petrov V.N., Moshnikov V.A., Aleshin A.N.,** Effect of Carbon Dots Concentration on Electrical and Optical Properties of Their Composites with a Conducting Polymer, Molecules 27 (2022) 8000.
8. **Kuznetsov A., Prithu Roy, Grudinin D.V., Kondratev V.M., Kadinskaya S.A., Vorobyev A.A., Kotlyar K.P., Ubyivovk E.V., Fedorov V.V., Cirlin G.E., Mukhin I.S., Arsenin A.V., Volkov V.S., Bolshakov A.D.,** Self-assembled Photonic structure: Ga optical antenna on GaP Nanowire, Nanoscale, 15 (2023) 2332–2339.
9. **Zhang, Y., Liu H.,** Nanowires for High-Efficiency, Low-Cost Solar Photovoltaics, Crystals, 9 (2019) 87.
10. **Fedorov V.V., Berdnikov Y., Sibirev N.V., Bolshakov A.D., Fedina S.V., Sapunov G.A., Dvoretckaia L.N., Cirlin G., Kirilenko D.A., Tchernycheva M., Mukhin I.S.,** Tailoring Morphology and Vertical Yield of Self-catalyzed GaP Nanowires on Template-Free Si substrates, Nanomaterials. 11 (8) (2021) 1949.
11. **Chen H., Li J., Cao S., Deng W., Zhang Y.,** InAs nanowire visible-infrared detector photoresponse engineering, Infrared Physics & Technology, 133 (2023) 104785.

12. **Li T., Fang F., Jia H., Li J., Wang X., Fang D., Fang X., Tang J., Wang X., Wei Z.,** Synthesis and Structural Properties of ZnO Nanowires Modified by Carbon Quantum Dots, 2015 International Conference on Optoelectronics and Microelectronics (ICOM), (2015) 400–403.

13. **Xu X., Ray R., Gu Y., Ploehn H.J., Gearheart L., Raker K., Scrivens W.A.,** Electrophoretic Analysis and Purification of Fluorescent Single-Walled Carbon Nanotube Fragments, J. Am. Chem. Soc., 126 (2004) 12736.

14. **Rud' V.Yu., Melebaev D., Krasnoshchekov V., Ilyin I., Terukov E., Diuldin M., Andreev A., Shamuhammedowa M., Davydov V.,** Photosensitivity of Nanostructured Schottky Barriers Based on GaP for Solar Energy Applications, Energies, 16 (2023) 2319.

15. **Dvoretckaia L.N., Bolshakov A.D., Mozharov A.M., Sobolev M.S., Kirilenko D.A., Baranov A.I., Mikhailovskii V.Yu., Neplokh V.V., Morozov I.A., Fedorov V.V., Mukhin I.S.,** GaNP-based photovoltaic device integrated on Si substrate. Solar Energy Materials and Solar Cells, 206 (2020) 110282.

16. **Roy P., Bolshakov A.D.,** Ga-GaP nanowire hybrid optical system for enhanced coupling, focusing and steering of light. Journal of Physics D: Applied Physics, 53 (29) (2020) 295101.

17. **Kuznetsov A., Roy P., Kondratev V.M., Fedorov V.V., Kotlyar K.P., Reznik R.R., Vorobyev A.A., Mukhin I.S., Cirlin G.E., Bolshakov A.D.,** Anisotropic Radiation in Heterostructured "Emitter in a Cavity" Nanowire. Nanomaterials, 12 (2) (2022) 241.

THE AUTHORS

KOZKO Ivan A.
ivkozko@gmail.com
ORCID: 0009-0006-0923-1501

KARASEVA Elizaveta P.
liza.karaseva@gmail.com
ORCID: 0009-0005-0777-6746

SOSNOVITSKAIA Zlata F.
sosnozlat@yandex.ru
ORCID: 0009-0006-2988-5027

ISTOMINA Maria S.
istomina_ms@almazovcentre.ru
ORCID: 0000-0002-2497-653X

FEDOROV Vladimir V.
burunduk.uk@gmail.com
ORCID: 0000-0001-5547-9387

SHMAKOV Stanislav V.
stas-svs@list.ru
ORCID: 0000-0002-9658-5036

KONDRATEV Valeriy M.
kvm_96@mail.ru
ORCID: 0000-0002-3469-5897

BOLSHAKOV Alexey D.
acr1235@mail.ru
ORCID: 0000-0001-7223-7232

Received 14.12.2023. Approved after reviewing 05.02.2024. Accepted 05.02.2024.

Conference paper
UDC 538.975
DOI: https://doi.org/10.18721/JPM.171.119

Temperature evolution of GaP nanowires photoelectronic properties

E.P. Karaseva [1] ✉, I.A. Kozko [2], M.A. Rider [3], M.S. Kovova [3],
V.V. Zakharov [3], S.V. Fedina [1], V.M. Kondratev [1, 4], A.D. Bolshakov [1, 4, 5, 6]

[1] Alferov University, St. Petersburg, Russia;
[2] Peter the Great St. Petersburg Polytechnic University, St. Petersburg, Russia;
[3] ITMO University, St. Petersburg, Russia;
[4] Moscow Institute of Physics and Technology (State University), Dolgoprudny, Moscow Region, Russia;
[5] Yerevan State University, Yerevan, Armenia;
[6] St. Petersburg State University, St. Petersburg, Russia
✉ karaseva_st21@spbau.ru

Abstract. This work is devoted to study photoelectric properties of GaP nanowires (NWs) modified by carbon nanodots (CDs). Photoelectric properties of samples were studied by electrochemical impedance spectroscopy (EIS) over a wide frequency range. Impedance spectra were shown in Nyquist plot in dark conditions and under ultraviolet (UV) illumination allowed to evaluate changes of active resistance of the NWs before and after modification with the CDs, in terms of resistance response. Temperature evolution of GaP NWs impedance spectra in the range from 25 to 205 °C before and after the modification was studied also in dark and UV conditions. The largest response reached 25% and was detected at room temperature in modified NWs. Heating of the samples lead to decreasing of response down to 25% with modified NWs, whereas for GaP the response did not exceed 13%. The result is interesting for processing of photosensitive detectors working in room temperature.

Keywords: nanowires, GaP, carbon nanodots, electrochemical impedance spectroscopy

Funding: This study was funded by Ministry of Science and Higher Education of the Russian Federation (Agreement 075-03-2023-106, project FSMG-2021-0005).

Citation: Karaseva E.P., Kozko I.A., Rider M.A., Kovova M.S., Zakharov V.V., Fedina S.V., Kondratev V.M., Bolshakov A.D., Temperature evolution of GaP nanowires photoelectronic properties, St. Petersburg State Polytechnical University Journal. Physics and Mathematics. 17 (1.1) (2024) 119–124. DOI: https://doi.org/10.18721/JPM.171.119

This is an open access article under the CC BY-NC 4.0 license (https://creativecommons.org/licenses/by-nc/4.0/)

Материалы конференции
УДК 538.975
DOI: https://doi.org/10.18721/JPM.171.119

Температурная эволюция фотоэлектронных свойств нитевидных нанокристаллов фосфида галлия

Е.П. Карасева [1] ✉, И.А. Козко [2], М.А. Ридер [3], М.С. Ковова [3],
В.В. Захаров [3], С.В. Федина [1], В.М. Кондратьев [1, 4], А.Д. Большаков [1, 4, 5, 6]

[1] Академический университет им. Ж.И. Алфёрова РАН, Санкт-Петербург, Россия;
[2] Санкт-Петербургский политехнический университет Петра Великого, Санкт-Петербург, Россия;
[3] Университет ИТМО, Санкт-Петербург, Россия;
[4] Московский физико-технический институт (государственный университет),

© Karaseva E.P., Kozko I.A., Rider M.A., Kovova M.S., Zakharov V.V., Fedina S.V., Kondratev V.M., Bolshakov A.D., 2024.
Published by Peter the Great St. Petersburg Polytechnic University.

г. Долгопрудный, Московская обл., Россия;
[5] Ереванский государственный университет, Ереван, Армения;
[6] Санкт-Петербургский государственный университет, Санкт-Петербург, Россия
✉ karaseva_st21@spbau.ru

Аннотация. Данная работа направлена на изучение фоторезистивных свойств нитевидных нанокристаллов фосфида галлия, а также путей их модификации углеродными наноточками (УТ). Свойства изучались в терминах спектроскопии электрохимического импеданса в широком диапазоне частот (100 Hz–500 kHz). Наибольшее изменение сопротивления при засветке ультрафиолетовым светом по сравнению с темновыми условиями показывают модифицированные УТ нитевидные нанокcристаллы GaP при 25 °C. Таким образом, эта работа может быть интересна при создании фотодетектора, работающего при комнатной температуре.

Ключевые слова: нитевидные нанокристаллы, углеродные точки, спектроскопия электрохимического импеданса, фотодетектор

Финансирование: Министерство науки и высшего образования Российской Федерации (соглашение 075-03-2023-106, грант FSMG-2021-0005).

Ссылка при цитировании: Карасева Е.П., Козко И.А., Ридер М.А., Ковова М.С., Захаров В.В., Федина С.В., Кондратьев В.М., Большаков А.Д. Температурная эволюция фотоэлектронных свойств нитевидных нанокристаллов фосфида галлия // Научно-технические ведомости СПбГПУ. Физико-математические науки. 2024. Т. 17. № 1.1. С. 119–124. DOI: https://doi.org/10.18721/ JPM.171.119

Статья открытого доступа, распространяемая по лицензии CC BY-NC 4.0 (https://creativecommons.org/licenses/by-nc/4.0/)

Introduction

Gallium phosphide (GaP) is a semiconductor material that is widely used in photonics, nanooptics and nanoelectronics. GaP and other III-V nanowires (NWs) can be obtained by molecular beam epitaxy (MBE) [1], chemical-vapor deposition (CVD) [2] and via another techniques [3]. GaP NWs exhibit peculiar optical properties. The latter allowed to develop optical cavities [4], waveguides [5] and light emitting devices [6]. GaP is not widely used as a material for photodetectors due to its wide bandgap (2.27eV) making it transparent in the visible range. Here we propose surface modification of GaP NWs allowing to tailor their optical properties. Heterostructured compositions based on GaP nanowires and organic photoabsorbing agents can be effectively used for the development of new generation photodetector devices. This work is aimed at studying the evolution of photoresistive properties of GaP NWs decorated with carbon dots (CDs) at different temperature conditions.

Materials and Methods

GaP NWs were grown on (111) Si substrate by molecular beam epitaxy (MBE) using a Veeco GEN III epitaxy machine. Morphology of NWs was investigated by scanning electron microscopy using Zeiss Supra25 (Carl Zeiss, Germany) at 5 kV accelerating voltage. NWs were separated from the substrate by ultrasonication (50 kHz, 30 seconds) in 120 μl of deionized water. CDs synthesized via hydrothermal method [7] were used to decorate the NWs. The CDs solution was shared between the two tubes. To decorate the NWs, 2 μl of CDs solution was added into one of tubes and shacked in a spin mixer. A few drops of each solution were applied onto the substrate with interdigitated gold contacts (DropSens Co. Ltd., Spain). Contact strip width/gap was 10 μm. Substrates were dried for 24 hours at room temperature. Overall three samples were fabricated: the first covered with pristine NWs, the second one with NWs decorated with the CDs and the third one covered with CDs.

Optical images of the samples were taken using Zeiss LSM 710, Carl Zeiss MicroImaging GmbH confocal microscope (Jena, Germany). 405 nm laser light illumination was used, collected light was filtered by 387–415 nm or 439–634 nm filters.

© Карасева Е.П., Козко И.А., Ридер М.Аю, Ковова М.С., Захаров В.В., Федина С.В., Кондратьев В.М., Большаков А.Д., 2024. Издатель: Санкт-Петербургский политехнический университет Петра Великого.

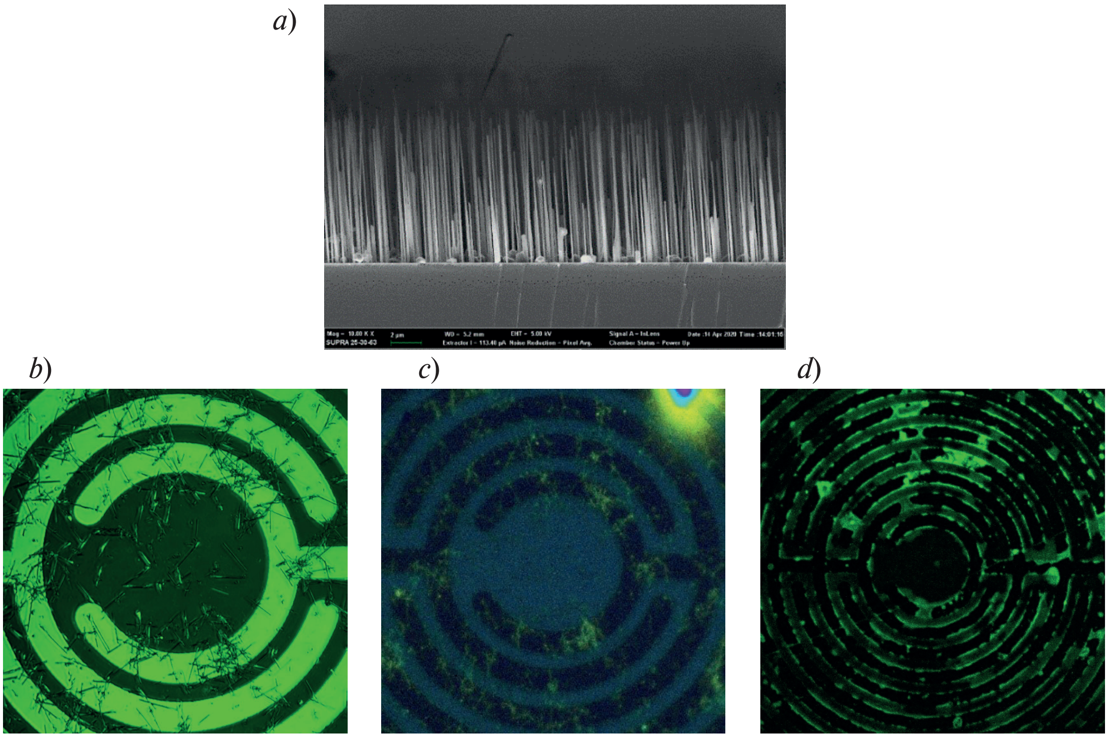

Fig. 1. SEM image of GaP NWs (*a*), bright field confocal microscopy image of GaP NWs on substrate with interdigitated contacts at 10 μm pitch (*b*), confocal microscopy image of GaP NWs covered with CDs with colors close to real (*c*), confocal microscopy image of CDs with colors close to real (*d*)

Study of the photoelectric properties of the obtained samples were carried out with the use of a Z500P impedance meter (Elins, Russia) in dark conditions and under ultraviolet (UV) diode illumination with optical power of 1200 mW. For all the samples the experiments were carried out at 25, 105, 155 and 205 °C to study the temperature effects. The impedance spectroscopy was employed at 100 mV bias in the 100 Hz–500 kHz frequency range, allowing for analysis of various electronic processes that may occur upon the UV exposure. Further analysis was made by plotting results in Nyquist coordinates [3].

Results and Discussion

The shape of the synthesized NWs is shown in Fig. 1, *a*. They are approximately 20 μm long and about 250 nm thick. Fig. 1, *b* shows the confocal image of GaP NWs on the substrate with interdigital gold contacts. A 405 nm laser, a 387–415 nm filter and a Fluar 20x/0.75 lens were used. Evidently, the light reflected from the gold contacts and places where the light is reflected in GaP NWs. These places are seen well because of high refractive index of GaP (about 4). When the filter is changed to 439–634 nm the image of this sample turns dark. Fig. 1, *c* shows the sample with modified GaP NWs under the 405 nm laser illumination. Here a 439–634 nm filter and an EC Epiplan-Apochromat 50x/0.95 lens are used. The optical image is taken in lambda-mode, i.e., each point of the sample was consecutively illuminated and excited photoluminescence was recorded. Pumping light is removed by filter from the reflected beam and bright spot in the image appears due to CD luminescence. Colors in Fig. 1, *b* are close to the real ones. It is clearly seen that GaP NWs covered with CDs are distributed all over the contact surface and some of them are able to provide electric connection between the pads. The image in Fig 1, *d* is also taken under 405 nm laser illumination and signal collected through 439–634 nm filter in lambda mode. It demonstrates that CDs are filling the space between the contacts but almost no CDs could be seen on the pads.

To study photoelectric properties of the samples, electro-chemical impedance spectra were measured and plotted in Nyquist coordinates (see Fig. 2, *a*–*c*). Impedance spectra of pristine GaP NWs sample taken at 25, 105, 155 and 205 °C in the dark and under UV illumination are shown in Fig. 2, *a*. Fig. 2, *b* shows spectra of sample with decorated NWs

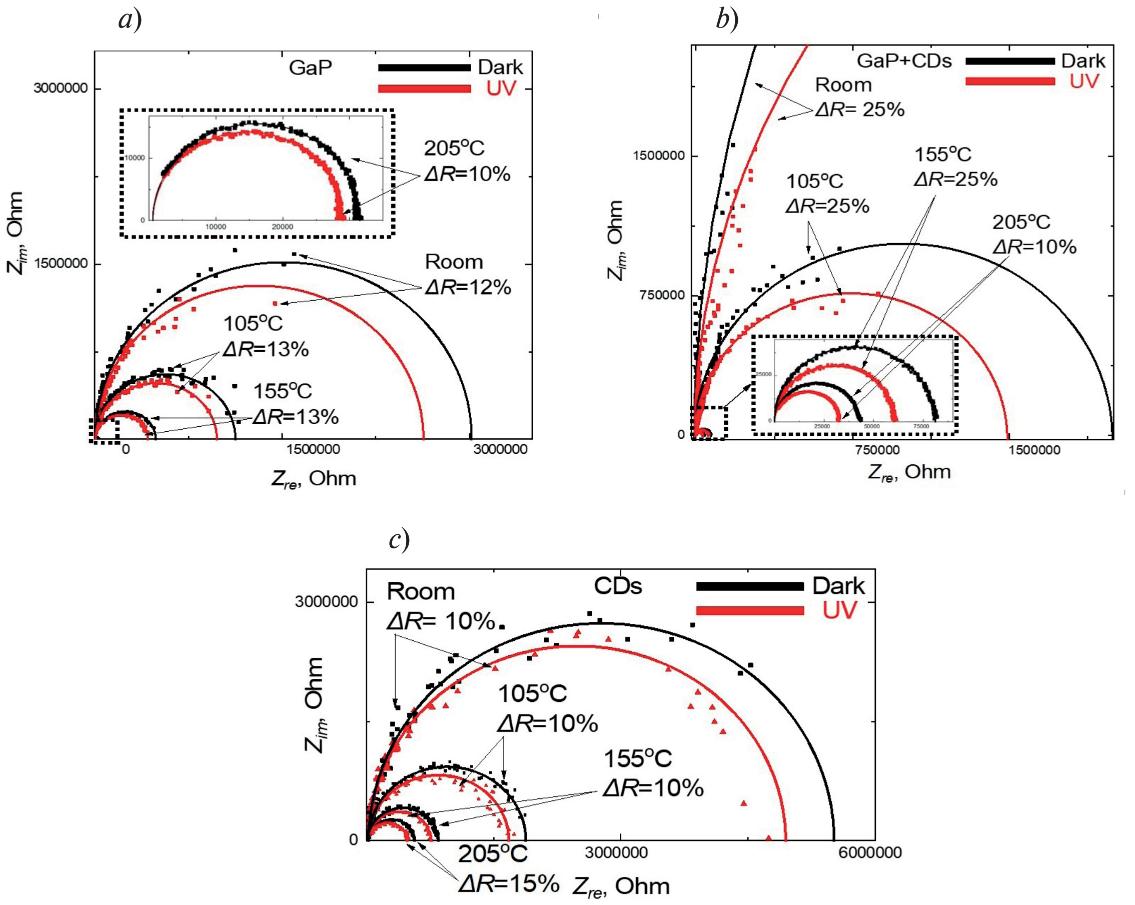

Fig. 2. Impedance spectroscopy of pristine GaP NWs (*a*), modified GaP NWs (*b*) and CDs on substrate with interdigital contacts (*c*)

taken in the same conditions is shown, Fig. 2, *c* shows spectra corresponding to CD-covered substrate. Impedance is a complex number or vector rotating in the complex polar ohmic plane: $Z = Z_{Re} - iZ_{Im}$. In Nyquist coordinates, the real part of impedance (Z_{Re}) is plotted on the x-axis, while the frequency-dependent imaginary part (Z_{Im}) is plotted on the *y*-axis. Each point on the impedance spectrum corresponds to a specific frequency of the measurement voltage, and the angle of inclination of the line connecting the origin of the coordinates with each point describes the phase of the measurement voltage. The projection of the spectrum on the x-axis indicates the active resistance of the sensor (R) under UV and dark conditions. The response of the samples in terms of ΔR was estimated using a simple expression $(R_{dark} - R_{UV})/R_{dark} \cdot 100\%$. For every sample, it is shown that its resistance decreases when the temperature increases. Furthermore, in every experiment the resistance in the dark was higher than under the UV light.

The difference in resistance for every sample at various temperatures is presented in Table. As shown in Table 1, for sample with pristine GaP NWs, the largest difference in the resistance between dark and light conditions is between 105–155 °C (13%), the lowest effect of illumination is at 205 °C (10%). Overall, the change of that difference is only about 3%. Thus, temperature has small influence on the electronic processes that takes place. On the other hand, substrate with CDs exhibits the highest response difference: 15% at high temperature (205 °C), whereas for the temperature range from 25 to 155 °C, the difference is about 10%. Resistance of the sample with modified GaP NWs drops with temperature rising, the highest response is obtained at 25 °C, the lowest at 205 °C. From all the experiments, the largest difference is for modified NWs at room temperature. Thus, it was found out that modification by CDs increased the photoabsorption. The highest impact was obtained at room temperature.

Table

UV-reaction of samples at different temperatures

Sample	Temperature, °C	Response, %
GaP	room	12
	105	13
	155	13
	205	10
CDs	room	10
	105	10
	155	10
	205	15
GaP+CDs	room	25
	105	25
	155	25
	205	10

Conclusion

Thus, in this work properties of GaP NWs and GaP NWs covered with CDs were studied. Modification by Carbon nanodots leads to a 4-fold increase in response compared to dark conditions, but with increasing temperature the difference decreases. The difference is vanished when the temperature rich 205 °C. So modified GaP NWs can be used for creating photodetectors working in room temperature.

Acknowledgments

A.D.B. and V.M.K. thanks the Ministry of Science and Higher Education of the Russian Federation (Agreement 075-03-2023-106, project FSMG-2021-0005) for support of experiments.

REFERENCES

1. **Kuznetsov A., Moiseev E., Abramov A.N., Fominykh N., Sharov V.A., Kondratev V.M., Shishkin I. I., Kotlyar K.P., Kirilenko D.A., Fedorov V.V., Kadinskaya S.A., Vorobyev A.A., Mukhin I.S., Arsenin A.V., Volkov V.S., Kravtsov V., Bolshakov A.D.,** Elastic Gallium Phosphide Nanowire Optical Waveguides – Versatile Subwavelength Platform for Integrated Photonics, Small. 19 (28) (2023) 1–11.

2. **Sun L., Yuan G., Gao L., Yang J., Chhowalla M., Gharahcheshmeh M.H., Gleason K.K., Choi Y.S., Hong B.H., Liu Z.,** Chemical vapour deposition, Nature reviews methods primers. 1 (5) (2021) 1–20.

3. **Kondratev V.M., Vyacheslavova E.A., Shugabaev T., Kirilenko D.A., Kuznetsov A., Kadinskaya S.A., Shomakhov Z.V., Baranov A.I., Nalimova S.S., Moshnikov V.A., Gudovskikh A.S., Bolshakov A.D.,** Si Nanowire-Based Schottky Sensors for Selective Sensing of NH3 and HCl via Impedance Spectroscopy, ACS Applied Nano Materials, 6 (13) (2023) 11513–11523.

4. **Kuznetsov A., Prithu Roy, Grudinin D.V., Kondratev V.M., Kadinskaya S.A., Vorobyev A.A., Kotlyar K.P., Ubyivovk E.V., Fedorov V.V., Cirlin G.E., Mukhin I.S., Arsenin A.V., Volkov V.S., Bolshakov A.D.,** Self-assembled Photonic structure: Ga optical antenna on GaP Nanowire, Nanoscale, 15 (2023) 2332–2339.

5. **Anikina M.A., Roy P., Kadinskaya S.A., Kuznetsov A., Kondratev V.M., Bolshakov A.D.,** Numerical Study of GaP Nanowires: Individual and Coupled Optical Waveguides and Resonant Phenomena, Nanomaterials. 13 (1) (2023) 1–11.

6. **Kuznetsov A., Roy P., Kondratev V.M., Fedorov V.V., Kotlyar K.P., Reznik R.R., Vorobyev A. A., Mukhin I.S., Cirlin G.E., Bolshakov A.D.,** Anisotropic Radiation in Heterostructured "Emitter in a Cavity" Nanowire, Nanomaterials. 12 (2) (2022) 1–13.

7. **Stepanova M., Dubavik A., Efimova A., Konovalova M., Svirshchevskaya E., Zakharov V., Orlova A.,** Magneto-Luminescent Nanocomposites Based on Carbon Dots and Ferrite with Potential for Bioapplication, Nanomaterials. 12 (9) (2022) 1–15.

THE AUTHORS

KARASEVA Elizaveta P.
karaseva_st21@spbau.ru
ORCID: 0009-0005-0777-6746

KOZKO Ivan A.
ivkozko@gmail.com
ORCID: 0009-0006-0923-1501

RIDER Maxim A.
riderm24@mail.ru
0009-0003-4890-683X

KOVOVA Maria S.
mariakovova@mail.ru
0009-0003-7988-7520

ZAKHAROV Viktor V.
viktor-zah@yandex.ru
0000-0001-9626-8543

FEDINA Sergey V.
ORCID: 0000-0001-7521-3754

KONDRATEV Valeriy M.
kvm_96@mail.ru
ORCID: 0000-0002-3469-5897

BOLSHAKOV Alexey D.
acr1235@mail.ru
ORCID: 0000-0001-7223-7232

Received 16.12.2023. Approved after reviewing 28.02.2024. Accepted 28.02.2024.

St. Petersburg Polytechnic University Journal. Physics and Mathematics. 2024 Vol. 17. No. 1.1
Научно-технические ведомости СПбГПУ. Физико-математические науки. 17 (1.1) 2024

Conference paper
UDC 538.911
DOI: https://doi.org/10.18721/JPM.171.120

Individual GaP nanowire conductivity studied with atomic force microscopy and numerical modeling

V.A. Sharov [1, 2] ✉, P.A. Alekseev [2], V.V. Fedorov [1], I.S. Mukhin [1]

[1] Alferov University, St. Petersburg, Russia;
[2] Ioffe Institute, St. Petersburg, Russia
✉ vl_sharov@mail.ru

Abstract. Growth strategies for achieving highly-doped GaP nanowires are investigated. Eight nanowire arrays are synthesized under different growth parameters via molecular beam epitaxy with the use of silicon and beryllium as *n*- and *p*- dopants. Electrical conductivity of individual nanowires from each array is investigated via conductive atomic force microscopy. The obtained current-voltage characteristics are numerically analyzed, the impact of nanowire geometry, contact properties and doping on the conductivity is estimated.

Keywords: nanowires, GaP, gallium phosphide, conductivity, doping, atomic force microscopy

Funding: This study was funded by Russian Science Foundation, grant 23-72-01082.

Citation: Sharov V.A., Alekseev P.A., Fedorov V.V., Mukhin I.S., Individual GaP nanowire conductivity studied with atomic force microscopy and numerical modeling, St. Petersburg State Polytechnical University Journal. Physics and Mathematics. 17 (1.1) (2024) 125–130. DOI: https://doi.org/10.18721/JPM.171.120

This is an open access article under the CC BY-NC 4.0 license (https://creativecommons.org/licenses/by-nc/4.0/)

Материалы конференции
УДК 538.911
DOI: https://doi.org/10.18721/JPM.171.120

Исследование проводимости одиночных нитевидных нанокристаллов GaP с помощью атомно-силовой микроскопии и численного моделирования

В.А. Шаров [1, 2] ✉, П.А. Алексеев [2], В.В. Федоров [1], И.С. Мухин [1]

[1] Академический университет им. Ж.И. Алфёрова РАН, Санкт-Петербург, Россия;
[2] Физико-технический институт им. А.Ф. Иоффе РАН, Санкт-Петербург, Россия
✉ vl_sharov@mail.ru

Аннотация. С помощью проводящей атомно-силовой микроскопии получены вольтамперные характеристики одиночных нитевидных нанокристаллов фосфида галлия, легированных кремнием и бериллием, выращенных методом молекулярно-пучковой эпитаксии при различных условиях. Построена численная модель для расчета вольтамперных характеристик, оценено влияние на проводимость ННК их геометрии и легирования, а также подвижности носителей заряда и величины барьера Шоттки с зондом. На основании проведенного анализа установлены режимы роста, оптимальные для синтеза высоколегированных *n*- и *p*- ННК фосфида галлия.

© Sharov V.A., Alekseev P.A., Fedorov V.V., Mukhin I.S., 2024. Published by Peter the Great St. Petersburg Polytechnic University.

Ключевые слова: нитевидные нанокристаллы, GaP, фосфид галлия, проводимость, легирование, атомно-силовая микроскопия

Финансирование: Работа выполнена при поддержке Российского Научного Фонда, проект № 23-72-01082.

Ссылка при цитировании: Шаров В.А., Алексеев П.А., Федоров В.В., Мухин И.С. Исследование проводимости одиночных нитевидных нанокристаллов GaP с помощью атомно-силовой микроскопии и численного моделирования // Научно-технические ведомости СПбГПУ. Физико-математические науки. 2024. Т. 17. № 1.1. С. 125–130. DOI: https://doi.org/10.18721/ JPM.171.120

Статья открытого доступа, распространяемая по лицензии CC BY-NC 4.0 (https://creativecommons.org/licenses/by-nc/4.0/)

Introduction

III-V semiconductor nanowires are promising as components of optoelectronic devices. In particular, gallium phosphide nanowires are prospective as nanophotonic waveguides and components of flexible light emitting diodes [1]. Despite the extensive worldwide research in the past decades, the commercial implementation of nanowires is still difficult. Today, doping control at the nanoscale is considered to be the last fundamental difficulty towards nanowire-based devices [2, 3]. In this work we investigate the doping control in GaP nanowires grown via molecular beam epitaxy (MBE) and study Be and Si behavior as dopants. We synthesize Be- and Si-doped GaP nanowire arrays and investigate the electrical properties of individual nanowires via complementary experimental and numerical techniques. First, the current-voltage characteristics (*I*–*V* curves) of vertical nanowires are obtained. Then, the doping level is estimated via numerical modeling of these curves. Importantly, herein we analyze individual nanowires rather than the averaged response from the whole arrays, providing more insights about nanoscale phenomena, which in fact determine the performance of macroscale nanowire array device.

Materials and Methods

Nanowire growth was carried out using Veeco Gen III MBE setup equipped with Si, Be and Ga effusion cells and valved phosphorous cracker cell. The nanowire arrays were synthesized on highly-doped (111) Si substrates via self-catalyzed vapor-liquid-solid (VLS) growth mechanism assisted by Ga droplet avoiding the use of foreign metal contamination, and thus providing lower impurity level and electrically active defects. Formation of GaP nanowires occurs at the pinhole defects of the silicon surface oxide facilitating the formation of catalytic Ga droplets required for vertical nanowire growth.

Conductive atomic force microscopy (C-AFM) was utilized to obtain *I*-*V* curves of individual nanowires using NT-MDT NTegra AFM setup and conductive probes with TiN and W2C coatings. The idea of the method is to use the grounded conductive probe as a top electric contact to an individual nanowire which is possible due to nanometer scale tip curvature radius and atomic scale positioning precision [4, 5]. The nanowire coordinates are preliminarily obtained in AFM scan. Bias voltage is then applied to the growth substrate, and the current passing through the nanowire is registered.

The numerical modeling was carried out in Silvaco Atlas finite element computational package, which is designed for semiconductor device simulations, solving Poisson's equation, carrier continuity equations and transport equations [6]. The proposed model possesses cylindrical symmetry, includes a nanowire with two electric contacts (bottom corresponds to GaP/Si heterobarrier, top to GaP/probe Schottky barrier). The simulation utilizes Klaassen model [7] describing band-to-band tunneling and Matsuzawa's Universal Schottky Tunneling model [8], describing the thermionic emission at the metal/semiconductor interface and the spatially distributed tunneling calculated at each semiconductor around the interface.

© Шаров В.А., Алексеев П.А., Федоров В.В., Мухин И.С., 2024. Издатель: Санкт-Петербургский политехнический университет Петра Великого.

Results and Discussion

Eight samples were fabricated. SEM image of each sample as-grown are shown in Fig. 1. Samples 1–4 (Fig. 1, *a*–*d* respectively) were doped with beryllium, while samples 5–8 (Fig. 1, *e*–*h*) were doped with silicon. The growth parameters are summarized in Table. Samples 2, 5 and 8 were grown in two-stage process, when a low-doped core is grown first, then the P flux is increased so that the catalytic cap collapses and vertical growth stops. Then the dopant flux is increased and highly-doped shell is grown. Other samples are grown in a one-step VLS process. Growth temperatures and V/III ratios are chosen so that the dopant incorporation does not preventing the nanowire growth.

Table

Growth parameters

Sample		1	2	3	4	5	6	7	8
Dopant		Be	Be	Be	Be	Si	Si	Si	Si
V/III	step 1	12	12	12	20	30	20	12	30
	step 2	–	30	–	–	12	–	–	39
T_{growth}, °C		640	630	680	640	640	640	610	630

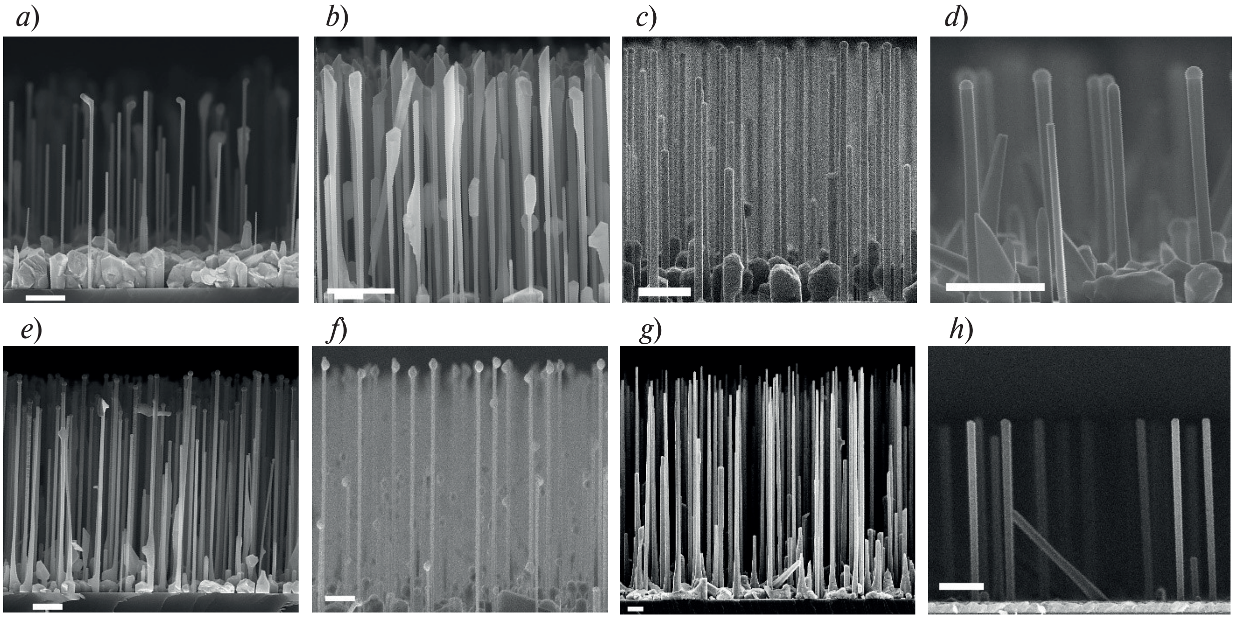

Fig. 1. SEM images of the grown samples. The panels from (*a*) to (*h*) correspond to samples 1–8 from Table
All scale bars are 1 μm long

Individual nanowire *I*–*V* curves of each sample were obtained with C-AFM. The experiment scheme is presented in Fig. 2, *a*. Several nanowires were investigated in each array, average obtained *I*–*V* curves are shown in Fig. 2, *b*. The obtained curves possess low noise level indicating that tip-nanowire electrical contact is stable. The curves were obtained in dark conditions to avoid the impact of photogeneration in Si substrate. All curves show rectifying behavior originating mainly from nanowire/tip Schottky and nanowire/substrate contacts. The curve shape varies significantly from sample to sample. Samples 1, 2, 5 show near-zero current. The most likely explanation for this lies in insufficient diameter of nanowires, so that the surface band bending takes place causing surface depletion which can't be compensated with moderate doping level. Sample 3 also shows near-zero current, indicating that the chosen growth temperature lies beyond the window of Be incorporation, which is in accordance with the literature [9]. Samples 6, 7 show

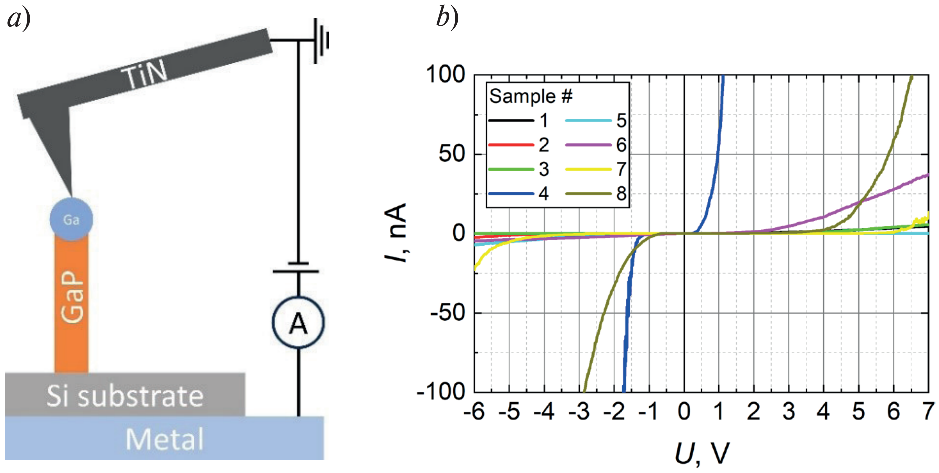

Fig. 2. C-AFM I-V curve measurement scheme (*a*), I—V curves from individual nanowires in each sample (*b*)

moderate current indicating that the doping level is high enough to create a conductive channel in the nanowire core. Samples 4 and 8 demonstrate the highest conductivity, which can be attributed with higher thickness followed by higher dopant incorporation rate.

Then, the numerical modeling of *I—V* curves was carried out in Silvaco TCAD. The nanowire is parametrized with its length *l*, radius *r*, doping level, carrier mobility μ, and GaP band parameters. The tip/nanowire contact is parametrized with Schottky barrier height, depending on probe work function Φ. Length *l* can be well estimated from SEM images while the exact *r* value for the studied wires is unknown, because nanowire thickness dispersion within the same array is pronounced. The accuracy of determining Φ and μ values is also limited. It is known that μ in nanowires can be several orders of magnitude lower than in bulk due to flat defects. Thus, we sweep μ from 0.1 to 20 cm^2/V·s. We also vary Φ from 4.5 to 5.2 eV based on the estimated values of the probe coatings work function.

Fig. 3 shows modeling results for 2 μm long p-doped nanowire grown on *p*-Si substrate, corresponding to sample 4. The dotted curves correspond to the experimental data. From the figure it follows that shifting carrier mobility, nanowire thickness or work function within physically reasonable range changes the current level within one order of magnitude. The curve shape is mainly governed by the nanowire doping level. 100 nm thick wire is fully depleted if the doping level is less than $1\cdot10^{19}$ cm^{-3}. However, increasing N_A twice, from $1\cdot10^{19}$ to $2\cdot10^{19}$ cm^{-3}, induces the increase of forward current by two orders of magnitude. Comparing the modeling results with the experimental curve from Fig. 2, we estimate the doping level of Sample 4 lies in the range from $1\cdot10^{19}$ to $3\cdot10^{19}$ cm^{-3}.

Fig. 4 shows the modeled *I—V* curves for 4 μm long *n*-GaP nanowire grown on *n*-Si substrate. The dotted curves correspond to the experimental data. The nanowire is considered to have core/shell structure with low doped core and high doped shell, which corresponds to the case of Sample 8. The core and shell are supposed to have the same thickness varying from 30 to 50 nm. The impact of core doping level N_D^{core} on nanowire conductivity is negligible until it is far less than the doping of the shell. The conductivity is determined by shell doping level N_D^{shell}. Increasing N_D^{shell} from $1\cdot10^{18}$ to $1\cdot10^{19}$ cm^{-3} leads to the increase of the forward current more than 2 orders of magnitude. Assuming $r_{core} = r_{shell} = 50$ nm, μ = 20 cm^2/V·s and Φ = 4.9 eV, the model predicts the doping level of sample 8 on the order of $3\cdot10^{18}$, a certain degree of discrepancy of modeled and experimental curves is probably due to more complicated real radial doping distribution and tip/nanowire contact geometry.

The dominating impact of doping level on nanowire conductivity can be explained via the balance between nanowire/substrate heterobarrier and nanowire/probe Schottky barrier. The current depends on the tunneling rate through the barriers, appearing at the high doping levels, rather than on thermionic emission. It should be noted that the proposed model does not take into account the nanowire surface states density and, as a consequence, the appearance of surface band bending on the nanowire side facets causing surface depletion. In fact, the nanowire conductivity

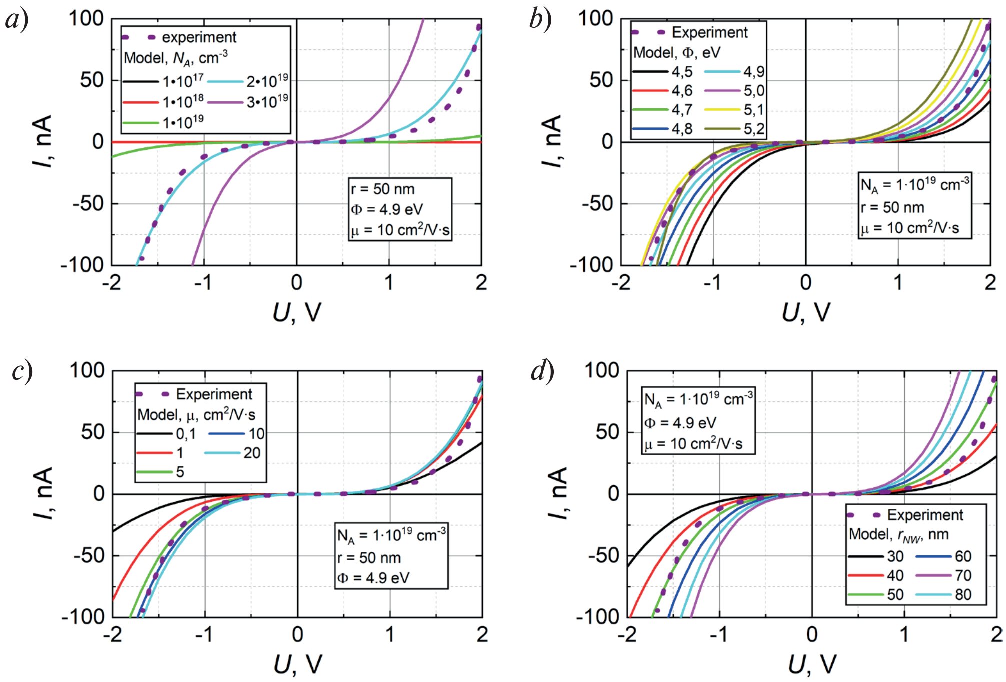

Fig. 3. Numerical modeling of I—V curves from p-GaP nanowire with varying doping level (a), work function (b), carrier mobility (c), radius (d)

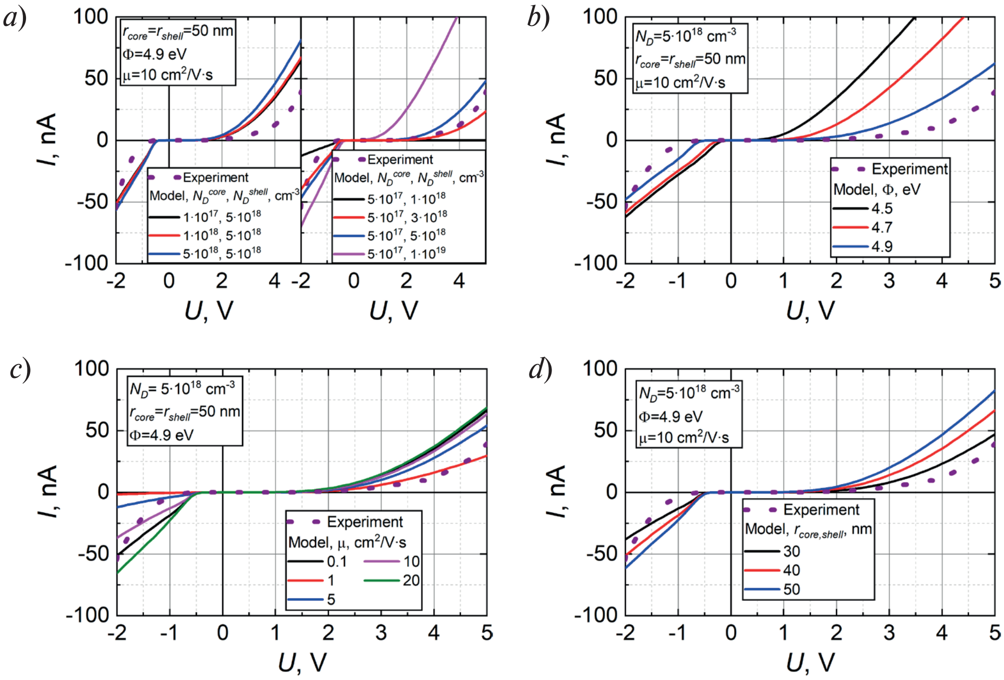

Fig. 4. Numerical modeling of I—V curves from n-GaP nanowire with varying doping level (a), Work function (b), carrier mobility (c), radius (d)

is determined by the doping level in conjunction with the nanowire thickness. However, the modeled samples are thick enough and their doping level is high enough so that the radius of surface depletion region is negligible, and the proposed doping estimations are valid.

Conclusion

Conductivity of individual MBE-grown Si- and Be- doped gallium phosphide nanowires is investigated via C-AFM by obtaining I—V curves following by their numerical analysis. The impact of nanowire geometry, doping level, carrier mobility and contact barrier on the conductivity is studied, the dominating role of the doping level is established. From the experiment it follows that *p*-GaP nanowires with high conductivity can be synthesized under flux ratio V/III = 20 and the growth temperature T_{gr} = 640 °C. The proposed model works well for homogenous Be-doped nanowire giving the doping level on the order of $1{\cdot}10^{19}$ cm^{-3}. In case of two-stage core/shell grown Si-doped nanowires, the model predicts the doping level on the order of $3{\cdot}10^{18}$ cm^{-3}.

Acknowledgments

V.A.S acknowledges support of the electric measurements and numerical modeling by Russian Science foundation (Grant No. 23-72-01082).

REFERENCES

1. **Kuznetsov A., Moiseev E., Abramov A.N., Fominykh N., Sharov V.A., Kondratev V.M., Shishkin I.I., Kotlyar K.P., Kirilenko D.A., Fedorov V.V., Kadinskaya S.A., Vorobyev A.A., Mukhin I.S., Arsenin A.V., Volkov V.S., Kravtsov V., Bolshakov A.D.,** Elastic Gallium Phosphide Nanowire Optical Waveguides—Versatile Subwavelength Platform for Integrated Photonics, Small. 19 (28) (2023) 2301660.

2. **Kim W., L. Güniat L., Fontcuberta A. Morral, Piazza V.,** Doping challenges and pathways to industrial scalability of III—V nanowire arrays, Applied Physics Reviews. 1 (8) (2021) 011304.

3. **Miroshnichenko A.S., Deriabin K.V., Baeva M., Kochetkov F.M., Neplokh V., Fedorov V.V., Mozharov A.M, Koval O.Yu., Krasnikov D.V., Sharov V.A., Filatov N.A., Gets D.S., Nasibulin A.G., Makarov S.V., Mukhin I.S., Kukushkin V.Yu., Islamova R.M.,** Flexible Perovskite $CsPbBr_3$ Light Emitting Devices Integrated with GaP Nanowire Arrays in Highly Transparent and Durable Functionalized Silicones. The Journal of Physical Chemistry Letters, 12 (39) (2021) 9672—9676.

4. **Alekseev P.A., Sharov V.A., Dunaevskiy M.S., Kirilenko D.A., Ilkiv I.V., Reznik R.R., Cirlin G.E., Berkovits V.L.,** Control of Conductivity of $In_xGa_{1-x}As$ Nanowires by Applied Tension and Surface States, Nano Letters. 19 (7) (2019) 4463—4469.

5. **Alekseev P.A., Sharov V.A., Borodin B.R., Dunaevskiy M.S., Reznik R.R., Cirlin G. E.,** Effect of the uniaxial compression on the GaAs nanowire solar cell, Micromachines. 11 (6) (2020) 581.

6. **Sarkar A.,** Device simulation using Silvaco ATLAS tool, in: Technology Computer Aided Design, CRC Press, 2018

7. **Hurkx G.A. M., Klaassen D., Knuvers M.,** A new recombination model for device simulation including tunneling, IEEE Transactions on Electron Devices. 39 (2) (1992) 331—338.

8. **Matsuzawa K., Uchida K., Nishiyama A.,** A unified simulation of Schottky and ohmic contacts, IEEE Transactions on Electron Devices. 47 (1) (2000) 103—108.

9. **Casadei A., Krogstrup P., Heiss M., Röhr J.A., Colombo C., Ruelle T., Upadhyay S., Sørensen C.B., Nygård J., Fontcuberta A. Morral,** Doping incorporation paths in catalyst-free Be-doped GaAs nanowires, Applied Physics Letters. 102 (1) (2013) 013117.

THE AUTHORS

SHAROV Vladislav A.
vl_sharov@mail.ru
ORCID: 0000-0001-9693-5748

FEDOROV Vladimir V.
burunduk.uk@gmail.com
ORCID: 0000-0002-2283-0086

ALEKSEEV Prokhor A.
npoxep@gmail.com
ORCID: 0000-0002-8143-4606

MUKHIN Ivan S.
imukhin@spbau.ru
ORCID: 0000-0001-9792-045X

Received 14.12.2023. Approved after reviewing 12.02.2024. Accepted 18.02.2024.

St. Petersburg Polytechnic University Journal. Physics and Mathematics. 2024 Vol. 17. No. 1.1
Научно-технические ведомости СПбГПУ. Физико-математические науки. 17 (1.1) 2024

Conference paper
UDC 533.922
DOI: https://doi.org/10.18721/JPM.171.121

Quality factor enhancement of spherical resonators by radial anisotropy

A. Eghbali [1] ✉, A.A. Vyshnevyy [1]

[1] Center for Photonics and 2D Materials, Moscow Institute of Physics and Technology (MIPT), Dolgoprudny, Russia

✉ eghbali.amir@phystech.edu

Abstract. High-quality resonances in open systems have ubiquitous applications in nanophotonics. However, it is challenging to achieve high quality factor in compact resonators due to the limitations on the refractive index of materials. Recently a novel family of high index materials was discovered, i.e., van der Waals materials. In addition to record-high refractive indices, they feature strong negative optical anisotropy, therefore their promise for the use in nanoresonators is not evident. Motivated by the progress in fabrication of spherical nanoparticles from these materials, here we study the effect of radial anisotropy on the quality of homogeneous nanospheres that support the Mie resonances. Our study reveals that material anisotropy can enhance the quality factor of Mie resonances. In particular, we show that the quality factor of electric dipole mode of the nanosphere made of radially anisotropic material is up to 29% higher than that of the optically isotropic nanosphere which has the same refractive index.

Keywords: nanoresonators, nanoparticles, van der Waals materials, giant optical anisotropy, Mie resonance

Funding: This study was funded the Russian Science Foundation grant 22-79-10312.

Citation: Eghbali A., Vyshnevyy A.A., Quality factor enhancement of spherical resonators by radial anisotropy, St. Petersburg State Polytechnical University Journal. Physics and Mathematics. 17 (1.1) (2024) 131–136. DOI: https://doi.org/10.18721/JPM.171.121

This is an open access article under the CC BY-NC 4.0 license (https://creativecommons.org/licenses/by-nc/4.0/)

Материалы конференции
УДК 533.922
DOI: https://doi.org/10.18721/JPM.171.121

Повышение добротности сферических резонаторов с помощью радиальной анизотропии

А. Эгбали [1] ✉, А.А. Вишневый [1]

[1] Центр фотоники и двумерных материалов, Московский физико-технический институт (национальный исследовательский университет), г. Долгопрудный, Россия

✉ eghbali.amir@phystech.edu

Аннотация. В данной работе выполнено исследование влияния оптической анизотропии на добротность Ми резонансов сферических наночастиц. Показано, что добротность электрической дипольной моды наносферы из радиально анизотропного материала может превышать доброcть аналогичной моды изотропной наносферы до 29%.

Ключевые слова: нанорезонаторы, наночастицы, ван-дер-ваальсовы материалы, гигантская оптическая анизотропия

© Eghbali A., Vyshnevyy A.A., 2024. Published by Peter the Great St. Petersburg Polytechnic University.

Финансирование: Работа выполнена при поддержке Российского научного фонда (грант № 22-79-10312).

Ссылка при цитировании: Эгбали А., Вишневый А.А. Повышение добротности сферических резонаторов с помощью радиальной анизотропии // Научно-технические ведомости СПбГПУ. Физико-математические науки. 2024. Т. 17. № 1.1. С. 131–136. DOI: https://doi.org/10.18721/ JPM.171.121

Статья открытого доступа, распространяемая по лицензии CC BY-NC 4.0 (https://creativecommons.org/licenses/by-nc/4.0/)

Introduction

Light confinement is a topic of great significance in the field of nanophotonics due to its wide-ranging applications [1–3]. Nanoresonators with high quality factors (Q-factors) are suitable for light confinement with a sufficient lifetime in a small volume. Such resonators can enhance the performance of various optical devices such as lasers [4], optical sensors [5] and solar cells [6]. The use of metallic cladding or high-refractive index dielectric materials can enhance the quality factor of compact nanoresonators. However, the use of metal leads to the intrinsic ohmic losses and the Q-factor of high-index dielectric Mie nanoresonators remains small due to the limitations on the refractive index of the materials, so alternative approaches are in high demand.

Our proposed solution in this study utilizes optical anisotropy. To ensure pure Mie resonances, it is crucial to maintain spherical symmetry within the resonator. Therefore, our focus is solely on examining the impact of radial anisotropy on the quality factor. By comparing the results, we observe that negative anisotropy increases the Q-factor even though it decreases the effective refractive index inside the anisotropic medium. Fortunately, transition metal dichalcogenides (TMDC) possess a remarkable ability to exhibit giant negative anisotropy [7], and there have been successful endeavors to fabricate spherical nanoparticles, which feature onion-like crystalline structure and, consequently, radially anisotropic dielectric permittivity tensor [8]. Our findings hold significant potential for the design of Mie resonators with high Q-factors. Also, we provide a tentative physical explanation of the counter-intuitive increase of Q-factor by strong negative anisotropy.

Materials and Methods

The complex eigenfrequencies $\omega = \omega' + i\omega''$ of the electric dipole (ED) resonances were found as poles of ED contribution to the scattering cross-section [9]. For calculations of the scattering cross-section at real and complex frequencies, we employed the spherical transfer matrix method [10] with the necessary adaptations to describe media with radially anisotropic optical response [11]. Finally, to calculate the quality factor of an eigenmode, we used:

$$Q = \frac{\omega'}{2|\omega''|}. \tag{1}$$

Our tentative explanations employ the notion of effective refractive index. Typically, for uniaxial media with a dielectric tensor $\varepsilon = \mathrm{diag}\,(\varepsilon_{||}, \varepsilon_{||}, \varepsilon_{\perp})$, this index is defined as

$$n_{eff}^{p} = \frac{\beta}{\beta_0} = \sqrt{\frac{\varepsilon_{\wedge}\varepsilon_{P}}{\varepsilon_{P}\sin^2\theta_1 + \varepsilon_{\wedge}\cos^2\theta_1}}, \tag{2}$$

where β and β_0 are the wavenumbers of p-polarized wave in the anisotropic medium and in vacuum respectively and θ_1 is the angle between the wavevector of the plane wave and the optical axis. When the refraction at the interface normal to the optical axis is considered, the angle of incidence and refraction obey Snell's law $n_{eff}^{p}\sin\theta_1 = n_2\sin\theta_2$, where n_2 is the refractive index of the adjacent medium and θ_2 is the angle of refraction.

Given these properties, one might expect that amplitude of reflection of p-polarized wave at

© Эгбали А., Вишневый А.А., 2024. Издатель: Санкт-Петербургский политехнический университет Петра Великого.

the interface is given by the Fresnel equation as $r = \dfrac{n_{eff}^{p} \cos\ \theta_2 - n_2 \cos\ \theta_1}{n_{eff}^{p} \cos\ \theta_2 + n_2 \cos\ \theta_1}$. However, this statement is wrong, and the reflection amplitude is actually given by [12]:

$$r = \frac{\dfrac{\varepsilon_P}{n_{eff}^{p}} \cos\theta_2 - n_2 \cos\theta_1}{\dfrac{\varepsilon_P}{n_{eff}^{p}} \cos\theta_2 + n_2 \cos\theta_1}. \tag{3}$$

It is evident from Eq. 3 that an “interface-related” effective refractive index should be introduced:

$$n_{eff}^{i} = \varepsilon_P / n_{eff}^{p}. \tag{4}$$

In fact, not only reflection amplitude but the whole transfer-matrix that connects complex amplitudes of plane waves across the interface can be calculated assuming that anisotropic medium is replaced by the isotropic one with a refractive index of n_{eff}^{i} [12]. To distinguish n_{eff}^{i} and n_{eff}^{p}, we will further refer to them as ‘propagation-related’ and ‘interface-related’ effective indices.

Results and Discussion

Before the determination of eigenmodes, we calculate ED contribution to the scattering cross-section spectra of homogeneous spheres of radius 100 nm with isotropy Fig. 1, *a* and with negative radial anisotropy Fig. 1, *b*) which would allow us to determine approximate locations and quality of the eigenmodes from resonant peaks. Refractive index n in the isotropic case and the tangential component nt of the refractive index in the anisotropic case were set to 5, which is close to the highest refractive index of transition metal dichalcogenides in their transparency range [13]. For a spherically symmetric structure such as ours, the resonant modes are divided into the transverse-magnetic (TM) modes and the transverse-electric (TE) modes [14, 15]. Since TE modes have no electric field component along the radial direction, they are not affected by the radial anisotropy,

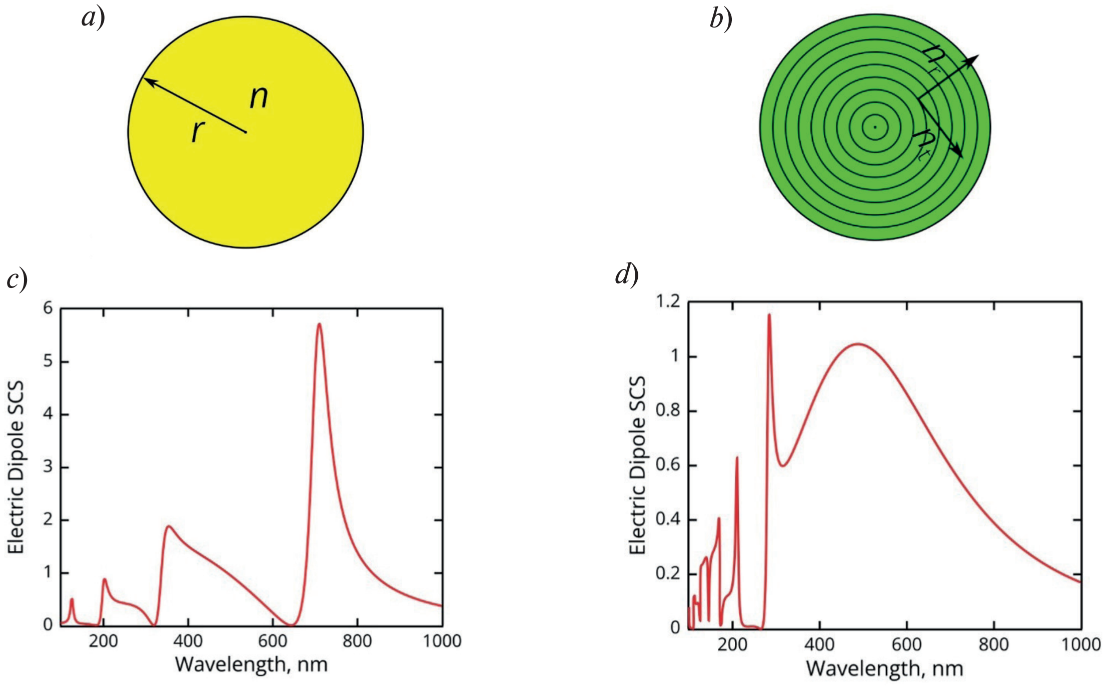

Fig. 1. Schematic view of a spherical nanoparticle made of material with isotropic (*a*) and radially anisotropic (*b*) optical response. Scattering cross-section (SCS) spectra into an eclectic dipole channel for uniform nanoparticles with isotropic ($n = 5$) (*c*) and radially anisotropic ($n_t = 5$, $n_r = 1$) (*d*) optical properties

hence here we studied TM modes only. In particular, we focused on the ED Mie mode since it can be supported by the most compact nanoparticles.

The impact of anisotropy on the resonance frequencies can be observed in Fig. 1 by comparing the scattering cross-section spectra. As we can see, the resonances undergo a blue shift, meaning they are shifted towards shorter wavelengths. The blue shift can be explained by the decreased propagation-related n^p_{eff} by the negative anisotropy as predicted by Eq. 3 and illustrated in Fig. 3, *c*. Such behavior aligns with the isotropic case, where a lower refractive index necessitates photons of greater energy (shorter wavelength) to excite resonance of the same order. At the same time, resonance peaks in the anisotropic case are visibly sharper, which indicates higher quality factor of the corresponding eigenmode.

To gain more understanding of sharper resonances in the anisotropic case, we proceeded with evaluation of the quality factor and the field distribution of the fundamental ED eigenmode (Fig. 2). We varied the radial component of the refractive index from 1 to 10, which allowed us to study the influence of positive and negative optical anisotropy at the same time. We see that positive anisotropy ($n_r > 5$) leads to an increase in the quality factor which may result from the increase in the effective index of waves propagating inside the anisotropic sphere. However, when nr decreases from 5 to 1, the quality factor first decreases, reaching its minimum at $n_r = 2.7$. Subsequently, the quality factor starts to increase again, and at $n_r = 1$, it is 29% higher than the quality factor in the isotropic case ($n_r = 5$) (Fig. 2, *a*). The field distribution in the anisotropic nanoparticle also shows drastic contrast with ED modes in isotropic ones. The maximum of the electric field intensity is observed not in the center. Instead, the electric field is localized in two areas that are close to the surface of the nanosphere (Fig. 2, *b*). We think that this effect is related to large gradients of dielectric permittivity tensor near the center of anisotropic nanosphere.

In isotropic structures, quality factor is known to increase with the refractive index due to the increased momentum mismatch between light inside the resonator and the background [16]. That is why the increase of quality factor with the decrease of radial refractive index appears counterintuitive. To give an intuitive explanation for this phenomenon, we neglected the curvature of the interface between the core and ambient medium and examined the light reflection from planar interface between the isotropic and anisotropic media, as shown schematically in Fig. 3, *a*. The electromagnetic field inside the core can be seen as a superposition of plane waves impinging the interface at different angles. As we found, at a sufficiently strong anisotropy, the reflectance of light incident from the anisotropic medium is greater than that of any incident wave in the isotropic case (see Fig. 3, *b*). The increase in reflectance arises from the fact that the negative anisotropy increases n^i_{eff}, as illustrated in Fig. 3, *c*. As a result, it is more difficult for light to escape from the anisotropic medium which leads to the increase in the quality factor of the ED eigenmode.

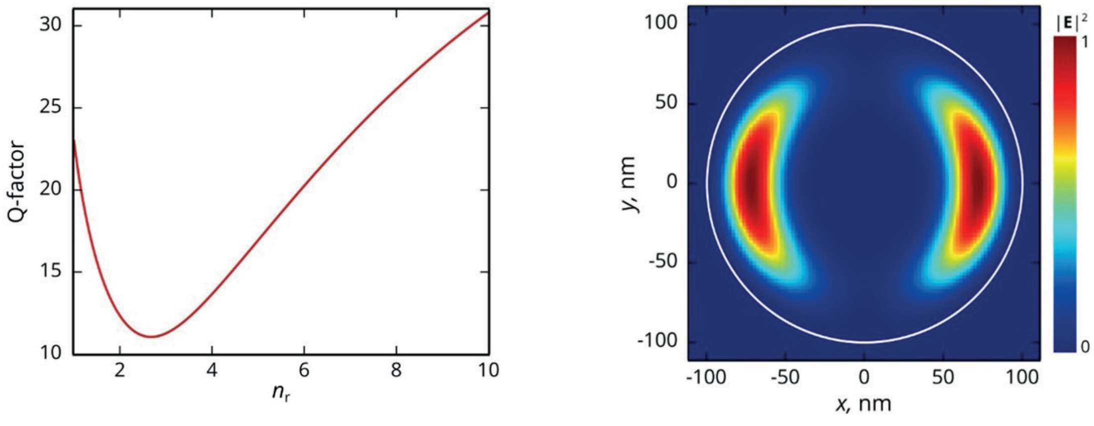

Fig. 2. Quality factor of the ED quasi-normal mode in a radially anisotropic nanosphere as a function of the radial component of the refractive index (*a*). Distribution of the electric field of the mode at $n_t = 5$, $n_r = 1$ (*b*)

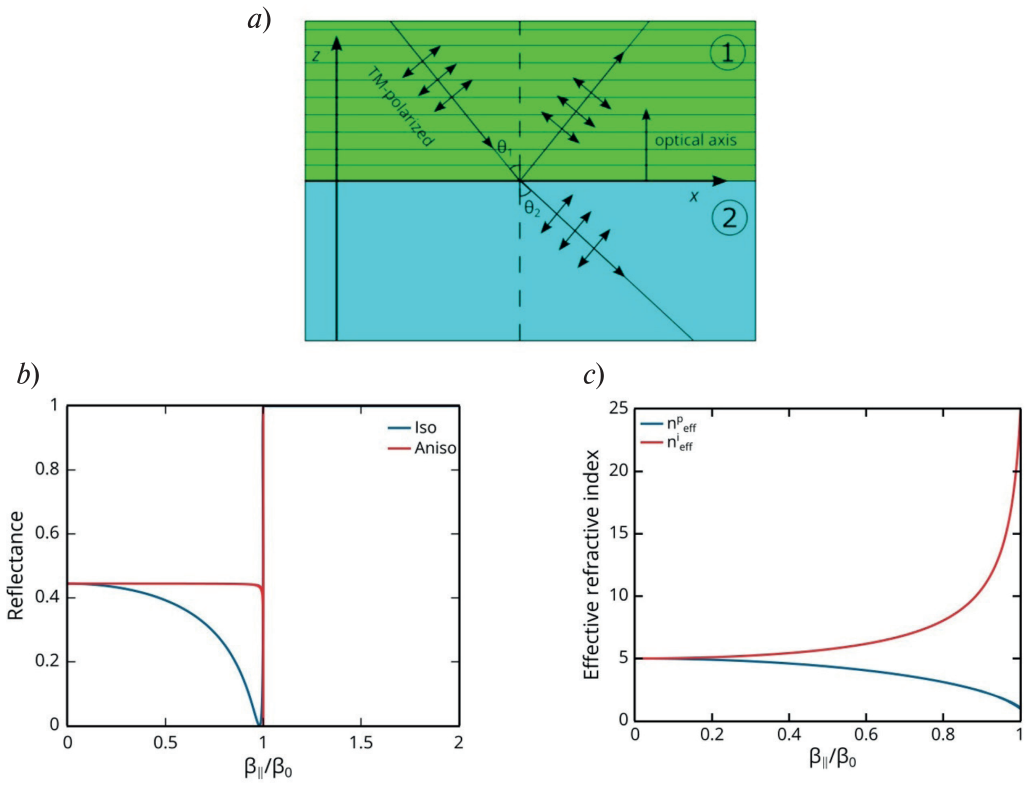

Fig. 3. Schematic representation of a TM-polarized light scattering from the interface of anisotropic and isotropic materials (*a*). Reflectance as a function of β_1/β_0 or anisotropic case ($n_t = 5$, $n_z = 1$ and $n_2 = 1$) and for isotropic case ($n_1 = 5$ and $n_2 = 1$) where $\beta_1 = \beta_0 n^p_{eff} \sin\theta_{in}$ is an in-plane component of the wavevector (*b*). Effective refractive indices governing light propagation and interface scattering for the anisotropic medium with $n_t = 5$, $n_z = 1$ (*c*)

Conclusion

In conclusion, we studied the impact of radial anisotropy on homogeneous spherical resonators. Our findings revealed that, contrary to expectations, strong negative anisotropy typical for high-index TMDCs can enhance the quality factor of the resonator and produce dramatic changes in the field distribution in the ED mode. Blue shift of the ED mode and increase in the quality factor upon decrease of the radial component of the refractive index are explained by the decrease in the propagation-related refractive index and increase in the interface-related index, correspondingly. Our results show that optical anisotropy, especially the strong optical anisotropy of van der Waals materials, is a promising resource for the efficient light manipulation at the nanoscale.

REFERENCES

1. **Prasad P.N.,** Nanophotonics, John Wiley & Sons. (2004) 355–379.

2. **Yu Z., Raman A., Fan S.,** Fundamental limit of nanophotonic light trapping in solar cells. Proceedings of the National Academy of Sciences of the United States of America. 107 (2010) 17491–17496.

3. **Fang Y., Sun M.,** Nanoplasmonic waveguides: towards applications in integrated nanophotonic circuits, Light: Science & Applications. 4 (2015) e294–e294.

4. **Mizrahi A., Lomakin V., Slutsky B.A., Nezhad M.P., Feng L., Fainman Y.,** Low threshold gain metal coated laser nanoresonators, Optics Letters. 33 (2008) 1261–1263.

5. **Chen H.J., Zhu K.D.,** Graphene-based nanoresonator with applications in optical transistor and mass sensing. Sensors. 14, (2014) 16740–16753.

6. **Lee K.T., Jang J.Y., Zhang J., Yang S.M., Park S., Park H.J.,** Highly efficient colored perovskite solar cells integrated with ultrathin subwavelength plasmonic nanoresonators, Scientific Reports. 7 (2017) 10640.

7. **Ermolaev G.A., Grudinin D.V., Stebunov Y.V., Voronin K.V., Kravets V.G., Duan J., Mazitov A.B., Tselikov G.I., Bylinkin A., Yakubovsky D.I., Novikov S.M., Baranov D.G., Nikitin A.Y., Kruglov I.A., Shegai T., Alonso-González P., Grigorenko A.N., Arsenin A.V., Novoselov K.S., Volkov V.S.,** Giant optical anisotropy in transition metal dichalcogenides for next-generation photonics, Nature Communications. 12 (2021) 854.

8. **Tselikov G.I., Ermolaev G.A., Popov A.A., Tikhonowski G.V., Panova D.A., Taradin A.S., Vyshnevyy A.A., Syuy A.V., Klimentov S.M., Novikov S.M., Evlyukhin A.B., Kabashin A.V., Arsenin A.V., Novoselov K.S., Volkov V.S.,** Transition metal dichalcogenide nanospheres for high-refractive-index nanophotonics and biomedical theranostics, Proceedings of the National Academy of Sciences of the United States of America. 119 (2022) e2208830119.

9. **Krasnok A., Baranov D., Li H., Miri M.A., Monticone F., Alú A.,** Anomalies in light scattering, Advances in Optics and Photonics. 11 (2019) 892.

10. **Rasskazov I.L., Scott Carney P., Moroz A.,** STRATIFY: a comprehensive and versatile MATLAB code for a multilayered sphere, OSA Continuum. 3 (2020) 2290–2306.

11. **Qiu C.-W., Li L.-W., Yeo T.-S.,** Scattering by rotationally symmetric anisotropic spheres: Potential formulation and parametric studies, Physical Review E. 75 (2007) 026609.

12. **Eghbali A., Vyshnevyy A.A., Arsenin A.V., Volkov V.S.,** Optical Anisotropy and Excitons in MoS Interfaces for Sensitive Surface Plasmon Resonance Biosensors. Biosensors. 12 (2022) 582.

13. **Hsu C., Frisenda R., Schmidt R., Arora A., de Vasconcellos S.M., Bratschitsch R., van der Zant H.S.J., Castellanos-Gomez A.,** Thickness-dependent refractive index of 1L, 2L, and 3L MoS_2, $MoSe_2$, WS_2, and WSe_2, Advanced Optical Materials. 7 (2019) 1900239.

14. **Kerker M.,** The Scattering of Light and Other Electromagnetic Radiation, Elsevier. (2016) 27–96.

15. **Liu W., Miroshnichenko A.E., Oulton R.F., Neshev D.N., Hess O., Kivshar Y.S.,** Scattering of core-shell nanowires with the interference of electric and magnetic resonances. Optics Letters. 38 (2013) 2621–2624.

16. **Liu W., Miroshnichenko A. E., Kivshar Y. S.,** Q-factor enhancement in all-dielectric anisotropic nanoresonators, Physical Review B. 94(19), (2016) 195436.

THE AUTHORS

EGHBALI Amir
eghbali.amir@phystech.edu
ORCID: 0000-0002-3905-9531

VYSHNEVYY Andrey A.
vyshnevyi.aa@mipt.ru
ORCID: 0000-0003-1394-4169

Received 14.12.2023. Approved after reviewing 23.01.2024. Accepted 06.03.2024.

Conference paper
UDC 538.9
DOI: https://doi.org/10.18721/JPM.171.122

Potentially flexible sensor based on the ZnO-PDMS matrix for measuring mechanical load

A.V. Nikolaeva [1] ✉, V.M. Kondratev [1, 2], S.A. Kadinskaya [1, 2], D.E. Markina [1, 3],
V.V. Lendyashova [1], L.N. Dvoretckaia [1], A.O. Monastyrenko [1],
F.M. Kochetkov [1], A.D. Bolshakov [1, 2, 4]

[1] Alferov University, Saint Petersburg, Russia;
[2] Moscow Institute of Physics and Technology, Dolgoprudny, Russia;
[3] Peter the Great St. Petersburg Polytechnic University, Russia;
[4] Yerevan State University, Yerevan, Armenia
✉ nikolaeva_alex@spbau.ru

Abstract. This study presents zinc oxide (ZnO) microstructures encapsulated in a poly(dimethylsiloxane) (PDMS) polymer matrix for the fabrication of a flexible mechanical load sensor. The resistance and capacitance properties of the ZnO-PDMS membrane in the presence of mechanical load in the range of 0—500 g have been studied using electrochemical impedance spectroscopy. The obtained impedance spectra reveal a decrease in active resistance (R) with increasing load mass. This decrease is attributed to an increase in contact area between the ZnO crystals and the upper electrode, leading to enhanced conductivity of the ZnO-PDMS membrane. Apart from the resistive response, the sensor exhibits capacitive response. The volume fraction of ZnO and PDMS in the membrane has been estimated, and the electrical capacity of the sensor has been determined. The obtained results are found promising for fabrication of various applications in sensing, human health diagnostics, and wearable electronics.

Keywords: ZnO, PDMS, sensor

Funding: The Ministry of Science and Higher Education of the Russian Federation (Grant FSRM-2023-0009; Grant FSRM 2023-0007, 075-03-2023-088); agreement 075-03-2023-106, project FSMG-2021-0005, state order no. 0791-2023-0004. The Russian Science Foundation (Grant 23-72-01133).

Citation: Nikolaeva A.V., Kondratev V.M., Kadinskaya S.A., Markina D.E., Lendyashova V.V., Dvoretckaia L.N., Monastyrenko A.O., Kochetkov F.M., Bolshakov A.D., Potentially flexible sensor based on the ZnO-PDMS matrix for measuring mechanical load, St. Petersburg State Polytechnical University Journal. Physics and Mathematics. 17 (1.1) (2024) 137—142. DOI: https://doi.org/10.18721/JPM.171.122

This is an open access article under the CC BY-NC 4.0 license (https://creativecommons.org/licenses/by-nc/4.0/)

Материалы конференции
УДК 538.9
DOI: https://doi.org/10.18721/JPM.171.122

Потенциально гибкий сенсор на основе матрицы ZnO-ПДМС для измерения механической нагрузки

А.В. Николаева [1]✉, В.М. Кондратьев [1, 2], С.А. Кадинская [1, 2], Д.Е. Маркина [1, 3],
В.В. Лендяшова [1], Л.Н. Дворецкая [1], А.О. Монастыренко [1],
Ф.М. Кочетков [1], А.Д. Большаков [1, 2, 4]

© Nikolaeva A.V., Kondratev V.M., Kadinskaya S.A., Markina D.E., Lendyashova V.V., Dvoretckaia L.N., Monastyrenko A.O., Kochetkov F.M., Bolshakov A.D., 2024. Published by Peter the Great St. Petersburg Polytechnic University.

[1] Академический университет им. Ж.И. Алфёрова РАН, Санкт-Петербург, Россия;
[2] Московский физико-технический институт (национальный исследовательский университет), г. Долгопрудный, Россия;
[3] Санкт-Петербургский политехнический университет Петра Великого, Санкт-Петербург, Россия;
[4] Ереванский государственный университет, г. Ереван, Армения
✉ nikolaeva_alex@spbau.ru

Аннотация. Работа посвящена созданию сенсора механического давления на основе микроструктур оксида цинка (ZnO), синтезированных низкотемпературным гидротермальным методом и инкапсулированных в полимерную матрицу полидиметилсилоксана (ПДМС). Зависимости электрофизических характеристик сенсора от величины приложенной механической нагрузки в диапазоне масс 0 г - 500 г были исследованы с помощью метода спектроскопии электрического импеданса. Полученные спектры импеданса свидетельствуют о снижении активного сопротивления (R) с увеличением массы нагрузки. Это уменьшение объясняется увеличением площади контакта между кристаллами ZnO и верхним электродом, что приводит к повышению проводимости мембраны ZnO-PDMS. Помимо резистивного отклика, датчик также демонстрирует емкостной отклик. Была оценена объемная доля ZnO и PDMS в мембране и определена электрическая емкость датчика. Полученные результаты представляют интерес в области сенсорики, диагностики здоровья человека и носимой электроники.

Ключевые слова: ZnO, ПДМС, сенсор

Финансирование: Министерство науки и высшего образования Российской Федерации (грант № FSRM-2023-0009, грант № FSRM 2023-0007, 075-03-2023-088); Соглашение 075-03-2023-106 от 13.01.2023, проект FSMG-2021-0005, государственное задание № 0791-2023-0004. Российский Научный Фонд (грант 23-72-01133).

Ссылка при цитировании: Николаева А.В., Кондратьев В.М., Кадинская С.А., Маркина Д.Е., Лендяшова В.В., Дворецкая Л.Н., Монастыренко А.О., Кочетков Ф.М., Большаков А.Д. Потенциально гибкий сенсор на основе матрицы ZnO-ПДМС для измерения механической нагрузки // Научно-технические ведомости СПбГПУ. Физико-математические науки. 2024. Т. 17. № 1.1. С. 137–142. DOI: https://doi.org/10.18721/JPM.171.122

Статья открытого доступа, распространяемая по лицензии CC BY-NC 4.0 (https://creativecommons.org/licenses/by-nc/4.0/)

Introduction

Micro- and nanoscale structures of various materials [1] found broad applications in sensorics [2] and electronics [3]. Furthermore, the combination of semiconductor structures with polymer matrices enables the fabrication of flexible and wearable electronics devices [4].

Zinc oxide (ZnO) is a chemically stable, non-toxic, wide bandgap semiconductor material (E_g = 3.36 eV at room temperature) with a wurtzite-type crystal structure [5]. Due to its unique optical and electronic properties, as well as its versatility in synthesis methods, zinc oxide is an appealing material for the development of photosensitive sensors [6], piezoelectric elements, and mechanical pressure sensors [7]. Despite several approaches on ZnO-based mechanical pressure sensors [8–10], they suffer from low feasibility, high cost, and a limited range of detectable masses.

This study focuses on the hydrothermal synthesis of ZnO in the shape of vertical microwires, followed by encapsulation in a polymer matrix and processing into a mechanical load sensor. The aim is to address challenges in sensorics, human health diagnostics, and wearable electronics.

Materials and Methods

In this study, we utilised equimolar (100 mmol/L) aqueous solutions of zinc nitrate ($Zn(NO_3)_2$) and hexamethylenetetramine (HMTA–$C_6H_{12}N_4$) for the hydrothermal synthesis of zinc oxide (ZnO) nanostructures. $Zn(NO_3)_2$ serves as the source of Zn^{2+} ions, while HMTA acts as a slightly soluble base, providing an alkaline environment and the necessary amount of OH^- ions in the solution.

© Николаева А.В., Кондратьев В.М., Кадинская С.А., Маркина Д.Е., Лендяшова В.В., Дворецкая Л.Н., Монастыренко А.О., Кочетков Ф.М., Большаков А.Д., 2024. Издатель: Санкт-Петербургский политехнический университет Петра Великого.

The equilibrium state of the reactions can be altered by adjusting growth parameters, such as temperature, precursor concentration, and pH of the growth medium. These parameters have an impact on the morphology and crystalline quality of the obtained structures [11].

However, a major drawback of the hydrothermal synthesis method is the lack of control over the size and density of the synthesised structures. To overcome this, a photolithography technique [12] was employed using spherical quartz lenses with a diameter of 1.5 µm. Subsequently, the growth Si substrate was etched to fabricate an array of holes in the silicon oxide layer (SiO_2), which served as nucleation centres for ZnO microcrystals. The result of the substrate preparation is depicted in Fig. 1, *a* as scanning electron microscopy (SEM) images obtained using ZEISS Supra 25 (Zeiss, Germany). On the next step, ZnO microstructures were successfully synthesised on the surface of the prepared substrate, as depicted in Figure 1, *b*.

Using the g-coating method [13], the synthesised array of ZnO 5 µm long microwires was encapsulated in poly(dimethylsiloxane) (PDMS). This method allows the polymer to cover the space between the crystals, resulting in their encapsulation within the polymer matrix [13]. To expose the tops of the ZnO crystals, the PDMS layer was etched in KOH, the top view of the final structure as shown in Fig. 1, *c*. The top and bottom electrodes were carbon nanotubes (CNTs) and a thermal-sprayed aluminium layer, respectively (see the schematic in Fig. 1, *d*).

To study the resistive and capacitive properties of the ZnO-PDMS membrane electrical impedance spectroscopy was employed. This method allows to evaluate resistive and capacitive characteristics by measuring the electrical impedance of the object over a wide range of frequencies of the applied voltage. Impedance is a complex number or vector rotating in the complex polar ohmic plane: $Z = R - iX$. In Nyquist coordinates, the real part of impedance (R) is plotted on the x-axis, while the frequency-dependent imaginary part (X) is plotted on the y-axis.

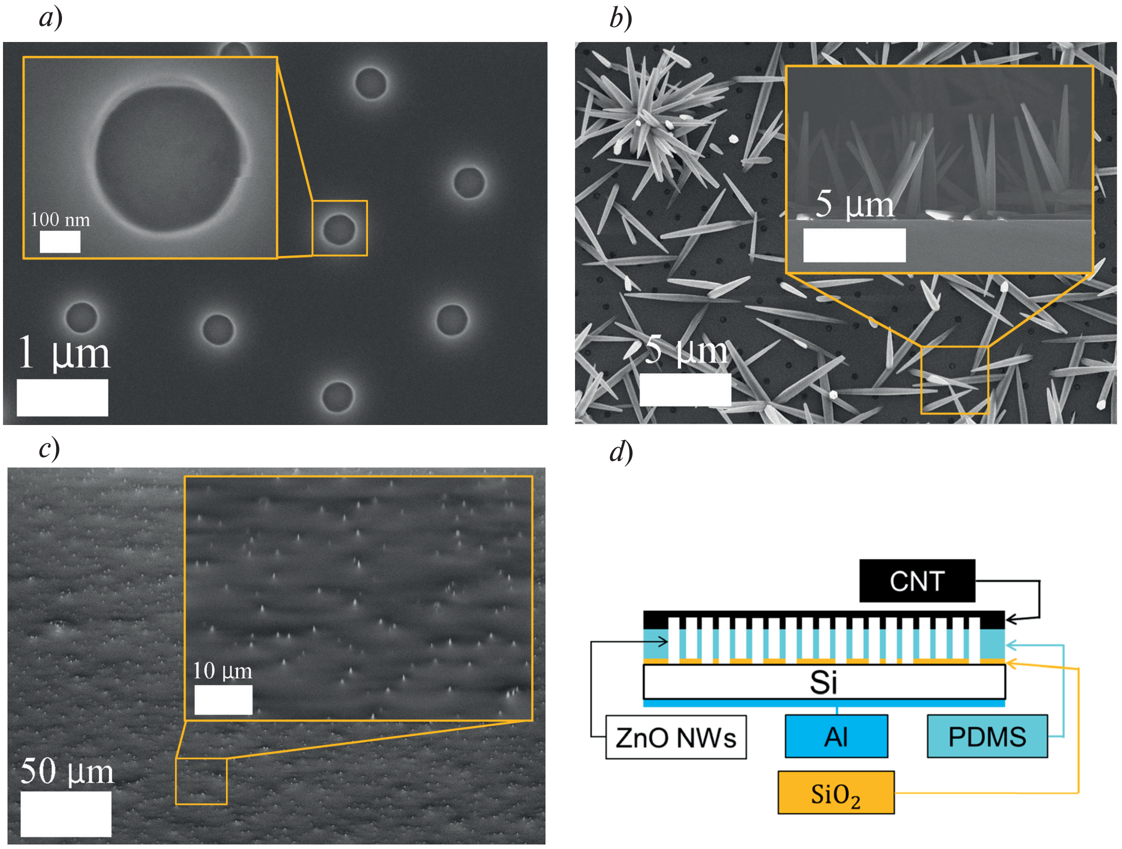

Fig. 1. Studied structure. SEM image of the array of holes formed in the SiO_2 layer on the surface of the growth Si substrate (*a*). SEM image of ZnO hydrothermal structures synthesised on the growth substrate (*b*). Top-view SEM image of ZnO hydrothermal structures encapsulated in PDMS (*c*). Circuit diagram illustrating the pressure sensor (*d*)

Results and Discussion

To assess its performance of the fabricated sensor structure, it was tested using a Z500P impedance metre (Elins Ltd., Russia) in a frequency range of 500 Hz to 500 kHz while being mechanically loaded with a 100 g to 500 g masses. The impedance spectra obtained under these conditions are presented in Fig. 2, *a*. The projection of the spectrum on the *x*-axis indicates the active resistance of the sensor (R) under different loads. To determine the specific value of R for each load mass, the projections of the impedance spectrum on the *x*-axis were determined and used to plot the graph shown in Fig. 2, *b*.

We interpret the change in impedance spectra as a decrease in the sensor's active resistance R when the load mass is increased. The encapsulated ZnO crystals within the polymer matrix vary in size and protrude from the PDMS layer at different heights. When a mechanical load is applied, the upper flexible electrode adheres more tightly to the ZnO-PDMS membrane, increasing conductance between the crystals and the CNTs. Consequently, as the load increases, more crystals come into contact with the upper electrode. These crystals serve as conduction channels, thus increasing the conductivity of the ZnO-PDMS membrane and decreasing the system's resistance.

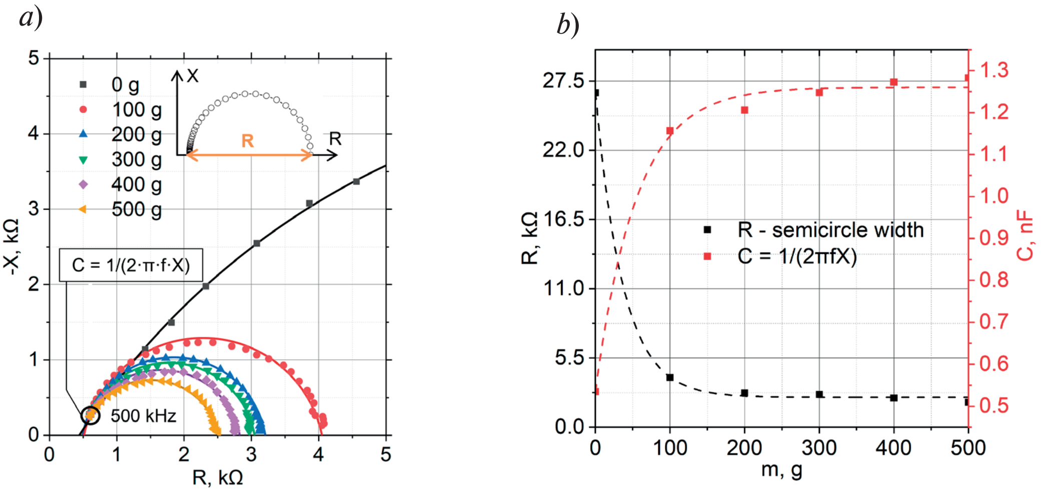

Fig. 2. Spectra showing the impedance of the sensor under mechanical load in the mass range from 0 g to 500 g (*a*). Correlation between the real part of the resistance and electrical capacitance of the sensor and the mass represented as R, $C(m)$ (*b*)

The parameter C, representing the sensor response to different loads, was estimated as inversely related to the imaginary part of impedance X at a maximum frequency of 500 kHz. The sensor can be approximated as a planar capacitor:

$$C = \frac{\varepsilon_0 \cdot \varepsilon_k \cdot S}{d}, \tag{1}$$

where ε_0 is the dielectric constant ($8.854 \cdot 10^{-12}$ F/m), ε_k represents the relative permittivity of the medium (ZnO-PDMS), S denotes the area of the shells ($1.360 \cdot 10^{-3}$m^2), and d refers to the distance between the shells (microcrystal length, 5 μm).

In the case of heterogeneous systems, there exists an analytical model known as Lichtenecker's equation, which establishes a relation between the relative permittivity of the composition and the relative permittivities of its components [14]:

$$\ln \varepsilon_k = \theta_1 \cdot \ln \varepsilon_{k1} + \theta_2 \cdot \ln \varepsilon_{k2}, \tag{2}$$

where ε_k is the relative permittivity of the composite material, ε_{k1} and ε_{k2} are the relative permittivities of the components ($\varepsilon_{\text{ZnO}} = 8.500$, $\varepsilon_{\text{PDMS}} = 3.150$), and θ_1 and θ_2 are the volume fractions of the first and second components, respectively. The relative dielectric constant of the ZnO-PDMS membrane was determined using Lichtenecker's equation (2):

$$\ln \varepsilon_{\mathrm{ZnO+PDMS}} = 0.095 \cdot \ln \varepsilon_{\mathrm{ZnO}} + 0.905 \cdot \ln \varepsilon_{\mathrm{PDMS}}; \quad (3)$$

$$\varepsilon_{\mathrm{ZnO+PDMS}} = 3.448. \quad (4)$$

Using these data, the electrical capacity of the ZnO - PDMS membrane, based on the flat capacitor approximation, was determined to be 8.3 nF, which is in accordance with the experimental data (0.5 nF) shown in Fig. 2, *b* (0 g). It is worth mentioning that the calculation error may be attributed to variations in the surface density of crystals as well as deviations in their cross section and length.

Furthermore, based on the flat capacitor approximation (1), the distance between the contacts, denoted as '*d*', can be estimated. For 0 g, this distance corresponds to the length of the microcrystal, which is 5 μm. Conversely, for a weight load of 500 g, taking into account the experimental values of the electrical capacity, the estimated distance was found to be 3.89 μm. Thus, at the maximum weight load on the sensor, the membrane thickness experiences a 22% change. Consequently, a decrease in the thickness of the ZnO-PDMS membrane layer between the electrodes results in an increase in the electrical capacity of the sensor, supporting the findings of the flat capacitor approximation (1) and the dependence depicted in Fig. 2, *b*.

Conclusion

We demonstrate the potential use of hydrothermal ZnO microstructures encapsulated in a PDMS polymer matrix for the fabrication of a flexible mechanical load sensor. The sensor exhibits both resistive and capacitive characteristics, allowing it to effectively respond to varying mechanical loads. With a wide sensitivity range, this sensor holds promise for applications such as sensing, human health diagnostics, and wearable electronics.

Acknowledgments

A.D.B. thanks Ministry of Science and Higher Education of the Russian Federation (agreement 075-03-2023-106, project FSMG-2021-0005) for support of the experiments.

V.M.K. and A.V.N. thanks Ministry of Science and Higher Education of the Russian Federation (Grant FSRM-2023-0009) for support of analysis of the experimental data.

K.F.M. and M.D.E. thanks the Ministry of Science and Higher Education of the Russian Federation (Grant FSRM 2023-0007, 075-03-2023-088).

V.V.L. thanks Ministry of Science and Higher Education of the Russian Federation as part of state order no. 0791-2023-0004 for support of the substrate preparation.

D.L.N. thanks Russian Science Foundation (Grant 23-72-01133) for financial support.

REFERENCES

1. **Bolshakov A.D., Fedorov V.V., Koval O.Yu., Sapunov G.A., Sobolev M.S., Pirogov E.V., Kirilenko D.A., Mozharov A.M., Mukhin I.S.,** Effective Suppression of Antiphase Domains in GaP(N)/GaP Heterostructures on Si(001), Cryst Growth Des, 19 (8) (2019) 4510–4520.
2. **Kondratev V.M., Morozov I.A., Vyacheslavova E.A., Kirilenko D.A., Kuznetsov A., Kadinskaya S.A., Nalimova S.S., Moshnikov V.A., Gudovskikh A.S., Bolshakov A.D.,** Silicon Nanowire-Based Room-Temperature Multi-environment Ammonia Detection, ACS Appl Nano Mater, 5 (7) (2022) 9940–9949.
3. **Kuznetsov A., Roy P., Kondratev V.M., Fedorov V.V., Kotlyar K.P., Reznik R.R., Vorobyev A.A., Mukhin I.S., Cirlin G.E., Bolshakov A.D.,** Anisotropic Radiation in Heterostructured "Emitter in a Cavity" Nanowire, Nanomaterials, 12 (2) (2022) 241.
4. **Lim H., Kim H. S., Qazi R., Kwon Y., Jeong J., Yeo W.,** Advanced Soft Materials, Sensor Integrations, and Applications of Wearable Flexible Hybrid Electronics in Healthcare, Energy, and Environment, Advanced Materials 32 (15) (2020).
5. **Özgür Ü., Alivov Ya.I., Liu C., Teke A., Reshchikov M.A., Doğan S., Avrutin V., Cho S.-J., Morkoç H.,** A comprehensive review of ZnO materials and devices, J Appl Phys 98 (4) (2005).
6. **Kadinskaya S.A., Kondratev V.M., Kindyushov I.K., Kuznetsov A., Punegova K.N.,** Hydrothermal ZnO-based Nanostructures: Geometry Control and Narrow Band UV Emission, in: 2022 Conference

of Russian Young Researchers in Electrical and Electronic Engineering (ElConRus), IEEE, 2022: Pp. 958–961.

7. **Wei A., Pan L., Huang W.,** Recent progress in the ZnO nanostructure-based sensors, Materials Science and Engineering: B, 176 (18) (2011) 1409–1421.

8. **Tan Y., Yang K., Wang B., Li H., Wang L., Wang C.,** High-performance textile piezoelectric pressure sensor with novel structural hierarchy based on ZnO nanorods array for wearable application, Nano Res, 14 (11) (2021) 3969–3976.

9. **Li W., Jin X., Zheng Y., Chang X., Wang W., Lin T., Zheng F., Onyilagha O., Zhu Z.,** A porous and air gap elastomeric dielectric layer for wearable capacitive pressure sensor with high sensitivity and a wide detection range, J Mater Chem C Mater, 8 (33) (2020) 11468–11476.

10. **Tripathy A.R., Choudhury A., Dash A., Panigrahi P., Kumar S.S., Pancham P.P., Sahu S.K., Mallik S.,** Polymer matrix composite engineering for PDMS based capacitive sensors to achieve high-performance and broad-range pressure sensing, Applied Surface Science Advances, 3 (2021) 100062.

11. **Gerbreders V., Krasovska M., Sledevskis E., Gerbreders A., Mihailova I., Tamanis E., Ogurcovs A.,** Hydrothermal synthesis of ZnO nanostructures with controllable morphology change, CrystEngComm, 22 (8) (2020) 1346–1358.

12. **Dvoretckaia L.N., Mozharov A.M., Gavrilov M.S., Fedorov V.V.,** Microspherical lithography for selective epitaxy, in: 2022 International Conference Laser Optics (ICLO), IEEE, 2022: Pp. 1–1.

13. **Neplokh V., Kochetkov F.M., Deriabin K.V., Fedorov V.V., Bolshakov A.D., Eliseev I.E., Mikhailovskii V.Yu., Ilatovskii D.A., Krasnikov D.V., Tchernycheva M., Cirlin G.E., Nasibulin A. G., Mukhin I.S., Islamova R.M.,** Modified silicone rubber for fabrication and contacting of flexible suspended membranes of n-/p-GaP nanowires with a single-walled carbon nanotube transparent contact, J Mater Chem C Mater, 8 (11) (2020) 3764–3772.

14. **Goncharenko A.V., Lozovski V.Z., Venger E.F.,** Lichtenecker's equation: applicability and limitations, Opt Commun 174(1-4) (2000) 19–32.

THE AUTHORS

NIKOLAEVA Aleksandra V.
nikalex2000@bk.ru
ORCID: 0009-0008-4344-4863

KONDRATEV Valeriy M.
kvm_96@mail.ru
ORCID: 0000-0002-3469-5897

KADINSKAYA Svetlana A.
skadinskaya@bk.ru
ORCID: 0000-0003-2508-2244

MARKINA Diana E.
diana666167@gmail.com
ORCID: 0009-0007-9013-7973

LENDYASHOVA Vera V.
erilerican@gmail.com
ORCID: 0000-0001-8192-7614

DVORETCKAIA Liliia N.
Liliyabutler@gmail.com
ORCID: 0000-0002-4172-940X

MONASTYRENKO Anatoliy O.
monas@spbau.ru
ORCID: 0009-0009-7051-8458

KOCHETKOV Fedor M.
azemerat@rambler.ru
ORCID: 0000-0002-2209-6483

BOLSHAKOV Alexey D.
acr1235@mail.ru
ORCID: 0000-0001-7223-7232

Received 01.12.2023. Approved after reviewing 23.01.2024. Accepted 15.04.2024.

St. Petersburg Polytechnic University Journal. Physics and Mathematics. 2024 Vol. 17. No. 1.1
Научно-технические ведомости СПбГПУ. Физико-математические науки. 17 (1.1) 2024

Conference paper
UDC 538.958
DOI: https://doi.org/10.18721/JPM.171.123

Terahertz and infrared photoluminescence in a structure based on *n*-GaAs with a waveguide for the near-infrared range

N.Yu. Kharin [1] ✉, V.Yu. Panevin [1], M.Ya. Vinnichenko [1],
I.A. Norvatov [1], V.V. Fedorov [2], D.A. Firsov [1]

[1] Peter the Great St. Petersburg Polytechnic University, St. Petersburg, Russia;
[2] Alferov University, St. Petersburg, Russia
✉ kharin.nikita66@gmail.com

Abstract. The results of a study of near-infrared (IR) and terahertz photoluminescence in doped GaAs layers placed in a near-IR optical waveguide are presented. Terahertz radiation under optical interband pumping is associated with transitions of nonequilibrium electrons from the conduction band to impurity states. Stimulated interband near-IR emission involving impurity states was obtained. An accelerated increase in the integral intensity of terahertz radiation has been demonstrated at pump intensities exceeding the threshold for stimulated emission in the near-IR range. The increase in intensity is associated with the accelerated depopulation of the ground state of the impurity by stimulated emission.

Keywords: photoluminescence, terahertz radiation, impurity transition, epitaxial layer, bulk semiconductor, stimulated emission

Funding: The reported study was funded by Russian Science Foundation (Grant 22-22-00105).

Citation: Kharin N.Yu., Panevin V.Yu., Vinnichenko M.Ya., Norvatov I.A., Fedorov V.V., Firsov D.A., Terahertz and infrared photoluminescence in a structure based on n-GaAs with a waveguide for the near-infrared range, St. Petersburg State Polytechnical University Journal. Physics and Mathematics. 17 (1.1) (2024) 143–148. DOI: https://doi.org/10.18721/JPM.171.123

This is an open access article under the CC BY-NC 4.0 license (https://creativecommons.org/licenses/by-nc/4.0/)

Материалы конференции
УДК 538.958
DOI: https://doi.org/10.18721/JPM.171.123

Терагерцовая и инфракрасная фотолюминесценция в структуре на основе *n*-GaAs с волноводом для ближнего ИК диапазона

Н.Ю. Харин [1] ✉, В.Ю. Паневин [1], М.Я. Винниченко [1],
И.А. Норватов [1], В.В. Федоров [2], Д.А. Фирсов [1]

[1] Санкт-Петербургский политехнический университет Петра Великого, Санкт-Петербург, Россия;
[2] Академический университет им. Ж.И. Алфёрова РАН, Санкт-Петербург, Россия
✉ kharin.nikita66@gmail.com

Аннотация. Приведены результаты исследования фотолюминесценции ближнего инфракрасного (ИК) и терагерцового диапазонов в легированных слоях GaAs, помещенных в оптический волновод ближнего ИК диапазона. Терагерцовое излучение при оптической межзонной накачке связывается с переходами неравновесных электронов из зоны проводимости на состояния примеси. Получено стимулированное излучение

© Kharin N.Yu., Panevin V.Yu., Vinnichenko M.Ya., Norvatov I.A., Fedorov V.V., Firsov D.A., 2024. Published by Peter the Great St. Petersburg Polytechnic University.

ближнего ИК диапазона с участием примесных состояний. Продемонстрирован ускоренный рост интегральной интенсивности терагерцового излучения при интенсивностях накачки, превышающих порог стимулированного излучения ближнего ИК диапазона. Рост интенсивности связан с ускоренным опустошением основного состояния примеси стимулированным излучением.

Ключевые слова: фотолюминесценция, терагерцовое излучение, примесный переход, эпитаксиальный слой, объемный полупроводник, стимулированное излучение

Финансирование: Исследование выполнено при финансовой поддержке Российского научного фонда (грант № 22-22-00105).

Ссылка при цитировании: Харин Н.Ю., Паневин В.Ю., Винниченко М.Я., Норватов И.А., Федоров В. В., Фирсов Д.А. Терагерцовая и инфракрасная фотолюминесценция в структуре на основе *n*-GaAs с волноводом для ближнего ИК диапазона // Научно-технические ведомости СПбГПУ. Физико-математические науки. 2024. Т. 17. № 1.1. С. 143–148. DOI: https://doi.org/10.18721/ JPM.171.123

Статья открытого доступа, распространяемая по лицензии CC BY-NC 4.0 (https://creativecommons.org/licenses/by-nc/4.0/)

Introduction

Despite significant advances in the development of quantum cascade lasers in the terahertz (THz) spectral range, consisting, for example, in the recent creation of such sources that do not require cooling with liquid gases [1], in recent years there has been continued interest in the development of effective low-cost solid-state sources of terahertz radiation. A good basis for creating such sources can be optical transitions of charge carriers involving impurity states in semiconductors and semiconductor nanostructures. Terahertz radiation upon optical interband excitation of nonequilibrium charge carriers has been observed in doped bulk semiconductors [2, 3] and structures with quantum wells [4]. The radiation arose due to optical transitions of nonequilibrium electrons from the conduction band or excited impurity states to the ground state of the donor impurity. The depopulation of the ground state of the impurity occurred due to the spontaneous recombination of electrons and nonequilibrium holes in the valence band. It was shown in [5], considering the radiation associated with intraband transitions of electrons between levels of quantum dots in diode laser structures, that stimulated laser radiation during interband transitions of electrons effectively depopulate the ground level of a quantum dot, which leads to an increase in the intensity of intraband (interlevel) optical transitions. This approach was implemented in [6] to increase the intensity of terahertz radiation during electron transitions from the conduction band to the ground state of the impurity. The radiation intensity increased due to the effective depopulation of the impurity state by stimulated interband radiation arising in the structure under study during optical interband pumping of structures with GaAs/AlGaAs quantum wells.

Near-IR laser lasing was realized in [7] through the ground donor state under interband optical pumping in a structure with a doped *n*-GaAs epitaxial layer and terahertz radiation associated with impurity transitions was detected. In this work, photoluminescence (PL) in the near-infrared and terahertz spectral ranges in doped GaAs epitaxial layers is studied in detail at various levels of optical pumping, including studies under conditions of generation of stimulated interband emission.

Materials and Methods

Donor-doped GaAs layers with a thickness of 0.52 μm were grown by molecular beam epitaxy. The donor concentration (Si) was $1.0\cdot10^{16}$ cm^{-3}. The epitaxial layer was enclosed in a waveguide, which was formed by layers of an $Al_xGa_{1-x}As$ solid solution with a composition gradient x. From the grown wafer, samples were formed by cleavage, representing a high Q-factor total internal reflection resonator with dimensions of 400×400 μm. The sample was soldered with indium to a copper holder of a Janis PTCM-4-7 closed-cycle optical cryostat;

© Харин Н.Ю., Паневин В.Ю., Винниченко М.Я., Норватов И.А., Федоров В.В., Фирсов Д.А., 2024. Издатель: Санкт-Петербургский политехнический университет Петра Великого.

studies were carried out at a temperature of 4.2 K. The surface of the sample was uniformly illuminated with radiation from a pulsed laser with a wavelength of 532 nm, a frequency of 8 kHz, and a pulse duration of 250 ns. The pump radiation was modulated by a mechanical chopper at 180 Hz to employ the synchronous detection technique. The photoluminescence signal in the near-IR range was recorded from the end of the sample using a Horiba Jobin Yvon FHR-640 grating monochromator. A silicon CCD matrix was used as a near-IR radiation detector. A photodetector made of gallium-doped germanium was used to record integral radiation in the terahertz spectral range arising under conditions of interband optical pumping due to transitions of nonequilibrium electrons involving impurity states. The Ge<Ga> crystal was located in close proximity to the sample on the same copper holder. Thus, the operating temperature of the detector was close to 4.2 K. The distance between the THz radiation detector and the sample was 12 mm. On all sides, except for the input face, the detector was shielded with metal foil to protect it from the background thermal terahertz radiation of the room. Filters made of black polyethylene and high-resistivity germanium were installed in front of the input face to prevent pump radiation from reaching the detector. Terahertz radiation was recorded from normal to the sample surface. The signal from the detector was fed to the SR-570 current preamplifier, and from there to the SR-830 lock-in amplifier, synchronized with the chopper frequency.

Results and Discussion

It was previously shown that, due to the presence of a waveguide and a total internal reflection resonator in the structure under study, stimulated emission in the near-IR range occurs at sufficiently high levels of optical interband excitation [7]. The near-IR photoluminescence spectra of the sample studied in the present work are shown in Fig. 1.

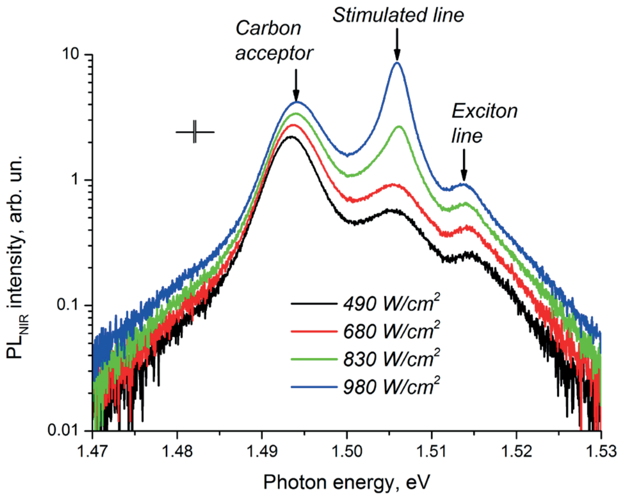

Fig. 1. Photoluminescence spectra in the near-IR range at different levels of optical pumping

From the obtained spectra, it is clear that stimulated emission occurs at photon energy of about 1.507 meV. This radiation in our sample is associated with the epitaxial layer and the silicon donor impurity [8]. The emission line designated “*Exciton line*” corresponds to the energy of a free exciton in GaAs [9]. The peak at an energy of 1.494 eV (designated “*Carbon acceptor*”) corresponds to radiative electron transitions from the conduction band to acceptor states of an uncontrolled carbon acceptor impurity arising in the structure during growth.

Fig. 2 shows the dependence of the integrated intensity of photoluminescence in the near-IR spectral range on the level of optical interband pumping. The results obtained demonstrate the presence of a stimulated emission threshold. This dependence was obtained by integrating the photoluminescence spectra.

Previously, terahertz radiation associated with transitions of nonequilibrium electrons from the conduction band to the impurity level was discovered in similar samples, and its spectra

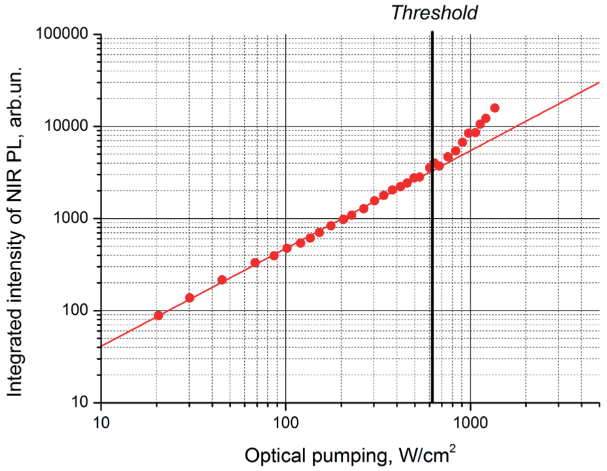

Fig. 2. Integral intensity of photoluminescence in the near-IR spectral range depending on the pump power

were obtained [8]. It was also demonstrated in [8] that the spectrum of terahertz radiation lies in the range of 6–30 meV. In order to clarify the influence of stimulated radiation, which should accelerate the depopulation of the ground impurity state, on the generation efficiency of terahertz radiation, in this work we studied the integral intensity of terahertz radiation using a Ge<Ga> detector, which has a spectral sensitivity that corresponds quite well to the radiation spectrum of the sample. The sensitivity spectrum of the photodetector, obtained using a Bruker Vertex v80 Fourier spectrometer, is shown in Fig. 3.

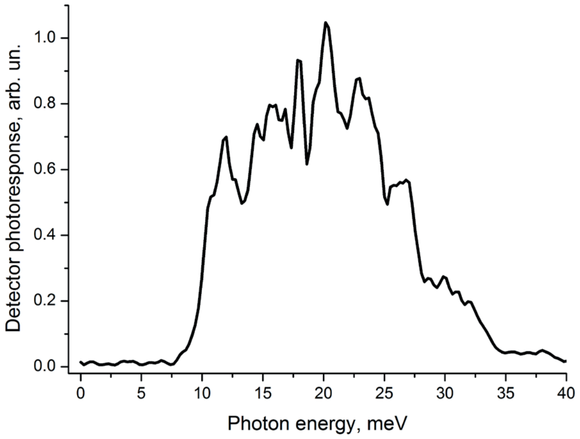

Fig. 3. Sensitivity spectrum of a gallium-doped germanium crystal, which was used as a THz radiation detector

Thus, the dependence of the integral intensity of terahertz photoluminescence on the intensity of optical pumping was obtained, shown in Fig. 4. The graph shows a significant increase in the growth rate of terahertz photoluminescence at optical pumping intensities exceeding 600 W/cm^2. This value corresponds to the pump level at which stimulated emission of the near-IR range occurs on electron transitions from the main impurity level to the valence band. The results obtained allow us to conclude that stimulated radiation in the near-IR range has a significant effect on the characteristics of terahertz radiation. The use of stimulated interband radiation for accelerated depopulation of the ground impurity state leads to an increase in the efficiency of the terahertz radiation source.

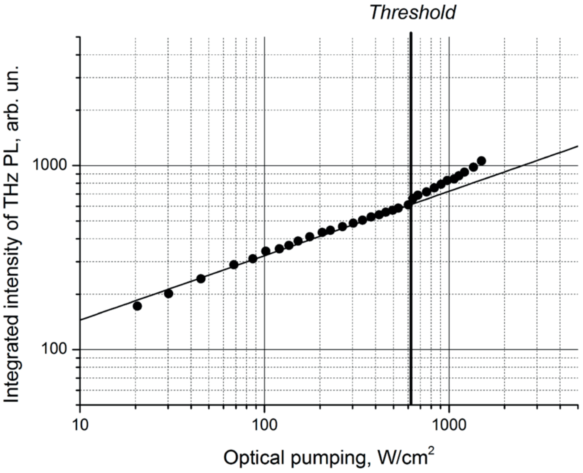

Fig. 4. Integral intensity of terahertz photoluminescence depending on the optical pump power

Conclusion

A semiconductor structure containing a doped GaAs epitaxial layer placed in an optical waveguide supporting near-IR radiation has been studied. Under conditions of optical interband pumping, stimulated emission was obtained related to electron transitions from the ground state of the impurity to the valence band. The structure under study is also a source of terahertz radiation, which occurs when nonequilibrium electrons are captured from the conduction band to impurity levels. At pump intensities exceeding the threshold of stimulated interband emission, the rate of growth of the integral intensity of terahertz radiation increases significantly with increasing optical excitation level. The observed effect is associated with accelerated depopulation of the main impurity level by stimulated interband emission and allows the development of a terahertz radiation source with increased efficiency.

Acknowledgments

The study was financially supported by the Russian Science Foundation, grant 22-22-00105.

REFERENCES

1. **Khalatpour A., Paulsen A.K., Deimert C., Wasilewski Z.R., Hu Q.,** High-power portable terahertz laser systems, Nature Photonics, 15 (2021) 16–20.
2. **Andrianov A.V., Zakhar’in A.O., Ivanov Y.L., Kipa M.S.,** Terahertz impurity luminescence under the interband photoexcitation of semiconductors, JETP letters, 91 (2010) 96–99.
3. **Zakhar’in A.O., Andrianov A.V., Egorov A.Y., Zinov’ev N.N.,** Terahertz photoluminescence from GaAs doped with shallow donors at interband excitation, Applied physics letters, 96 (21) (2010) 211118.
4. **Firsov D.A., Vorobjev L.E., Panevin V.Y., Sofronov A.N., Balagula R.M., Makhov I.S., Kozlov D.V., Vasil’ev A.P.,** Terahertz radiation associated with the impurity electron transition in quantum wells upon optical and electrical pumping, Semiconductors, 49 (2015) 28–32.
5. **Vorob’ev L.E., Firsov D.A., Shalygin V.A., Tulupenko V.N., Shernyakov Y.M., Ledentsov N.N., Ustinov V.M., Alferov Z.I.,** Spontaneous far-IR emission accompanying transitions of charge carriers between levels of quantum dots, Journal of Experimental and Theoretical Physics Letters, 67 (1998) 275–279.
6. **Makhov I.S., Panevin V.Y., Firsov D.A., Vorobjev L.E., Vasil'ev A.P., Maleev N.A.,** Terahertz photoluminescence of the donor doped GaAs/AlGaAs quantum wells controlled by the near-infrared stimulated emission, Journal of Luminescence, 210 (2019) 352–357.
7. **Petruk A.D., Kharin N.Yu., Vinnichenko M.Ya., Norvatov I.A., Fedorov V.V., Firsov D.A.,** Terahertz and stimulated near-infrared photoluminescence in bulk n-GaAs layers, St. Petersburg State Polytechnical University Journal: Physics and Mathematics. 1.3 (2023) 14–19.

8. **Kharin N.Yu., Panevin V.Yu., Petruk A.D., Vinnichenko M.Ya,, Norvatov I.A., Fedorov V.V., Firsov D.A.,** Influence of stimulated interband emission on terahertz photoluminescence in n-type gallium arsenide layers, St. Petersburg State Polytechnical University Journal: Physics and Mathematics, 3 (2023) 29–38.

9. **Nam S.B., Reynolds D.C., Litton C.W., Almassy R.J., Collins T.C., Wolfe C.M.,** Free-exciton energy spectrum in GaAs, Phys. Rev. B. 13 (2) (1976) 761–767.

THE AUTHORS

KHARIN Nikita Yu.
kharin.nikita66@gmail.com
ORCID: 0000-0002-2220-881X

PANEVIN Vadim Yu.
pvyu@rphf.spbstu.ru
ORCID: 0000-0003-4424-1722

VINNICHENKO Maxim Ya.
mvin@spbstu.ru
ORCID: 0000-0002-6118-0098

NORVATOV Ilya A.
norv2@mail.ru
ORCID: 0000-0002-0048-7512

FEDOROV Vladimir V.
burunduk.uk@gmail.com
ORCID: 0000-0001-5547-9387

FIRSOV Dmitry A.
dmfir@rphf.spbstu.ru
ORCID: 0000-0003-3947-4994

Received 04.12.2023. Approved after reviewing 05.12.2023. Accepted 11.12.2023.

St. Petersburg Polytechnic University Journal. Physics and Mathematics. 2024 Vol. 17. No. 1.1
Научно-технические ведомости СПбГПУ. Физико-математические науки. 17 (1.1) 2024

Conference paper
UDC 538.9
DOI: https://doi.org/10.18721/JPM.171.124

Photocurrent in MIS structures based on germanosilicate films

G.A. Hamoud [1, 2] ✉, G.N. Kamaev [1, 2], M. Vergnat [3], V.A. Volodin [1, 2] ✉

[1] Rzhanov Institute of Semiconductor Physics, Siberian Branch of RAS, Novosibirsk, Russia;
[2] Novosibirsk State University, Novosibirsk, Russia;
[3] Université de Lorraine, Nancy, France
✉ k.gaisaa@g.nsu.ru, ✉ volodin@isp.nsc.ru

Abstract. The photocurrent in metal-insulator-semiconductor (MIS) structures based on germanosilicate films on n-type silicon with a transparent top electrode made of indium tin oxide has been studied. The first structure contained a $GeO[SiO_2]$ layer as a dielectric, and the second structure contained an additional Ge layer 3 nm thick, separated from the silicon substrate by a tunnel-thin layer of SiO_2. High photosensitivity was obtained for both structures, both as-deposited and after annealing at 500 °C for 30 minutes. A mechanism for the generation of photocurrent is proposed, based on the absorption of photons in a depletion region of silicon and tunneling of charge carriers through the dielectric. In the case of the second structure, an additional mechanism for the occurrence of photocurrent associated with the absorption of photons in the Ge layer is assumed. The studied MIS structures can be used in simple, inexpensive photodiodes that do not require the creation of *p–n* junctions.

Keywords: germanosilicate films, MIS-structures, photocurrent

Funding: This work was supported by the Ministry of Science and Higher Education of the Russian Federation, project FSUS-2024-0020.

Citation: Hamoud G.A, Kamaev G.N, Vergnat M., Volodin V.A., Photocurrent in MIS structures based on germanosilicate films, St. Petersburg State Polytechnical University Journal. Physics and Mathematics. 17 (1.1) (2024) 149–154. DOI: https://doi.org/10.18721/JPM.171.124

This is an open access article under the CC BY-NC 4.0 license (https://creativecommons.org/licenses/by-nc/4.0/)

Материалы конференции
УДК 538.9
DOI: https://doi.org/10.18721/JPM.171.124

Фототок в МДП-структурах на основе германосиликатных плёнок

Г.А. Хамуд [1, 2] ✉, Г.Н. Камаев [1, 2], М. Вернья [3], В.А. Володин [1, 2] ✉

[1] Новосибирский государственный университет, г. Новосибирск, Россия
[2] Институт физики полупроводников им. А.В. Ржанова Сибирского отделения РАН, г. Новосибирск, Россия
[3] Университет Лотарингии, г. Нанси, Франция
✉ k.gaisaa@g.nsu.ru, ✉ volodin@isp.nsc.ru

Аннотация. Исследован фототок в структурах металл-диэлектрик-полупроводник (МДП) на основе германосиликатных плёнок на кремнии n-типа с прозрачным верхним электродом из оксида индия и олова. Первая структура содержала в качестве диэлектрика слой $GeO[SiO_2]$, а вторая содержала ещё слой Ge толщиной 3 нм, отделённый от подложки кремния туннельно-тонким слоем SiO_2. Получена высокая фоточувствительность обеих структур, как исходных так и после отжига 500 °C, 30 минут. Предложен механизм возникновения фототока, основанный на поглощении фотонов в

© Hamoud G.A, Kamaev G.N, Vergnat M., Volodin V.A., 2024. Published by Peter the Great St. Petersburg Polytechnic University.

обеднённом слое кремния и туннелировании носителей заряда через диэлектрик. В случае второй структуры предположен дополнительный механизм возникновения фототока, связанный с поглощением фотонов в слое Ge. Исследованные МДП-структуры можно использовать в простых, недорогих фотодиодах, не требующих создания *p*–*n*-переходов.

Ключевые слова: германосиликатные пленки, МДП-структуры, фототок

Финансирование: Работа выполнена при финансировании МНВО РФ по госзаданию FSUS-2024-0020.

Ссылка при цитировании: Хамуд Г.А., Камаев Г.Н., Вернья М., Володин В.А. Фототок в МДС структурах на основе германосиликатных пленок // Научно-технические ведомости СПбГПУ. Физико-математические науки. 2024. Т. 17. № 1.1. С. 149–154. DOI: https://doi.org/10.18721/ JPM.171.124

Статья открытого доступа, распространяемая по лицензии CC BY-NC 4.0 (https://creativecommons.org/licenses/by-nc/4.0/)

Introduction

In recent years, there has been increasing interest in the use of metal-insulator-semiconductor (MIS) structures in photovoltaics. Typically, in MIS photodiodes and optical detectors, tunnel or thick layers of SiO_x are used as a dielectric [1]. To improve photosensitivity, Ge quantum dots were included in SiO_x layers [2]. Germanosilicate films ($GeSi_xO_y$) have some advantages over SiO_x. The purpose of this work is to study the photocurrent effect in MIS structures based on $GeSi_xO_y$ (including those with Ge inclusions).

Materials and Methods

High-vacuum electron beam vapor deposition technique was employed to deposit the non-stoichiometric germanosilicate glass layers $GeSi_xO_y$, on *n*-Si (100) substrates (specific conductivity $\rho = 5.5 \pm 1$ Ohm·cm) at room temperature. The targets were evaporated and co-evaporated in a vacuum of about 10^{-7}–10^{-6} Torr, and using a quartz microbalance, the deposition rate was maintained within a range of about angstroms per second. The targets were powders of various materials, such as GeO_2, SiO_2, and Ge. It is known that when germanium dioxide powder evaporates the $GeO_{1.1-1.2}$ films are deposited [3]. More details are provided about the growth conditions and stoichiometry of the deposited films in [3].

In order to explain the mechanism of photocurrent appearance in the $GeSi_xO_y$ based MIS-structures, it is important to know where the light is absorbed in the substrate or in the films. To clarify this, the $GeSi_xO_y$ films and many-layer structures were deposited on special satellite substrates - glass coated with a special transparent conductive fluorine-tin-oxide (FTO). Since the top electrode of the MIS structures was made of ITO, it was important to know how transparent it was. So, a layer of transparent indium-tin-oxide (ITO) was also deposited on a transparent sapphire substrate without a mask, and then the reflection and transmission spectra of all samples were measured separately using an SF-56 spectrophotometer (produced by LOMO-Spectr, Russia), with a spectral resolution of 2 nm and the measuring range from 190 to 1100 nm. A special PS-9 setup was employed to register the reflection spectra, that have a reflectance with an incidence angle close to the normal of about 9°. The recorded spectrum was then normalized to the spectrum of silicon with a natural oxide with thickness of 2.5 nm as the reference spectrum.

Fig. 1, *a*, c shows the schematic structure of the samples. The $GeO[SiO_2]$ layers were obtained by co-evaporation for target powders (GeO_2 and SiO_2). As for the ITO top electrodes, they were deposited using special mask and magnetron sputtering. The thickness of ITO was 200 nm with a surface resistance of about 40 Ohm/□, an area of top electrodes was 0.49 mm^2. Both as-deposited and annealed MIS-structures were studied. The time of annealing was 30 minutes at a temperature of 500 °C in atmospheric air. The *I*–*V* characteristics were studied before and after annealing using an Agilent B2902A parameter analyzer, the bottom electrodes were a silicon substrate with indium-gallium paste that was grounded during the experiment and the top electrodes was the ITO

© Хамуд Г.А., Камаев Г.Н., Вернья М., Володин В.А., 2024. Издатель: Санкт-Петербургский политехнический университет Петра Великого.

contacts to which positive and negative voltages were applied. Moreover, the *I*–*V* characteristics were studied in the dark and under illumination of a halogen lamp. The light spot was focused on one of the ITO top electrode. The size of the spot was about 1 mm^2. The optical power density was about 1000 Watts per square meter, so about 0.5 milliwatts fell on the top electrode area.

Results and Discussion

Fig. 1, *a*, *b*, *c*, *d* shows the *I*–*V* characteristics in the dark and when illuminated with a halogen lamp for samples 1 (without Ge inclusion) and 2 (with 3 nm thick Ge layer) before and after annealing. As one can see from dark *I*–*V* characteristics of all as-deposited and annealed samples, they all have diode characteristics. It is also clear for all samples that photocurrent occurs especially with reverse bias. Next, we consider the effect of annealing on the *I*–*V* characteristics for both samples.

For the structure of the as-deposited sample 1 (without Ge inclusion), one can see that with the reverse bias the dark current is relatively large (Fig. 1, *a*), photocurrent exceeds dark current by 2–3 times. As seen from Fig. 1, *b*, the annealing leads to notable reduction of dark current and to slight decrease of light current. Presumably, after annealing, the properties of the MIS structure change, due to formation of amorphous germanium nanoclusters in GeO[SiO$_2$] layer during annealing, which alter the transport properties of GeSi$_x$O$_y$ films [3]. It is worth noting that the light current exceeds the dark current by about four orders of magnitude under reverse bias and that there is a significant light current under direct bias (Fig. 1, *b*).

As for the *I*–*V* characteristics of sample 2 (before annealing, with Ge inclusion), Fig. 1, *c* shows good diode characteristics and relatively high photocurrent under the negative (reverse) bias. Some hysteresis is also seen in light *I*–*V* characteristics, which can be associated with charging of the germanium layer. Evidently, annealing also led to modification of the *I*–*V* characteristics (Fig. 1, *d*). It can be observed from the dark *I*–*V* characteristics that the current minimum is

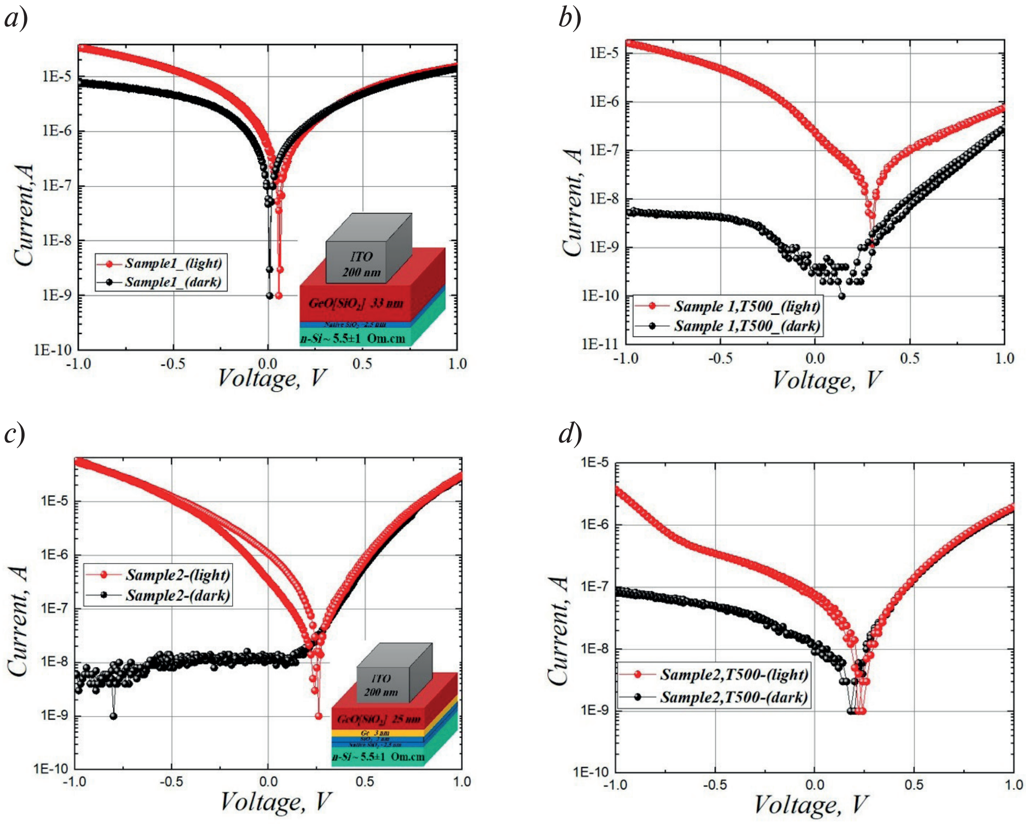

Fig. 1. *I*–*V* characteristics (dark marked by black circles and light by red circles) of MIS structures: sample 1 without annealing (*a*); sample 1 after annealing (*b*); sample 2 without annealing (*c*); sample 2 after annealing (*d*)

not observed at zero voltage bias. This is due to the effect assumed above, i.e., charging of the germanium layer. Notice that annealing of this sample did not improve photosensitivity, as the difference between the ratio of light current to dark current decreased (Fig. 1, *c* and 1, *d*), in contrast to sample 1, where the annealing leads to improving of photosensitivity. However, as already noted, as-deposited sample 2 has very good photosensitivity.

To find out where the light is absorbed (in the ITO contacts, in the GeSi$_x$O$_y$ films, or in the silicon substrate), we studied the reflection and transmission spectra of: ITO contacts on transparent sapphire substrates; glass with FTO; sample 1 deposited on glass with FTO; the sample 2 deposited on a glass substrate with FTO. It was obtained from the analysis of the transmission and reflection spectra of the ITO film on sapphire (the spectra are not shown here) that the ITO top electrodes are practically transparent to light in the range from 400 nm to 800 nm and showed no absorption of light in this range. For the glass with FTO, as Fig. 2, *a* shows, the sum of the transmission spectrum with reflection spectrum in the range of green light (wavelength ~ 500 nm) is about 85% (Fig. 2, *a*). The same value was obtained for sample 1 deposited on the glass with FTO (Fig. 2, *b*). This means that the GeO[SiO$_2$] film in this sample does not absorb light and most of the light is absorbed in the Si substrate (in the case of MIS-structure). But for sample 2 deposited on the glass with FTO, the sum of reflection and transmittance is about 70% (Fig. 2, *c*). This leads us to the conclusion that ~ 15% of the light falling on sample 2 is absorbed in the multilayered structure, especially in the germanium layer, and the rest of the light is absorbed in the Si substrate (in the case of MIS-structure). It is worth noting that although the maximum spectral power of a halogen lamp is in the red range, there is a noticeable amount of green and blue light in its spectrum.

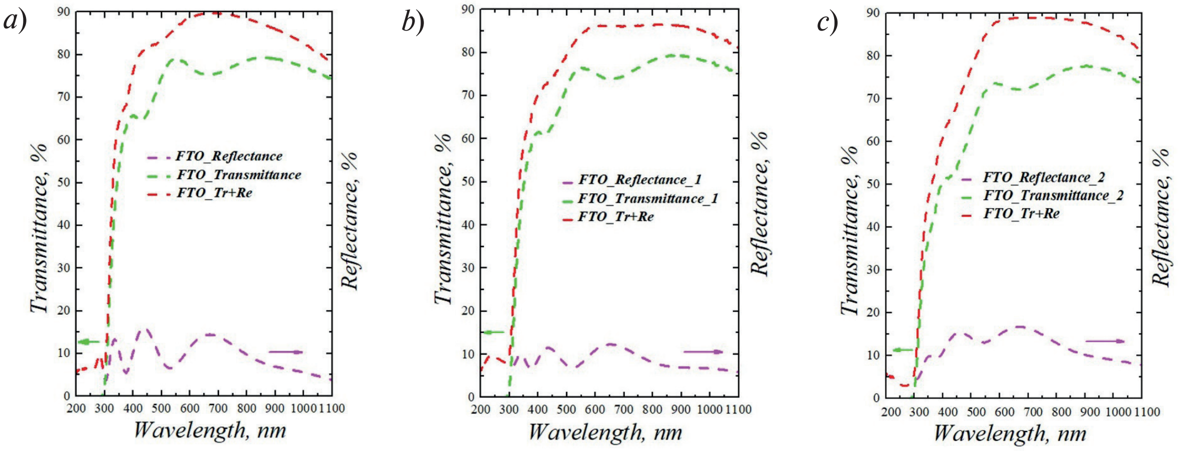

Fig. 2. Transmittance, reflectance spectra, and its sum: FTO film on a glass substrate (*a*); sample 1 on a glass substrate with FTO (*b*); sample 2 on a glass substrate with FTO (*c*)

Now we can conclude that most of the light is absorbed in the Si substrate for both MIS-structures (samples 1 and 2), but part of the light is absorbed in the germanium layer for the second MIS-structure (sample 2). Both mechanisms of photocurrent appearance are shown in Fig. 3. The mechanism that occurs here is analogous to the photocurrent mechanism that happens in solar cells with Schottky barriers [4]. For the first sample, the reverse bias creates a large region of space charge, namely, the depletion region, which can be estimated based on the known relationship of the Irwin curves for silicon. According to Irwin curves, the donor concentration corresponding to the value of the resistivity of 5.5 ± 1 Ohm·cm is 10^{15} cm^{-3}. Therefore, the width of the depletion region at half a volt is 0.8 micrometers and increases with increasing voltage value, reaching 3.2 micrometers at -8 V. This region absorbs the incident photons, which generate the electron-hole pairs that contribute to increasing the photocurrent. The photoelectrons drift to the bottom electrode due to reverse bias. The photoholes drift to the native-SiO$_2$/GeO[SiO$_2$] (sample 1) or to the SiO$_2$/Ge/GeO[SiO$_2$] multilayered structure (sample 2). It is important to note here that the silicon dioxide layer between the silicon substrate and the GeO[SiO$_2$] film (sample 1) or the Ge/GeO[SiO$_2$] multilayered structure (sample 2) is tunnel thin, as in the case of Ge quantum-dot-based photodetector [2]. So, photoholes can tunnel through it. There are then two possible paths for photoholes. They can move through the traps to reach the ITO top electrode (blue path, Fig. 3) or they can recombine in the GeO[SiO_2] film (sample 1) or in the Ge layer (sample 2) with electrons, which can drift from ITO top electrode due to reverse bias.

For the sample 2, there is an additional mechanism where some of the light is absorbed in the germanium layer and an electron-hole pair is generated in this layer. Electrons can pass easily (due to tunneling) through the insulating layer (SiO_2 ~ 4.5 nm) since the Ge/Si is a type II heterostructure, so the energy level for electrons in Ge is higher than the energy level for electrons in Si. But for the photoholes, the Ge layer is quite a deep trap. Also here, the photoelectrons can pass through the circuit as in the previous mechanism. While for holes, they either can move through the traps to reach the ITO contacts and recombine with the electrons injected from them, or they can recombine with the electrons which can drift through the traps from the ITO top electrode.

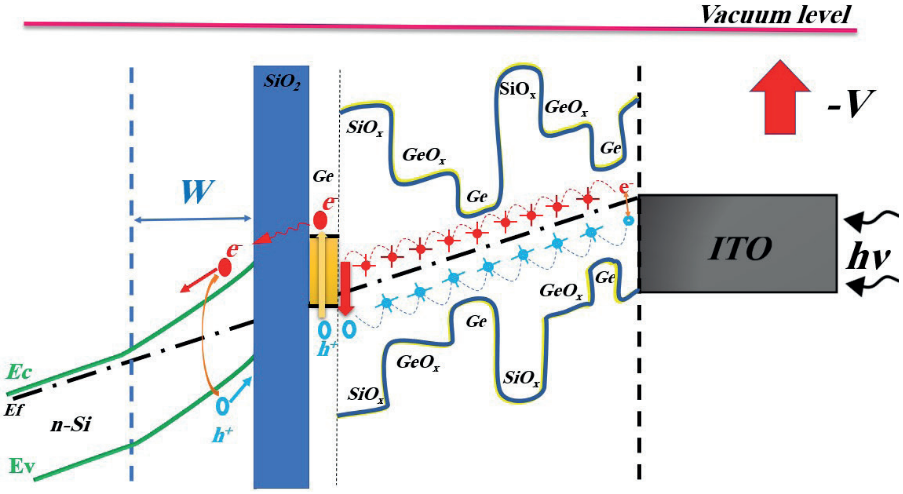

Fig. 3. Mechanism of photocurrent occurrence in the sample with and without a Ge layer

Conclusion

1) The possibility of using $GeSi_xO_y$ films in photosensors has been demonstrated, and a good ratio of photocurrent to dark current (photosensitivity) has been obtained. The annealing has improved this ratio for the sample without a Ge layer, as this photosensitivity reached 4000 at the -1 V bias, and worsened it for the sample with a Ge layer, as the photosensitivity at the -1 V bias decreased from 6250 to 50. We point out that our photosensitivity is much better than the optical sensitivity obtained in work [2] using quantum dots of germanium.

2) The use of a MIS structure including Ge layers can presumably make it possible to expand the sensitivity edge of photodetectors to the long-wavelength region.

Acknowledgments

The authors acknowledge the Shared Research Center "VTAN" of the Novosibirsk State University.

REFERENCES

1. **Simón Z.J.H., López J.A.L., de la Luz Á.D.H., Salgado G.G., Leyva K.M., López J.C., Conde G.O.M., Lara A.B., Hernández H.P.M., Hernández E.G., Méndez J.F.,** SiO_x films deposited by HFCVD: Their conduction response to light and intrinsic photovoltaic effect, Surfaces and Interfaces. 26 (2021) 101411 (1–15).

2. **Mansour Aouassa, Ridha M'gaieth, Azeza B., Berbézier I., Favre L.,** Highly Improved MIS Photodetector Sensitivity Using Ge Nanocrystals, Research Square (Research Square). (2021).

3. **Yushkov I.D., Yin L., Kamaev G.N., Prosvirin I.P., Geydt P.V., Vergnat M., Volodin V.A.,** Memristors Based on Many-Layer Non-Stoichiometric Germanosilicate Glass Films, Electronics. 12 (2023) 873 (1–14).

4. **Kobayashi H., Ishida T., Yoshihiro Nakato, Mori H.,** Mechanism of carrier transport through a silicon-oxide layer for ⟨indium-tin-oxide/silicon-oxide/silicon⟩ solar cells, Journal of Applied Physics. 78 (6) (1995) 3931–3939.

THE AUTHORS

HAMOUD Ghaithaa A.
k.gaisaa@g.nsu.ru
ORCID: 0009-0001-6796-4432

KAMAEV Gennadiy N.
kamaev@isp.nsc.ru
ORCID: 0000-0002-6413-0969

VERGNAT Michel
michel.vergnat@univ-lorraine.fr
ORCID: 0000-0001-5237-9014

VOLODIN Vladimir A.
volodin@isp.nsc.ru
ORCID: 0000-0002-1431-8242

Received 06.12.2023. Approved after reviewing 22.01.2024. Accepted 22.01.2024.

St. Petersburg Polytechnic University Journal. Physics and Mathematics. 2024 Vol. 17. No. 1.1
Научно-технические ведомости СПбГПУ. Физико-математические науки. 17 (1.1) 2024

Conference paper
UDC 681.782.473
DOI: https://doi.org/10.18721/JPM.171.125

High-temperature high-voltage *p–i–n* diodes based on low doped heteroepitaxial layers AlGaAs and AlGaAsSb

F.Yu. Soldatenkov [1] ✉, A.E. Ivanov [1, 2], D.A. Malevskiy [1], S.V. Levin [1]

[1] Ioffe Institute, St. Petersburg, Russia;
[2] Submicron Heterostructures for Microelectronics Research and Engineering Center of the RAS, St. Petersburg, Russia
✉ f.soldatenkov@mail.ioffe.ru

Abstract. The article investigates the temperature dependences of the current–voltage characteristics and reverse recovery of high-voltage $Al_xGa_{1-x}As$ and $Al_xGa_{1-x}As_{1-y}Sb_y$ *p–i–n* diodes manufactured by liquid-phase epitaxy when heated to 350 °C. It was found that with an increase in the Al content in the base layers, the operating temperatures of the diodes increase from 250 °C at $x = 0$ to 350 °C at $x \sim 0.45$, while the forward voltage drops of the diodes also increase. It is shown that the use of small Sb additions in AlGaAs layers reduces the reverse recovery times of diodes by almost an order of magnitude, from 40–80 ns to 5–8 ns.

Keywords: AlGaAsSb, heterostructure, high-voltage p^0–i–n^0 junction, diode, liquid-phase epitaxy, lattice mismatch, reverse recovery of diodes

Funding: The study was carried out at the expense of a Russian Science Foundation grant 23-29-00245, https://rscf.ru/project/23-29-00245/.

Citation: Soldatenkov F.Yu., Ivanov A.E., Malevskiy D.A., Levin S.V., High-temperature high-voltage *p–i–n* diodes based on low doped heteroepitaxial layers AlGaAs and AlGaAsSb, St. Petersburg State Polytechnical University Journal. Physics and Mathematics. 17 (1.1) (2024) 155–159. DOI: https://doi.org/10.18721/JPM.171.125

This is an open access article under the CC BY-NC 4.0 license (https://creativecommons.org/licenses/by-nc/4.0/)

Материалы конференции
УДК 681.782.473
DOI: https://doi.org/10.18721/JPM.171.125

Высокотемпературные высоковольтные *p–i–n* диоды на основе слаболегированных гетероэпитаксиальных слоев AlGaAs и AlGaAsSb

Ф.Ю. Солдатенков [1] ✉, А.Е. Иванов [1, 2], Д.А. Малевский [1], С.В. Левин [1]

[1] Физико-технический институт им. А.Ф. Иоффе РАН, Санкт-Петербург, Россия;
[2] Научно-технологический центр микроэлектроники и субмикронных гетероструктур РАН, Санкт-Петербург, Россия
✉ f.soldatenkov@mail.ioffe.ru

Аннотация. В работе исследованы температурные зависимости вольт-амперных характеристик и обратного восстановления высоковольтных $Al_xGa_{1-x}As$ и $Al_xGa_{1-x}As_{1-y}Sb_y$ *p–i–n* диодов, изготовленных методом жидко-фазной эпитаксии, при нагреве до 350 °C. Выяснено, что с увеличением доли Al в базовых слоях рабочие температуры диодов повышаются от 250 °C при $x = 0$ до 350 °C при $x \sim 0.45$, при этом увеличиваются прямые падения напряжения диодов. Показано, что применение малых добавок Sb в слои AlGaAs позволяет уменьшить времена обратного восстановления диодов почти на порядок, с 40–80 нс до 5–8 нс.

© Soldatenkov F.Yu., Ivanov A.E., Malevskiy D.A., Levin S.V., 2024. Published by Peter the Great St. Petersburg Polytechnic University.

Ключевые слова: AlGaAsSb, гетероструктура, высоковольтный p^0–i–n^0-переход, диод, жидко-фазная эпитаксия, рассогласование по параметру решетки, обратное восстановление диодов

Финансирование: Исследование выполнено за счет гранта Российского научного фонда № 23-29-00245, https://rscf.ru/project/23-29-00245/.

Ссылка при цитировании: Солдатенков Ф.Ю., Иванов А.Е., Малевский Д.А., Левин С.В. Высокотемпературные высоковольтные *p*–*i*–*n* диоды на основе слаболегированных гетероэпитаксиальных слоев AlGaAs и AlGaAsSb // Научно-технические ведомости СПбГПУ. Физико-математические науки. 2024. Т. 17. № 1.1. С. 155–159. DOI: https://doi.org/10.18721/ JPM.171.125

Статья открытого доступа, распространяемая по лицензии CC BY-NC 4.0 (https://creativecommons.org/licenses/by-nc/4.0/)

Introduction

Modern power electronics and pulse technique are developing to create high-speed devices capable of operating at increased frequencies and temperatures. Using wide-band AlGaAs solid solutions allows to increase operating temperatures above 300 °C [1]. Introducing small amounts of Sb or In additives into GaAs or AlGaAs-based layers can increase device speed and reduce electrical losses during switching by controlling the formation of structural defects in heterostructures with a specific lattice parameter mismatch [2].

Materials and Methods

Epitaxial growth of high-voltage low doped gradual AlGaAs and AlGaAsSb p^0–i–n^0 junctions was carried out using a modified liquid-phase epitaxy (LPE) method in a piston-type graphite container. The growing processes were carried out on p^+-GaAs substrates with an orientation of (100), doped with zinc up to $5{\cdot}10^{18}$ cm^{-3}, from a confined solution-melt Al–Ga–As or Al–Ga–As–Sb, at temperatures ranging from 900–850 °C to 750–700 °C. This was followed by the growth of a tellurium-doped n^+-GaAs emitter layer with a doping concentration of $2{\cdot}10^{18}$ cm^{-3}. The technique for obtaining gradual Al$_x$Ga$_{1-x}$As p^0–i–n^0 junctions from a single solution melt due to autodoping with background impurities was described earlier in [1, 3]. Samples of diodes (chips) had the form of mesa structures, which were obtained by chemical etching of active layers down to the substrate. A multilayer AgMn–Ni–Au contact was applied to the p^+-GaAs substrate, and AuGe–Ni–Au was applied to the n^+-GaAs emitter.

Measurements of the device characteristics were conducted in continuous and pulsed modes at temperatures ranging from 20 °C to 350 °C. The maximum test temperature for the diodes was limited by the capabilities of the measurement equipment utilized.

The temperature dependence of the effective minority carrier lifetime (τ_{eff}) using the reverse recovery time of p^+–p^0–i–n^0–n^+ diodes [4, 5] were investigated. The reverse recovery method involves applying rectangular pulses of forward (I_{f}) and reverse current (I_{r}) to the diode with specific signal amplitudes and durations. The reverse recovery time of a diode, which is the time it takes for the diode to switch from the conducting state to the blocking state, is composed of two phases: the duration of high reverse conductivity t_1 (during which the magnitude of the reverse current remains constant) and the decay of the reverse current t_2. The total recovery time $t_{\mathrm{r}} = t_1 + t_2$ depends on the effective lifetime of minority carriers, and, consequently, on the density of defects and impurities with deep levels and their capture cross sections. By maintaining a constant ratio of forward and reverse current pulse amplitudes ($I_{\mathrm{f}}/I_{\mathrm{r}} \sim 5$–6), it can be approximated that $t_1 \approx \tau_{\mathrm{eff}}$ [5].

Results and Discussion

The current–voltage characteristics at different temperatures and reverse recovery time of p^+–p^0–i–n^0–n^+ diodes based on high-voltage low doped layers of GaAs, GaAs$_{1-y}$Sb$_y$, Al$_x$Ga$_{1-x}$As and Al$_x$Ga$_{1-x}$As$_{1-y}$Sb$_y$ with different compositions were obtained. Fig. 1 shows the temperature dependence of the forward current–voltage characteristic in the static mode of *p*–*i*–*n* diodes

© Солдатенков Ф.Ю., Иванов А.Е., Малевский Д.А., Левин С.В., 2024. Издатель: Санкт-Петербургский политехнический университет Петра Великого.

based on a low doped $GaAs_{1-y}Sb_y$ layer (with $y \sim 0.02$) and a wider bandgap $Al_xGa_{1-x}As$ layer (with a maximum AlAs content in the layer x up to 0.45). It was found that increasing the Al content in the layers (and consequently the bandgap) leads to an increase in the operating temperatures of the diodes from approximately 250 °C at $x = 0$ to around 350 °C at $x \sim 0.45$, accompanied by an increase in the forward voltage drop (U_f) of the diodes. Small additions of Sb (y up to 0.05) do not significantly affect the static current–voltage characteristics of the diodes under investigation.

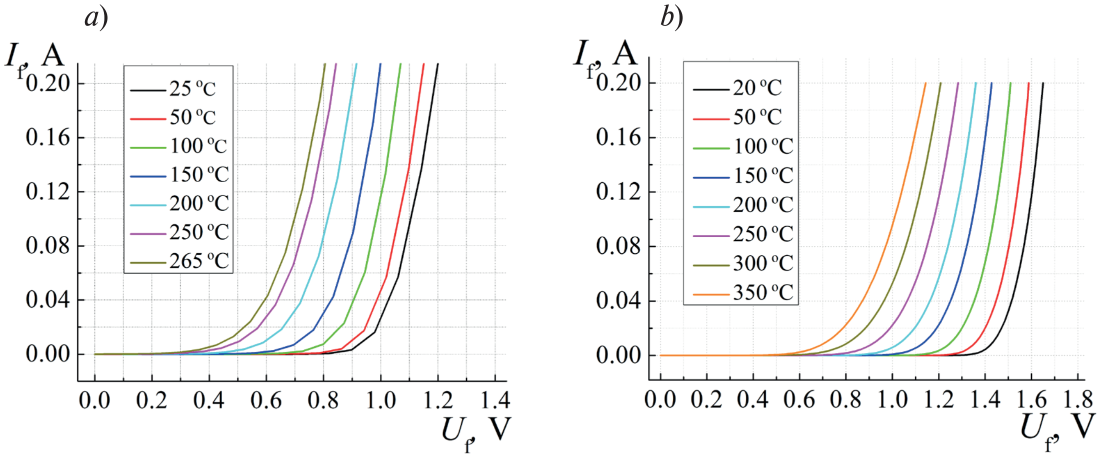

Fig. 1. Forward voltage drops in diodes with high-voltage $GaAs_{1-y}Sb_y$ p^0–i–n^0 layers with y up to 0.02 (a) and $Al_xGa_{1-x}As$ with $x \sim 0.45$ (b) at temperatures from 25 to 350 °C. Sample area $S \sim 0.65$ mm^2

Fig. 2 shows switching oscillograms of diodes with base layers $Al_xGa_{1-x}As$ and $Al_xGa_{1-x}As_{1-y}Sb_y$, demonstrating the influence of small Sb additives in AlGaAs layers, leading to the controlled formation of spatial defects, on the dynamics of diode switching. From Figure 2, it can be observed that the effective lifetime of nonequilibrium charge carriers τ_{eff} (assuming $\tau_{eff} \sim t_1$) and, accordingly, the reverse recovery time of a diode with an $AlxGa_{1-x}As$ base layer is more than an order of magnitude greater than τ_{eff} of a diode based on an $Al_xGa_{1-x}As_{1-y}Sb_y$ layer (the figure compares diodes with approximately the same aluminum content in both base layers).

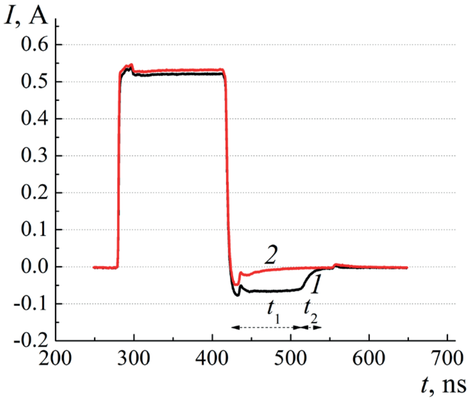

Fig. 2. Oscillograms of switching p–i–n diodes with base layers of $AlxGa_{1-x}As$ (1) and $Al_xGa_{1-x}As_{1-y}Sb_y$ (2) with $x \sim 0.30$ and y up to 0.05

Also, for some samples, the temperature dependences of the effective lifetime of nonequilibrium charge carriers τ_{eff} in the base layers of the diodes were determined (Fig. 3). The measurements showed a significant (up to five times) increase in the duration of the t_1 phase (and, accordingly, τ_{eff}) in the temperature range of 25–350 °C when switching the $Al_xGa_{1-x}As$ diode. However, the turn-off time of the GaAs diode did not depend so much on the temperature. This can be explained by the fact that in the layers under study, the lifetimes of nonequilibrium charge carriers are determined by different centers with deep levels. In GaAs p^0–i–n^0 junctions grown by the LPE method [6], τ_{eff} can be determined by hole traps HL2 and HL5 (related with a gallium vacancies), as well as electron trap EL2 related with the antisite defect of arsenic in the gallium site (arsenic in the gallium sublattice). In $Al_xGa_{1-x}As$ p^0–i–n^0 junctions (with $x \geq 0.21$), we believe that the relaxation time of nonequilibrium carriers, as well as its temperature dependence, are determined by the thermal capture of holes to the negatively charged level (DX) of the DX-center associated with residual donor impurities Se and Te [1].

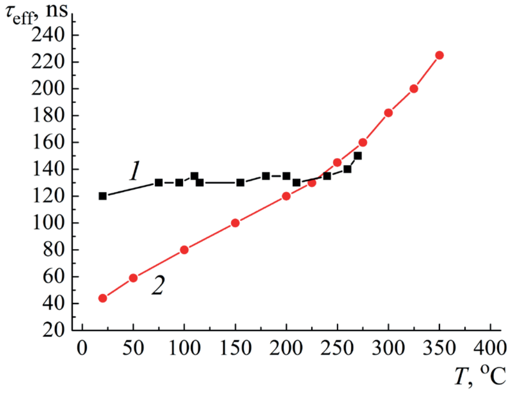

Fig. 3. Temperature dependences of the effective lifetime of nonequilibrium carriers in p–i–n diodes based on GaAs (*1*) and AlxGa$_{1-x}$As with x ~ 0.45 (*2*)

Conclusion

In the research, the operating temperatures of diodes based on AlxGa$_{1-x}$As and AlxGa$_{1-x}$As$_{1-y}$Sb$_y$ solid solutions were determined. The temperature range for which the diodes retain rectifying properties was found to be from 250–280 °C at $x = 0$ to at least 350 °C at $x \sim 0.45$, with an increase in the Al content in the layers. The current and temperature dependences of the forward voltage drops of diodes with $Al_xGa_{1-x}As_{1-y}Sb_y$ layers (with y up to 0.05) differed slightly from diodes with $Al_xGa_{1-x}As$ layers of the same aluminum composition. One notable result of adding small amounts of Sb to AlGaAs layers was a significant reduction in the reverse recovery time of high-voltage diodes based on them. The reverse recovery time decreased from 40–80 ns for diodes with AlGaAs base layers to 5–8 ns for AlGaAsSb structures with dislocations.

REFERENCES

1. **Sobolev M.M., Soldatenkov F.Y., Danil'chenko V.G.,** Deep-level defects in high-voltage AlGaAs p–i–n diodes and the effect of these defects on the temperature dependence of the minority carrier lifetime, Journal of Applied Physics. 128 (2020) 095705.

2. **Sobolev M.M., Soldatenkov F.Yu., Shul'pina I.L.,** Misfit dislocation-related deep levels in InGaAs/GaAs and GaAsSb/GaAs p–i–n heterostructures and the effect of these on the relaxation time of nonequilibrium carriers, Journal of Applied Physics. 123 (2018) 161588.

3. **Sobolev M.M., Soldatenkov F.Y.,** Capacitance Spectroscopy of Heteroepitaxial AlGaAs/GaAs p–i–n Structures, Semiconductors. 54 (2020) 1260–1266.

4. **Soldatenkov F.Yu., Danil'chenko V.G., Korol'kov V.I.,** Carrier lifetime control in high-voltage p–i–n diodes on the base of the $In_xGa_{1-x}As$/GaAs heterostructures, Semiconductors. 41 (2007) 211–214.

5. **Nosov Yu.R.,** Switching in semiconductor diodes, Plenum Press, New York, 1969.

6. **Sobolev M.M., Soldatenkov F.Yu., Kozlov V.A.,** Study of deep levels in GaAs p–i–n structures, Semiconductors. 50 (2016) 924–928.

THE AUTHORS

SOLDATENKOV Fedor Yu.
f.soldatenkov@mail.ioffe.ru
ORCID: 0000-0002-6154-7208

IVANOV Anton E.
a-e-ivano-v@yandex.ru
ORCID: 0000-0003-2819-1534

MALEVSKIY Dmitriy A.
dmalevsky@scell.ioffe.ru
ORCID: 0000-0002-9337-4137

LEVIN Sergey V.
sergiolevin733@gmail.com

Received 13.12.2023. Approved after reviewing 11.02.2024. Accepted 11.02.2024.

St. Petersburg Polytechnic University Journal. Physics and Mathematics. 2024 Vol. 17. No. 1.1
Научно-технические ведомости СПбГПУ. Физико-математические науки. 17 (1.1) 2024

Conference paper
UDC 08.1; 08.2; 08.3
DOI: https://doi.org/10.18721/JPM.171.126

Deep-level transient spectroscopy of solar cells based on HJT architecture under influence of electron irradiation

O.P. Mikhaylov [1] ✉, A.I. Baranov [2], A.S. Gudovskikh [2], E.I. Terukov [3]

[1] St. Petersburg Electrotechnical University "LETI", St. Petersburg, Russia;

[2] Alferov University, St. Petersburg, Russia;

[3] Ioffe Institute, St. Petersburg, Russia

✉ oleg.mikhaylov.00@gmail.com

Abstract. In this work, we study the effect of irradiation as in low Earth orbits on heterojunction technology structures (*p*)*a*-Si:H/(*n*)*c*-Si. To compare the photoelectric properties, three samples were created: the original (without electron irradiation) and two irradiated ones with the fluence of irradiation of $5 \cdot 10^{14}$ cm^{-2} and $1 \cdot 10^{15}$ cm^{-2}. Catastrophic deterioration of photoelectrical properties were observed for this irradiation: short-circuit current falls almost by two times, and open-circuit voltage drops by 150–200 mV. By measurements of deep-level transient spectroscopy, formation of A-center (V-O, vacancy-oxygen) with 0.16–0.17 eV in silicon wafer in bulk material were shown, and its concentration increases with growth of irradiation dose. Its arising leads to degradation of solar cells.

Keywords: solar cells, heterojunction, irradiation, defects

Citation: Mikhaylov O.P., Baranov A.I., Gudovskikh A.S. Terukov E.I., Deep-level transient spectroscopy of solar cells based on HJT architecture under influence of electron irradiation, St. Petersburg State Polytechnical University Journal. Physics and Mathematics. 17 (1.1) (2024) 160–164. DOI: https://doi.org/10.18721/JPM.171.126

This is an open access article under the CC BY-NC 4.0 license (https://creativecommons.org/licenses/by-nc/4.0/)

Материалы конференции
УДК 08.1; 08.2; 08.3
DOI: https://doi.org/10.18721/JPM.171.126

Нестационарная спектроскопия глубоких уровней в солнечных элементах HJT архитектуры под действием облучения электронами

О.П. Михайлов [1] ✉, А.И. Баранов [2], А.С. Гудовских [2], Е.И. Теруков [3]

[1] Санкт-Петербургский государственный электротехнический университет
«ЛЭТИ» им. В. И. Ульянова (Ленина), Санкт-Петербург, Россия;

[2] Академический университет имени Ж.И. Алфёрова РАН, Санкт-Петербург, Россия;

[3] Физико-технический институт им. А.Ф. Иоффе РАН, Санкт-Петербург, Россия

✉ oleg.mikhaylov.00@gmail.com

Аннотация. В данной работе проводится исследование влияния сходного с космическим излучения на околоземных орбитах на дефектообразование в СЭ на подложках кремния *n*-типа с технологией гетероперехода, выращенных методом плазмохимического осаждения. Для сравнения фотоэлектрических свойств были созданы три образца: исходный (без электронного облучения) и два облученных с флюенсом облучения $5 \cdot 10^{14}$ cm^{-2} и $1 \cdot 10^{15}$ cm^{-2}. Продемонстрировано катастрофическое падение параметров солнечных элементов: ток короткого замыкания падает почти в два раза, а напряжение холостого хода на 180–200 мВ. Измерения методом нестационарной спектроскопии глубоких уровней продемонстрировали формирование А-центров (V-O, комплекс

© Mikhaylov O.P., Baranov A.I., Gudovskikh A.S. Terukov E.I., 2024. Published by Peter the Great St. Petersburg Polytechnic University.

вакансия-кислород) с энергией активации 0.16—0.17 эВ во всем объеме подложки кремния, а их концентрация растет с увеличением дозы облучения. Таким образом, их формирование ответственно за ухудшение фотоэлектрических свойств рассматриваемых солнечных элементов на *n*-Si.

Ключевые слова: солнечные элементы, гетеропереход, космическое излучение, дефекты

Ссылка при цитировании: Михайлов О.П., Баранов А.И., Гудовских А.С. Теруков Е.И. Нестационарная спектроскопия глубоких уровней в солнечных элементах HJT архитектуры под действием облучения электронами // Научно-технические ведомости СПбГПУ. Физико-математические науки. 2024. Т. 17. № 1.1. С. 160—164. DOI: https:// doi.org/10.18721/ JPM.171.126

Статья открытого доступа, распространяемая по лицензии CC BY-NC 4.0 (https:// creativecommons.org/licenses/by-nc/4.0/)

Introduction

The technology of silicon solar cells with a heterojunction, also known as HJT solar cells (heterojunction technology), combines the advantages of crystalline and amorphous silicon, demonstrating the potential to achieve high solar energy conversion efficiency using less silicon and lower manufacturing temperatures, not exceeding 200—250 °C, compared to traditional diffusion technologies [1]. The first HJT solar cells were developed in the 1990s by Sanyo with an efficiency of 12% [2]. After many years of research, this technology has enabled achieving an efficiency of over 26%, which is a record for single-junction silicon solar cells [3].

Solar elements based on HJT technology, actively used on Earth, are of interest for space applications. However, due to the presence of radiation in outer space, which can negatively impact the electro-optical characteristics of solar elements, research is needed to study the influence of space radiation on HJT structure. Currently, there is much less research in this area compared to A3B5 elements. Nevertheless, there are articles investigating the impact of electron flux on HJT structure. For example, according to the results of the article [4], it was found that when irradiating the heterostructure of the solar element on an n-type silicon substrate, the peak quantum efficiency decreases by 60%, and the short-circuit current and fill factor decrease by approximately two times. Presumably, this is due to the increase in energy required for minimum electrical conductivity of doped layers of amorphous hydrogenated silicon. Additionally, deterioration of absorption in silicon-based heterostructure solar elements after proton irradiation has been demonstrated [5]. In our previous work, we explored irradiated by electros HJT by admittance spectroscopy. Admittance spectroscopy revealed a defect with a conductivity activation energy of 0.18 eV in irradiated structures, which could probably be responsible for degradation of photoelectrical properties, and its concentration increases with increasing fluence [6]. However, this method is mostly sensitive to interface states and defect located near to heterojunction in space charge region of silicon wafer, so it is complicated to obtain information about bulk properties of silicon wafer.

Therefore, in this study deep-level transient spectroscopy will be applied to HJT samples to profile silicon wafer far from heterojunction *a*-Si:H/*c*-Si.

Materials and Methods

The paper discusses solar cells grown on *n*-Si ($n = 3{\cdot}10^{15}$ cm^{-3}) substrates using plasma-enhanced chemical vapor deposition. To passivate surface defects on the front and rear sides of the substrate, layers of intrinsic amorphous hydrogenated silicon (*i*-*a*-Si:H) are applied. To create ohmic contact on the rear side and a heterojunction on the front side, layers of doped *n*- and *p*-*a*-Si:H are deposited on the intrinsic layers. Layers of conducting transparent material ITO (indium tin oxide) were applied onto the doped amorphous silicon layers on the rear and front sides, serving also as an anti-reflective coating. Metallic contacts were formed using the screen-printing method with silver paste.

© Михайлов О.П., Баранов А.И., Гудовских А.С. Теруков Е.И., 2024. Издатель: Санкт-Петербургский политехнический университет Петра Великого.

These structures were affected by electron irradiation with an energy of 1 MeV at fluences of $5\cdot10^{14}$ cm^{-2}, $1\cdot10^{15}$ cm^{-2}. The chosen irradiation parameters were selected due to the resulting equivalent fluence ($1\cdot10^{13} - 3\cdot10^{15}$ cm^{-2}) corresponds to the exposure of the investigated silicon photovoltaic converters in low Earth orbits, significantly lower than the corresponding value in radiation-hazardous orbits (> 2000 km). The $I-V$ curves under AM1.5G (100 mW/cm^2) were measured using Abet Technology SunLite simulator and Keithley 2400 source-meter.

Deep-level transient spectroscopy (DLTS) is the powerful method for exploration defect levels in semiconductor devices and heterojunction. The method is based on measurement of capacitance relaxation of the space charge region after filling it with a bias voltage pulse. The rate of capacitance relaxation is determined by the rate of charge carrier emission from possible deep levels within the semiconductor bandgap, which, in turn, depends on the temperature. Capacitance deep-level transient spectroscopy were done using an automated installation based on a Boonton-7200B capacitance bridge in the temperature range of 40–300 K in Janis CCS-400H/204 helium cryostat. The setup allows to apply bias voltage with different amplitude, all measurements were carried out in the LabView environment.

Results and Discussion

The current-voltage characteristics of the studied samples are presented in Fig. 1. Measurement results indicate that the $I-V$ curves significantly depend on the irradiation dose, and the photoelectric properties sharply deteriorate after irradiating the reference. At an irradiation fluence of $5\cdot10^{14}$ cm^{-2}, the open-circuit voltage and short-circuit current dropped by approximately 30%, from 0.7 V to 0.52 V and from 33 mA/cm^2 to 22 mA/cm^2, respectively. Further increasing the fluence to $1\cdot10^{15}$ cm^{-2} leads to additional deterioration in the photoelectric properties, although not as significantly. Such behavior is explained by centers of non-radiative recombination in silicon wafer.

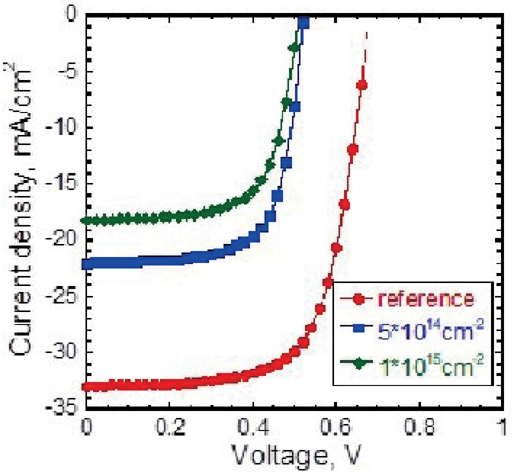

Fig. 1. Current-voltage characteristics under AM1.5G illumination at 25 °C of the studied samples

Further capacitance methods were applied to HJT solar cells. Firstly, capacitance-voltage characteristics for 1 MHz for initial sample is presented in Fig. 2, also dependence of depth on applied voltage is shown. As a result, electron concentration of $3\cdot10^{15}$ cm^{-3} is estimated which corresponds to doping of silicon wafer. $I-V$ characteristics for irradiated samples are similar.

Secondly, DLTS measurements were done for two different modes: $V_{init} = 0$ V, $V_{pulse} = +2$ V and $V_{init} = -8$ V, $V_{pulse} = +5$ V, pulse time is 50 ms, and relaxation was measured during 150 ms. Such two modes allow to detect defects in different space in silicon wafer: first one is near to heterojunction (not deeper than 550 nm, Fig. 2), and second one in bulk of wafer (in depth 1000° - 2000 nm, Fig. 2). DLTS spectra for rate window of 50 s^{-1} for three samples are presented in Fig. 3, *a* and 3, *b* for first mode and second one respectively. In the $S(T)$ graph of the reference HJT the response with high amplitude in the range of 40–55 K is observed, and the similar response was obtained in two irradiated samples. For *a*-Si:H the position of the Fermi level weakly depends on temperature due to high density of states (DOS) in the mobility gap.

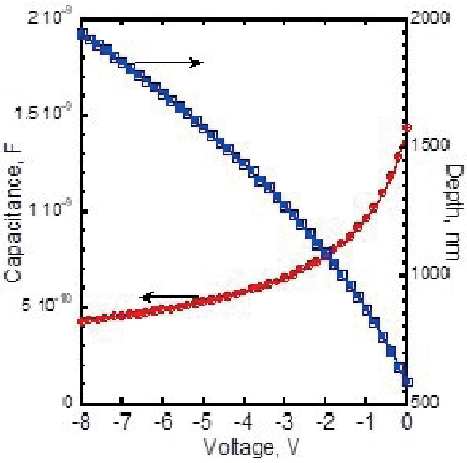

Fig. 2. Capacitance-voltage and depth-voltage characteristics for initial HJT solar cell

This effect is called pinning of the Fermi level. As a consequence electron (or hole for *p*-type) charge carrier density and conductivity has an exponential dependence on the temperature.

This temperature dependence is usually used to determine conductivity activation energy (being related to the position of the Fermi level) from Arrhenius plot (conductivity vs. $1/T$) [6]. It corresponds to the excitation energy of the impurity atom required to create the inactivation energy purity electrical conductivity of the *p*-*a*-Si:H semiconductor and is independent of irradiation, and is also detected using admittance spectroscopy [7]. Also, the response with $E_a = 0.07$ eV in the range of 100—150 K is detected in all samples, even in reference near to heterojunction (Fig. 3, *a*) unlike in bulk material (Fig. 3, *b*). But its parameters is not critical for photoelectric properties due to low capture cross section and E_a. However, in HJT solar cell irradiated by fluences of $5{\cdot}10^{14}$ cm^{-2} additional peak appears in 90 K corresponding to defect level with $E_a = 0.16$—0.17 eV, indicating the deep defects. Furthermore, these the amplitude of appeared peaks grows in two times with the increase in irradiation dose, suggesting a direct correlation between the electron fluence and the appearance of defects. The detected defect is probably an A-center (V-O, oxygen vacancy) [8], which arises as a result of the oxygen atom being displaced from a lattice site to the nearest interstitial site [9]. Furthermore, similar responses were detected in depth of silicon (Fig. 3, *b*), and estimated concentration (10^{12}—10^{13} cm^{-3}) is similar in both modes. It suggests arising of detected defects in the common silicon wafer, which leads to a deterioration in the photoelectric properties of the HJT of all solar cells of this series after irradiation. This result in

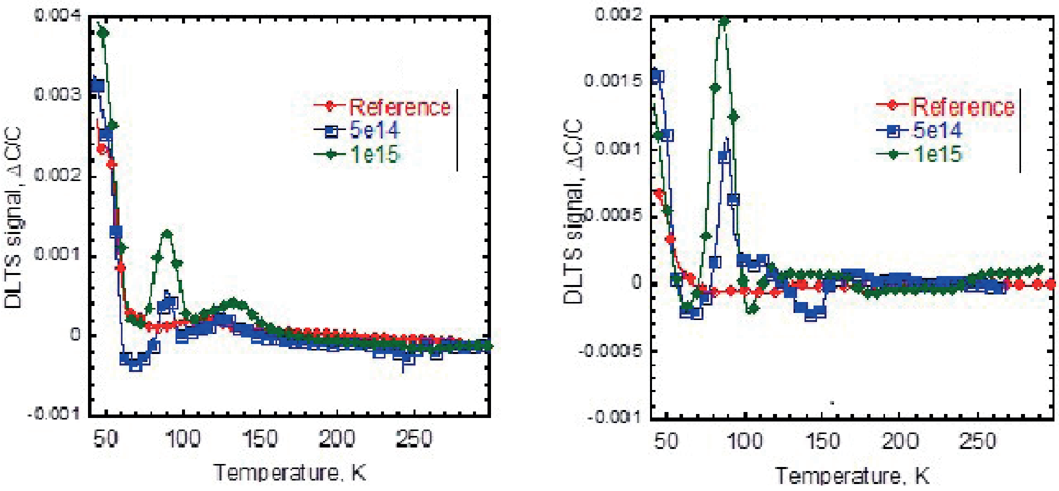
a) *b*)

Fig. 3. DLTS spectra for rate window of 50 s^{-1} for all samples obtained under conditions $V_{init} = 0$ V, $V_{pulse} = +\,2$V (*a*) and $V_{init} = -\,8$V, Vpulse = + 5V (*b*)

good correlation with measurement of admittance spectroscopy, but here we prove formation of A-center in the entire volume of the silicon wafer.

Conclusion

In result, influence of irradiation as in low Earth orbits on properties of solar cells based on heterojunction $(p)a$-Si:H/$(n)c$-Si were studied. Catastrophic deterioration of photoelectrical properties were observed for this irradiation: short-circuit current falls almost in two times, and open-circuit voltage drops by 150–200 mv. By measurements of deep-level transient spectroscopy, formation of A-center (V-O, vacancy-oxygen) with 0.16–0.17 eV in silicon wafer in bulk material were shown, and its concentration increases with growth of irradiation dose. Its arising leads to degradation of solar cells.

Acknowledgments

The work was carried out within the framework of the state assignment of the Ministry of Science and Higher Education of the Russian Federation (project number 0791-2023-0007).

REFERENCES

1. **Green M.A., Dunlop E.D., Yoshita M., Kopidakis N., Bothe K., Siefer G., HaoX.,** Prog. Photovoltaics Res. Appl., 31 (7) (2023) 1.
2. **Tanaka M., Taguchi M., Matsuyama T., Sawada T., Tsuda S., Nakano S., Hanafusa H., Kuwano Y.,** Jpn. J. Appl. Phys., 31 (11) (1992) 3518.
3. **Yoshikawa K., Yoshida W., Irie T., Kawasaki H., Konishi K., Ishibashi H., Asatani T., Adachi D., Kanematsu M., Uzu H., Yamamoto K.,** Sol. Energy Mater. Sol. Cells., 173, 37 (2017).
4. **van Swaaij R. A. C. M. M., Klaver A.,** J. Non. Cryst. Solids., 354, 2464 (2008) 19–25.
5. **Verkerk A.D., Rath J.K., Schropp R.E.I,** Energy Procedia. Elsevier, 2 (1), 221 (2010).
6. **Madan A., Shaw M.P.,** The physics and applications of amorphous semiconductors (Boston San Diego–N.Y.–London–Sydney–Tokyo–Toronto, Academic Press), 1988, 132.
7. **Mikhaylov O.P., Baranov A.I., Gudovskikh A.S., Terukov Ye.I., Kochergin A.V., Ataboev O.K.,** Journal of Technical Physics Letters, 2023 (accepted).
8. **Li Zh., Kraner H.W., Verbitskaya E., Eremin V., Ivanov A., Rattaggi M., Rancoita P.G., Rubinelli F.A., Fonash S.J., Dale C., Marshall P.,** IEEE Trans. Nucl. Sci., 39 (6) (1992) 1730.
9. **Ögmundsson A., Monakhov E.V., Hansen T.E., Grepstad J.K., Svensson B.G.,** Nucl. Instruments Methods Phys. Res. Sect. A Accel. Spectrometers, Detect. Assoc. Equip, 552 (1–2) 61 (2005).

THE AUTHORS

MIKHAYLOV Oleg P.
oleg.mikhaylov.00@gmail.com
ORCID: 0009-0005-6836-4091

BARANOV Artem I.
baranov_art@spbau.ru

GUDOVSKIKH Alexander S.
gudovskikh@gmail.com

TERUKOV Evgeny E.I.
eug.terukov@mail.ioffe.ru

Received 14.12.2023. Approved after reviewing 31.01.2024. Accepted 31.01.2024.

Conference paper
UDC 621.315.592
DOI: https://doi.org/10.18721/JPM.171.127

Thermally stable connecting GaAs/AlGaAs tunnel diodes for laser radiation multi-junction photoconverters

V.S. Kalinovskii [1], N.A. Maleev [1], A.P. Vasilyev [2], E.V. Kontrosh [1] ✉,
I.A. Tolkachev [1], K.K. Prudchenko [1], V.M. Ustinov [1]

[1] Ioffe Institute, St. Petersburg, Russia;
[2] Submicron Heterostructures for Microelectronics, Research & Engineering Center, RAS, St. Petersburg, Russia
✉ kontrosh@mail.ioffe.ru

Abstract. A new type of thermally stable GaAs/AlGaAs tunnel diode with an intermediate *i*-layer is proposed as a connecting element between photoactive sub-elements in monolithic multijunction photoconverters. In the temperature range of (25–80) °C, the current-voltage characteristics for two types of n^{++}-GaAs(δSi)/p^{++}-$Al_{0.4}Ga_{0.6}As$(C) and n^{++}-GaAs(δSi)/*i*-GaAs/p^{++}-$Al_{0.4}Ga_{0.6}As$:(C) structures of connecting tunnel diodes were studied. The temperature dependences of the peak tunneling current density – (J_p) and differential resistance – (R_d) were obtained. In the samples of tunnel diodes of the structure with an *i*-layer, an order of magnitude higher J_p values and an order of magnitude lower R_d values were obtained, with higher temperature stability than in the samples of the structure without an *i*-layer. The results obtained are useful in the development and creation of monolithic multijunction photoconverters of high-power laser radiation.

Keywords: tunnel diode, photoactive *p*-*n* junctions, multijunction laser radiation photoconverters, current-voltage characteristics, peak tunnel current density, differential resistance

Citation: Kalinovskii V.S., Maleev N.A., Vasilyev A.P., Kontrosh E.V., Tolkachev I.A., Prudchenko K.K., Ustinov V.M., Thermally stable connecting GaAs/AlGaAs tunnel diodes for laser radiation multi-junction photoconverters, St. Petersburg State Polytechnical University Journal. Physics and Mathematics. 17 (1.1) (2024) 165–170. DOI: https://doi.org/10.18721/JPM.171.127

This is an open access article under the CC BY-NC 4.0 license (https://creativecommons.org/licenses/by-nc/4.0/)

Материалы конференции
УДК 621.315.592
DOI: https://doi.org/10.18721/JPM.171.127

Термостабильные соединительные туннельные диоды GaAs/AlGaAs для многопереходных фотопреобразователей лазерного излучения

В.С. Калиновский [1], Н.А. Малеев [1], А.П. Васильев [2], Е.В. Контрош [1] ✉,
И.А. Толкачев [1], К.К. Прудченко [1], В.М. Устинов [1]

[1] Физико-технический институт им. А.Ф. Иоффе РАН, Санкт-Петербург, Россия;
[2] НТЦ микроэлектроники РАН, Санкт-Петербург, Россия
✉ kontrosh@mail.ioffe.ru

Аннотация. Предложен новый тип термостабильного GaAs/AlGaAs туннельного диода с промежуточным *i*-слоем, как соединительный элемент между фотоактивными суб-элементами в монолитных многопереходных фотопреобразователях лазерного излучения. В температурном диапазоне (25–80) °С исследованы вольтамперные

© Kalinovskii V.S., Maleev N.A., Vasilyev A.P., Kontrosh E.V., Tolkachev I.A., Prudchenko K.K., Ustinov V.M., 2024. Published by Peter the Great St. Petersburg Polytechnic University.

характеристики двух типов структур соединительных туннельных диодов: n^{++}-GaAs(δSi)/p^{++}-$Al_{0.4}Ga_{0.6}As$(C) и n^{++}-GaAs(δSi)/*i*-GaAs/p^{++}-$Al_{0.4}Ga_{0.6}As$:(C). Получены температурные зависимости основных параметров ТД: плотности пикового туннельного тока – (J_p) и дифференциального сопротивления – (R_d). В образцах туннельных диодов структуры с *i*-слоем, получены на порядок большие значения J_p и на порядок меньшие значения R_d, с более высокой температурной стабильностью, чем в образцах структуры без *i*-слоя. Полученные результаты полезны при разработке и создании монолитных многопереходных фотопреобразователей мощного лазерного излучения.

Ключевые слова: туннельный диод, фотоактивные *p*-*n* переходы, многопереходные лазерные фотопреобразователи, вольтамперные характеристики, пиковое значение плотности туннельного тока, дифференциальное сопротивление

Ссылка при цитировании: Калиновский В.С., Малеев Н.А., Васильев А.П., Контрош Е.В., Толкачев И.А., Прудченко К.К., Устинов В.М. Термостабильные соединительные туннельные диоды GaAs/AlGaAs для многопереходных фотопреобразователей лазерного излучения // Научно-технические ведомости СПбГПУ. Физико-математические науки. 2024. Т. 17. № 1.1. С. 165–170. DOI: https://doi.org/10.18721/ JPM.171.127

Статья открытого доступа, распространяемая по лицензии CC BY-NC 4.0 (https://creativecommons.org/licenses/by-nc/4.0/)

Introduction

Improving the parameters of monolithic multijunction photoconverters (MJ PCs) of laser radiation [1] is associated with an increase in the number of photoactive sub-elements connected to each other by back-to-back nanosized and optically transparent tunnel diodes (TDs). The process of epitaxial growth of the structure of a monolithic MJ PCs leads to blurring of profiles and mutual compensation, for example, Si and Be dopant atoms in degenerate nanolayers of GaAs/AlGaAs TD, and, as a consequence, to degradation of the current-voltage characteristic of the TD and MJ PCs parameters. A possible solution to eliminate the degradation of the current-voltage characteristic is the use, for example, carbon as an acceptor impurity. Additionally, we proposed the use of an intermediate, undoped *i*-nanolayer of GaAs between the degenerate n^{++} and p^{++} layers [2]. According to previous numerical simulations of n^{++}-GaAs/*i*-GaAs/p^{++}-$Al_xGa_{1-x}As$ ($x \geq 0.2$) TDs, the inclusion of an *i*-nanolayer makes it possible to increase the peak tunneling current density (J_p). Using models of nonlocal band-to-band quantum tunneling and trap assisted tunneling, the nonmonotonic dependence of the tunneling current J_p on the *i*-nanolayer thickness with the presence of a maximum was shown. In addition, the operating temperature of an MJ PCs in the photovoltaic mode when excited by powerful monochromatic radiation can increase up to 80 °C [3, 4], depending on the efficiency of heat removal and the magnitude of the incident optical power. As the operating temperature increases, the connecting TDs in the MJ PCs must provide consistently high J_p values exceeding the photocurrent density and low differential resistance values while maintaining maximum optical transparency. The lack of temperature stability of the TD parameters will affect the photoelectric parameters of the MJ PCs. Taking into account the results of previously performed modeling [2], in the temperature range from 25 °C to 80 °C, studies of the current-voltage characteristics of TDs based on two types of n^{++}-GaAs/p^{++}-$Al_{0.4}Ga_{0.6}As$ and n^{++}-GaAs/*i*-GaAs/p^{++}-$Al_{0.4}Ga_{0.6}As$ structures were carried out.

Materials and Methods

Using the molecular beam epitaxy (MBE) method, two types of TD structures were grown on *n*-type GaAs substrates (diameter 76.2 mm): A (see Table 1) and B (see Table 2). The structures are a tunnel n^{++}-GaAs/p^{++}-$Al_{0.4}Ga_{0.6}As$ heterojunction. Degenerate GaAs n^{++}-type δ-layers are doped with Si, and p^{++}-$Al_{0.4}Ga_{0.6}As$ layers are doped with C atoms. The doping levels of the n^{++} and p^{++} layers in the structures were, respectively, $\geq 1 \cdot 10^{19}$ cm^{-3} and ~ $1 \cdot 10^{20}$ cm^{-3}. The growth of heavily doped regions for both structures was carried out in identical modes at a substrate temperature of ~ 535–550 °C.

© Калиновский В.С., Малеев Н.А., Васильев А.П., Контрош Е.В., Толкачев И.А., Прудченко К.К., Устинов В.М., 2024. Издатель: Санкт-Петербургский политехнический университет Петра Великого.

Table 1

Design of TD structure A

Layer type	Thickness, nm	$N_{A,D}$, cm^{-3}
p^+-GaAs:(C)	50	$2\cdot10^{19}$
p^+-Al$_{0.6}$Ga$_{0.4}$As:(C)	50	$1\cdot10^{19}$
p^{++}-Al$_{0.4}$Ga$_{0.6}$As:(C)	10	$1\cdot10^{20}$
n^{++}-GaAs:(δSi)	10	$\geq 1\cdot10^{19}$
n^+-Al$_{0.6}$Ga$_{0.4}$As:(δSi)	50	$4\cdot10^{18}$
n^+-GaAs:(Si)	200	$3\cdot10^{18}$
n^+-GaAs:(Si)	600000	$(1–3)\cdot10^{18}$

Table 2

Design of TD structure B

Layer type	Thickness, nm	$N_{A,D}$, cm^{-3}
p^+-GaAs:(C)	50	$2\cdot10^{19}$
p^+-Al$_{0.6}$Ga$_{0.4}$As:(C)	50	$1\cdot10^{19}$
p^{++}-Al$_{0.4}$Ga$_{0.6}$As:(C)	10	$1\cdot10^{20}$
i-GaAs	7	$\geq 5\cdot10^{14}$
n^{++}-GaAs:(δSi)	10	$\geq 1\cdot10^{19}$
n^+-Al$_{0.6}$Ga$_{0.4}$As:(δSi)	50	$4\cdot10^{18}$
n^+-GaAs:(Si)	200	$3\cdot10^{18}$
n^+-GaAs:(Si)	600000	$(1–3)\cdot10^{18}$

In comparison with structure A, in structure B an undoped i-GaAs layer with a thickness of ~ 7 nm was grown between degenerate n^{++}-GaAs:(δSi) and p^+-Al$_{0.6}$Ga$_{0.4}$As:(C) layers. The thickness of the i-layer was chosen taking into account the influence of temperature diffusion of the Si impurity during the subsequent growth of the monolithic structure of the MJ PCs [2]. The structures contained wide-gap n^+-Al$_{0.6}$Ga$_{0.4}$As:(δSi) and p^+-Al$_{0.6}$Ga$_{0.4}$As:(C) layers adjacent to the degenerate TD regions. These layers are necessary to prevent the temperature diffusion of dopant atoms from degenerate layers into the layers of photoactive sub-elements of the MJ PC. After completion of epitaxial growth of the grown heterostructures were annealing in an MBE chamber simulating the growth process of an MJ PC. The structures were annealed for 2 hours at a temperature of 580 °C at a pressure $p = 2\cdot10^{-7}$ Torr. TD chips with a mesa diameter of 225 μm were formed on the grown structures.

Results and Discussion

Directly on parts of structures A and B with manufactured TDs, current-voltage characteristics were measured in the temperature range from 25 °C to ~ 80 °C. The results are presented in Fig. 1, *a* (structure A) and Fig. 1, *b* (structure B), the current-voltage characteristics for structures without temperature annealing are indicated “before annealing”, and for structures after annealing – “after annealing”. The current-voltage characteristics were measured at a positive bias voltage of up to 0.6 V. It can be seen that the shape of the current-voltage characteristics of samples of structure A corresponds to a backward diode, which is explained by the insufficient level of degeneracy of the n^{++}-GaAs:(δSi) region [5]. The current-voltage characteristic does not show a section with a negative differential resistance, however, in the voltage range from 0 to 50 mV there is a quasi-linear section corresponding to band-to-band quantum tunneling.

In structure B, due to the presence of an undoped i-GaAs nanolayer between the degenerate n and p regions, a typical current-voltage characteristic of a TD (Esaki) is observed. Similar to structure A, the low Jp values for structure B compared to the results obtained earlier in [2] are due to an insufficient doping level of n^{++}-GaAs:(δSi) region (Table 1, 2), [2, 5].

The Fig. 2 illustrates the spread of J_p values for the quasi-linear section of the current-voltage characteristics of structure A and B. The type of structure is indicated on the abscissa axis, where A and B correspond to diodes without annealing, and “A anneal.” and “B anneal.” – diodes on annealed plate fragments. It can be seen that the maximum J_p value of the TD structure B is an order of magnitude higher compared to structure A. After annealing, the average J_p values for samples of both structures increased. Before annealing, the densities of the peak tunneling current in the quasi-linear section of structure A and the peak tunneling current of structure B are ~ 0.1 A/cm^2 and ~ 1 A/cm^2, and after annealing, ~ 0.15 A/cm^2 and ~ 1.5 A/cm^2, respectively. In addition, after annealing, the spread of J_p values increased, which may be due to uneven doping with carbon atoms and uneven diffusion of the Si impurity over the area of the epitaxial wafers due to the temperature gradient during the annealing process.

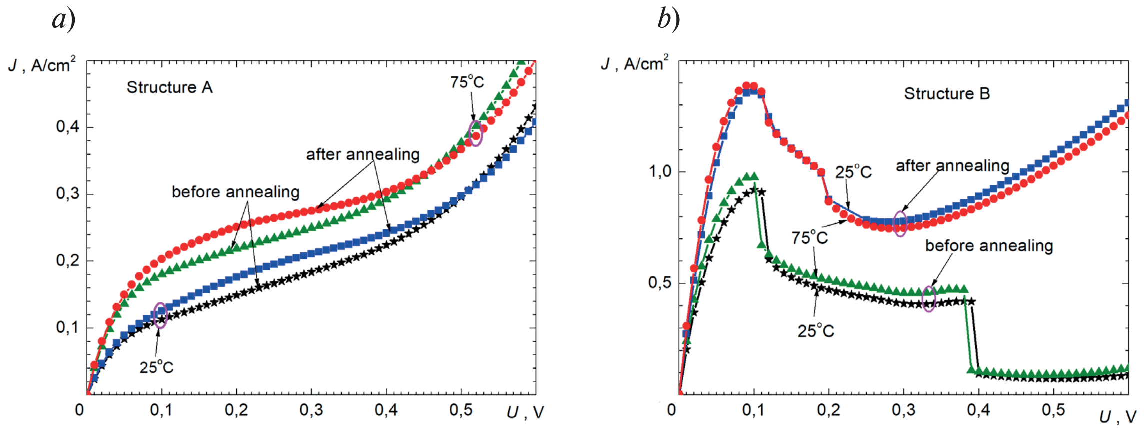

Fig. 1. Current-voltage characteristics of TD structures A-(*a*) and B-(*b*) at temperatures of 25 and 75 °C

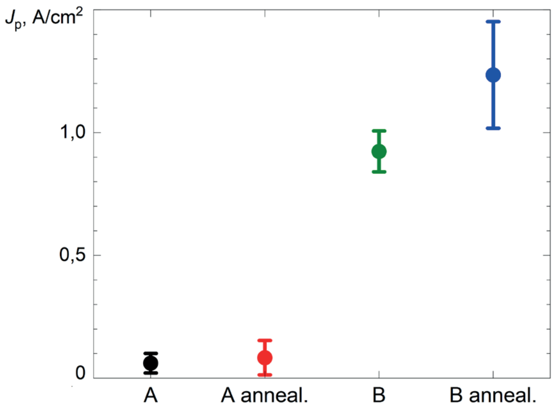

Fig. 2. Peak tunneling current density values for structures A and B before annealing (A, B) and after annealing (“A anneal.”, “B anneal.”)

From the current-voltage characteristics of TD structures A and B, measured in the temperature range (25–80) °C, the values of – J_p (Fig. 3, *a*) and differential resistance – R_d, which are responsible for parasitic losses when the voltage drops on the connecting TDs in MJ PCs, are calculated (Fig. 3, *b*). The temperature dependences of the calculated J_p и R_d parameters are presented in Fig. 3.

When heated from 25 to ~ 80 °C for structures A and B, an increase in J_p values is observed. This is due to a decrease in the band gap (E_g) of the semiconductor, a decrease in the height of the potential barrier, and an increase in the probability of quantum tunneling [6]. The best temperature stability of J_p is observed for TD samples of structure B (see Fig. 3, *a*), with the J_p value before annealing increasing by 6% and by 2% after annealing. For samples of structure A, the change in the maximum value of current density J_p is ~ 40%.

With an increase in the operating temperature of the TD from 25 to ~ 80 °C, a decrease in R_d values is observed for both structures. After annealing for TD structure B at T = 25 °C, R_d decreased by ~ 30% (from 67 mOhm·cm^2 to 46 mOhm·cm^2), and for structure A by ~ 6% (from 565 to 530 mOhm·cm2). For effective operation of the MJ PC, the connecting elements must provide the resistance of the linear section of the current-voltage characteristic at a forward bias voltage of less than 10 mOhm·cm^2 [4]. The increase in R_d can be due both to the diffusion of impurities and erosion of doping profiles, and to the presence of potential barriers created by isotype wide-gap n^+-$Al_{0.6}Ga_{0.4}As$:(δSi) and p^+-$Al_{0.6}Ga_{0.4}As$:(C) layers (Table 1 and 2), adjacent to the degenerate layers of the TD, which interfere with the transport of charge carriers [7]. The presence of the *i*-layer between the degenerate layers limits the interdiffusion of impurities and reduces the degradation of the current-voltage characteristics of the TD. The best temperature stability of R_d is observed for TD samples of structure B (see Fig. 3, *b*). When heated over the entire

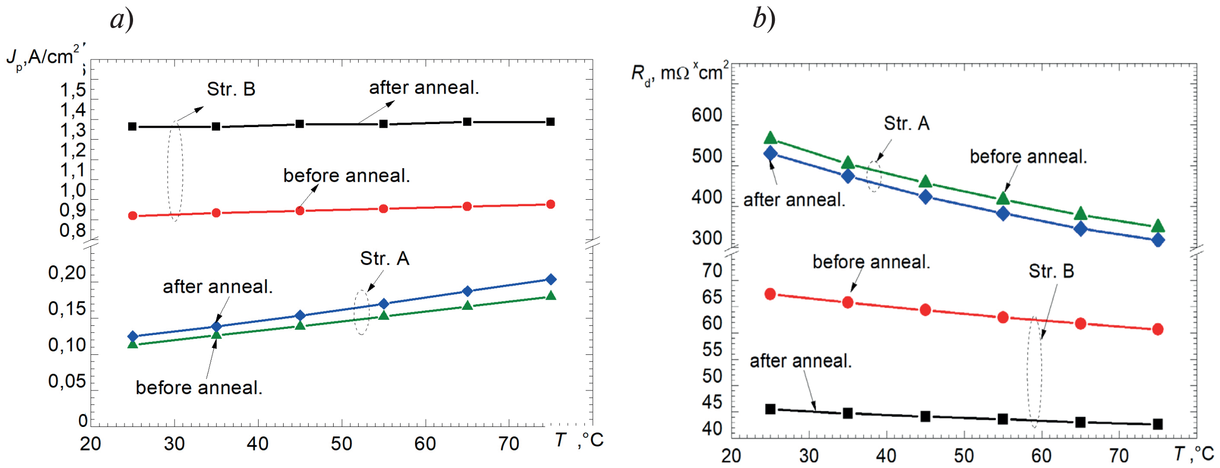

Fig. 3. Experimental temperature dependences of the parameters J_p (*a*) and R_d (*b*) for the samples of structures of types A and B before annealing and after annealing

temperature range, R_d for TD samples of structure B decreases by 9% from 67 to 61 mOhm·cm^2 before annealing and by 7% after annealing from 46 to 43 mOhm·cm^2. For structure A, upon heating, the R_d value changes by ~ 40% from 565 to 349 mOhm·cm^2 for TD samples before annealing and from 530 to 318 mOhm·cm^2 after annealing.

Conclusion

It has been experimentally demonstrated that the inclusion of a nanosized *i*-GaAs layer ($N_D \geq 5 \cdot 10^{14}$ cm^{-3}) between the degenerate n^{++}-GaAs:(δSi) (10nm) and p^{++}-Al$_{0.4}$Ga$_{0.6}$As:(C) (10 nm) regions of the connecting tunnel diode, even at a relatively low doping level of the n^{++}-layer, $N_D \geq 1 \cdot 10^{19}$ cm^{-3} ensures the presence of a tunneling current-voltage characteristic and promotes an increase in the peak tunneling current J_p by an order of magnitude compared to an identical structure, but without an *i*-GaAs layer. The results obtained are in qualitative agreement with the results of previously performed mathematical modeling of charge carrier transport in the proposed *p-i-n* structure of tunnel junction diodes. Tunnel diodes grown using molecular beam epitaxy n^{++}-GaAs:(δSi)/*i*-GaAs/p^{++}-Al$_{0.4}$Ga$_{0.6}$As:(C) provide an order of magnitude lower resistance values in the tunnel section of the current-voltage characteristic, higher temperature stability and maximum J_p values compared to the structure without *i*-layer. The proposed new design of the connecting TD provides good stability of characteristics under temperature influences corresponding to the regimes of epitaxial growth of monolithic MJ PC structures.

REFERENCES

1. **Zaitsev D.F., Andreev V.M., Bilenko I.A., Berezovsky A.A., Vladislavsky P.Yu., Gurfinkel Yu.B., Tsvetkova L.I., Kalinovsky V.S., Kondratyev N.M., Kosolobov V.N., Kurochkin V.F., Slipchenko S.O., Smirnov N.V., Yakovlev B.V.,** First radiophoton phased antenna array, Radiotekhnika. 85 (4) (2021) 153–164 (in Russian).

2. **Kalinovskii V.S., Kontrosh E.V., Klimko G.V., Ivanov S.V., Yuferev V.S., Ber B.Y., Andreev V.M.,** Development and Study of the *p–i–n* GaAs/AlGaAs tunnel diodes for multijunction converters of high-power laser radiation, Semiconductors. 54 (3) (2020) 355–361.

3. **Hoheisel R., Bett A.W., Warner J.H., Walter R., Jenkins P.,** Low temperature low intensity effects in III-V photovoltaic devices for deep space missions, Proc. IEEE 7th World Conf. Photovoltaic Energy Conversion (WCPEC) (A Joint Conf. 45th IEEE PVSC, 28th PVSEC & 34th EU PVSEC). June 10–15 (2018) 3763–3767.

4. **Lumb M.P., González M., Yakes M.K., Affouda C.A., Bailey C.G., Walters R.,** High temperature current–voltage characteristics of InP-based tunnel junctions, Prog. Photovoltaic. 23 (6) (2015) 773–782.

5. **Walukiewicz W.,** Intrinsic limitations to the doping of wide-gap semiconductors, Physica B: Condensed Matter. 302–303 (2001) 123–134.

6. **Sze S.M.,** Physics of semiconductor devices, 2nd Ed., A Wiley-Interscience Publ., J. Wiley & Sons, New York, Chichester, Brisbar, Toronto, Singapore, 1981.

7. **Bertness K.A., Friedman D.J., Olson J.M.,** Tunnel junction interconnects in GaAs-based multijunction solar cells, Proc. IEEE 1st World Conf. Photovoltaic Energy Conversion (WCPEC) (A Joint Conference of PVSC, PVSEC and PSEC). December 5–6 (1994) 1859–1862.

THE AUTHORS

KALINOVSKII Vitaliy S.
vitak.sopt@mail.ioffe.ru
ORCID: 0000-0003-4858-7544

MALEEV Nikolay A.
Maleev@beam.ioffe.ru
ORCID: 0000-0003-2500-1715

VASILYEV Aleksey P.
vasiljev@mail.ioffe.ru

KONTROSH Evgeniy V.
kontrosh@mail.ioffe.ru
ORCID: 0000-0003-1812-3714

TOLKACHEV Ivan A.
TolkachevIA@mail.ioffe.ru
ORCID: 0000-0001-8202-7087

PRUDCHENKO Kseniia K.
prudchenkokk@mail.ioffe.ru
ORCID: 0000-0003-4437-2984

USTINOV Viktor M.
Vmust@beam.ioffe.ru
ORCID: 0000-0002-6401-5522

Received 14.12.2023. Approved after reviewing 10.01.2024. Accepted 11.01.2024.

St. Petersburg Polytechnic University Journal. Physics and Mathematics. 2024 Vol. 17. No. 1.1
Научно-технические ведомости СПбГПУ. Физико-математические науки. 17 (1.1) 2024

Conference paper
UDC 537.9
DOI: https://doi.org/10.18721/JPM.171.128

Formation and light-emitting properties of ion-synthesized Ga_2O_3 nanoinclusions in the Al_2O_3/Si matrix

K.S. Matyunina [1] ✉, A.A. Nikolskaya [1], R.N. Kriukov [1],
P.A. Yunin [2, 1], D.S. Korolev [1]

[1] Lobachevsky State University of Nizhni Novgorod, Nizhny Novgorod, Russia
[2] Institute for Physics of Microstructures, Afonino, Nizhny Novgorod region, Russia
✉ matyunina.ks@gmail.com

Abstract. The regularities of ion synthesis of gallium oxide nanocrystalline inclusions by implantation of gallium and oxygen ions into dielectric Al_2O_3 films on silicon substrates and subsequent thermal annealing are considered. The composition of the implanted samples before and after annealing was investigated by X-ray photoelectron spectroscopy with layer-by-layer profiling. The formation of Ga-O chemical bonds was demonstrated, and after annealing gallium is predominantly in the fully oxidized state. According to X-ray diffraction data, the formation of β-Ga_2O_3 crystalline phase was confirmed. The study of photoluminescence of the synthesized samples revealed the presence of luminescence band, which is presumably caused by radiative recombination of donor-acceptor pairs.

Keywords: nanocrystals, gallium oxide, ion synthesis, photoluminescence, X-Ray photoelectron spectroscopy, X-Ray diffraction

Funding: This research was funded by Russian Science Foundation, grant number 21-79-10233 (https://rscf.ru/en/project/21-79-10233/). XRD measurements were carried out in Laboratory of Diagnostics of Radiation Defects in Solid State Nanostructures established, with the financial support of Ministry of Science and Higher Education of Russian Federation (No. 0030-2021-0030).

Citation: Matyunina K.S., Nikolskaya A.A., Kriukov R.N., Yunin P.A., Korolev D.S., Formation and light-emitting properties of ion-synthesized Ga_2O_3 nanoinclusions in the Al_2O_3/Si matrix, St. Petersburg State Polytechnical University Journal. Physics and Mathematics. 17 (1.1) (2024) 171–177. DOI: https://doi.org/10.18721/JPM.171.128

This is an open access article under the CC BY-NC 4.0 license (https://creativecommons.org/licenses/by-nc/4.0/)

Материалы конференции
УДК 537.9
DOI: https://doi.org/10.18721/JPM.171.128

Формирование и светоизлучающие свойства ионно-синтезированных нановключений Ga_2O_3 в матрице Al_2O_3/Si

К.С. Матюнина [1] ✉, А.А. Никольская [1], Р.Н. Крюков [1],
П.А. Юнин [2, 1], Д.С. Королев [1]

[1] Нижегородский государственный университет им Н.И. Лобачевского, г. Нижний Новгород, Россия;
[2] Институт Физики Микроструктур РАН, д. Афонино, Нижегородская обл., Россия
✉ matyunina.ks@gmail.com

Аннотация. Рассмотрены закономерности ионного синтеза нанокристаллических включений оксида галлия при имплантации ионов галлия и кислорода в

© Matyunina K.S., Nikolskaya A.A., Kriukov R.N., Yunin P.A., Korolev D.S., 2024. Published by Peter the Great St. Petersburg Polytechnic University.

диэлектрические пленки Al_2O_3 на подложках кремния и последующего термического отжига. Методом рентгеновской фотоэлектронной спектроскопии с послойным профилированием исследован состав имплантированных образцов до и после отжига. Продемонстрировано образование химических связей Ga-O, причем после отжига галлий находится преимущественно в полностью окисленном состоянии. По данным рентгеновской дифракции подтверждено формирование кристаллической фазы β-Ga_2O_3. Исследование фотолюминесценции синтезированных образцов выявило наличие полосы люминесценции, которая предположительно обусловлена излучательной рекомбинацией донорно-акцепторных пар.

Ключевые слова: нанокристаллы, оксид галлия, ионный синтез, фотолюминесценция, рентгеновская фотоэлектронная спектроскопия, рентгеновская дифракция

Финансирование: Исследование выполнено при финансовой поддержке Российского научного фонда, грант № 21-79-10233 (https://rscf.ru/en/project/21-79-10233/). XRD-измерения проведены в Лаборатории диагностики радиационных дефектов в твердотельных наноструктурах, созданной при финансовой поддержке Министерства науки и высшего образования РФ (№ 0030-2021-0030).

Ссылка при цитировании: Матюнина К.С., Никольская А.А., Крюков Р.Н., Юнин П.А., Королев Д.С. Формирование и светоизлучающие свойства ионно-синтезированных нановключений Ga_2O_3 в матрице Al_2O_3/Si // Научно-технические ведомости СПбГПУ. Физико-математические науки. 2024. Т. 17. № 1.1. С. 171–177. DOI: https://doi.org/10.18721/ JPM.171.128

Статья открытого доступа, распространяемая по лицензии CC BY-NC 4.0 (https:// creativecommons.org/licenses/by-nc/4.0/)

Introduction

The study of properties of gallium oxide-based materials has attracted great interest in the last few years due to its unique properties, including a large band gap width (~ 5 eV), high values of breakdown voltages, as well as sensitivity to UV radiation and various gases [1]. This opens up prospects for the application of Ga_2O_3 as a basic material for a new generation of power electronics devices, solar-blind photodetectors, gas sensors and other devices. Despite the availability of technology for the growth of large-diameter single-crystal wafers, due to their low availability and high cost, they have not yet found practical application. Difficulties also remain in the development of thin-film technology of Ga_2O_3 deposition on crystalline substrates. An alternative to such approaches is the development of technology for the fabrication of Ga_2O_3-based nanostructures. However, to date, the results have been obtained only for the synthesis of nanoinclusions using chemical technologies [2], which is not compatible with microelectronics. One of the promising variants for the development of technology of nanostructuring is the ion synthesis of Ga_2O_3 nanocrystals (nc-Ga_2O_3) in solid-state matrices. Ion implantation has already demonstrated its efficiency in Ga_2O_3 technology [3, 4]. At the same time, the ion synthesis method has also been successfully validated for the formation of semiconductor nanoinclusions of Si [5], SiC [6], ZnO [7] and In_2O_3 [8]. Previously, the possibility of ion synthesis of nc-Ga_2O_3 in SiO_2/Si matrix was demonstrated [9, 10]. In this work, we investigate the formation and light-emitting properties of ion-synthesized Ga_2O_3 nanoinclusions in Al_2O_3/Si matrix.

Materials and Methods

Al_2O_3 films (200 nm) deposited on Si (100) substrates by electron-beam evaporation were used as initial samples. The samples were irradiated with Ga^+ ($5\cdot10^{16}$ cm^{-2}, 80 keV) and O^+ ($6\cdot10^{16}$ cm^{-2}, 23 keV) ions with variation of the irradiation order. Implantation of only Ga^+ ions without additional oxygen irradiation was also carried out. The irradiation parameters were selected for maximum coincidence of the ion distribution profiles calculated with the SRIM program (www.srim.org). The samples were annealed in a tube furnace at temperatures of 300, 500, 700, and 900 °C (30 min each) in dried N_2 atmosphere.

© Матюнина К.С., Никольская А.А., Крюков Р.Н., Юнин П.А., Королев Д.С., 2024. Издатель: Санкт-Петербургский политехнический университет Петра Великого.

The chemical composition of implanted samples before and after annealing was studied by X-ray photoelectron spectroscopy (XPS) with layer-by-layer ion etching. The photoelectron lines O 1*s*, C 1*s*, Ga $2p_{3/2}$ and Si 2*s* were registered. To obtain the depth distribution profiles, etching with 1-keV Ar^+ ions was used. The depth calibration was carried out by measuring the step height after etching by atomic force microscopy. The structure of the samples was studied by X-ray diffraction (XRD) on a Bruker D8 Discover diffractometer using Cu Kα radiation. The spectra were recorded using a LinxEye linear PSD detector. Photoluminescence (PL) spectra were recorded using the standard lock-in technique at room temperature. Laser-driven light source XWS-65 with optical light filter, highlighting the spectral region with a width of ~ 10 nm with a maximum at a wavelength of 245 nm, was used as a source.

Results and Discussion

Ion synthesis of nanocrystalline inclusions in dielectric matrices assumes the appearance of chemical bonds between phase-forming atoms with the subsequent formation of first small clusters and then clusters of large size. To analyze the chemical composition of the implanted samples before and after annealing, the XPS method was used, which, along with information on the depth distribution of elements, also provides information on their chemical state. Fig. 1 shows the depth distributions of implanted gallium with regard to its chemical state for different ion synthesis variants used. Let us consider the chemical bonding distribution for the implanted Al_2O_3/Si samples without annealing. In the sample implanted only with Ga^+ without oxygen ion irradiation, all gallium atoms are presented in the elemental state. The observed effect is different from the case of Ga^+ implantation in the SiO_2/Si matrix, where its oxidation was previously found when implanted under the same conditions without additional annealing [10].

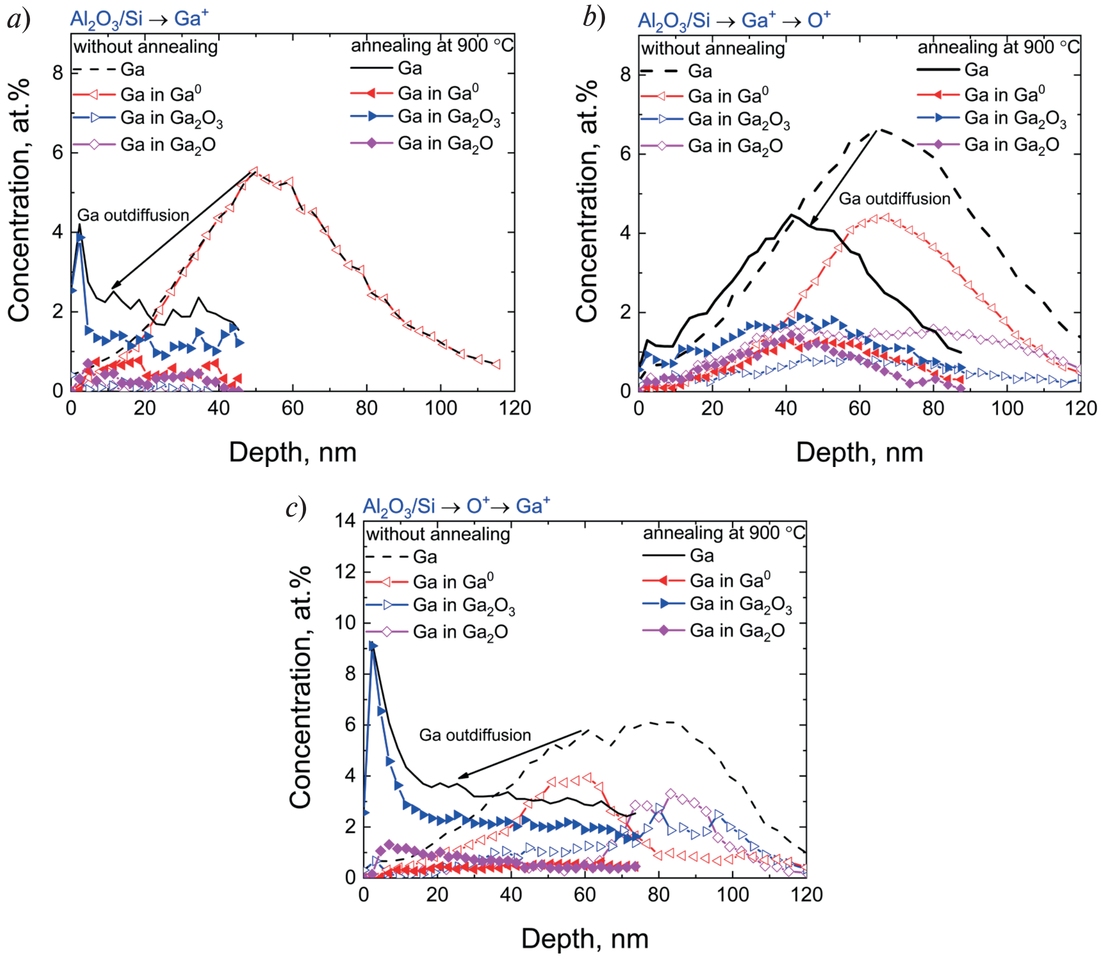

Fig. 1. XPS spectra for the Al_2O_3/Si samples, implanted with Ga^+ (*a*), $Ga^+ \to O^+$ (*b*) and $O^+ \to Ga^+$ (*c*), before and after annealing at 900 °C

Apparently, this may be due to the higher resistance of the Al_2O_3 matrix to ion irradiation compared to the SiO_2 matrix. Oxygen ion irradiation after Ga^+ irradiation leads to partial oxidation of gallium mainly in the oxygen-deficient state (Ga_2O). In the case of O^+ ion irradiation before Ga^+ implantation, a bimodal profile of impurity distribution is observed, with the first maximum containing gallium mainly in the elemental state and located closer to the surface, whereas the deeper maximum is due to gallium in the oxidized state with approximately the same concentration in the stoichiometric (Ga_2O_3) and non-stoichiometric (Ga_2O) states. It can be assumed that Ga^+ ion irradiation of a sample supersaturated with oxygen promotes redistribution of the latter toward greater depths as a result of interaction with stopping gallium atoms. This leads to the fact that a part of implanted gallium stopped closer to the surface, where it forms the elemental gallium phase, while its other part in the region of the end of ion range appears in the strongly oxygen supersaturated region, which leads to more favorable conditions for gallium oxidation.

Annealing at 900 °C leads to a significant outdiffusion of implanted gallium. This effect is most noticeable for implantation of Ga^+ ions only, where a decrease in its concentration to a value not exceeding 2 at % is observed. In the sample implanted in the $Ga^+ \rightarrow O^+$ order, annealing leads to a slight decrease in the total gallium concentration in the sample, with the concentration of Ga in the elemental state decreasing, whereas the concentration of gallium in the stoichiometric Ga_2O_3 state increased compared to the sample without annealing. For the sample in which O^+ ions were implanted before gallium, a significant change in the shape of the distribution profile with a pronounced diffusion of gallium atoms towards the surface is observed. At the same time, practically all the introduced gallium appears in the oxidized state of stoichiometric oxide Ga_2O_3. This fact demonstrates that annealing leads to an increase in the efficiency of formation of Ga-O chemical bonds, which is a necessary condition for the formation of Ga_2O_3 nanoinclusions.

The structure of the samples after annealing at 900 °C was studied by X-ray diffraction in θ-2θ geometry. The diffraction patterns are shown in Fig. 2. For the sample irradiated only with Ga^+ ions, no diffraction peaks appeared. In the case of additional irradiation with oxygen ions, both before and after Ga^+ implantation, a peak at $2\theta \approx 31.5°$ appears on the diffraction curves, which corresponds to the reflection from the (002) planes for crystalline β-Ga_2O_3 (JCPDS Card No. 41-1103). The intensity of this peak is rather low, which indicates a small volume fraction of the formed nanocrystals.

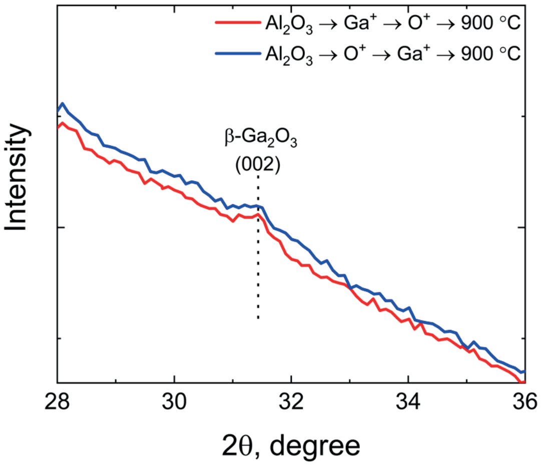

Fig. 2. XRD spectra for the Al_2O_3/Si samples, implanted with Ga^+ and O^+ ions with the different sequence of irradiation, after annealing at 900 °C

Let's proceed to consideration of light-emitting properties of irradiated samples before and after annealing (Fig. 3). The study of photoluminescence of irradiated samples without annealing and samples after annealing at 300 °C did not reveal the appearance of luminescent lines in the studied region. Annealing at 500 °C leads to the appearance of PL in the region of 400–500 nm for the sample irradiated first by Ga^+ ions, then by O^+ ions. Increasing the annealing temperature up to 700 °C leads to the appearance of PL also for the sample irradiated only by Ga^+ ions, and after the final annealing at 900 °C PL in the region of 380–550 nm is observed for all the

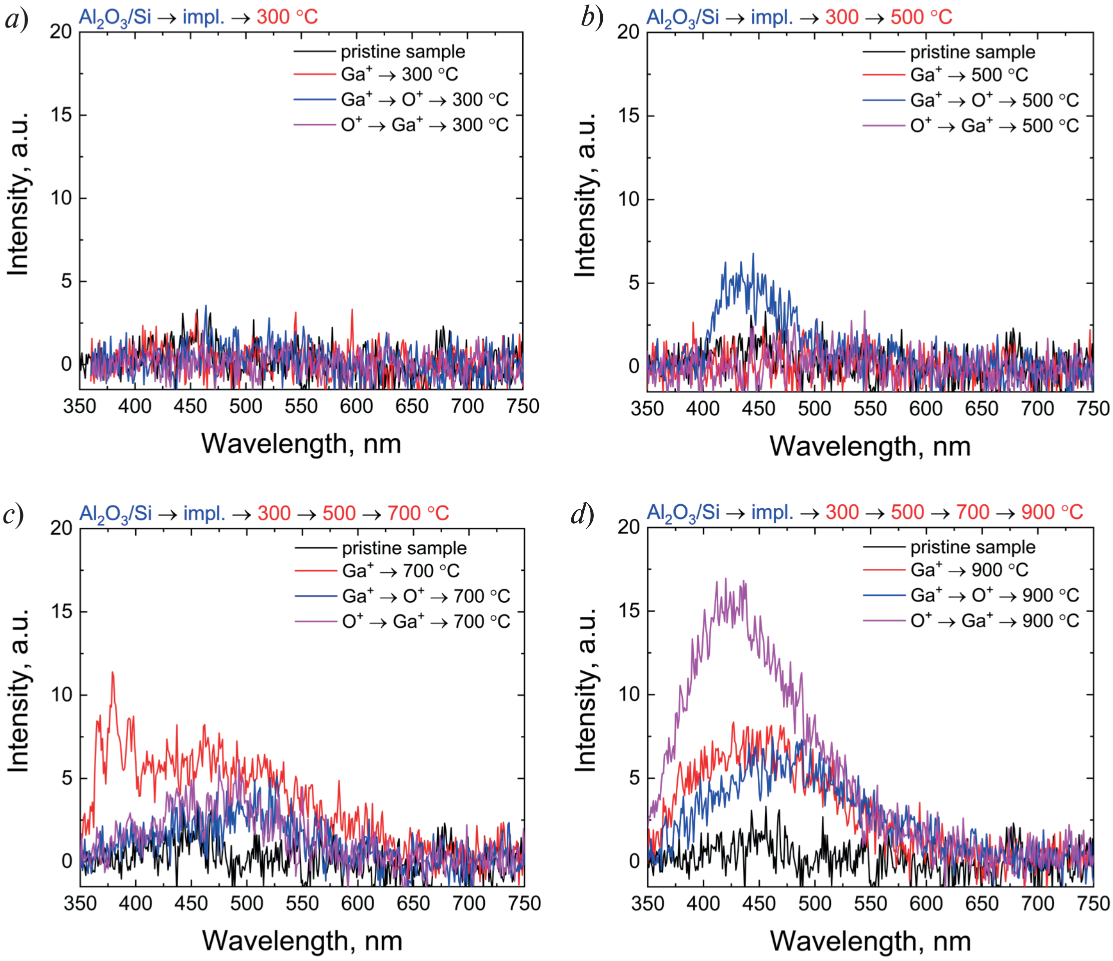

Fig. 3. PL spectra for the Al_2O_3/Si samples, implanted with Ga^+ and O^+ ions, after annealing at 300 (*a*), 500 (*b*), 700 (*c*) and 900 °C (*d*)

studied samples, while the intensity and shape of the line depends on the order of ion irradiation. The sample that was irradiated with oxygen before gallium implantation has the highest PL intensity. This correlates with the XPS data, according to which this sample shows the maximum concentration of gallium in the stoichiometric Ga_2O_3 oxide state.

The most probable mechanism of PL occurrence in the studied samples is radiative recombination of donor-acceptor pairs (DAP), where an oxygen vacancy (V_O) acts as a donor and a defect complex consisting of a pair of gallium and oxygen vacancies ($V_{Ga} + V_O$) acts as an acceptor. The spectral composition of this line is determined primarily by the defect composition of the synthesized nc-Ga_2O_3, since the energy of the radiative transition depends on the position of the V_O in the unit cell, which takes part in the formation of the defect complex – O_I, O_{II} or O_{III} [11]. The energies of these transitions, according to [11], are 3.04, 2.66, and 2.86 eV, respectively. The contribution to the resulting PL spectrum is determined by the ratio between the concentrations of these defects. Another important factor is a possible quantum-size effect with a shift of the luminescence maximum as a function of the nanoparticle size [12]. In favor of this factor is evidenced by the fact that the PL spectra differ for different synthesis conditions of nc-Ga_2O_3. Additional studies are required to establish precisely the mechanism of the observed PL.

Conclusion

The regularities of formation of light-emitting Ga_2O_3 nanoinclusions obtained by ion synthesis in Al_2O_3/Si matrix have been investigated. The study of the chemical composition demonstrated the formation of Ga-O bonds, which are the structural element for the formation of nanoinclusions, both before and after high-temperature annealing. Annealing leads to gallium outdiffusion, however, the content of gallium in the stoichiometric Ga_2O_3 oxide state increases. X-ray diffraction study of the structure revealed the appearance of a diffraction peak due to reflection from the (002) planes for β-Ga_2O_3 nanocrystals. Annealing at 900 °C for all used variants of ion synthesis leads to the appearance of photoluminescence in the region of 400–500 nm, presumably associated with the recombination of donor-acceptor pairs in gallium oxide. Thus, in this work, the possibility of synthesizing light-emitting Ga_2O_3 nanocrystals in Al_2O_3 on silicon matrix was demonstrated. This opens up the prospect of using this approach for creating gallium oxide nanomaterials for the development of new generation electronic devices.

Acknowledgments

This research was funded by Russian Science Foundation, grant number 21-79-10233 (https://rscf.ru/en/project/21-79-10233/). XRD measurements were carried out in Laboratory of Diagnostics of Radiation Defects in Solid State Nanostructures, with the financial support of Ministry of Science and Higher Education of Russian Federation (No. 0030-2021-0030). The authors are grateful to V.K. Vasiliev and D.V. Guseinov for ion irradiation experiments, and to A.V. Zdoroveyshchev for sputtering Al_2O_3 films.

REFERENCES

1. **Pearton S.J., Yang J., Cary P.H., Ren F., Kim J., Tadjer M.J., Mastro M.A.,** A review of Ga_2O_3 materials, processing, and devices, Applied Physics Review. 5 (2018) 011301.

2. **Chiang J.-L., Yadlapalli B., Chen Mu-I, Wuu D.-S.,** A Review on Gallium Oxide Materials from Solution Processes, Nanomaterials. 12 (2022) 3601.

3. **Azarov A., Fernández J. G., Zhao J., Djurabekova F., He H., He R., Prytz O., Vines L., Bektas U., Chekhonin P., Klingner N., Hlawacek G., Kuznetsov A.,** Universal radiation tolerant semiconductor, Nature Communications. 14 (2023) 4855.

4. **Nikolskaya A., Okulich E., Korolev D., Stepanov A., Nikolichev D., Mikhaylov A., Tetelbaum D., Almaev A., Bolzan C.A., Buaczik, Jr.A., Giulian R., Grande P.L., Kumar A., Kumar M., Gogova D.,** Ion implantation in β-Ga_2O_3: Physics and technology, Journal of Vacuum Science & Technology A. 39 (2021) 030802.

5. **Shimizu-Iwayama T., Nakao S., Saitoh K.,** Visible photoluminescence in Si-implanted thermal oxide films on crystalline Si, Appl. Phys. Lett. 65 (1994) 1814.

6. **Garrido B., López M., Ferré S., Romano-Rodríguez A., Pérez-Rodríguez A., Ruterana P., Morante J.R.,** Visible Photoluminescence of SiO2 Implanted with Carbon and Silicon, Nucl. Instruments Methods Phys. Res. Sect. B. 120 (1996) 101–105.

7. **Parkhomenko I., Vlasukova L., Komarov F., Makhavikou M., Milchanin O., Wendler E., Zapf M., Ronning C.,** Luminescence of ZnO Nanocrystals in Silica Synthesized by Dual (Zn, O) Implantation and Thermal Annealing, J. Phys. D. Appl. Phys. 54 (2021) 265104.

8. **Rajamani S., Arora K., Konakov A., Belov A., Korolev D., Nikolskaya A., Mikhaylov A., Surodin S., Kriukov R., Nikolitchev D., Sushkov A., Pavlov D., Tetelbaum D., Kumar A., Kumar M.,** Deep UV narrow-band photodetector based on ion beam synthesized indium oxide quantum dots in Al_2O_3 matrix, Nanotechnology. 29 (2018) 305603.

9. **Korolev D.S., Matyunina K.S., Nikolskaya A.A., Kriukov R.N., Nezhdanov A.V., Belov A.I., Mikhaylov A.N., Sushkov A.A., Pavlov D.A., Yunin P.A., Drozdov M.N., Tetelbaum D.I.,** Ion-Beam Synthesis of Gallium Oxide Nanocrystals in a SiO_2/Si Dielectric Matrix, Nanomaterials. 12 (2022) 1840.

10. **Korolev D.S., Kriukov R.N., Matyunina K.S., Nikolskaya A.A., Belov A.I., Mikhaylov A.N., Sushkov A.A., Pavlov D.A., A. and Tetelbaum D.I.,** Structure and Chemical Composition of Ion-Synthesized Gallium Oxide Nanocrystals in Dielectric Matrices, Nanomaterials. 13 (2023) 1658.

11. **Zhu X., Zhang Y.-W., Zhang S.-N., Huo X.-Q., Zhang X.-H., Li Z.-Q.,** Defect energy levels in monoclinic β-Ga_2O_3, Journal of Luminescence. 246 (2022) 118801.

12. **Wang T., Farvid S., Abulikemu M., Radovanovic P.,** Size-Tunable Phosphorescence in Colloidal Metastable γ-Ga_2O_3 Nanocrystals, J. Am. Chem. Soc. 132 (2010) 9250–9252.

THE AUTHORS

MATYUNINA Kristina S.
matyunina.ks@gmail.com
ORCID: 0000-0002-9856-3543

NIKOLSKAYA Alena A.
nikolskaya@nifti.unn.ru

KRIUKOV Ruslan N.
kryukov@unn.ru

YUNIN Pavel A.
Yunin@ipmras.ru

KOROLEV Dmitry S.
dmkorolev@phys.unn.ru

Received 14.12.2023. Approved after reviewing 30.01.2024. Accepted 21.02.2024.

CONFERENCE ORGANIZERS AND SPONSORS

Organizers

Peter the Great St. Petersburg Polytechnic University (SPbPU)
Alferov University, Saint Petersburg
Ioffe Institute, Saint Petersburg
St. Petersburg State University
Russian-Armenian University, Yerevan

Sponsors

Ministry of Science and Higher Education of the Russian Federation (state assignment)
St. Petersburg Electrotechnical University
Tydex LLC, Saint Petersburg

Program Committee

R.A. Suris, Ioffe Institute, St. Petersburg (*Chair*)
D.A. Firsov, Peter the Great St. Petersburg Polytechnic University (*Vice-Chair*)

V.Ya. Aleshkin, Istitute for Physics of Microstructures, Nizhny Novgorod

V.F. Agekyan, St. Petersburg State University

S.Yu. Verbin, St. Petersburg State University

M.M. Glazov, Ioffe Institute, St. Petersburg

A.E. Zhukov, Alferov University, Saint Petersburg

V.I. Zubkov, Saint-Petersburg Electrotechnical University

M.S. Kagan, Institute of Radioengineering and Electronics, Moscow

V.P. Kochereshko, Ioffe Institute, St. Petersburg

I.V. Rozhansky, Ioffe Institute, St. Petersburg

H.A. Sarkisyan, Russian-Armenian University, Yerevan

D.R. Khokhov, Moscow State University

T.V. Shubina, Ioffe Institute, St. Petersburg

Organizing Committee

D.A. Firsov, Peter the Great St. Petersburg Polytechnic University, (Chair)
M.Ya. Vinnichenko, SPbPU, Peter the Great St. Petersburg Polytechnic University (Vice-Chair)
N.Yu. Kharin, SPbPU, Peter the Great St. Petersburg Polytechnic University (*Secretary*)

*E.V. Vladimirskay*a, SPbPU
T.A. Gavrikova, SPbPU
V.E. Gasumyants, SPbPU
A.Yu. Egorov, Alferov University
V.A. Zykov, SPbPU
V.P. Kochereshko, Ioffe Institute
G.A. Melentev, SPbPU
V.Yu. Panevin, SPbPU
A.D. Petruk, SPbPU
H.A. Sarkisyan, Russian-Armenian University
A.V. Filimonov, Alferov University
V.A. Shalygin, SPbPU
I.I. Schipacheva, SPbPU

Journal

ST. PETERSBURG STATE POLYTECHNICAL UNIVERSITY JOURNAL: PHYSICS AND MATHEMATICS

Vol. 17, No. 1.1, 2024

Founder and publisher: Peter the Great St. Petersburg Polytechnic University

The journal is registered with the Federal Service for Supervision of Communications,
Information Technology and Mass Media (Roskomnadzor).
Certificate ПИ ФС77-51457 issued 19.10.2012.

Editorial Office

Dr. Prof. *V.K. Ivanov*, Editor-in-Chief
Dr. Prof. *A.E. Fotiadi*, Deputy Editor-in-Chief
Dr. Prof.*V.V. Dubov*
Dr. Prof. *P.A. Karaseov*
Dr. Assoc. Prof. *V.M. Kapralova*
A.S. Kolgatina, translator
N.A. Bushmanova, editorial manager

All papers presented are final author versions
Peer review is under responsibility of the Program Committee

Phone +7 (812) 552-62-16

Website https://physmath.spbstu.ru/

E-mail: physics@spbstu.ru

Typesetting by *N.A. Bushmanova*

Published 30.04.2024. Format 60x84/8. Digital print.

Printer's sheets   Print circulation 1000. Order ID .
